NUMERICAL STUDY OF ABUTMENT SCOUR IN COHESIVE SOILS

A Dissertation

by

XINGNIAN CHEN

Submitted to the Office of Graduate Studies of
Texas A&M University
in partial fulfillment of the requirements for the degree of

DOCTOR OF PHILOSOPHY

December 2008

Major Subject: Civil Engineering

NUMERICAL STUDY OF ABUTMENT SCOUR IN COHESIVE SOILS

A Dissertation

by

XINGNIAN CHEN

Submitted to the Office of Graduate Studies of
Texas A&M University
in partial fulfillment of the requirements for the degree of

DOCTOR OF PHILOSOPHY

Approved by:

Co-Chairs of Committee,	Jean-Louis Briaud
	Hamn-Ching Chen
Committee Members,	Kuang-An Chang
	William R. Bryant
Head of Department,	David V. Rosowsky

December 2008

Major Subject: Civil Engineering

ABSTRACT

Numerical Study of Abutment Scour in Cohesive Soils.

(December 2008)

Xingnian Chen, B.En., Tongji University, China;

M.En., Tongji University, China

Co-Chairs of Advisory Committee: Dr. Jean-Louis Briaud
Dr. Hamn-Ching Chen

This research is part of the extension of the SRICOS-EFA method for predicting the maximum scour depth history around the bridge abutment. The basic objective is to establish the equation for predicting the maximum bed shear stress around the abutment at the initial condition of scouring. CHEN3D (**C**omputerized **H**ydraulic **EN**gineering program for **3D** flow) program is utilized to perform numerical simulations and predict bed shear stress before scouring. The Chimera technique incorporated in CHEN3D makes the program capable of simulating all kinds of complex geometry and moving boundary. CHEN3D program has been proven to be an accurate method to predict flow field and boundary shear stress in many fields and used in bridge scour study in cohesive soils for more than ten years.

The maximum bed shear stress around abutment in open rectangular channel is studied numerically and the equation is proposed. Reynolds number is the dominant parameter, and the parametric studies have been performed based on the dimensional analysis. The influence of channel contraction ratio, abutment aspect ratio, water depth, abutment shape, and skew angle has been investigated, and the corresponding correction

factors have been proposed. The study of the compound channel configuration is conducted further to extend the application of the proposed equation.

Numerical simulations of overtopping flow in straight rectangular channel, straight compound channel and channel bend have been conducted. The bridge deck is found to be able to change the flow distribution and the bed shear stress will increase significantly once overtopping. The influence of the channel bend curvature, abutment location in the channel bend, and the abutment shape is also investigated. The corresponding variation of the bed shear stress has been concluded.

The scour models, including the erosion rate function, roughness effect, and the turbulence kinetic energy, have been proposed and incorporated into the CHEN3D program. One flume test case in NCHRP 24-15(2) has been simulated to determine the parameters for the roughness and the turbulence kinetic energy. The prediction of the maximum scour depth history with the proposed model is in good agreement with the measurement for most cases. The influence of overtopping flow on the abutment scour development is also studied and the corresponding correction factor is proposed.

ACKNOWLEDGMENTS

I would like to express my heartfelt gratitude to my co-chair, Dr. Jean-Louis Briaud, for giving me the opportunity to study at Texas A&M University. Dr. Briaud can always look deep into the situation to lead the best direction of the research. He is always ready to help and encourage me.

I would like to express my special gratitude to my co-chair, Dr. Hamn-Ching Chen for his time, effort and guidance. Dr. Chen took me into the world of computational fluid dynamics. It is my honor to have the opportunity to work with him.

I also would like to thank Dr. Kuang-An Zhang for his valuable discussion and guidance during the entire period of study at Texas A&M University. I wish to thank Dr. William R. Bryant for his constant support during my Ph.D. program.

I wish to express my particular appreciation to my fellow students Sueng Jae Oh, Po-Hung Yeh, Chao-Ming Chi, Wei Wang, and Jun Wang for their friendship and help during different phases of this research. I would like to especially thank Sueng Jae Oh for providing valuable experimental data.

This work is supported by NCHRP-Project 24-15(2) where Mr. David Reynaud is the contact person.

Finally, my appreciation goes to my wife, Yufen Shao, and my parents, for their encouragement and support during my study at Texas A&M University.

.

TABLE OF CONTENTS

Page

CHAPTER Page

LIST OF FIGURES

FIGURE Page

FIGURE Page

FIGURE Page

FIGURE Page

FIGURE Page

LIST OF TABLES

TABLE Page

CHAPTER I

INTRODUCTION

1.1 Background

Scour is the result of the erosive action of flowing water, excavating and carrying away materials from the bed and banks of streams and from around hydraulic structures, such as the piers and abutments of bridges. Based on the statistical data in HEC-18 (Richardson and Davis, 2001), scour is the most common cause of river bridge failures and responsible for 60% of 1000 bridge failures investigated from 1961 to 1991 (Shirole and Holt 1991).

Laboratory studies have been conducted extensively to evaluate the bridge scour on cohesionless soils, which have been well summarized in HEC-18 (Richardson and Davis, 2001). These methods are also valid for the bridge scour problem on cohesive soils since the ultimate scour depth in cohesive soils can be as deep as scour in cohesionless soils. However, the erosion rates are quite different for cohesionless and cohesive soils. Under constant flow rate, scour will reach maximum depth in cohesionless soils in hours, while it will take days for cohesive soils. Hence, to design the bridge cost-effectively, the time factor must be considered for the prediction of bridge scour in cohesive soils. In addition, flume tests used to derive the equations in HEC-18 (Richardson and Davis, 2001) were performed on simple channel geometry and flow conditions. Those complicated situations, such as bridge scour on channel bend, on

---

This dissertation follows the style and format of the *Journal of Fluid Mechanics.*

compound channel and under pressure flow, are still not investigated.

The recent NCHRP 24-15 project (Briaud, 2003) of bridge scour on cohesive soils has taken the time factor into the consideration, which solved the bridge scour prediction for complex pier and contracted channel, leaving the abutment scour on cohesive soils unsolved.

This research is part of the research project NCHRP 24-15(2) “Abutment Scour in Cohesive Soils”. The objective of NCHRP 24-15(2) is to develop a method for the prediction of abutment scour in cohesive soils consistent with the method developed for pier and contraction scour prediction in NCHRP Project 24-15. Briaud et al. (1999) have proposed a method called SRICOS to predict the scour depth versus time around a cylindrical bridge pier founded in cohesive soils. In NCHRP 24-15, SRICOS method has been extended to include the prediction of the maximum scour depth around complex piers and in the contracted river section. There are two important parameters in SRICOS method. One is the maximum scour depth around the bridge foundation and at the contracted section. The other one is the maximum bed shear stress at the location of the deepest scour hole.

1.2 Objectives

This research is concerned with the numerical study of the abutment scour in cohesive soils. The specific objectives of this study are:

1. To develop equation of the maximum bed shear stress around abutment on rectangular channel, taking into account the effect of water depth, the effect of channel contraction ratio, the effect of aspect ratio of the abutment and the

approach embankment, the effect of the abutment shape and the effect of attack angle of flow.

2. To further extend the equation of maximum bed shear stress equation around abutment on rectangular channel for compound channel situations, taking into account the effect of the compound channel configuration.
3. To study maximum bed shear stress around the abutment under complicated flow and geometry situations, such as pressure flow, bend channel and the confluence of the channel.
4. To verify the shear-stress model in the scour simulation on compound channel and further improve the prediction by including the roughness and the influence of flow turbulence.

1.3 Methodology

1.3.1 SRICOS-EFA method

Scour process on cohesive soils is usually termed as clear water scour. The basic mechanism, causing clear water scour on the bed of the streams and from around the bridge foundations, is the bed shear stress generated by the flow exceeding the critical shear stress of bed materials. Scour will initiate whenever the bed shear stress is higher than the critical shear stress. The difference of the bed shear stress and the critical shear stress determines the initial erosion rate. The bed shear stress is decreasing with the development of the scour. And the scouring ceases when the shear stress caused by the flow equals the critical shear stress of the bed materials. The hyperbolic equation has been successfully used to describe the scour depth development versus time, which

implies that the scour process depends on the initial scour rate and the ultimate scour depth (Briaud et al. 1999, 2001).

SRICOS stands for Scour Rate In COhesive Soil; it is a method to predict the scour depth versus time curve around a hydraulic structure founded in a cohesive soil. The detailed explanation of the method is presented in Briaud et al. (1999). The basic procedure is summarized in the following:

1. Obtain 76.2-mm diameter Shelby tube samples as close to the hydraulic structure as possible.
2. Perform EFA (Erosion Function Apparatus) tests on the samples to obtain the relation of the erosion rate $\dot{z}$ to the hydraulic shear stress τ.
3. Determine the initial maximum bed shear stress τ_{max} around the hydraulic structure before the scour process.
4. Obtain the initial scour rate $\dot{z}_i$ corresponding to τ_{max} on the $\dot{z}$ - τ curve.
5. Calculate the maximum scour depth z_{max}.
6. Develop the complete scour depth z versus time t curve.

$$z = \frac{t}{\frac{1}{\dot{z}_i} + \frac{t}{z_{max}}} \tag{1.1}$$

7. Predict the scour depth at the time corresponding to the duration of the flood by reading the z - t curve.

This method has the advantages of being simple, site specific and suitable for complicated conditions of multi-floods, multilayer soils and has been well verified in the completed NCHRP 24-15 (Briaud et al., 2003).

1.3.2 CHEN3D program

The CHEN3D (Computerized Hydraulic ENgineering program for 3D flow) computer program (Chen & Patel 1988, Chen et al. 1990, Chen 2002) is utilized in current research to perform the numerical simulations. Chimera domain decomposition approach has been incorporated into CHEN3D for time-domain simulation of the flow around complex hydraulic configurations. The turbulent flow is performed using the Reynolds-Averaged form of the Navier-Stokes equations. The entire computational domain can be divided into two regions in order to facilitate the implementation of two-layer turbulent model approach. One is the thin layer region around the solid boundary, applying one-equation turbulence model to account for the wall-damping effects. And the other one is the fully turbulent region away from the wall, employing the standard $k-\varepsilon$ two equation model to resolve the fully turbulent flow.

1.3.3 Maximum bed shear stress

The primary objective of this research is to determine the maximum bed shear stress around the abutment in river channel. It is very difficult to measure the bed shear stress accurately in the flume test. Hence, numerical simulation is utilized to provide τ_{max} in SRICOS-EFA method. The approach of reference case and correction factors in HEC-18 is adopted to establish the equation of maximum bed shear stress around abutment. Dimensional analysis is performed to determine the important parameters to be studied.

Flume tests can provide the velocity measurements and the initial erosion rate of the river bed, which can be used to verify the numerical simulation indirectly.

1.3.4 Scour model

In the present scour prediction method, the scour rate equation is experimentally obtained from EFA tests. In the numerical simulations, the incremental scour depth is computed according to the local bed shear stress and the scour rate equation. After the new scour depth distribution is obtained, the boundary fitted grid is updated automatically for the next time flow field and bed shear stress calculation. Stream bed roughness and turbulence properties have also been incorporated into the scour model to improve the scour development prediction.

1.4 Dissertation Outline

This dissertation consists of a number of numerical studies of the abutment scour in cohesive soils. The work is divided into three major parts: maximum bed shear stress around abutment in open channel flow, bed shear stress distribution in complex channel and pressure flow, and prediction of clear water scour.

An overview of existing knowledge is given in Chapter II. This chapter presents the literature review of current knowledge in mechanism of scour, bed shear stress study of pier scour, contraction scour and abutment scour and the advance of the numerical simulation on clear water scour prediction.

Mathematical formulation is presented in Chapter III. The CHEN3D program with its boundary conditions is mathematically explained. To close the equation, this chapter also covers two-layer turbulence model employed in the code. Also, this chapter

shows the numerical method, which consists of transformed plane, finite analytic method, and velocity/pressure coupling. An overall procedure is provided to describe the algorithm of a computational technique.

Chapter IV presents the numerical studies of maximum bed shear stress around abutment in open channel flow. The systematic numerical matrix is designed and conducted. An equation for maximum bed shear stress around a bridge abutment is proposed, taking into account the effect of water depth, the effect of channel contraction ratio, the effect of abutment aspect ratio, the effect of abutment shape, the effect of attack angle and the effect of the compound channel configuration. The proposed equation of maximum bed shear stress around abutment is verified indirectly according to the initial erosion rates from the flume tests.

Chapter V presents the numerical studies of bed shear stress distribution on complex channel geometries and under pressure flow conditions. The studies of the complex channels include the flow in straight compound channel with different flood plain elevations on both sides, channel bends of different R/W and abutment location, and the confluence of upstream channel. The studies of overtopping flow include the overtopping flow in straight symmetric channel, straight asymmetric channel, and in channel bends. The influence of the bridge deck and the channel geometry has been discussed according to the simulation results.

Chapter VI presents the numerical studies on clear water scour prediction. Shear stress model has been applied in the simulation of flume test cases and modified to include the influence of roughness and the turbulence effect. The scour development

under overtopping conditions is also conducted with the variation of water depth and the recommendation is proposed.

Chapter VII addresses the conclusions of the dissertation and recommendations for future research.

CHAPTER II

LITERATURE REVIEW OF BRIDGE SCOUR

2.1 Fundamentals of Bridge Scour

Bridge scour is the erosive action of flowing water, excavating and carrying away material from the bridge contracted streambeds and from around the bridge foundations. Scour at the bridge contracted zone is one type of contraction scour, which belongs to general scour; while scour around the bridge foundations is termed as local scour, including pier scour and abutment scour.

Contraction scour at bridge crossing is due to the reduction of flow area by the existence of the bridge foundation on river channel. From the continuity law, a decrease in flow area results in an increase in average velocity and bed shear stress across the entire contracted channel. Contraction scour initiates when the bed shear stress exceeds the critical bed shear stress of the bed material. As the bed elevation is lowered, the flow area increases and the velocity and bed shear stress decrease until the relative equilibrium is reached again. Contraction scour usually involves removal of material from the bed across all or most of the channel width.

Local scour at pier or abutment results from the formation of vortices at their base, which are usually called horseshoe vortex. Water can only pile up to increase pressure or go down to dig the riverbed when hitting the obstruction like pier or abutment. Downflow forms the horse shoe vortex, which is the major reason for the local scour. Increasing of the pressure will accelerate the flow around the bridge

foundation and take away the eroded material. In addition to the horseshoe vortex around bridge foundation, there are vertical vortices at downstream called the wake vortex. Wake vortices also contribute to the removal of bed material around bridge foundation. However, the wake vortices behind the bridge foundation will diminish rapidly as the downstream distance increases.

Factors affecting local scour at bridge foundation include the approaching flow, the bridge foundation configuration and channel geometry. Extensive researches have been done to study these influence. The observations are summarized as follows.

The influence of approaching flow comes from approaching velocity and approaching water depth. The higher the velocity, the deeper the local scour. However, the scour depth will increase with the water depth only when the water depth is relatively shallower than the size of the bridge foundation. For bridge pier, the water depth will have no influence when the water depth is larger than two times of the bridge diameter. For abutment, the influence will also depend on the size of the abutment.

The influence of bridge foundation configuration usually includes the projected foundation length normal to the flow, the shape of the nose of a pier or abutment, the attack angle of flow to the pier or abutment. For pier, the scour depth will increase with the increase of the projected length. But, the increment is smaller and smaller when the project length is larger and larger. The projected length of the abutment is not always a good measure for the local scour depth around abutment, especially when the abutment is very long and setting on the floodplain. The shape of the bridge foundation can have up to a 20 percent influence on the scour depth. And the attacking angle of the flow to

the bridge foundation also has a significant effect on the scour depth, which can be up to 20 percent.

Channel geometry here is classified as rectangular channel or compound channel and straight channel or bend channel. The study of channel geometry on the local scour is not as extensive as the flow condition and the bridge foundation configuration. Most of the testing is conducted on straight rectangular channel. The flow field in the straight rectangular channel is usually very uniform; while the bend channel and the compound channel can redistribute the flow and further change the channel conveyance capacity at the different section of the channel.

Scour can be identified as live-bed scour and clear-water scour according to the sediment transport characteristics. Live bed scour occurs when there is import of the bed material from upstream reach into the crossing. Live scour is cyclic in nature; the scour hole that develops during the rising stage of a flood refills during the falling stage. Clear-water scour occurs when there is no refill or deposition at the crossing. In such a case, the scour hole will not be refilled once the materials removed. This dissertation is the study of abutment scour on cohesive soils. So, all the contents about scour simulation will focus on clear water scour.

The scour problem has been systematically documented in HEC-18 (Richardson & Davis, 2001). Only the fundamental of bridge scour is summarized here.

2.2 Bed Shear Stress at the Bridge Crossing

Open channel flow may be laminar, transitional or turbulent. What type of flow occurs depends on the Reynolds number, $\mathrm{Re} = VR_h / \nu$, where V is the average velocity

, R_h is the hydraulic radius of the channel and ν is the kinematic viscosity of water. The general rule is that open channel flow is laminar if $\mathrm{Re} < 500$, turbulent if $\mathrm{Re} > 12{,}500$, and transitional otherwise. In fact, typical Reynolds numbers are quite large, well above the transitional value and into the wholly turbulent regime. The channel resistant force is independent of Reynolds number, dependent only on the relative roughness.

The resistant force in the constant depth channel flow has been studied many years ago. Under the assumption of steady uniform flow, the bed shear stress can be determined by the unit weight of water γ, hydraulic radius R_h and the energy slope S as following (Munson et al., 1998)

$$\tau = \gamma R_h S \tag{2.1}$$

Manning's equation (in SI unit) provides the dependence of average channel velocity V on the hydraulic radius R_h and the energy slope S,

$$V = \frac{R_h^{2/3} S^{1/2}}{n} \tag{2.2}$$

The parameter n is the Manning's resistance coefficient. Its value is dependent on the surface material of the channels' wetted perimeter and is obtained from experiments, having the unit of $s/m^{1/3}$.

Hence, the popular used bed shear stress equation in open channel flow can be derived by substituting equation (2.2) into equation (2.1),

$$\tau = \gamma n^2 V^2 R_h^{-1/3} \tag{2.3}$$

Contraction scour means the uniform bed elevation change across the entire contracted channel. The scour depth at the center of the channel is usually chosen to be the representative value. The bed shear stress at the constricted channel center will still follow the same rule of the open channel flow and the influence of viscous force can be ignored. All the influence of the bridge foundation can be involved by the correction of the average velocity in equation (2.3).

Nurtjahyo (2003) numerically studied the maximum bed shear stress at the center of the channel under long contraction. The equation is generated by correcting the open channel flow equation (2.3), including the effect of the contraction ratio k_{c-R}, the effect of contraction transition angle $k_{c-\theta}$, the effect of the contraction length k_{c-L}.

$$\tau_{contr\_\max} = k_{c-R} k_{c-\theta} k_{c-L} \gamma n^2 V^2 R_h^{-\frac{1}{3}} \tag{2.4}$$

$$k_{c-R} = 0.62 + 0.38\left(\frac{B_1}{B_2}\right)^{1.75}$$

$$k_{c-\theta} = 1 + 0.9\left(\frac{\theta}{90}\right)^{1.5}$$

$$k_{c-L} = \begin{cases} 1 & , for \;\; k_{c-L} \geq 0.35 \\ 0.77 + 1.36\left(\frac{L}{B_1 - B_2}\right) - 1.98\left(\frac{L}{B_1 - B_2}\right)^2 & , for \;\; k_{c-L} < 0.35 \end{cases}$$

where, γ is the unit weight of water, n is the Manning's coefficient, R_h is hydraulic radius, V is the upstream averaged velocity, B_1 is the upstream channel width, B_2 is the

channel width at the contracted zone, L is the length of the contracted zone, θ is the contraction transition angle.

For local bridge scour, like pier scour and abutment scour, the location of scour hole is right around the hydraulic structures. The bed shear stress features will be quite different from the preceding open channel bed shear stress. Bridge foundation will come in and affect the magnitude and the distribution of the bed shear stress. Besides those affecting factors in the open channel flow, the geometry and the setting of the bridge foundations will also strongly affect the local bed shear stress. In the analysis of the open channel flow, the viscous force (represented by Reynolds number) is ignored. Here, on local scour analysis, it is going to be the dominant factor.

Many researchers have studied the flow structure at bridge foundations and found out the similarity of the flow in and around the scour hole at pier and abutment, especially when the abutment is relatively short compared with the water depth (Melville, 1997). This implies that the bed shear stress should also have the similar trend around bridge pier and abutment.

Hjorth (1975) investigated the bed shear stress around circular pier. Two circular piers of 0.05m and 0.075m diameter were used in the flume test, combined with two different velocities of 0.15m/s and 0.30m/s and two different approach depths of 0.1m and 0.2 m. A hot-film probe was used to measure bed shear stress on the rigid flume bed. Hjorth tried to correlate the local maximum bed shear stress around pier with the approach bed shear stress and found the amplification factor of $\tau_{\max}/\tau_{approach}$ ranging from 5 to 11 for a circular pier.

Wei et al. (1997) studied the maximum bed shear stress around circular pier on constant depth cannel with 3D simulation. The maximum bed shear stress equation is proposed based on pier Reynolds number rather than the commonly used approach bed shear stress in open channel flow. The maximum bed shear stress is also found independent of water depth when the upstream flow is deeper than twice of the pier diameter.

$$\tau_{\max} = 0.094\rho V^2 \left[\frac{1}{\log \mathrm{Re}} - \frac{1}{10} \right] \tag{2.5}$$

where, $\mathrm{Re} = \frac{VB}{\nu}$, ρ is the flow density, V is the upstream averaged velocity, B is the diameter of the pier, ν is the kinematic viscosity of water.

Nurtjahyo (2003) further extended Wei's equation to the complex pier conditions, including the effect of water depth k_w, the effect of pier spacing k_{sp}, the effect of shape k_{sh}, and the effect of attack angle k_α.

$$\tau_{\max} = k_w k_{sp} k_{sh} k_\alpha \times 0.094\rho V^2 \left[\frac{1}{\log \mathrm{Re}} - \frac{1}{10} \right] \tag{2.6}$$

$$k_w = 1 + 16e^{-4\frac{H}{B}}$$

$$k_{sp} = 1 + 5e^{-1.1\frac{S}{B}}$$

$$k_{sh} = 1.15 + 7e^{-4\frac{L}{B}}$$

$$k_\alpha = 1 + 1.5\left(\frac{\alpha}{90}\right)^{0.57}$$

where, $\mathrm{Re} = \frac{VB}{\nu}$, ρ is the flow density, V is the upstream averaged velocity, H is upstream water depth, B is the pier diameter, S is the pier spacing, L is the length of the pier in the flow direction, α is the flow attach angle.

Awazu (1967) proposed an equation for estimating maximum bed shear stress around a thin rectangular plate from 12 flume tests. Froude number was varied from 0.488, 0.508 to 0.526 and the opening ratio of channel was changed between 0.1 and 0.4. Awazu found that the blockage ratio affects the bed shear stress around spur dikes significantly, while the effect of the Froude number is negligible. The maximum amplification of $\tau_{\max} / \tau_{approach}$ is about 3.8 in his experiments. The maximum bed shear stress amplification around spur dikes is,

$$\log_{10}\left[\frac{\tau_{\max}}{\tau_{approach}}\right] = 1.4\left(1 - \frac{b}{B}\right) - 0.021 \tag{2.7}$$

where $\tau_{\max}$ is maximum bed shear stress around spur dike, $\tau_{appraoch}$ is approach bed shear stress, b is spur dike protrusion length, B is the channel width.

Zaghloul (1974) related bed shear stress around spur dike to the average velocity, and local vorticity. He proposed an empirical equation as

$$\tau = \frac{\gamma}{C^2} V\left(1 + K_1 \frac{\omega}{\omega_{nose}} + K_2\right) \tag{2.8}$$

where τ is bed shear stress, γ is the unit weight of water, V is the average velocity, ω is the vorticity at the point, ω_{nose} is the vorticity at the spur dike nose, C is the Chezy's

coefficient, K_1 and K_2 are the empirical constants. K_1 = 0.5 and K_2 is from 0 to 0.2 depending on the distance from the dike.

Rajaratman & Nwachuku (1983) reported 13 measurements of bed shear stress around groin-like structures. The amplification factor $\tau_{\max}/\tau_{approach}$ increases significantly from 3.0 to 4.5 when the blockage ratio varies from 0.08 to 0.16, whereas the influence of Froude number is negligible. The cylindrical pier was found to have slightly smaller amplification factor than that of the thin plate. However, the disturbed area is much smaller from cylindrical pier than from thin plate.

Tingsanchali & Maheswaran (1990) proposed an equation to calculate the bed shear stress around the groin according to the depth averaged velocity. A 2-D numerical simulation of depth-averaged $k-\varepsilon$ turbulence model was used to study the effect of streamline curvature and establish the correction factor near the groin.

$$\tau = \gamma n^2 V^2 y^{-1/3}\left[1+\tan^2(2\alpha_0)\right]^{0.5} \tag{2.9}$$

where τ is the bed shear stress, γ is the unit weight of water, n is Manning's coefficient V is the depth averaged velocity , y is the flow depth , α_0 is the turning angle between the surface streamline direction and the upstream approaching direction.

Molinas et al. (1998) proposed a maximum bed shear stress equation around abutment based on 15 experiments with vertical wall abutment on rectangular channel. The maximum bed shear stress around abutment $\tau_{\max}$ is taken as the summation of the shear stress at the contraction zone τ_{cont} and the shear stress increment due to abutment alone $\tau^*_{\max}$. From the testing, the contribution from channel contraction is negligible

when the length of the abutment is relatively short compared with the channel width. The equation is given below:

$$\tau_{\max} = \tau_{cont} + \tau^{*}_{\max} \tag{2.10}$$

$$\frac{\tau_{cont}}{\tau_{app}} = \left(\frac{c_1}{R}\right)\left[1 + c_2 R^{c_3} F_{app}^{c_4}\left(\frac{L_a}{y}\right)^{c_5}\right]$$

$$\frac{\tau^{*}_{\max}}{\tau_{app}} = \frac{m_0}{R^2}\sqrt{1+\tan^2\alpha_\omega} - 1$$

$$\alpha_\omega = \left[m_1 F_{app}^{m_2}\left(\frac{L_a}{y}\right)^{m_3}\right]$$

where c_1, c_2, c_3, c_4, c_5, m_0, m_1, m_2, m_3 are experimentally determined coefficients, $R = 1 - L_a / L$ is the opening ratio, L_a is the length of the abutment, L is the half width of the channel, F_{app} is the approached Froude number, y is the upstream water depth.

Nurtjahyo (2003) proposed the equation for the prediction of the maximum bed shear stress around abutment based on the correction of the open channel flow equation. The effect of the contraction and the effect of the contraction transaction angle are considered. He stated that the effect of the water depth has been included in the open channel flow equation; and the contraction length of the channel has little influence on the maximum bed shear stress around abutment.

$$\tau_{\max\_abut} = k_{a-R} k_{a-\theta} k_{a-y} k_{a-L} \gamma n^2 V^2 R_h^{-\frac{1}{3}} \tag{2.11}$$

$$k_{a-R} = 1.5\frac{B_1}{B_2} - 0.5$$

$$k_{a-\theta} = 1 + 1.9\left(\frac{\theta}{90}\right) - \left(\frac{\theta}{90}\right)^2$$

$$k_{a-L} \approx 1$$

$$k_{c-H} \approx 1$$

where, γ is the unit weight of the flow, V is the upstream averaged velocity, n is Manning's coefficient, R_h is hydraulic radius, B_1 is the upstream channel width, B_2 is the channel width at the contracted zone, L is the length of the contracted zone, θ is the contraction transition angle.

When flooding, the bridge deck may become partially or entirely submerged. Pressure flow occurs when the water surface exceeds the low chord of the bridge deck. And the floodwater is forced through under the bridge deck. Blockage ratio of the channel keeps increasing until the water surface begins to overtop the bridge deck. When the bridge deck totally submerged, the deck behaves like a broad crested weir. The flow changes from exclusively pressure flow to a combined weir and pressure flow. Pressure flow causes the increase of velocity under the bridge deck and further increase the bed shear stress and bridge scour. Studies of scour in pressure flow are still in the early stage. Abed (1991) first studied the clear water pier scour in pressure flow and found the scour depth 2.3-10 times greater than free surface pier scour; Jones et al (1993) extended Abed's study to isolate the deck scour from pier scour. One important finding is the magnitude of pier scour component under pressure flow as same as under free surface flow conditions. Jones suggested the components of pressure flow vertical deck contraction scour and the pressure flow pier scour be additive. Umbrell et al (1998)

analyzed the data in Jones' study and further improved the vertical deck contraction equation in pressure flow. Arneson (1997) proposed an equation for vertical deck contraction scour based on the similar flume tests study to Jones. ABSCOUR USERS MANUAL (2007) suggests 10% increase of the abutment scour depth when the approach water depth is equal to or greater than 1.2 of the distance of the height of the low chord above the riverbed. The limited literatures are all about the scour depth studies. As for the variation of the bed shear stress around bridge foundation under pressure flow is still unknown.

Laboratory studies of bridge scour have been extensively conducted on constant depth channel for simplicity while this is rare in the real world. Typical cross sections in rivers consist of a deep main channel and one or both sides of relatively shallow floodplain. Flood plain is often rougher than main channel. Consequently, velocities tend to be significantly greater in main channel than on floodplain. The velocity discrepancy between the main channel and flood plain causes the lateral momentum transfer and secondary circulation. The flood plain and main channel flow interaction have been studies by lots of researchers, Rajaratnam & Ahmadi (1979), Knight & Demetriou (1983), Myers & Brennan (1990), Wormleaton & Merrett (1990) and Naot et al. (1993). However, the velocity in flume test is generally uniformly distributed even for compound channel configuration. Hence, the geometric blockage of the abutment in the flume test will be very close to the discharge blockage; while in real rivers the geometric blockage is significantly different from the actual discharge blockage caused by the

abutment. The equations proposed based on the geometric blockage in the flume tests tend to overestimate the scour depth if the geometric blockage is used in the real cases.

2.3 Issues in the Numerical Simulation of Bridge Scour on Cohesive Soils

3D numerical simulation of bridge scour is a very young topic in the history of bridge scour study. It is a promising tool for the study of the interaction between flow field and soil erosion process. Its development depends on both the computational fluid dynamics and the soil erosion model. When talking about bridge scour on cohesive soils, it usually means clear water scour. The sediment transport equation will not be solved together with the fluid calculation. As for the erosion rate function of the cohesive soils, the current model is only limited to the simple shear stress model. The parameters appear in the model are the bed shear stress and the critical shear stress of the soils. Both of the CFD technique and the soil erosion model are under quick development now.

Wei et al. (1997) numerically studied pier scour process in cohesive soils. The scour rate was assumed to be a linear function of the streambed shear stress. The important flow features, such as horseshoe vortex in front of the pier and the wake vortices behind the pier, were observed in the simulation. Simulations showed the reasonable prediction of the time history of scour depth with the tuned erosion rate function.

Chen (2002) conducted the bridge scour simulations for the model scale complex rectangular pier configuration and the prototype complex circular pier configuration. The erosion rate is assumed linear with bed shear stress. Both of the global and local pier

scour have been observed in the simulations. This shows the applicability of the tridimensional numerical simulation in the real complicated engineering problems.

Jiang et al. (2004) applied the shear stress model in the estimation of contraction scour of firm clay riverbed. The erosion function of the cohesive soils is determined through a rotating cylinder device called SERF (Simulator of Erosion Rate Function). The linear shear stress model combined with the 3D shallow water hydrodynamic code was applied for the 5km river channel and yielded good agreement of scour depth prediction with the measurement.

2.3.1 Critical shear stress of the cohesive soils

Critical shear stress for cohesionless soils has been studies extensively by researchers and many equations have been proposed and applied in practice. It depends mainly on the size of the soil particles. While the critical shear stress for cohesive soils relates more to the cohesive force existing between the fine particles. The initiation of cohesive soils is more complex than cohesionless soils. Research indicates that the critical shear stress is influenced by the following parameters: Cation Exchange Capacity (CEC), Salinity, Sodium Adsorption Ratio (SAR), PH-level of pore water, temperature, w%, r, PI, Su, e, swell, D50, %200, clay mineral, dispersion ratio, turbulence, water chemical component, etc. (Winterwerp 1989, Cao 2001,).

Mirtskhoulava (1988) stated the two steps of the erosion of clay: (1) Initially, loosened particles and aggregates with weakened bonds to the other parts are removed in a short period. This process is very similar to the erosion of cohesionless soils and leads to a rougher surface. (2) The bonds between aggregates are destroyed gradually by the

pulsating drag and lift forces caused by the turbulent flow. And the aggregate will be carried away simultaneously when the holding cohesion force disappears.

Dunn (1959) studied the correlation of critical shear stress of soils to the vane shear strength experimentally. He concluded that the critical shear stress increases with the increase of the clay content and proposed the critical shear stress equation as following,

$$\tau_c = 0.02 + \frac{S_v \tan\theta}{1000} + 0.18\tan\theta \tag{2.12}$$

where S_v is the vane shear strength, and θ is the slope of the linear relation between critical shear stress and vane shear strength.

Smerdon and Beasley (1959) investigated the influence of plasticity index, dispersion ratio, and mean particle size of clay on the critical shear stress by conducting flume tests. The relation between the critical shear stress, τ_c, and the plasticity index, PI, and Middleton's dispersion ratio, D_r, were given by

$$\tau_c = 0.0034(PI)^{0.84} \tag{2.13}$$

$$\tau_c = 0.213(D_r)^{-0.63} \tag{2.14}$$

Ivarson (1998) proposed the relation between critical shear stress τ_c, unconfined compressive strength of clay soils S_u, and mean average velocity V, based on the stream stability criteria for cohesive soils by Flaxman as:

$$\tau_c = \frac{12.11\log S_u - 28.67}{V} \tag{2.15}$$

where, all terms are in English units;

Briaud et al (1999) argued the critical shear stress does not theoretically exist. However, he believed that the concept of critical shear stress is practically useful and future suggested that τ_c should be defined in the way based on a standardized small scour rate. This threshold scour rate is proposed as 1 mm/hr in the application of EFA (erosion function apparatus). The research also showed that large variance in the predicted τ_c among different researchers, from 0.02 to 100 Pa. Hence, they recommended to measure τ_c directly from EFA test.

2.3.2 Erosion rate of soils

The scour around bridge foundation can reach the equilibrium scour depth in cohesionless soils for just one flood since gravity is the mainly dominant factor. While it may take several floods to reach the final scour depth in cohesive soils and last about tens or hundreds of years. All those factors mentioned above affecting the critical shear stress in cohesive soils will continue to control the erosion rate of the cohesive soils.

Arulanandan (1975) proposed the erosion rate equation for cohesive soils according to the testing in the rotating cylinder apparatus with a number of different types of remolded clay. The erosion rate is found out to be linear proportional to the applied shear stress by the flow. The following relationship is given as:

$$\begin{aligned} \dot{z} &= M\left(\frac{\tau}{\tau_c}-1\right) && \tau \geq \tau_c \\ \dot{z} &= 0 && \tau < \tau_c \end{aligned} \tag{2.16}$$

where, M is a soils dependent erosion rate constant and varies from soil to soil.

Parchure and Mehta (1985) conducted a series of laboratory studies on the erosion of soft cohesive estuarial sediment deposits. They developed an experimental procedure involving layer-by-layer erosion under a successively increasing bed shear stress for a certain range. The concentration-time data joined with bed density profiles were used to establish the variation of the bed shear strength, τ_s, with depth as well as a relation for the erosion rate. The erosion rate equation for the estuarial soft clay sediments is proposed as following,

$$\ln\frac{\dot{z}}{\dot{z}_f}=\alpha\left(\tau-\tau_s\right)^{1/2} \tag{2.17}$$

where $\dot{z}$ is erosion rate, $g/cm^2-\min$; $\dot{z}_f$ is erosion rate when $\tau-\tau_b=0$, $g/cm^2-\min$; α is factor which is inversely proportional to the absolute temperature; τ is bed shear stress, N/m^2; τ_s is bed shear strength, N/m^2

Shaikh et al. (1988) studied the erosion rates of unsaturated compacted sodium and calcium montmorillonite clay. The erosion rate was found to be linear with the shear stress and presented as

$$\dot{z}=C\tau \tag{2.18}$$

$$C=4.41\left(SAR\right)^{-1.34}$$

where ε is erosion rate, $N/m^2/\min$; τ is shear stress, N/m^2; C is erosion rate coefficient, $\min^{-1}$

Briaud et al. (1999, 2001) applied EFA (Erosion Function Apparatus) to measure the erosion rate of soils directly. The soil in the Shelby tube is installed on the machine

and pushed out 1mm into the conduit by the piston as fast as it takes to erode the soil by water flowing over it. Erosion rate is recorded through the vertical shortness of the soil column per unit time with the corresponding flow velocity. And the shear stress could be evaluated from Moody Chart.

2.3.3 Effect of roughness

The influence of river bed roughness on the flow field can be separated into (1) particle resistance accounting for the interaction between the flow and the individual particles and (2) form resistance due to bedform configurations. The study of the particle roughness has been studies decades ago. And the most well known result was done by Nikuradse (1933) (see, Cebeci and Bradshaw, 1977) in pipe flows with sand-roughened surface. The principal result from the data of Nikuradse is the velocity distribution near a rough wall has the same slope (giving the same Karman constant, κ) as on smooth wall, but different intercepts, ΔB:

$$u^+ = \frac{1}{\kappa}\ln y^+ + B - \Delta B \tag{2.19}$$

where $u^+ = U/u_\tau$, $y^+ = u_\tau y/\nu$, y is the distance from the wall, κ=0.418, B is the additive constant (for pipe, $B=5.45$ and for open channel, $B=5.2$), ΔB is a function of $k_s^+ \left(= k_s u_\tau/\nu\right)$, k_s is the surface roughness.

Ioselevich and Pilipenko (1974) (see, Cebeci and Bradshaw, 1977) gave the analytic fit to the data of Nikuradse:

$$\Delta B=\begin{cases}0, & k_s^+<2.25\\ \left[B-8.5+\frac{1}{\kappa}\ln k_s^+\right]\sin\left[0.4258\left(\ln k_s^+-0.811\right)\right], & 2.25\le k_s^+<90\\ B-8.5+\frac{1}{\kappa}\ln k_s^+, & k_s^+>90\end{cases} \qquad (2.20)$$

In natural river channel, the river bed is rarely flat. The extensive studies on bed form configuration and geometry have been performed on river bed with cohesionless soils. Simons and Richardson (1963, 1966) classified bedforms into lower and upper flow regimes. The general bridge scour happens in lower regime, namely the flow in subcritical (Fr <1). And the typical types of bedforms are ripples and dunes. Ripple shapes vary from nearly triangular to almost sinusoidal. Dunes are larger than ripples, and often triangular with fairly gentle upstream and downstream slopes. Liu (1957), Chabert and Chauvin (1963), Simons and Richardson (1963, 1966), Yalin (1964) and van Rijn (1984a, 1984b, 1984c) proposed many predictors to predict the formation and size of ripples and dunes. For these types of the bedforms, the form roughness is dominant instead of particle roughness. Hence the roughness k_s in ΔB should include the contribution not only from particles, but also from the bedforms. As for the cohesive river bed, the soil particles are extremely fine. Hence, the bed form roughness is the dominant factor.

In order to cover surface roughness, many researchers tried to modify the existing turbulence models for hydraulic smooth boundary conditions, such as Patel & Yoon (1995), Zhang et al (1996), and Durbin et al. (2001). Zhang et al (1996) stated that the rough surface model can be classified into two categories: 1) equivalent sand grain

roughness models;2) topographic form-drag models. Patel (1998) pointed out that the turbulence model for roughness surface should consider two factors: (a) the model has the capability to classify three roughness regions, i.e. hydraulic smooth, transitional, and fully-rough surfaces, and (b) the model has the capability to describe separated flow.

Patel & Yoon (1995) proposed the roughness turbulence model based on the modifying of mixing length in two layer $k-\varepsilon$ model. The roughness effect could be included easily by changing the boundary conditions in $k-\omega$ model. By comparing these two models, they concluded that the $k-\omega$ model of Wilcox is better than the modified $k-\varepsilon$ model. And the modified $k-\varepsilon$ model needed further tune of the constants and dumping functions in the length-scale equations.

Zhang et al. (1996) built a new-low-Reynolds-number $k-\varepsilon$ model to simulate turbulence flow over smooth and rough surfaces. He continued to adopt the equivalent sand grain roughness concept and modified reduction factors in the low Reynolds number models. They showed the model is capable of predicting the log-law velocity profile, friction factors, turbulent kinetic energy and dissipation rate by comparing it with experiments.

Durbin et al. (2001) presented a modified two-layer $k-\varepsilon$ model. The new model modified the mixing length formula by adding a hydrodynamic roughness length into the wall distance and also modified the boundary condition for turbulence kinetic energy.

2.3.4 Effect of turbulence intensity

Nurtjahyo (2003) stated that the bridge scour simulation with shear stress model could not predict the scour pattern correctly, even if the scour depth was reasonable

compared with the flume tests. Li (2002) observed the deep scour at lee side of the circular pier. The bed shear stress at downstream of pier is pretty small; while the turbulent intensity is significant. This implies that the flow turbulence can contribute to the increase of the erosion ratio as well as bed shear stress. Nurtjahyo (2003) added the turbulence kinetic energy term into the erosion rate equation and improved the scour pattern prediction in the clear water pier scour simulations.

Dufresne et al (2007) investigated the influence of both the bed shear stress (BSS) and bed turbulent kinetic energy (BTKE) on the sedimentation and mass separation in storm-water tank pilot. The authors found out that BSS can only be used for no overflow cases; while BTKE should be chosen for overflow cases. Neither of them can predict the measurement well for both conditions.

The study of the effect of turbulence on the scour is still in the early stage. Only few literatures can be found very recently. It is believed that the turbulence affects the whole scour process and contributes to both the final scour depth and scour pattern.

CHAPTER III

GOVERNING EQUATIONS FOR CHEN3D PROGRAM

CHEN3D (**C**omputerized **H**ydraulic **EN**gineering program for **3D** flow) has been employed in conjunction with chimera domain decomposition approach for time-domain simulation of flow around complex hydraulic configurations. The turbulent flow is performed using the Reynolds-Averaged form of the Navier-Stokes equations. The entire computational domain can be divided into two regions in order to facilitate the implementation of two-layer turbulent model approach. One is the thin layer region around the solid boundary, applying one-equation turbulence model to account for the wall-damping effects. And the other one is the fully turbulent region away from the wall, employing the standard $k-\varepsilon$ two equation model to resolve the fully turbulent flow. The formulation has been described in detail in Chen and Patel (1988) and Chen and Korpus (1993). The CHEN3D program has been further developed to include the roughness and scour model in current research to simulate the clear water scour. The approach by Patel and Yoon (1995) is used to capture the effect of roughness. And the method proposed by Nurtjahyo (2003) is implemented to perform the scour development. A summary of the approach is given below.

3.1 Governing Equations for Hydrodynamics

The non-dimensional Reynolds-Averaged Navier-Stokes equations for incompressible, viscous flow in Cartesian coordinates $(x_i,t)=(x,y,z,t)$ are as follows:

$$\sum_{i=1}^{3} \frac{\partial U_i}{\partial x_i} = 0 \tag{3.1}$$

$$\frac{\partial U_i}{\partial t} + \sum_{j=1}^{3} \left(U_j \frac{\partial U_i}{\partial x_j} + \frac{\partial \overline{u_i u_j}}{\partial x_j} \right) + \frac{\partial p}{\partial x_i} - \frac{1}{\mathrm{Re}} \nabla^2 U_i = 0 \tag{3.2}$$

Equation (3.1) represents the continuity equation and equation (3.2) represents the momentum equations. $U_i = (U,V,W)$ and $u_i = (u,v,w)$ represent Cartesian components of the mean and the fluctuating velocities, t is time, p is pressure, $\mathrm{Re} = U_0 B/\nu$ is the Reynolds number based on the characteristic length B, the reference velocity U_0, and the kinematics viscosity ν. All quantities in the above equations, and those follows, are made dimensionless by U_0, B and fluid density ρ. Body force is ignored here. For open channel flow, the influence of gravity can be considered on the free surface boundary conditions.

In equation (3.2), the six additional Reynolds stresses terms $-\overline{u_i u_j}$ make the equations unsolvable without additional equations. Based on the assumption of Boussinesq, the Reynolds stresses can be expressed in terms of an isotropic eddy viscosity ν_t and the mean rate of strain, which is analogous to the molecular viscosity. The Reynolds stresses can then be written as:

$$-\overline{u_i u_j} = \nu_t \left(\frac{\partial U_i}{\partial x^j} + \frac{\partial U_j}{\partial x^i} \right) - \frac{2}{3} \delta_{ij} k \tag{3.3}$$

where $k = \left(\overline{uu} + \overline{vv} + \overline{ww} \right) / 2$ is the turbulent kinetic energy and δ_{ij} is the Kronecker delta. Substituting into (3.2) yields:

$$\frac{\partial U_i}{\partial t}+\sum_{j=1}^{3}\left(\left(U_j-\frac{\partial \nu_t}{\partial x_j}\right)\frac{\partial U_i}{\partial x_j}-\frac{\partial \nu_t}{\partial x_j}\frac{\partial U_j}{\partial x_i}\right)+\frac{\partial}{\partial x_i}\left(p+\frac{2}{3}k\right)-\frac{1}{R_U}\nabla^2 U_i=0 \qquad (3.4)$$

The quantity $1/R_U=1/\mathrm{Re}+\nu_t/\sigma_U$ represents the effective turbulent viscosity. The eddy viscosity can be computed from the turbulent kinetic energy k and its dissipation rate ε:

$$\nu_t=C_\mu\frac{k^2}{\varepsilon} \qquad (3.5)$$

where $C_\mu=0.09$ and the turbulent quantities of k and ε can be determined from the corresponding transportation equations:

$$\frac{\partial k}{\partial t}+\sum_{j=1}^{3}\left(U_j-\frac{1}{\sigma_k}\frac{\partial \nu_t}{\partial x_j}\right)\frac{\partial k}{\partial x_j}-\frac{1}{R_k}\nabla^2 k-G+\varepsilon=0 \qquad (3.6)$$

$$\frac{\partial \varepsilon}{\partial t}+\sum_{j=1}^{3}\left(U_j-\frac{1}{\sigma_\varepsilon}\frac{\partial \nu_t}{\partial x_j}\right)\frac{\partial \varepsilon}{\partial x_j}-\frac{1}{R_\varepsilon}\nabla^2\varepsilon-C_{\varepsilon 1}\frac{\varepsilon}{k}G+C_{\varepsilon 2}\frac{\varepsilon^2}{k}=0 \qquad (3.7)$$

$$G=\nu_t\sum_{j=1}^{3}\sum_{i=1}^{3}\left(\frac{\partial U_i}{\partial x_j}+\frac{\partial U_j}{\partial x_i}\right)^2 \qquad (3.8)$$

And the coefficients $C_{\varepsilon 1}=1.44$, $C_{\varepsilon 2}=1.92$ $\sigma_u=\sigma_k=1.0$ $\sigma_\varepsilon=1.3$ are given in Chen and Patel (1988). The effective viscosities in Equation (3.6) and (3.7) are taken as $1/R_k=1/\mathrm{Re}+\nu_t/\sigma_k$, and $1/R_\varepsilon=1/\mathrm{Re}+\nu_t/\sigma_\varepsilon$, respectively.

The standard $k-\varepsilon$ two equations model mentioned above is only applied in the fully turbulent regions. In the two-layer approach of Chen and Patel (1988), the one-equation of Wolfstein (1969) is employed in the near wall region. Close to the wall, the

dissipation rate is determined from the turbulent production and the dissipation length scale, rather than being solved from equation (3.7):

$$\varepsilon = \frac{k^{3/2}}{l_\varepsilon} \tag{3.9}$$

$$l_\varepsilon = C_l y\left[1 - \exp\left(-R_y / A_\varepsilon\right)\right]; R_y = \mathrm{Re}\sqrt{k}\, y \tag{3.10}$$

The inner layer was specified when the parameter $y^+ = U_\tau y/\nu \le 300 - 1000$, where y is the dimensionless normal distance from the wall and $U_\tau = \sqrt{\tau_w / \rho}$ is the friction or shear velocity. Using this relationship, the turbulent production can be determined from equation (3.6). The eddy viscosity is then found from:

$$v_t = C_\mu \sqrt{k} l_\mu \tag{3.11}$$

$$l_\mu = C_l y\left[1 - \exp\left(-R_y / A_\mu\right)\right] \tag{3.12}$$

The constants $C_l = \kappa C_\mu^{-0.75}$, $A_\mu = 70$, $A_\varepsilon = 2C_l$ and $\kappa = 0.418$ are given in Chen and Patel (1988) and chosen to yield a smooth transition of eddy viscosity between the two regions.

The above one equation model for the inner layer is based on the assumption of a hydrodynamic smooth wall. Patel and Yoon (1995) extended the model to a rough wall by modifying the two length scales:

$$l_\mu = C_l (y + \Delta y)\left[1 - \exp\left(-\frac{\left(R_y + \Delta R_y\right)}{A_\mu}\right)\right] \tag{3.13}$$

$$l_\varepsilon = C_l (y + \Delta y)\left[1 - \exp\left(-\frac{\left(R_y + \Delta R_y\right)}{A_\varepsilon}\right)\right] \tag{3.14}$$

$$\Delta R_y = \mathrm{Re}\sqrt{k}\Delta y \tag{3.15}$$

The Δy is normalized by shear velocity U_τ and kinematics viscosity ν to yield $\Delta y^+ = U_\tau \Delta y / \nu$, and Δy^+ is related to the roughness of the wall and expressed by:

$$\Delta y^+ = 0.9\left[\sqrt{k_s^+} - k_s^+ \exp\left(-\frac{k_s^+}{6}\right)\right] \tag{3.16}$$

where $k_s^+ = \mathrm{Re}\, k_s U_\tau$, and k_s is the dimensionless height of the sand grain. In case of non-uniform sand, k_s is usually taken as the median diameter D_{50}.

To facilitate the coding of the program, the transportation equations for U_i, k and ε are rewritten in the general form:

$$\nabla^2 \phi = R_\phi\left[\left(U_j - \frac{1}{\sigma_\phi}\frac{\partial \nu_t}{\partial x_j}\right)\frac{\partial \phi}{\partial x_j} + \frac{\partial \phi}{\partial t}\right] + s_\phi \tag{3.17}$$

where ϕ represents any of the transport quantities U_i k and ε. The source functions s_ϕ are:

$$s_{U_i} = R_U\left[\frac{\partial}{\partial x_i}\left(p + \frac{2}{3}k\right) - \sum_{j=1}^{3}\frac{\partial \nu_t}{\partial x_j}\frac{\partial U_j}{\partial x_i}\right] \tag{3.18}$$

$$s_k = -R_k\left(G - \varepsilon\right) \tag{3.19}$$

$$s_\varepsilon = -R_\varepsilon \frac{\varepsilon}{k}\left(C_{e1}G - C_{\varepsilon 2}\varepsilon\right) \tag{3.20}$$

To accurately solve the flow around the boundary of complex geometries, the boundary fitted coordinate system is used in CHEN3D. Hence, the Cartesian coordinate $(x_i, t) = (x, y, z, t)$ employed in the physical space, has to be transformed to a general

curvilinear coordinate system $\left(\xi^1,\xi^2,\xi^3,\tau\right)=\left(\xi,\eta,\zeta,\tau\right)$. The vector operations in the transformed coordinates are:

$$(\nabla\phi)_i=\frac{\partial\phi}{\partial x_i}=\frac{1}{J}\sum_{j=1}^{3}b_i^j\frac{\partial\phi}{\partial\xi^j} \tag{3.21}$$

$$\nabla^2\phi=\sum_{i=1}^{3}\sum_{j=1}^{3}(g^{ij}\frac{\partial^2\phi}{\partial\xi^i\xi^j}+\sum_{l=1}^{3}\Gamma_{ij}^l\frac{\partial\phi}{\partial\xi^l})=\sum_{i=1}^{3}\sum_{j=1}^{3}g^{ij}\frac{\partial^2\phi}{\partial\xi^i\xi^j}+\sum_{j=1}^{3}f^j\frac{\partial\phi}{\partial\xi^j} \tag{3.22}$$

$$\frac{\partial\phi}{\partial t}=\frac{\partial\phi}{\partial\tau}-\frac{1}{J}\sum_{i=1}^{3}\sum_{j=1}^{3}b_i^j\frac{\partial x_i}{\partial\tau}\frac{\partial\phi}{\partial\xi^j} \tag{3.23}$$

$$b_i^l=J\frac{\partial\xi^l}{\partial x_i}=\left(\frac{\partial x_j}{\partial\xi^m}\frac{\partial x_k}{\partial\xi^n}-\frac{\partial x_k}{\partial\xi^m}\frac{\partial x_j}{\partial\xi^n}\right) \tag{3.24}$$

$$g^{li}=\sum_{p=1}^{3}b_p^lb_p^i=\frac{1}{J^2}\left(g_{mj}g_{nk}-g_{mk}g_{nj}\right) \tag{3.25}$$

$$f^i=\nabla^2\xi^i=-\sum_{m=1}^{3}\sum_{n=1}^{3}g^{mn}\Gamma_{mn}^i=\frac{1}{J}\sum_{j=1}^{3}\frac{\partial}{\partial\xi^j}\left(Jg^{ij}\right) \tag{3.26}$$

$$g_{ij}=\sum_{m=1}^{3}\frac{\partial x_m}{\partial\xi^i}\frac{\partial x_m}{\partial\xi^j} \tag{3.27}$$

$$J^2=\det(g_{ij})=g_{11}g_{22}g_{33}+2g_{12}g_{13}g_{23}-g_{11}(g_{23})^2-g_{22}(g_{13})^2-g_{33}(g_{12})^2 \tag{3.28}$$

where b_i^l, g^{li}, and f^i are the geometric coefficients. Using these relationships, equations (3.1) and (3.17) are transformed into:

$$\sum_{i=1}^{3}\frac{\partial U_i}{\partial x_i}=\sum_{i=1}^{3}\sum_{j=1}^{3}\frac{\partial\xi^j}{\partial x_i}\frac{\partial U_i}{\partial\xi^j}=\frac{1}{J}\sum_{i=1}^{3}\sum_{j=1}^{3}\frac{\partial}{\partial\xi^j}(b_i^jU_i)=0 \tag{3.29}$$

$$\sum_{j=1}^{3}\left(g^{jj}\frac{\partial^2\phi}{\partial\xi^j\partial\xi^j}-2a_\phi^j\frac{\partial\phi}{\partial\xi^j}\right)=R_\phi\frac{\partial\phi}{\partial\tau}+S_\phi \tag{3.30}$$

where

$$2a_{\phi}^{j}=\frac{R_{\phi}}{J}\sum_{n=1}^{3}b_{n}^{j}\left(U_{n}-\frac{\partial x_{n}}{\partial\tau}-\frac{1}{J\sigma_{\phi}}\sum_{m=1}^{3}b_{j}^{m}\frac{\partial\nu_{t}}{\partial\xi_{m}}\right)-f^{j} \tag{3.31}$$

$$S_{\phi}=s_{\phi}-2\left(g^{12}\frac{\partial^{2}\phi}{\partial\xi^{1}\partial\xi^{2}}+g^{13}\frac{\partial^{2}\phi}{\partial\xi^{1}\partial\xi^{3}}+g^{23}\frac{\partial^{2}\phi}{\partial\xi^{2}\partial\xi^{3}}\right) \tag{3.32}$$

$$G=\frac{1}{2}\nu_{t}\sum_{j=1}^{3}\sum_{i=1}^{3}\left(\frac{1}{J}\sum_{l=1}^{3}\left(b_{j}^{l}\frac{\partial U_{i}}{\partial\xi^{l}}+b_{i}^{l}\frac{\partial U_{j}}{\partial\xi^{l}}\right)\right)^{2} \tag{3.33}$$

$$s_{U_{i}}=\frac{R_{U}}{J}\sum_{l=1}^{3}b_{i}^{l}\frac{\partial}{\partial\xi^{l}}\left(p+\frac{2}{3}k\right)-R_{U}\sum_{j=1}^{3}\left(\frac{1}{J}\sum_{l=1}^{3}b_{j}^{l}\frac{\partial\nu_{t}}{\partial\xi^{l}}\right)\left(\frac{1}{J}\sum_{l=1}^{3}b_{i}^{l}\frac{\partial U_{j}}{\partial\xi^{l}}\right) \tag{3.34}$$

$$s_{k}=-R_{k}\left(G-\varepsilon\right) \tag{3.35}$$

$$s_{\varepsilon}=-R_{\varepsilon}\frac{\varepsilon}{k}\left(C_{e1}G-C_{\varepsilon2}\varepsilon\right) \tag{3.36}$$

3.1.1 Finite analytic method

In CHEN3D program, the governing equation is locally linearized in each rectangular numerical element, $\Delta\xi=\Delta\eta=\Delta\zeta=2$, by calculating the coefficients at the interior node (P) of each local element. The second order accuracy time domain discretization scheme was proposed by Liu (2002). Based on Chen et al. (1990), the following is the final 13-point FAM formula for the equation as described in figure 3-1.

$$\begin{aligned}\phi_{p}^{n}=&\frac{1}{1+C_{p}\left[C_{U}+C_{D}+1.5R_{\phi}/\Delta\tau\right]}\\&\left\{\sum_{1}^{8}C_{nb}\phi_{nb}+C_{p}\left[C_{U}\phi_{U}+C_{D}\phi_{D}+\frac{R_{\phi}}{\Delta\tau}\left(2\phi_{p}^{n-1}-0.5\phi_{p}^{n-2}\right)\right]-C_{p}\left(S_{\phi}\right)_{p}\right\}\end{aligned} \tag{3.37}$$

The subscript nb denotes neighboring nodes (NE: northeast, NW: northwest, etc).

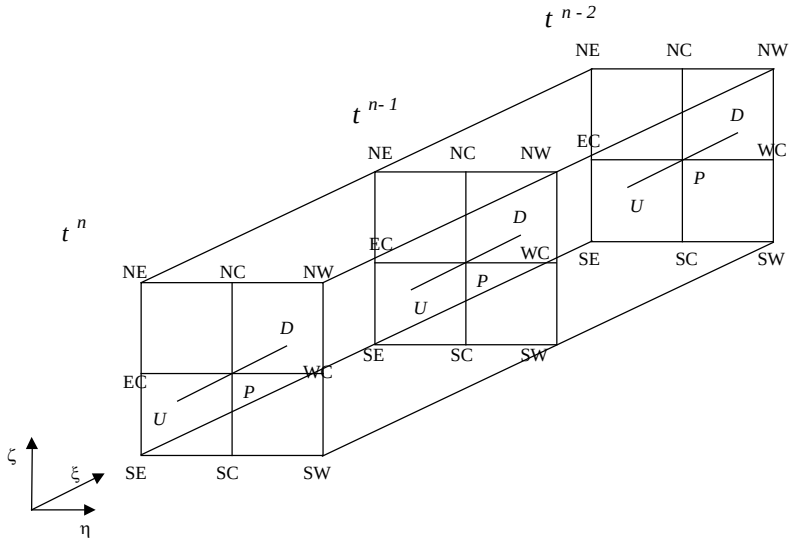

Figure 3-1 Finite analytic local element.

The finite analytic coefficients C_{nb}, C_P, C_U, C_D have been explained in detail by Chen and Chen (1982,1984). Equation (3.37) indicates that ϕ_P^n depends on all eight neighboring nodal values in the $\eta\zeta$ plane as well as the values of the upstream node U, the downstream node D, and the value at the previous time step (n-1) and (n-2). This equation is implicit in both space and time.

3.1.2 Continuity equation: velocity-pressure coupling

In most practical applications, the pressure is unknown and must be determined by requiring the velocity field to satisfy the continuity equation. Since a direct method for the simultaneous solution of all six equations is not feasible with present computer capacity, it is necessary to convert the continuity equation into an algorithm for the calculation of the pressure field appearing in the momentum equation. Chen and Patel (1989) have proposed the hybrid SIMPLER/PISO algorithm for velocity-pressure coupling. In the SIMPLER/PISO algorithm, it is convenient to use contravariant

components $\left(U^1, U^2, U^3\right)$ of the velocity vector in the body-fitted coordinates $\left(\xi^1, \xi^2, \xi^3, \tau\right)$. Hence, the continuity equation can be expressed as:

$$\sum_{i=1}^{3} \frac{\partial U^i}{\partial \xi^i} = 0 \tag{3.38}$$

Furthermore, the contravariant components of the velocity vector can be specified into a pressure dependent term and a pseudo-velocity term as below:

$$U^i = \hat{U}^i - E^{ii} \frac{\partial p}{\partial \xi^i} \tag{3.39}$$

where

$$\hat{U}^i = \sum_{n=1}^{3} b_n^i \hat{U}^n - E^{ij} \frac{\partial p}{\partial \xi^j} - E^{ik} \frac{\partial p}{\xi^k} \tag{3.40}$$

$$E^{ij} = \frac{R_\phi C_p}{J\left[1 + C_p\left(C_U + C_D + 1.5R_\phi / \Delta\tau\right)\right]} \sum_{m=1}^{3} b_m^i b_m^j \tag{3.41}$$

A relationship for pressure can now be derived by requiring the contravariant velocity field, U^i, to satisfy the equation of continuity. An approximating equation (3.38) with central differences and substituting equation (3.39) for each point in the stencil gives:

$$\begin{aligned} &\left(E_d^{11} + E_u^{11} + E_n^{22} + E_s^{22} + E_e^{33} + E_w^{33}\right) P_p \\ &= E_d^{11} P_D + E_u^{11} P_U + E_n^{22} P_{NC} + E_s^{22} P_{SC} + E_e^{33} P_{EC} + E_w^{33} P_{WC} - \hat{D} \end{aligned} \tag{3.42}$$

where

$$\begin{aligned} \hat{D} &= \hat{U}_d^1 - \hat{U}_u^1 + \hat{U}_n^2 - \hat{U}_s^2 + \hat{U}_e^3 - \hat{U}_w^3 \\ &= \frac{1}{2}\left(\hat{U}_D^1 - \hat{U}_U^1 + \hat{U}_{NC}^2 - \hat{U}_{SC}^2 + \hat{U}_{EC}^3 - \hat{U}_{WC}^3\right) \end{aligned} \tag{3.43}$$

3.2 Boundary Conditions

Boundary conditions described the interface between surroundings and the system that is modeled. The boundary conditions for the system can be classified into no-slip boundary, inlet boundary, outlet boundary and free surface boundary conditions.

3.2.1 No slip boundary condition

At the abutment surface or riverbed surface apply the no slip boundary for all directions, i.e.:

$$U_i = 0 \tag{3.44}$$

Extrapolation points near the solid boundary are used to determine the pressure at the solid boundary surface.

$$\frac{\partial p}{\partial n} = 0 \tag{3.45}$$

3.2.2 Outlet boundary condition

In the viscous flow, a zero gradient boundary condition is used at the far field, which can be expressed as:

$$\frac{\partial U_i}{\partial n} = \frac{\partial p}{\partial n} = 0 \tag{3.46}$$

3.2.3 Inlet boundary condition

On the inlet, the velocity and the pressure are prescribed. It is assumed:

$$U_1 = 1, U_2 = U_3 = p = 0 \tag{3.47}$$

3.2.4 Free surface boundary condition

The free surface elevation δ is a function of two other space directions and time, i.e., $\delta = z - z_{surf} = \delta(x, y, t)$, z_{surf} is the initial water surface elevation taken as the datum for the hydrostatic force. Based on the chain rule, the kinematics boundary conditions on the free surface are expressed as:

$$U_3 = \frac{d\delta}{dt} = \frac{\partial \delta}{\partial t} + U_1 \frac{\partial \delta}{\partial x} + U_2 \frac{\partial \delta}{\partial y} \tag{3.48}$$

Equation (3.48) ensures the fluid particles on the free surface remain on the free surface and it can be solved by simply extrapolating the velocities from the inner fluid domain. For open channel problem, gravity plays the important role, which has not been included in the momentum equation (3.2). By ignoring the surface tension and free surface turbulent boundary layer, the effect of the gravity could be considered in the pressure term. Conservation of momentum of a viscous fluid flow with a gravitational acceleration in the vertical direction can be written as:

$$\frac{\partial U_i}{\partial t} + \sum_{j=1}^{3}\left(U_j \frac{\partial U_i}{\partial x_j} + \frac{\partial \overline{u_i u_j}}{\partial x_j} \right) + \frac{\partial p}{\partial x_i} - \frac{1}{\mathrm{Re}} \nabla^2 U_i + \frac{\delta_{i3}}{Fr^2} = 0 \tag{3.49}$$

Fr is the Froude number, $Fr = \frac{U_0}{\sqrt{gB}}$, where g is the gravitational acceleration.

By introducing a new variable for the pressure, which includes both of the hydrostatic and static component of the pressure $\psi = p + \frac{x_3}{Fr^2}$, the equation of the momentum can be rewritten as:

$$\frac{\partial U_i}{\partial t} + \sum_{j=1}^{3}\left(U_j \frac{\partial U_i}{\partial x_j} + \frac{\partial \overline{u_i u_j}}{\partial x_j} \right) + \frac{\partial \psi}{\partial x_i} - \frac{1}{\mathrm{Re}} \nabla^2 U_i = 0 \tag{3.50}$$

The Froude number will now enter explicitly in the boundary condition instead of the governing equation. The procedure mentioned in the previous section can still be used to solve the open channel flow with the suitable boundary condition applied.

A dynamic condition has also to be fulfilled at the surface. If the surface tension is neglected and the flow is considered non viscous on the surface, the dynamic boundary conditions can be simplified to be $p = p_{atm}$, p_{atm} is the atmospheric pressure. The corresponding boundary condition for ψ becomes

$$\psi = p_{atm} + \frac{\delta}{Fr^2} \tag{3.51}$$

If we say $p_{atm} = 0$, then

$$\psi = \frac{\delta}{Fr^2} \tag{3.52}$$

3.3 Clear Water Scour

Clear water scour means the effect of the deposition can be ignored. Once the soil eroded, it is eroded. Basically, clear water scour appears on the cohesive riverbed. For cohesive soil, it is known that the scour rate, defined as the change of scour depth per unit time, mainly depends on the shear stress at the streambed surface. The initiation of the scour process is determined by the critical shear stress, the smallest streambed shear stress to start the erosion process. Based on this understanding, the scour rate can be

expressed as a function of the streambed shear stress and the critical shear stress. The scour rate equation can be written in the following dimensional form:

$$\dot{z} = \dot{z}(\tau_b, \tau_c) \tag{3.53}$$

where $\dot{z}$ is the scour rate, τ_b is the streambed shear stress, and τ_c is the critical shear stress. The τ_b is evaluated using the Newtonian stress-strain law:

$$\tau_b = \left| \rho \nu \frac{\partial q}{\partial z_n^*} \right| \tag{3.54}$$

where q is the magnitude of flow velocity, z_n^* is the normal distance from the streambed. In numerical computation, after the flow field is computed at each time step, the scour rate at each point is determined by the scour rate equation. The increase of scour depth is then evaluated by multiplying the scour rate by the time increment.

3.4 Overall Solution Algorithm

For the scour problem involving the grid movement on the river bed and free surface variation, the solution procedure can be summarized as follows:

1. Construct the grid for each component of the configuration.
2. Construct a boundary condition table specifying appropriate boundary conditions for each face.
3. Specify the initial condition for velocity, pressure, and turbulence fields.
4. Determine interpolation information to link the grids together using the PEGSUS program.
5. Calculate the geometric coefficients.
6. Calculate the finite analytic coefficients and source functions.

7. Solve the momentum equations (U_i) and turbulence equations (k, ε) using the iterative ADI scheme.
8. Calculate the pseudo velocities (V^i) and calculate pressure (p) using the iterative ADI scheme.
9. Repeat step 7 and 8.
10. Calculate the new free surface elevation using kinematics free surface boundary conditions.
11. For clear water scour, calculate the new bed surface elevation using the scour rate equation.
12. Adjust the volume grid to conform to free surface and riverbed elevations in z-direction.
13. Return to step 4 for next time step.

CHAPTER IV

MAXIMUM BED SHEAR STRESS AROUND ABUTMENT IN OPEN CHANNEL FLOW

The maximum bed shear stress around abutment, one of the two basic parameters in SRICOS method, is studied in this chapter. All the simulation results given in this chapter are with open channel flow. The maximum bed shear stress around abutment is studied first on the simple rectangular channel. After the establishment of the maximum bed shear stress equation on rectangular channel, compound channel correction factor is further proposed so that the equation can be extended to include compound channel situations. CHEN3D program introduced in chapter III is utilized to achieve all the numerical simulations. The flume test cases of NCHRP 24-15(2) are simulated numerically and used to verify the proposed equation. Finally, the apparent maximum bed shear stress around abutment is recommended based on the results of flume tests and the erosion function of the soils from EFA testing.

4.1 Methodology

The typical river channel including abutment and approach embankment is presented in figure 4-1. In the real world, the elevation of river bed may change gradually from the center of main channel to flood plain and have no clear main channel slope as shown in the diagram. Main channel slope β_m may vary in a large range, depending on the soil type, from a small number in sands to even vertical in cohesive

soils. However, β_m is believed to be a minor factor in current study so that a constant main channel slope (1V:1H) is used in the following compound channel study.

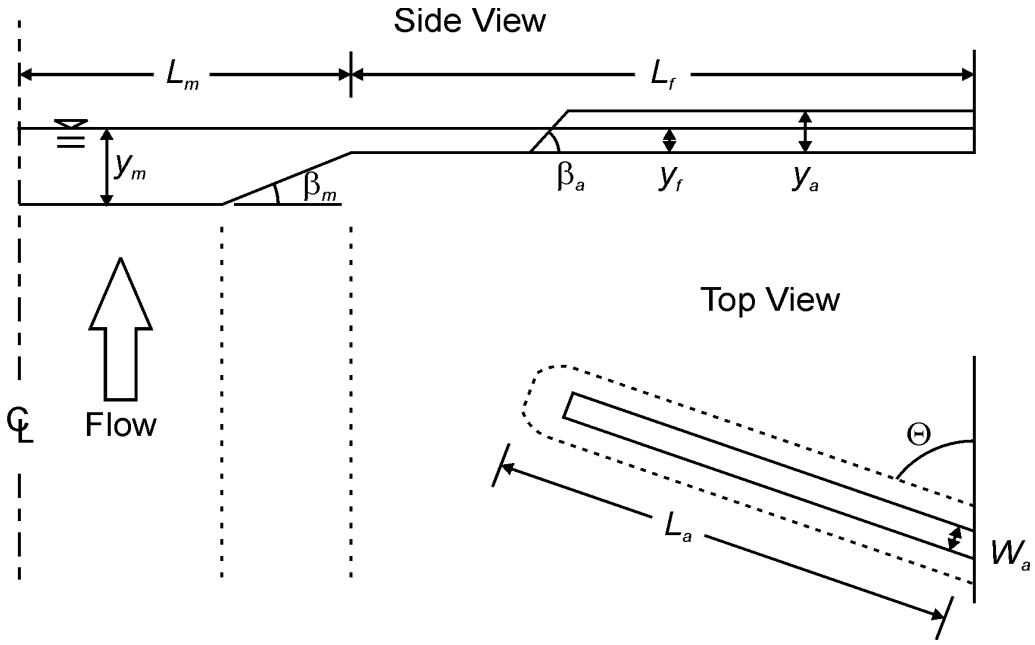

L: half width of channel	L_m: half width of main channel
y_m: water depth on main channel	L_a: Length of approach embankment
tan(β_a): slope of abutment (V:H)	V: upstream mean velocity
L_f: width of flood plain	Θ (°)skew angle of approach embankment
y_f: water depth on flood plain	W_a: top width of abutment
y: water depth for constant depth channel ($y = y_f = y_m$)	

Figure 4-1 Definition of the parameters in abutment scour problem.

To simplify the problem, the rectangular channel is studied first, with $\beta_m = 0$, $y_m = y_f = y$ and $L = L_m + L_f$ in figure 4-1. The maximum bed shear stress around an abutment on rectangular channel is believed to be dependent on the abutment

geometry, channel width, water depth, approach velocity, water density, fluid viscosity and gravitational acceleration. The relationship can be sought in the form:

$$\tau_{\max} = f\left[\rho, V, \nu, y, g, L_a, L, W_a, \beta_a, \Theta\right] \tag{4-1}$$

Where $\tau_{\max}$ = maximum bed shear stress around abutment, ρ = water density, V = upstream mean velocity, ν = kinematic viscosity of the fluid , y = upstream water depth, g = gravitational acceleration, L_a = length of abutment and the approach embankment(to the toe of the abutment), L = half width of the channel, W_a = top width of the abutment, β_a = slope of the abutment, and Θ = skew angle of approach embankment. For convenience, L_a is defined as the projected length normal to the flow in the flowing study.

Dimensional analysis of the equation (4-1) results in:

$$\frac{\tau_{\max}}{\rho V^2} = f\left[\frac{VW_a}{\nu}, \frac{V}{\sqrt{gy}}, \frac{L_a}{W_a}, \frac{L_a}{L}, \frac{y}{W_a}, \beta_a, \Theta\right] \tag{4-2}$$

It is desirable to use the top width of the abutment W_a as the characteristic length because W_a is typically fixed for a given bridge (same to the width of bridge deck). $\mathrm{Re} = \frac{VW_a}{\nu}$ is the abutment size based Reynolds number; $\frac{V}{\sqrt{gy}}$ is the upstream Froude number; $\frac{L_a}{W_a}$ is the aspect ratio of the abutment and approach embankment; $\frac{L_a}{L}$ is the blockage ratio; $\frac{y}{W_a}$ is the relative flow depth. For rectangular channel, the upstream

mean velocity could be assumed to be uniform across the entire channel. So the channel contraction ratio C_r defined by flow rate at upstream $\frac{Q_{total}}{Q_{total} - Q_{blocked}}$ is identical to the area ratio $\frac{A_{total}}{A_{total} - A_{blocked}}$. It is also worthwhile to note that C_r is equal to $\frac{L}{L - L_a}$ for the vertical wall and wing-wall abutments. For convenience, C_r based on the area ratio $\frac{A_{total}}{A_{total} - A_{blocked}}$ will be used to replace the blockage ratio in the dimensional analysis in the following study.

The methodology includes the determination of reference case and the parametric studies of the dimensionless parameters given in dimensional analysis. According to the previous study (Briaud et al. 1999, 2003), it is believed that Reynolds number is the determinant factor on maximum bed shear stress around abutment when the relative water depth is greater than two. Hence, the reference case is designed for the convenience of Reynolds study while other correction factors are taken as one. In parametric studies, only one dimensionless parameter is varied and all the others are kept identical to the reference case. The relationship between the varied dimensionless parameter and the maximum bed shear stress can then be determined through data regression. By assuming that these dimensionless parameters are independent, the equation of maximum bed shear stress around abutment on rectangular channel can be derived by timing them together. The influence of compound channel geometry will be investigated by comparing the results of a series cases simulated with different compound channel configuration.

4.2 Reference Case

The flow pattern at an abutment is considered to be similar to that around a pier of shape equivalent to the abutment and its mirror image with respect to the channel wall. The maximum bed shear stress at the abutment, however, should be less than that around the equivalent pier due to the retarding effects of channel wall on the flow (Melville, 1997). Based on previous research (NCHRP 24-15, Briaud et al., 2003), the influence of water depth on maximum bed shear stress around bridge pier can be ignored when water depth is deeper than two times of pier diameter, which is called deep water condition. Actually, this indicates the influence of Froude number is negligible as long as the relative flow depth is large enough. Therefore, it is convenient to define the reference case as a vertical wall abutment in a rectangular channel as shown in Figure 4-2. The abutment length is chosen to be one-half of the abutment width such that the abutment together with its mirror image forms a square pier. The orientation of the abutment is perpendicular to the flow direction and the water depth is twice of the abutment width to ensure that the influence of Froude number is negligible. Hence, the detailed dimensions of the reference case can be determined according to the flume tests in NCHRP 24-15(2). The width of the flume employed is 12ft, which is equal to the half width of the channel L since only half of the river is simulated in flume tests. And the top width of the abutment W_a is 1.5 ft. So the water depth is 3ft. As seen in Figure 4-2, the half width of the channel L is 8 times of the abutment width W_a, which gives a rather small contraction ratio of 1.07 (blockage ratio of 6.25%).

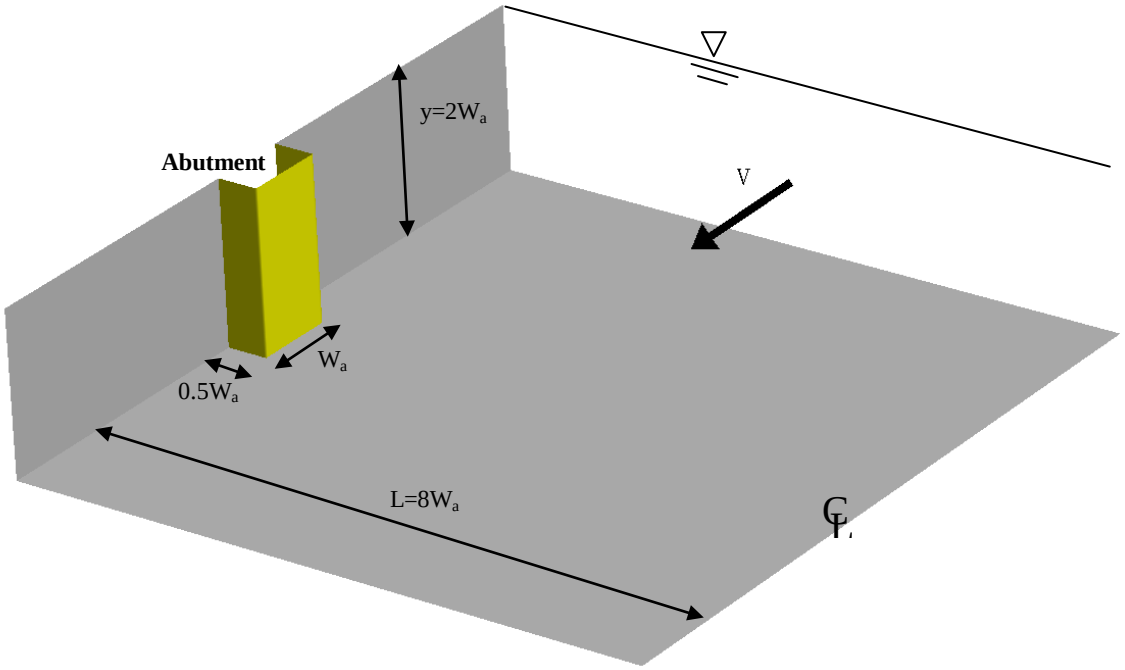

Figure 4-2 Diagram of the reference case.

Dimensionless (normalized by abutment top width W_a) Cartesian coordinate system (x,y,z) = (X/Wa, Y/Wa, Z/Wa) is employed in the numerical simulations. The xy plane is fixed on the horizontal river bottom; the z coordinate is pointed upward from riverbed to water surface; the x coordinate is pointed from upstream to downstream along the straight channel.

Orthogonal grid system is desirable in numerical simulations. Hence, the entire computation domain is decomposed into several blocks to facilitate the generation of the rectangular grids. As shown in Figure 4-3, fully-connected body-fitted grid system is utilized with one cell overlap between neighboring blocks. The numerical grid of the reference case consists of four blocks. The numbers of the grid points from Block1 to

Block 4 are 40×75×31, 29×54×31, 69×26×31, and 80×75×31, respectively. Multi-block grid is a special condition of Chimera grid and the data communication between difference blocks is performed through the PEGSUS program (Suhs &Tramel, 1991).

In CHEN3D program, the two layer method is implemented to solve the flow field all the way to the solid surface. One equation model is employed for the near-wall region and the standard $k-\varepsilon$ model is used in the outer region away from the wall. To accurately solve the near wall flow including the laminar sublayer and buffer layer, the first grid point near the solid surface should be placed within the viscous sublayer and satisfy the requirement of $y^+ < 1$, where $y^+ = \mathrm{Re}\, u_\tau y_n$, y_n = the normalized distance to the wall and u_τ = normalized friction velocity. Therefore, the grids in the near wall region must be extremely fine so that the velocity gradient can be resolved correctly. To reduce CPU time and the memory requirement, the channel is assumed to be symmetric and only one-half of the channel is studied.

As mentioned in the dimensional analysis, the Reynolds number $\mathrm{Re}=VW_a/\nu$ is defined based on the upstream mean velocity V, abutment top width W_a and kinematic viscosity ν (20°C). For the reference case, the Reynolds number of 10^5 is chosen. It is a typical magnitude in most flume tests, which is equivalent to 0.72ft/s upstream velocity and 1.5ft of abutment top width. No-slip boundary condition is applied on the river bottom and abutment face. The rigid lid is applied on free surface since the influence of water surface is negligible. Dimensionless time increment of 0.2 is chosen in the simulation. The result is found to be converged after 5000 iterations.

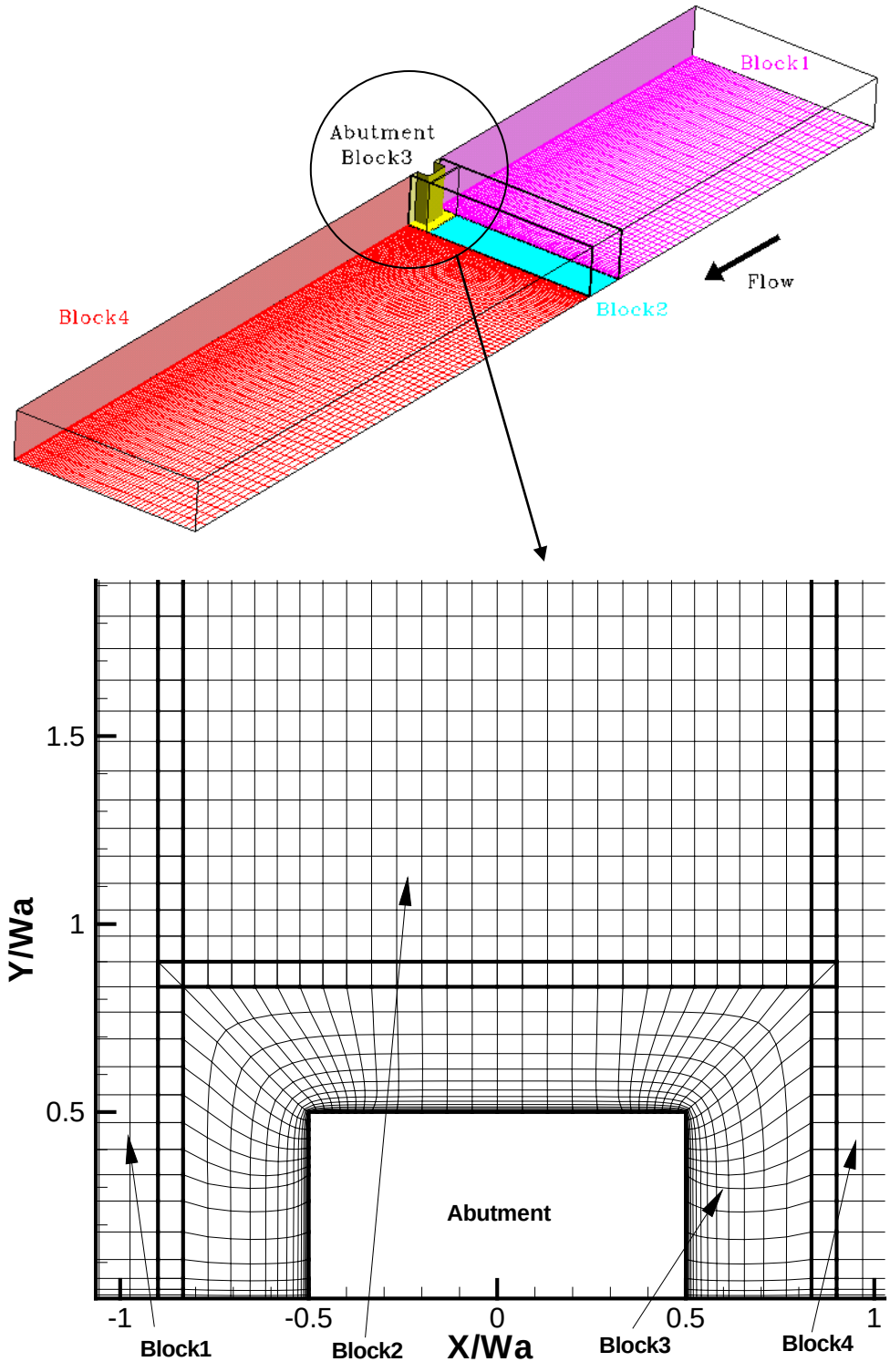

Figure 4-3 Numerical grid for the reference case.

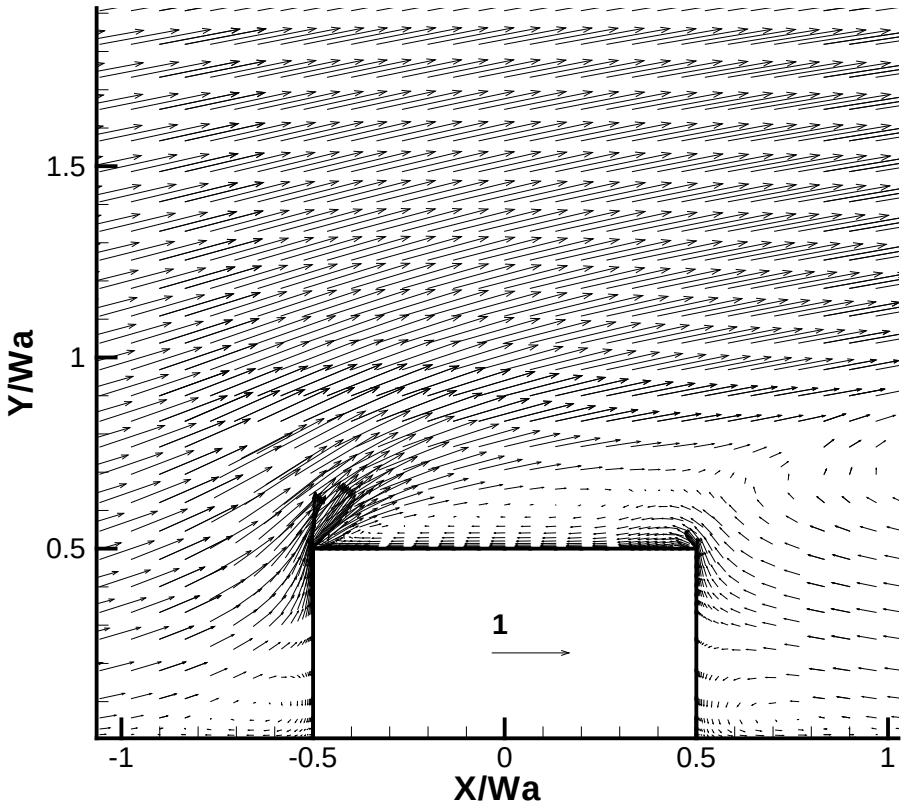

Figure 4-4 Velocity vectors on water surface (reference case).

Figure 4-4 shows the flow pattern around abutment on the free surface. The abutment causes complicated flow features, including vortex shedding, wake vortices and large recirculation behind the abutment. At upstream of the abutment, the affected area is very small, about one time of abutment length. At the downstream of the abutment, the affected area is very large. The area of the recirculation can be as large as several times of abutment length. This large recirculation continues to congest the flow and force the flow moving toward channel center. This is why the velocity magnitude is higher at the downstream instead of middle of the abutment along the channel center. At the upstream corner of the abutment, the flow is mostly accelerated and forced around

the abutment. The maximum velocity appears around the upstream corner. However, only in the region very adjacent to the abutment, the velocity increased significantly. In the transverse direction, the flow is disturbed seriously only in a narrow range in front of the abutment face. Outside of that range, the velocity vectors remain uniform. The influence can only be reflected from the flow direction and the velocity magnitude. The flow separation appears right on the abutment face.

Figure 4-5 shows the normalized pressure contours around abutment. At the upstream side, the higher pressure occurs due to the obstacle of the abutment. Pressure drops sharply at the upstream corner; this is consistent with the local velocity acceleration. The pressure recovers the uniform distribution very quickly away from the abutment.

Figure 4-6 presents the bed shear stress distribution. The maximum bed shear stress is about 0.5 Pa at the upstream corner of the abutment. This is the initial bed shear stress contour before scouring. The shear stress will continue to decrease with the development of the scour hole. The scour process stops when the bed shear stress reaches the critical shear stress of the bed soils.

To study the influence of the water surface boundary condition, the same cases with rigid lid and free surface boundary conditions have been simulated. The results show little influence of surface boundary to the maximum bed shear stress around abutment. The difference is within 2%. And for most of cases in actual engineering application, the blockage of the river will not be very large. Hence this assumption should be reasonable.

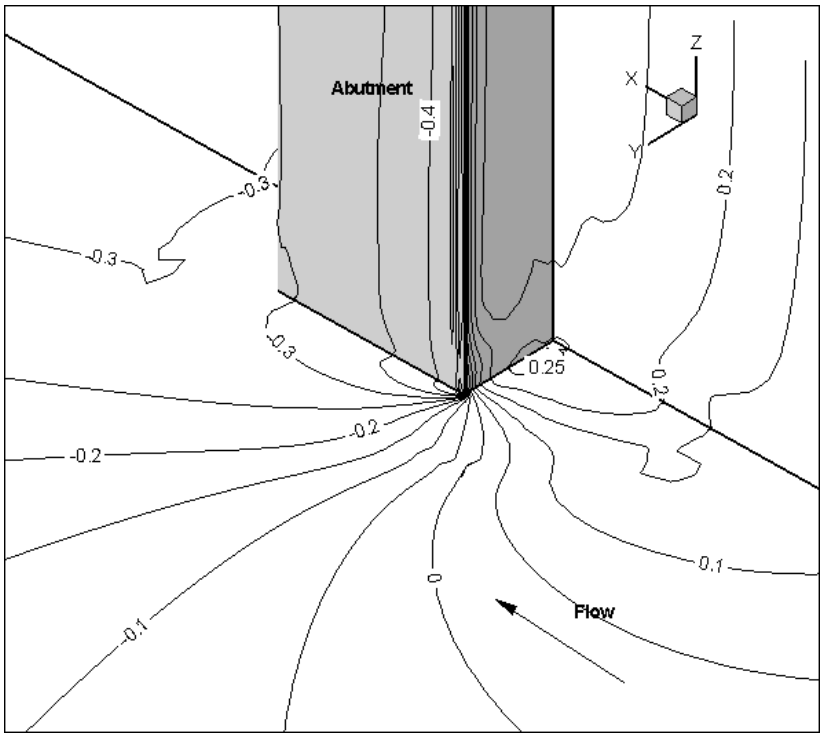

Figure 4-5 Normalized pressure contours around vertical wall abutment.

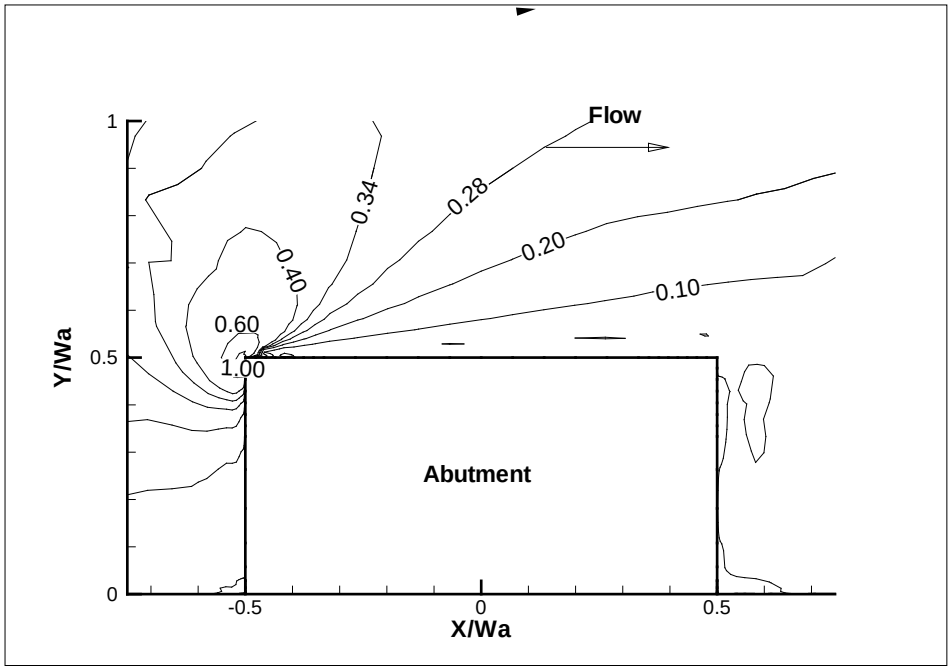

Figure 4-6 Bed friction coefficient ($\times 10^{-2}$) contour for Reynolds number 10^5.

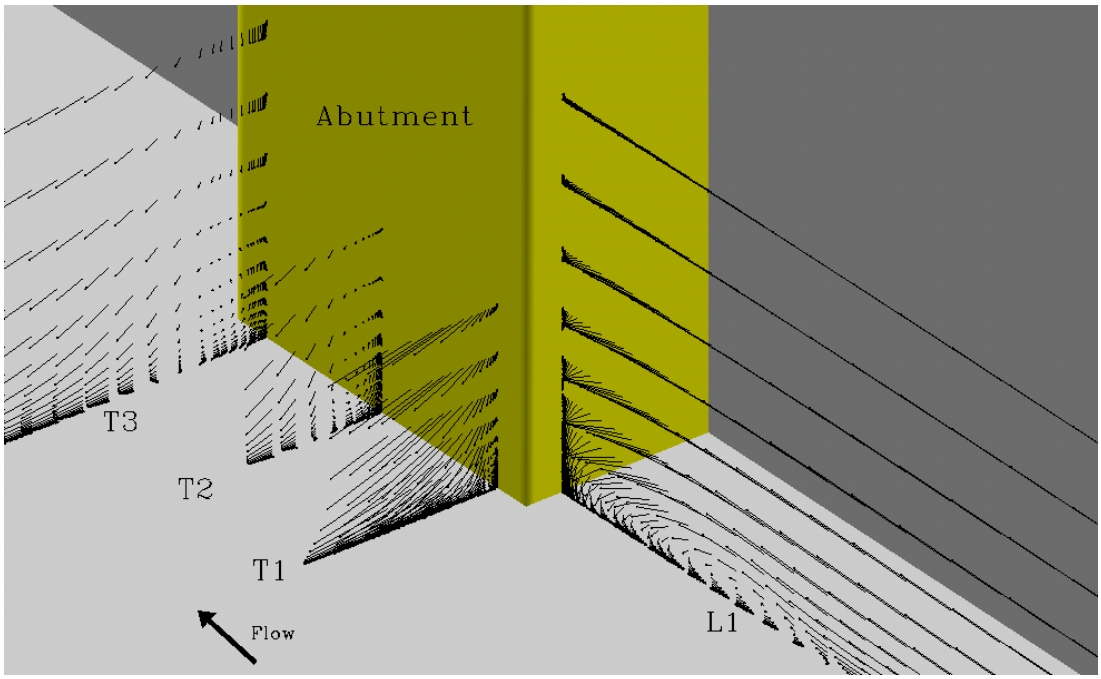

Figure 4-7 Projected velocity vectors on the cross sections around abutment.

Figure 4-7 is to show the detail variation of the velocity field around the abutment. The projected velocity vectors are plotted on these four cross sections. So, the cross section T1, T2, and T3 are showing the secondary flow in front of the abutment face. From the longitudinal cross section L1, the horse shoe vortex can be observed clearly. The downflow along the abutment upstream face hits the riverbed directly, which is the dominant factor in the scour process. The velocity magnitude is extremely high on cross section T1 since the flow direction is change seriously at the upstream corner. On cross sections of T2 and T3, the velocity magnitude adjacent to the abutment is not large. But the flow is extremely complicated in this area with very high turbulence intensity. According to the observation in the flume tests, the scour depth is still remarkable in this

area. This implies that both the velocity magnitude and the turbulence intensity can contribute to the scour development.

4.3 Parametric Studies

4.3.1 Influence of Reynolds number

For the pier study in NCHRP 24-15 (Briaud et al., 2003), half of the domain was computed with the symmetric line passing the center of circular pier. The symmetric boundary condition was applied on both the symmetric line and the other side away from the pier. In current study, symmetric assumption is also adopted and the symmetric line is along the center of the channel. No-slip boundary is applied on the side wall with abutment. So, the only difference between the previous pier study and the current abutment study is the boundary condition along with the hydraulic structures. To investigate the influence of the boundary conditions, the same grid has been tested for these two settings of pier and abutment (half of the circular pier). And the maximum bed shear stress around the abutment is about 2/3 of that around pier. This indicates that the influence of Reynolds number on the maximum bed shear stress around abutment is not identical to the proposed pier equation in previous report of NCHRP 24-15. Hence, there is a need to study the influence of Reynolds number on the maximum bed shear stress around the abutment. Another reason is that the typical abutment shape is vertical wall instead of circular cylinder. The influence of shape could be significant.

As discussed before, the maximum bed shear stress is believed to be the function of Reynolds number. The influence of Froude number is negligible as long as the relative flow depth is large enough. Further assuming the correction factors from all the

other dimensionless parameters are one for the reference case. The equation (4-2) can be further simplified as,

$$\frac{\tau_{\max}}{\rho V^2} = f\left[\frac{VW_a}{\nu}\right] \tag{4-3}$$

Numerical simulations were conducted for eight different Reynolds numbers ($Re=VW_a/\nu$) of 1×10^4, 2×10^4, 5×10^4, 1×10^5, 5×10^5, 1×10^6, 5×10^6 and 1×10^7 based on the same geometry as the reference case. Figure 4-8 shows the variation of the computed maximum bed friction coefficient (C_{f_vw}) around vertical wall abutment with Reynolds number. For completeness, the maximum bed friction coefficient C_{f_cp} equation for circular pier by Briaud et al. (1999) is also shown in the same figure. Both curves show that the normalized maximum bed shear stress decreases with the increase of Reynolds number. It should be noted that this does not mean that the dimensional bed shear stress also decreases with Reynolds number because it depends on not only Reynolds number but also the upstream velocity. The discrepancy, shown in figure 4-8, between the previous pier study and current abutment study is from both the hydraulic structure shape and the side boundary conditions. Generally, the bed shear stress is higher around vertical wall abutment than around circular pier. The separation point around vertical abutment is always at the sharp upstream corner in spite of the magnitude of the Reynolds number. While the separation point around circular pier is changing with Reynolds number. In figure 4-8, the curve for circular pier is much flatter than the one for vertical wall. C_{f_vw} is higher than C_{f_cp} when Reynolds number is smaller than 3×10^5. When the Reynolds number is higher than 3×10^5, the curve for vertical wall also tends to

be flat and the magnitude is lower than that for circular pier. There is one possibility that the influence from the boundary may also vary with the Reynolds number. According to the simulation results, the equation for circular pier is not suitable for the abutment analysis. Another interesting observation is that the difference between these two curves tends to be small when Reynolds number is very high. As show in Fig 4-8, these two curves are almost parallel in the high Reynolds region. Figures 4-9, 4-10, and 4-11 present the simulated bed friction coefficient contours for different Reynolds numbers.

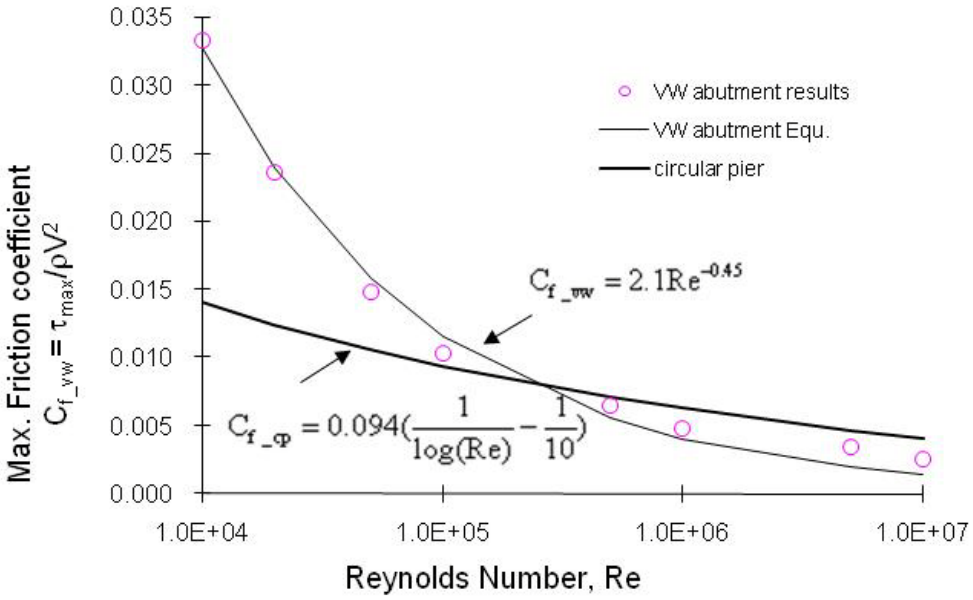

Figure 4-8 Normalized maximum bed shear stresses versus Reynolds number.

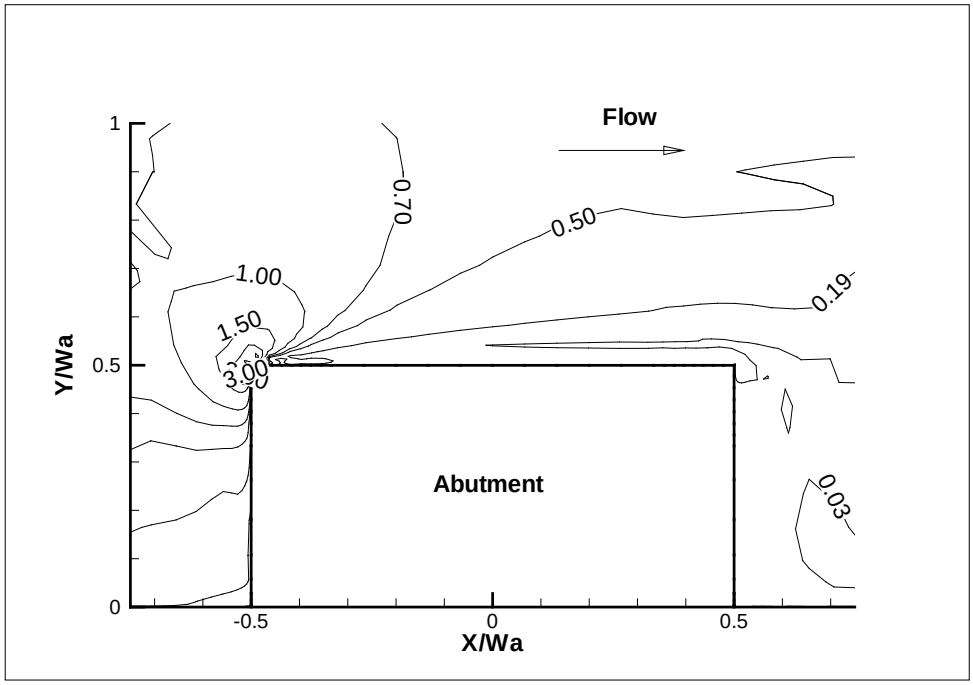

Figure 4-9 Bed friction coefficient ($\times 10^{-2}$) contour for Reynolds number 10^4.

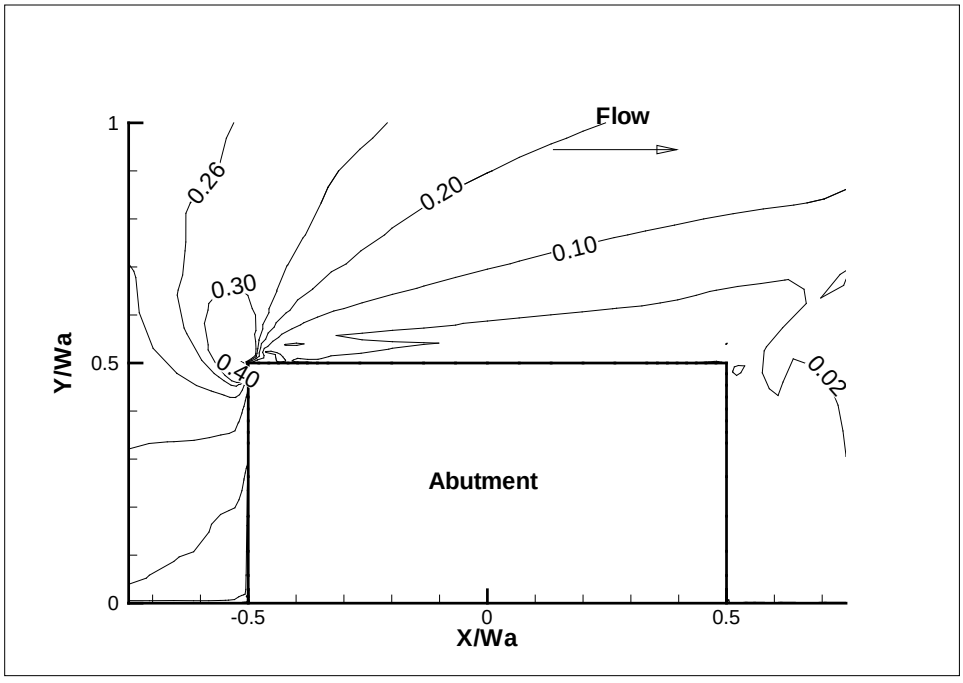

Figure 4-10 Bed friction coefficient ($\times 10^{-2}$) contour for Reynolds number 10^6.

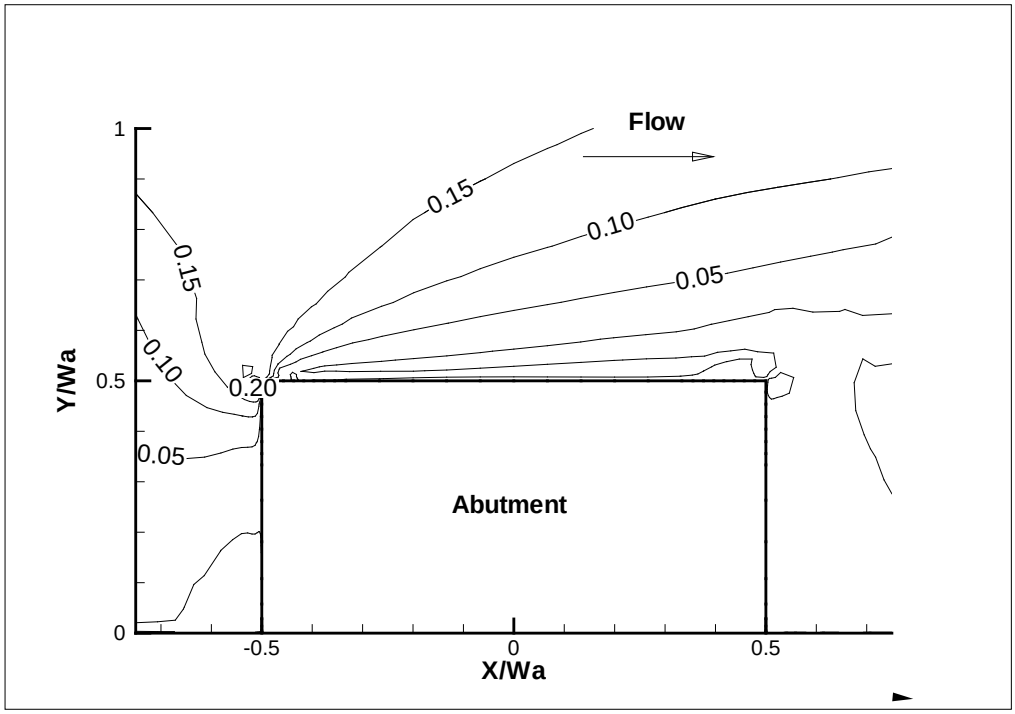

Figure 4-11 Bed friction coefficient ($\times 10^{-2}$) contour for Reynolds number 10^7.

4.3.2 Influence of water depth

It is feasible to adjust the grid of the reference case vertically and yield different relative water depth y/W_a. The vertical distribution of the grid points will change with y/W_a. But the vertical wall abutment together with the grid system can remain the same. The Reynolds number is kept same to the reference case as well as the boundary conditions. Five cases are performed with CHEN3D program to study the water depth variation, including y/W_a of 0.125, 0.25, 0.5, 1.0, and 2.0. Actually, Froude number is also changing with the relative water depth y/W_a. The corresponding value is 0.29, 0.21, 0.15, 0.10, and 0.07. It cannot be avoided since the Reynolds number is required to be constant. It is believed that both the Fr and y/W_a represent the influence of the water

depth on $\tau_{\max}$ around the abutment. So Froude number is used to in the data regression. One way to present the result is to plot $\tau_{\max} / \tau_{\max\_reference}$ as a function of Fr. The shallow water correction factor, K_w, is the ratio of $\tau_{\max} / \tau_{\max\_reference}$. Figure 4-12 presents the results of the five simulations. When the Froude number is smaller than 0.10, the influence of the water depth is negligible. Figures 4-13, 4-14, and 4-15 show the results of friction coefficient contours of different water depth. Water depth variation has little influence on the bed shear stresses away from the abutment.

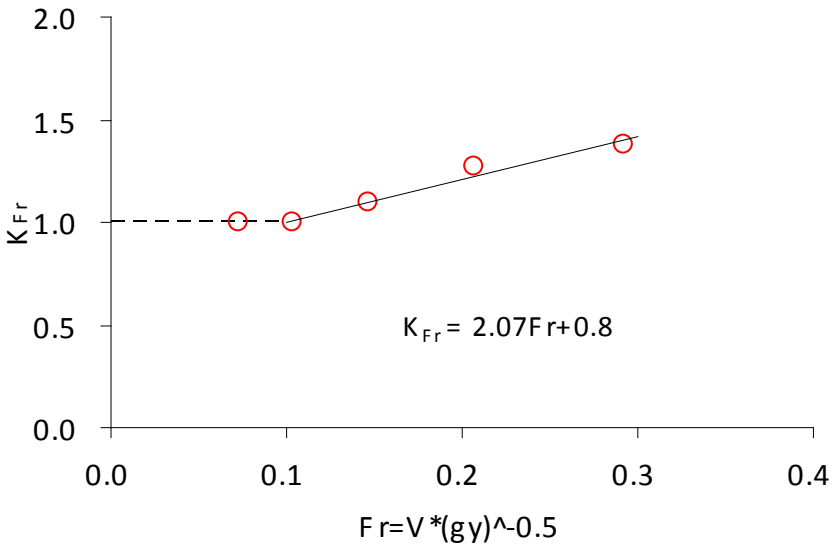

Figure 4-12 Correction factor for water depth.

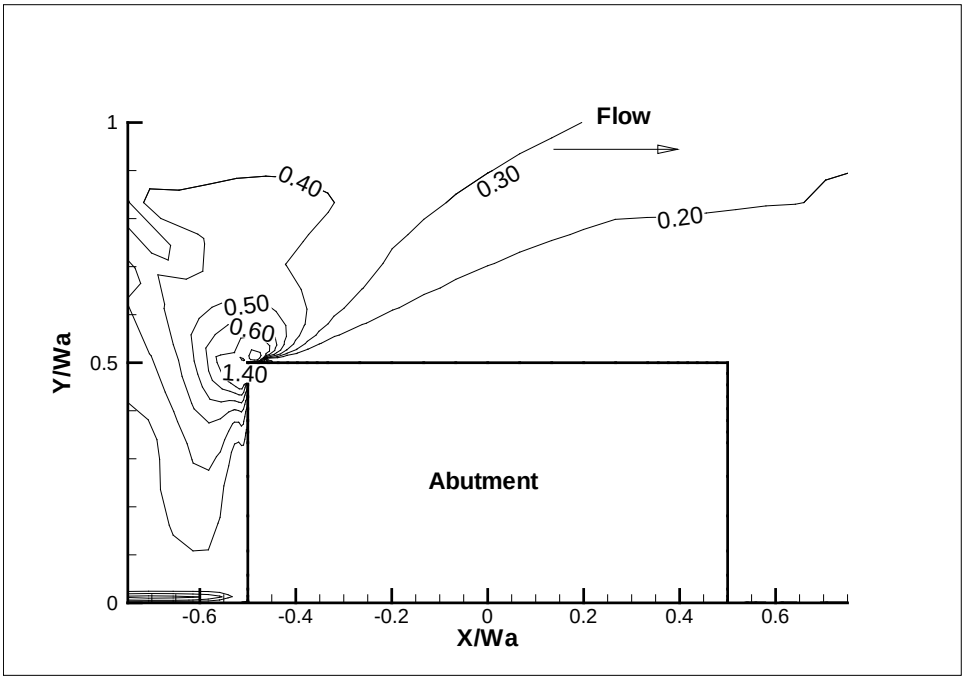

Figure 4-13 Bed friction coefficient ($\times 10^{-2}$) contour for y/W_a=0.25.

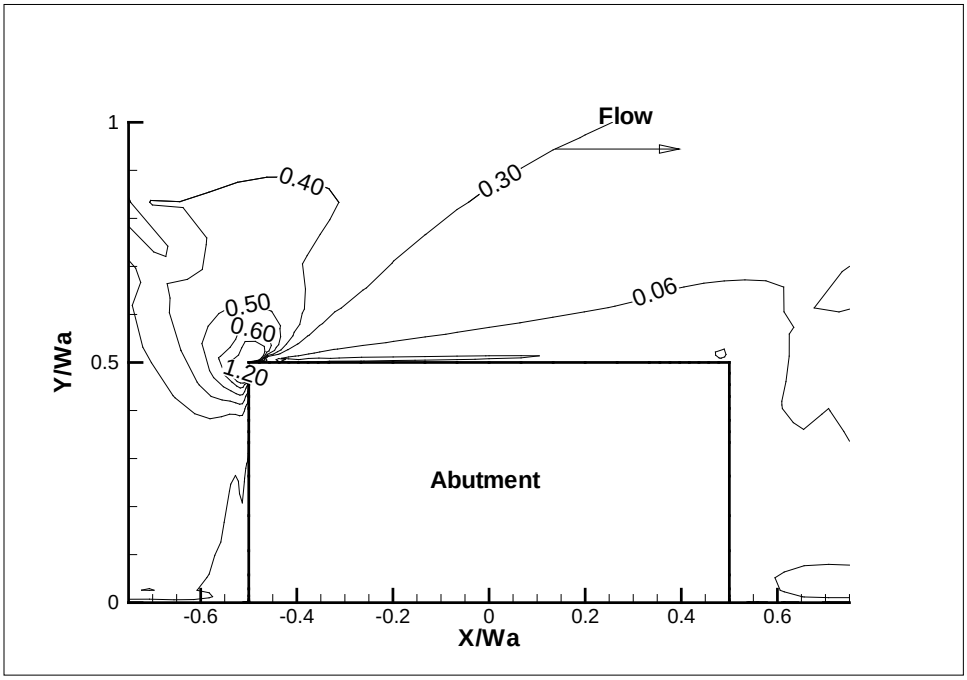

Figure 4-14 Bed friction coefficient ($\times 10^{-2}$) contour for y/W_a=0.5.

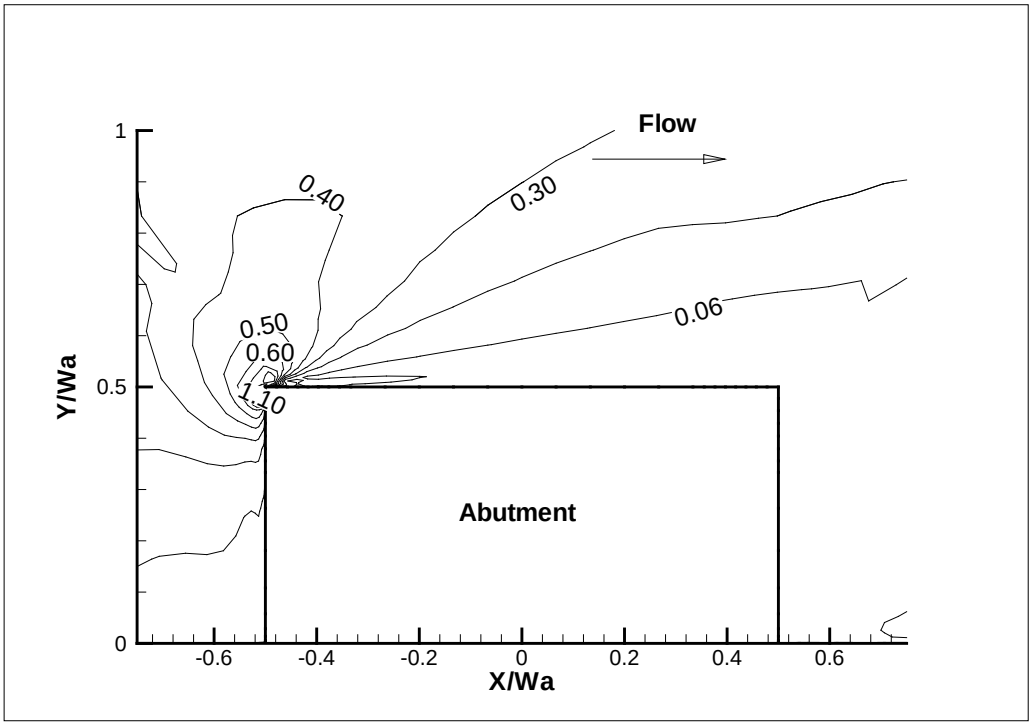

Figure 4-15 Bed friction coefficient ($\times 10^{-2}$) contour for y/W_a=1.0.

4.3.3 Influence of channel contraction ratio

The objective of this parametric study is to obtain the relationship between the maximum bed shear stress $\tau_{\max}$ and the channel contraction ratio C_r. The grid of reference case is modified to have L equal to $0.83W_a$, $1.25W_a$, and $2.5W_a$. All other parameters remain same as the reference case. Figure 4-16 presents the variation of the channel width. Figures 4-18, 4-19, and 4-20 show the contours of the normalized bed shear stress contours for different contraction ratios. The velocity and the bed shear stress increase with the increase of contraction ratio. The maximum bed shear stress $\tau_{\max}$ is the maximum shear stress that exists on the river bed just before the scour hole to develop. One way to present the data is to plot $\tau_{\max} / \tau_{\max\_reference}$ as a function of

contraction ratio C_r shown in figure 4-17. The contraction ratio correction factor, K_{Cr}, is the ratio of $\tau_{\max} / \tau_{\max\_reference}$. The data points on figure 4-17 correspond to the results of the three simulations and the reference case. By data regression, the correction factor K_{Cr} is found to be linear proportional with the contraction ratio C_r. Higher contraction ratio means that the channel is highly blocked. It should be noted that the contraction ratio C_r for the reference case is 1.07 and the corresponding correction factor K_{Cr} is equal to 1.0. For the limiting case of a very wide channel with $C_r \rightarrow 1$, it is anticipated that the maximum shear stress around the abutment will be approximately 20% lower (i.e., K_{Cr} = 0.8) than the corresponding value for the reference case.

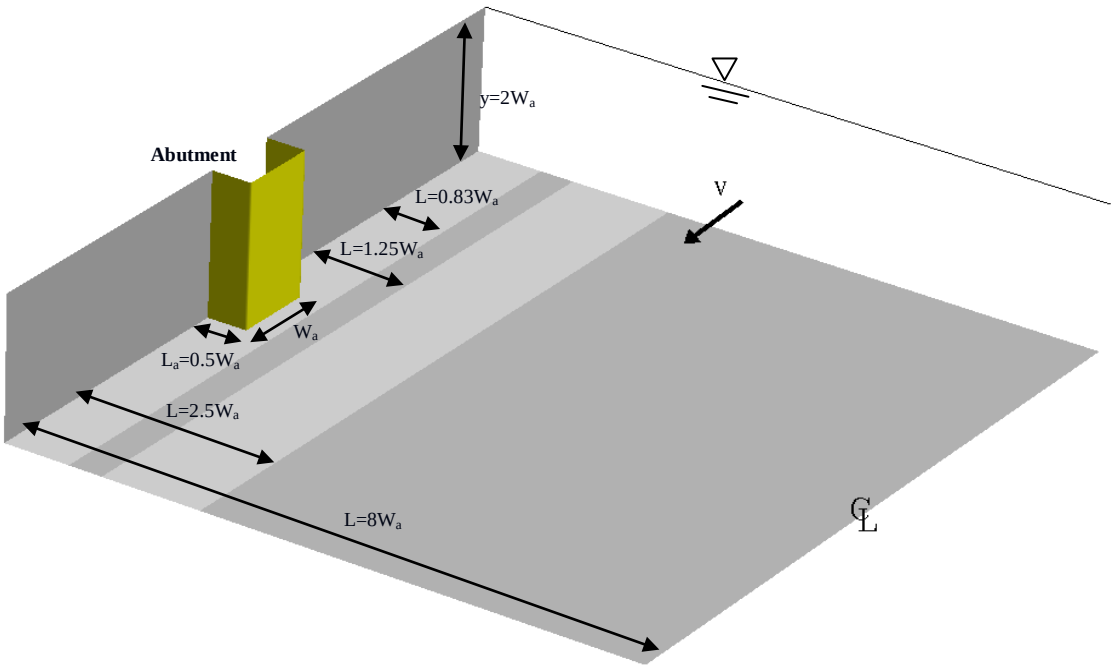

Figure 4-16 Geometries for channel contraction ratio study.

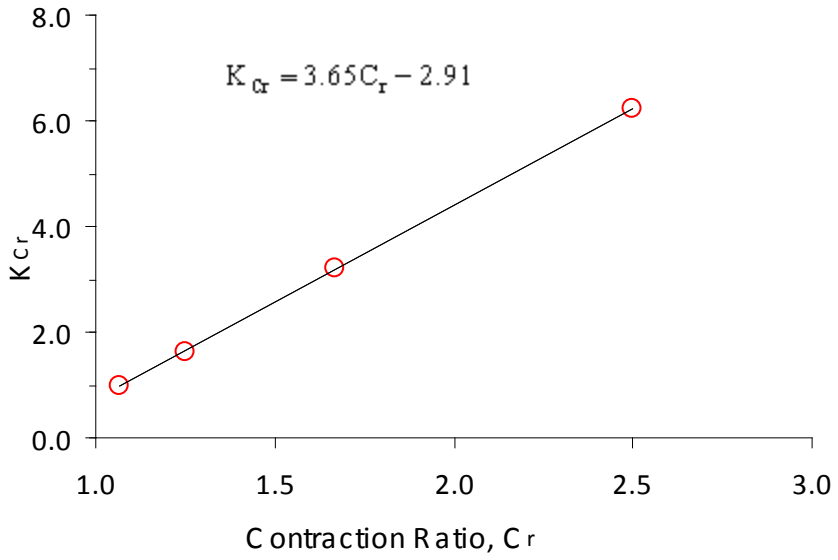

Figure 4-17 Correction factor for channel contraction ratio.

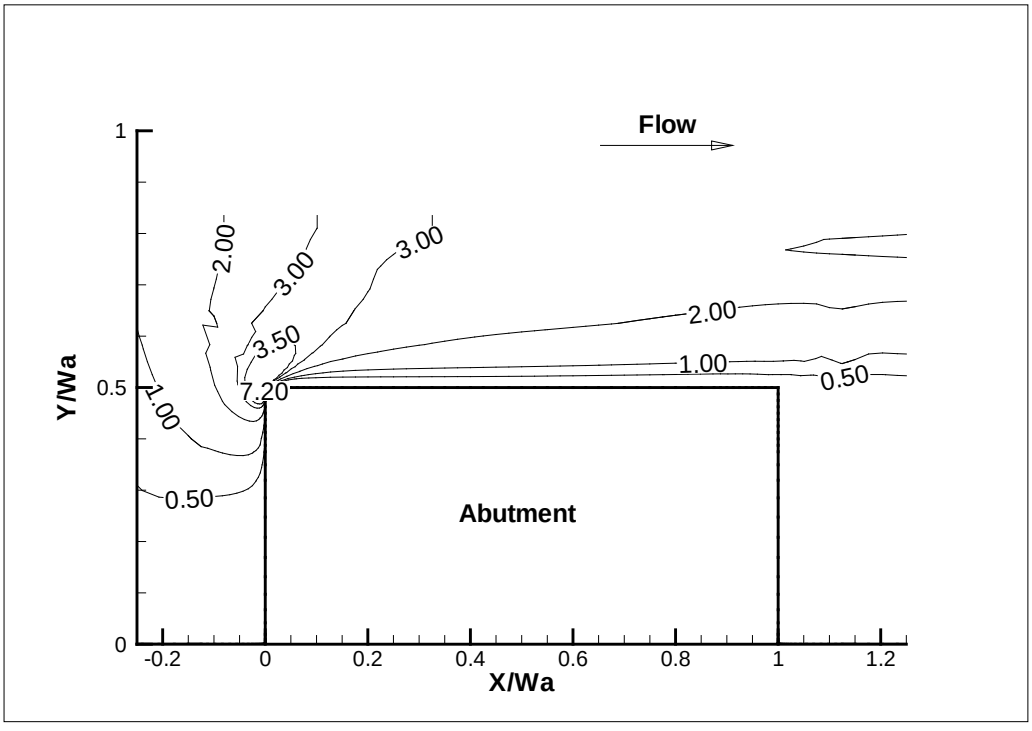

Figure 4-18 Bed friction coefficient ($\times 10^{-2}$) contour for C_r =0.4.

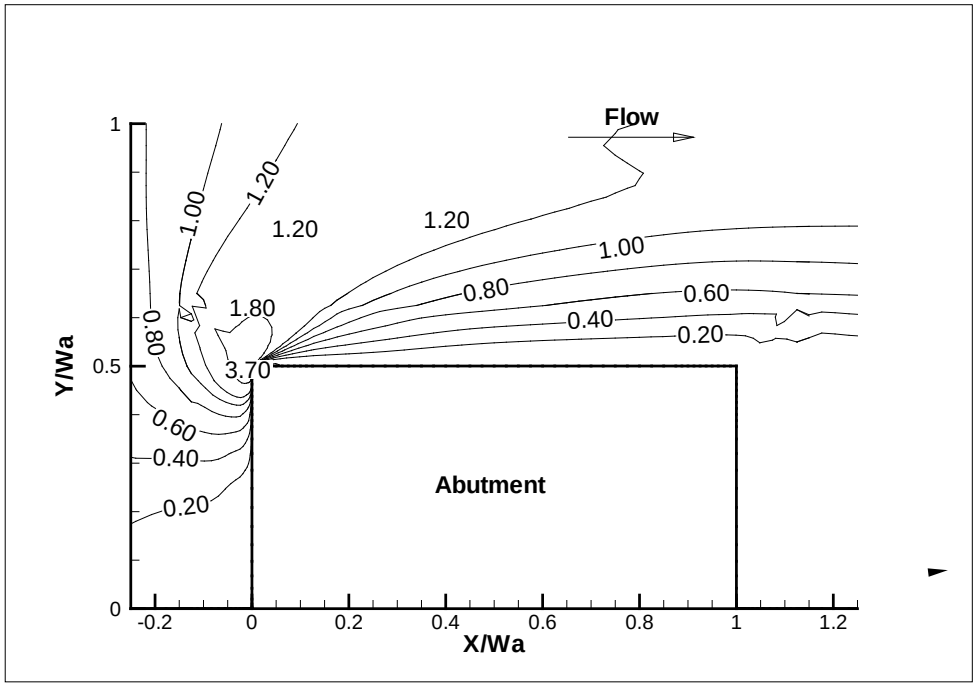

Figure 4-19 Bed friction coefficient ($\times 10^{-2}$) contour for C_r =0.6.

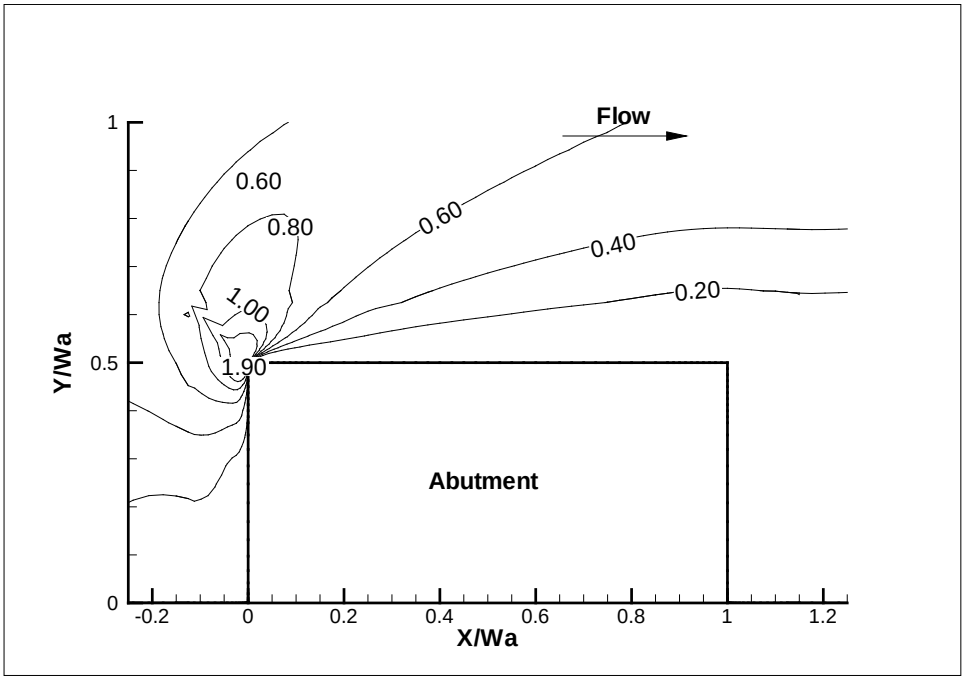

Figure 4-20 Bed friction coefficient ($\times 10^{-2}$) contour for C_r =0.8.

4.3.4 Influence of aspect ratio of the abutment

The objective of this section is to obtain the relationship between the maximum bed shear stress $\tau_{\max}$ and the aspect ratio L_a / W_a of the abutment and approach embankment. The length of the abutment in the reference case is modified to generate six new cases with different aspect ratio L_a / W_a. These six new cases have same abutment top width W_a, half channel width L, water depth y and upstream mean velocity V as the reference case. Fig 4-21 shows the variation of the abutment length. One way to present the result is to plot $\tau_{\max} / \tau_{\max\_reference}$ as a function of L_a / W_a. It should be noted that both aspect ratio L_a / W_a and contraction ratio C_r vary with the abutment length L_a because the channel width is fixed. Therefore, the variation of $\tau_{\max}$ with the abutment length has two contributors. It is necessary to exclude the influence of contraction ratio in the data analysis in order to obtain the aspect ratio correction factor, K_{sh}. The aspect ratio correction factor is the corrected $\tau_{\max} / \tau_{\max\_reference}$. Table 4-1 lists the detailed calculation of aspect ratio correction factor K_{sh} for the six cases and the reference case. The correction factor K_{sh} is plotted in Figure 4-22 as a function of abutment aspect ratio L_a / W_a. K_{sh} is found to decrease with the increase of L_a / W_a. The aspect ratio correction factor drops very faster when L_a / W_a increases from 1 to 3. When L_a / W_a is larger than 3, the correction factor tends to be steady. The influence of aspect ratio is not as significant as contraction ratio. Figures 4-23, 4-24, 4-

25, and 4-26 gives some of the normalized bed shear stress contours for the aspect ratio study.

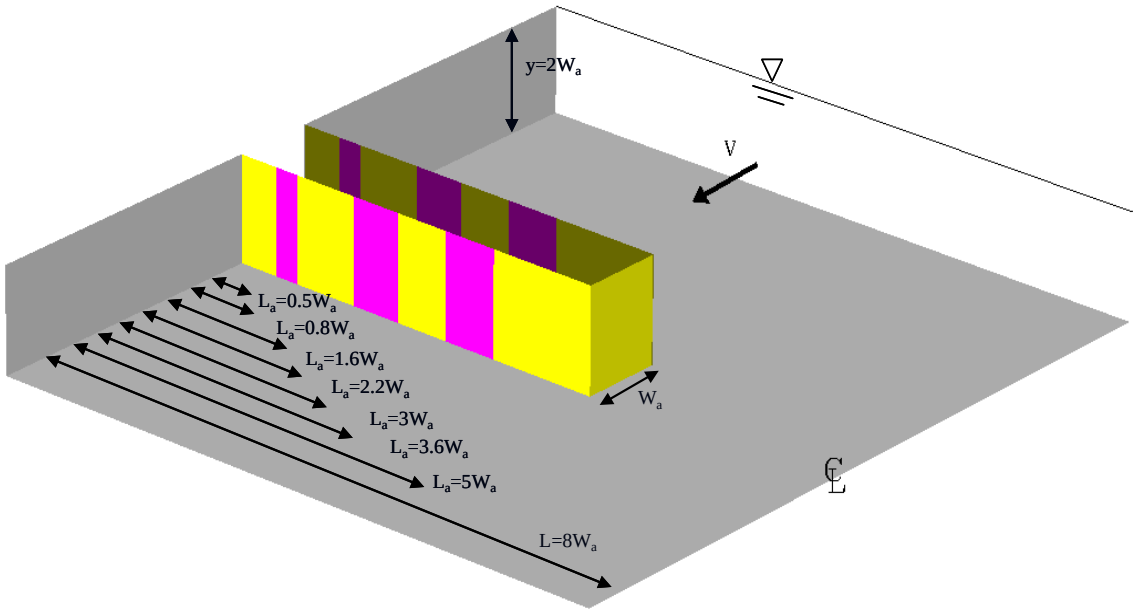

Figure 4-21 Geometries for the study of abutment aspect ratio.

L_a	y	V	W_a	C_{f_max}	Re	Cr	K_{Cr}	L_a/W_a	K_{sh}
ft	ft	ft/s	ft	----	----	----	----	----	----
0.75	3.00	0.72	1.50	0.0115	1.00E+05	1.07	1.00	0.50	1.00
1.2	3.00	0.72	1.50	0.0119	1.00E+05	1.11	1.15	0.80	0.89
2.4	3.00	0.72	1.50	0.0146	1.00E+05	1.25	1.66	1.60	0.76
3.33	3.00	0.72	1.50	0.0169	1.00E+05	1.38	2.15	2.22	0.68
4.33	3.00	0.72	1.50	0.0221	1.00E+05	1.56	2.81	2.89	0.68
5.33	3.00	0.72	1.50	0.0283	1.00E+05	1.80	3.67	3.55	0.67
7.33	3.00	0.72	1.50	0.0412	1.00E+05	2.57	6.48	4.89	0.55

Table 4-1 Physical parameters and the correction factors in aspect ratio study.

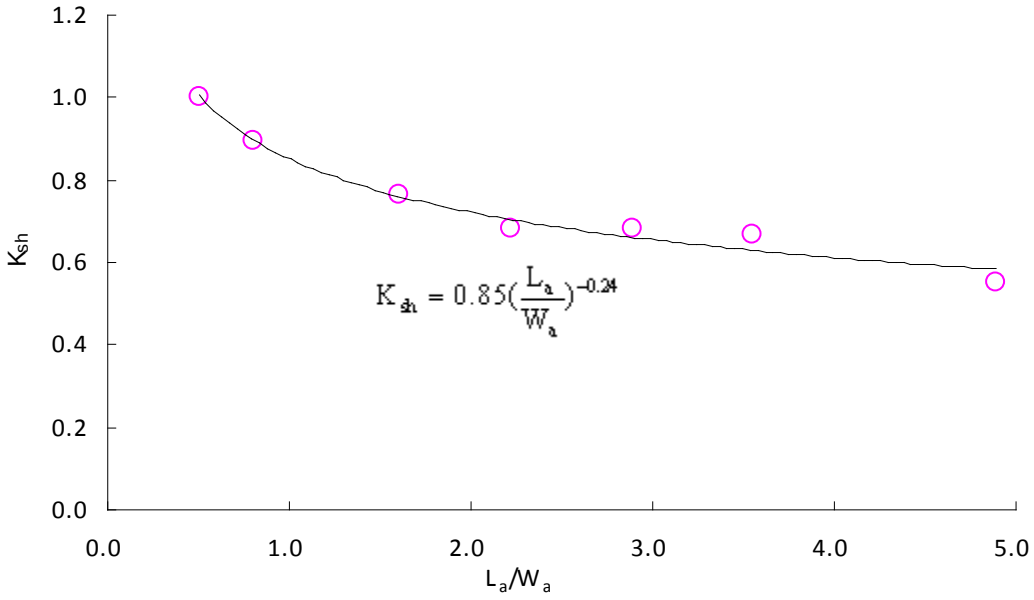

Figure 4-22 Correction factor for abutment aspect ratio.

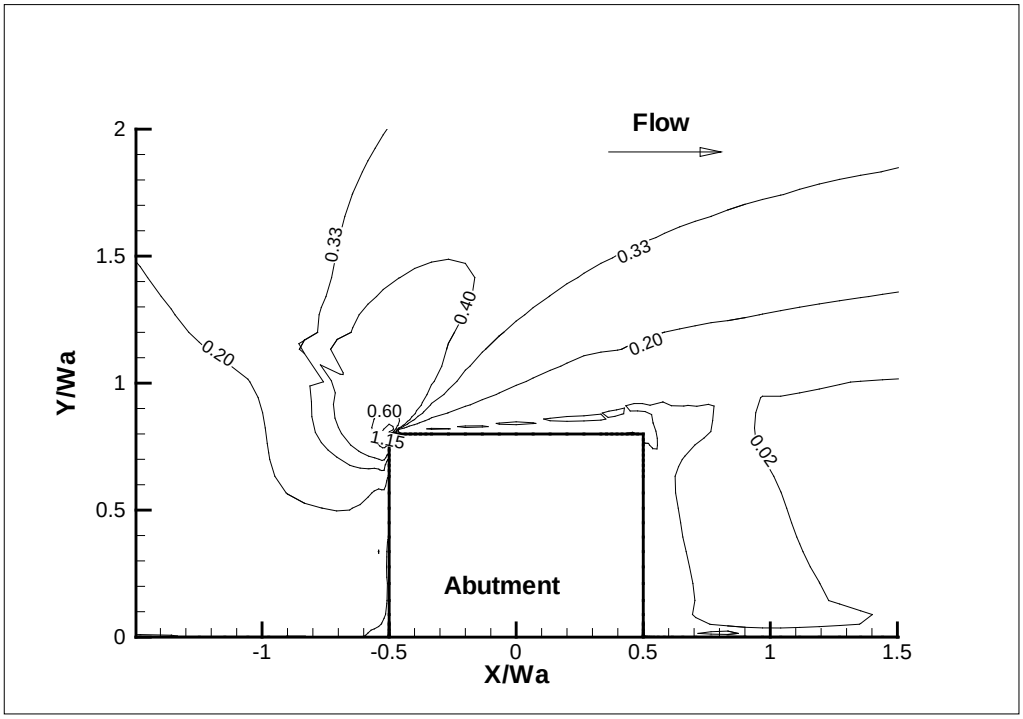

Figure 4-23 Friction coefficient ($\times 10^{-2}$) contour for L_a=1.2ft.

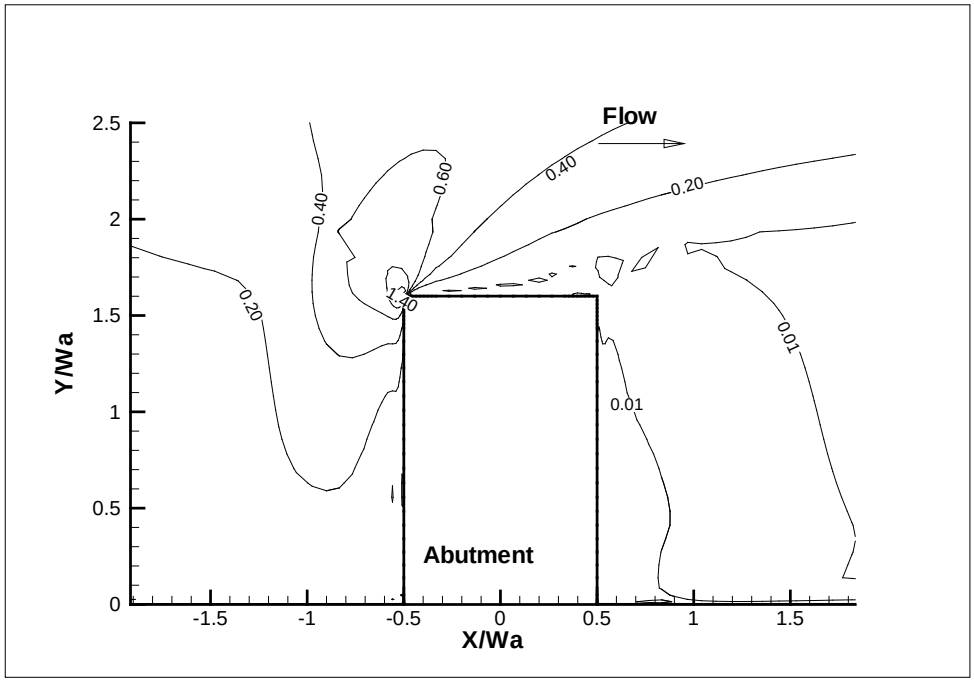

Figure 4-24 Bed friction coefficient ($\times 10^{-2}$) contour for L_a=2.4ft.

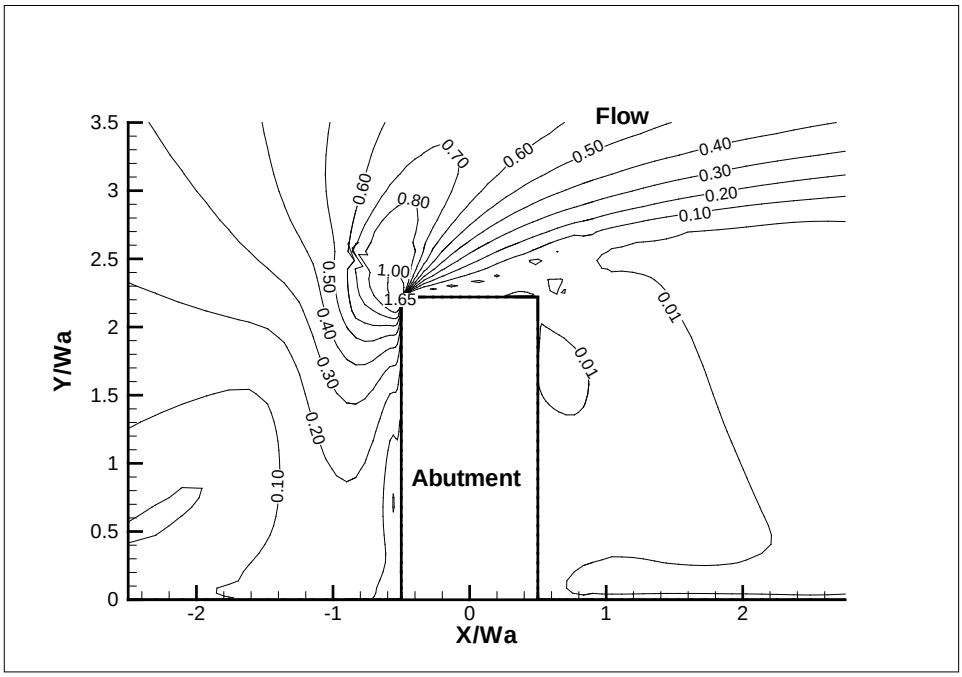

Figure 4-25 Bed friction coefficient ($\times 10^{-2}$) contour for L_a=3.33ft.

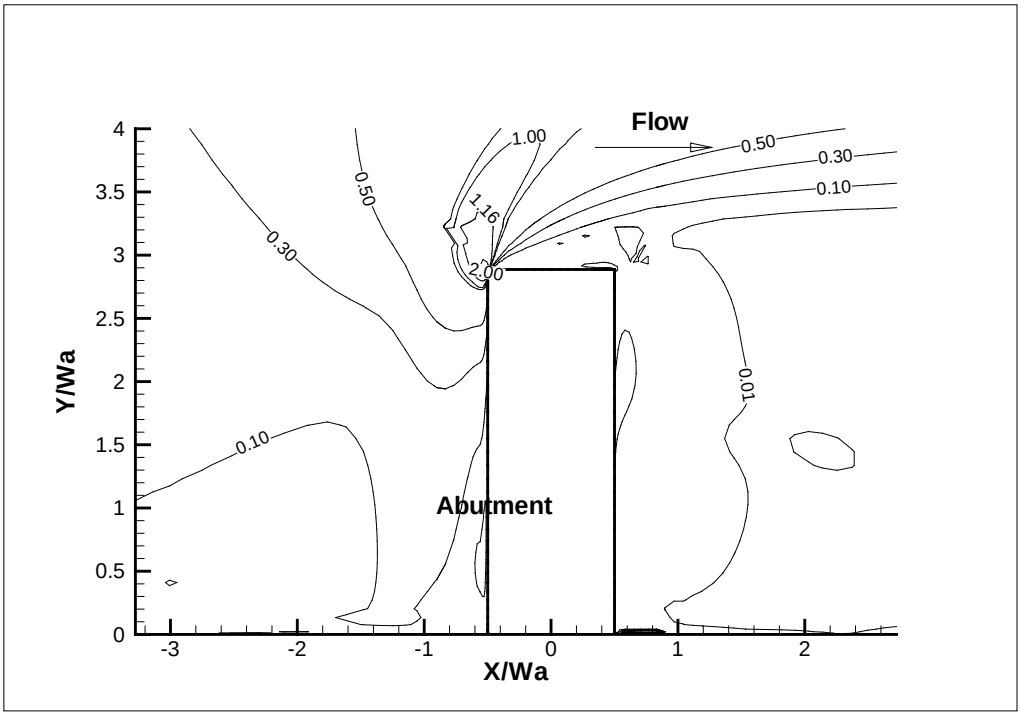

Figure 4-26 Bed friction coefficient ($\times 10^{-2}$) contour for L_a =4.33ft.

4.3.5 Influence of the abutment shape

The objective of this section is to obtain the relationship between the maximum bed shear stress and the abutment shape. Four flume tests with wing-wall abutment in rectangular channel are simulated. They have same approach velocity, water depth, channel width but different abutment lengths. Another two sets of same simulations are performed with wing-wall abutment replaced by vertical wall and spill-through shape. The contraction ratios are identical for cases with wing-wall and vertical wall abutment if they have same abutment length. So the shape correction factor K_s of wing-wall abutment can be determined directly by the ratio of $\tau_{\max\_WW} / \tau_{\max\_VW}$, as tabulated in table 4-2. Vertical wall abutment is adopted in the reference case. So, K_s for vertical wall

abutment is one. The influence of abutment length on the shape factor can also be investigated in table 4-2. The shape correction factors of wing-wall abutment are nearly constant, though the value tends to be smaller with the increase of abutment length. Based on table 4-2, a constant correction factor of 0.65 was proposed for the wing-wall abutments for convenience. Figures 4-27 to 4-30 show the detail normalized bed shear stress (C_f) contours of these four cases with wing wall abutment.

y	V	L	L_a	W_a	$C_{f\_max\_WW}$	$C_{f\_max\_VW}$	K_s
ft	ft/s	ft	ft	ft	----	----	----
1.20	1.09	12.00	3.33	1.50	0.0107	0.0165	0.65
1.20	1.09	12.00	4.33	1.50	0.0138	0.0211	0.65
1.20	1.09	12.00	5.33	1.50	0.0161	0.0257	0.63
1.20	1.09	12.00	7.33	1.50	0.0260	0.0450	0.58

Table 4-2 Shape correction factors of wing-wall abutment.

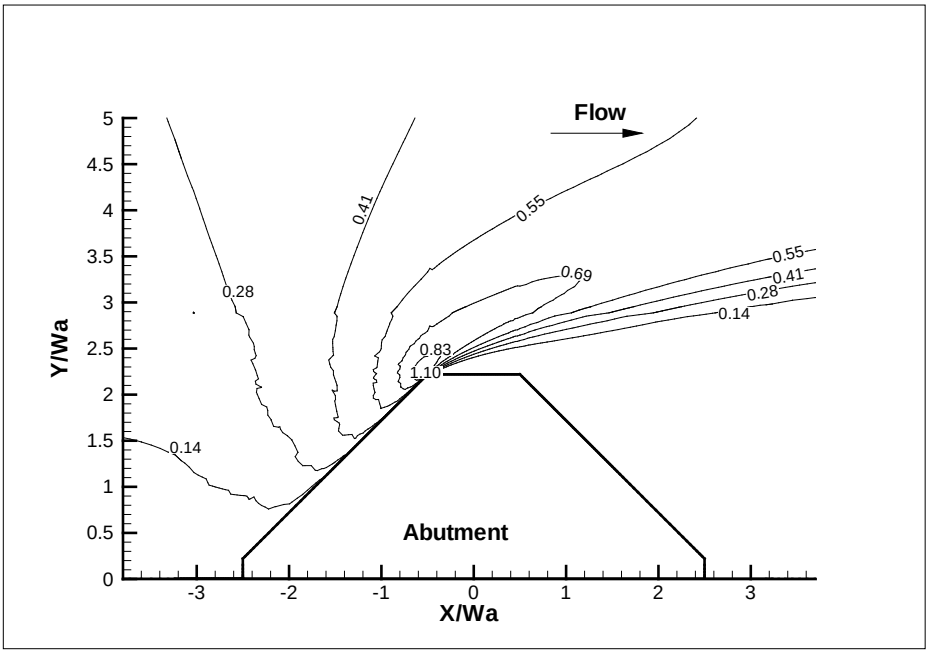

Figure 4-27 Bed friction coefficient ($\times 10^{-2}$) contour for L_a = 3.33ft (WW abutment).

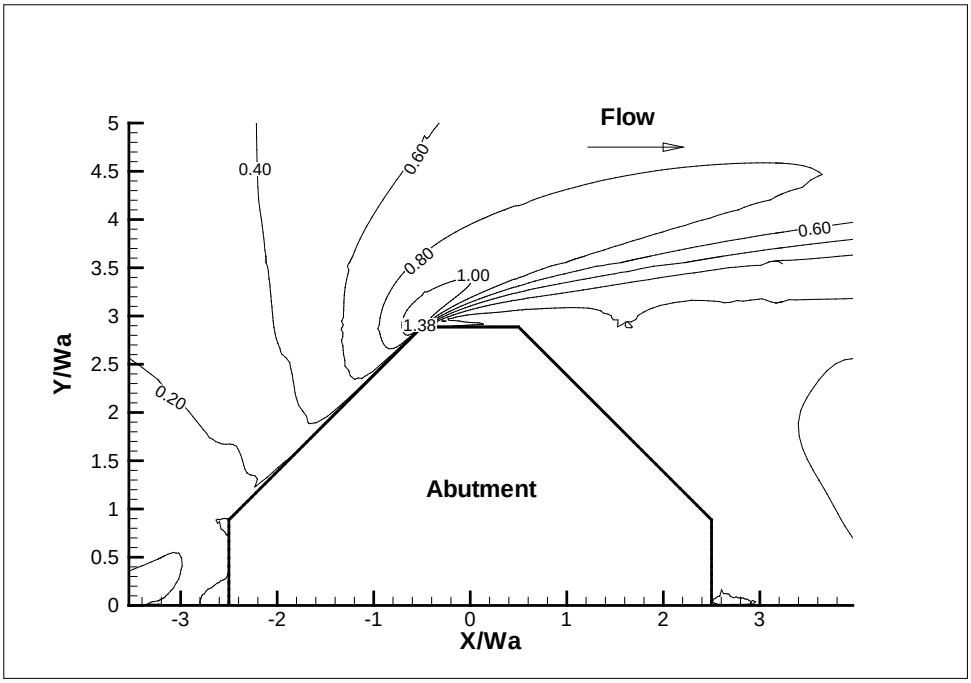

Figure 4-28 Bed friction coefficient ($\times 10^{-2}$) contour for L_a = 4.33ft (WW abutment).

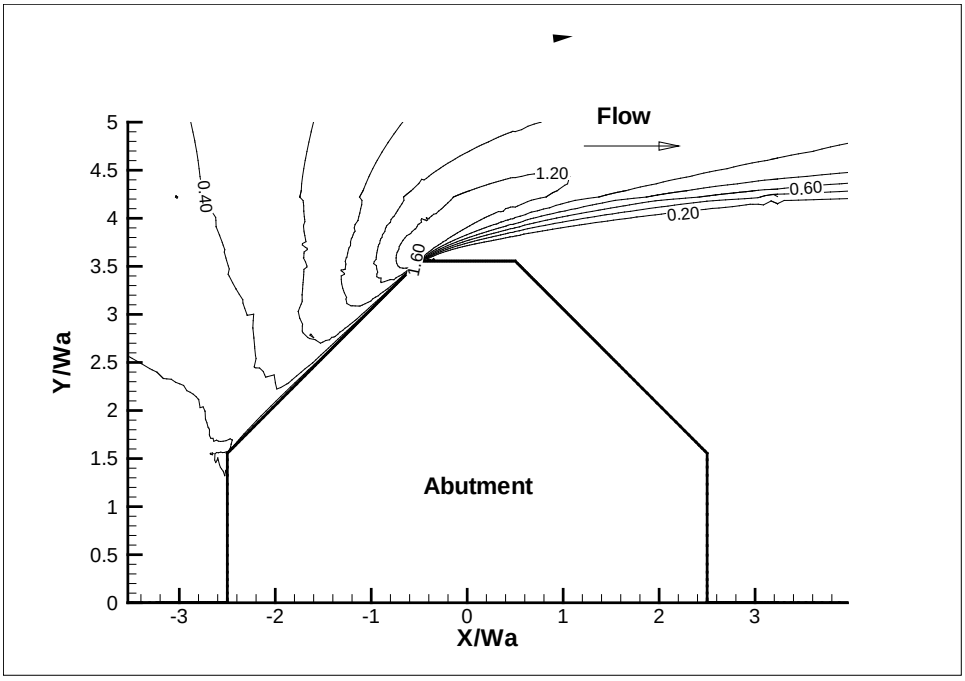

Figure 4-29 Bed friction coefficient ($\times 10^{-2}$) contour for L_a = 5.33 ft (WW abutment).

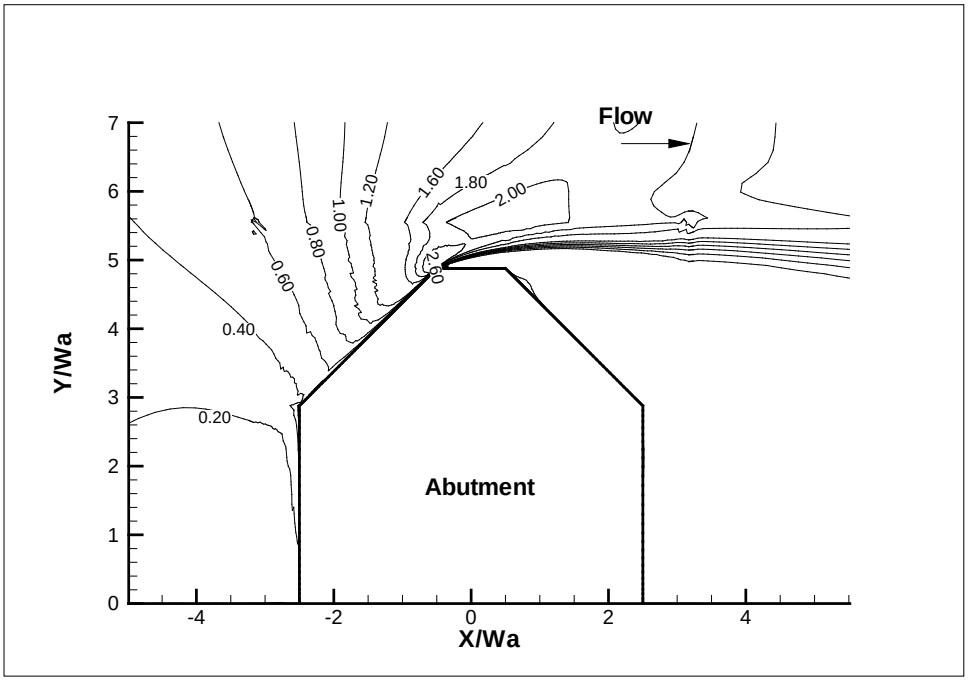

Figure 4-30 Bed friction coefficient ($\times 10^{-2}$) contour for L_a = 7.33ft (WW abutment).

Same approach can also be applied to study spill-through abutment. The case of spill-through abutment, however, has lower contraction ratio C_r than the case with same length of vertical wall abutment. Hence, $K_s = \tau_{\max\_ST} / \tau_{\max\_VW}$ listed in table 4-3 includes the influence of contraction ratio. It is necessary to exclude the influence of contraction ratio and get $K_s = (\tau_{\max\_ST} / K_{Cr\_ST}) / (\tau_{\max\_VW} / K_{Cr\_VW})$. As shown in table 4-4, K_s of spill-through abutment decreases with the increase of C_r. When the contraction is low, spill through abutment and wing-wall abutment have almost same K_s. However, K_s of spill though abutment drops faster when the contraction is large. For simplicity, an average correction factor of 0.58 for the spill-through abutment is proposed. Figures 4-31 to 4-34 shows the contours of C_f for these four cases with spill-through abutment.

L_a	y	V	W_a	$C_{f\_max\_ST}$	$C_{f\_max\_VW}$	K_s
ft	ft	ft/s	ft	----	----	----
3.33	1.2	1.09	1.50	0.0076	0.0165	0.46
4.33	1.2	1.09	1.50	0.0097	0.0211	0.46
5.33	1.2	1.09	1.50	0.0107	0.0257	0.42
7.33	1.2	1.09	1.50	0.0152	0.0450	0.34

Table 4-3 Shape correction factors of spill-through abutment (w/o correction).

L_a	y	W_a	C_{r_ST}	C_{r_VW}	K_{Cr_ST}	K_{Cr_VW}	K_s
ft	ft	ft	----	----	----	----	----
3.33	1.2	1.50	1.22	1.38	1.53	2.14	0.65
4.33	1.2	1.50	1.35	1.56	2.03	2.80	0.63
5.33	1.2	1.50	1.52	1.80	2.66	3.66	0.57
7.33	1.2	1.50	2.04	2.57	4.55	6.47	0.48

Table 4-4 Shape correction factors of spill-through abutment (with correction).

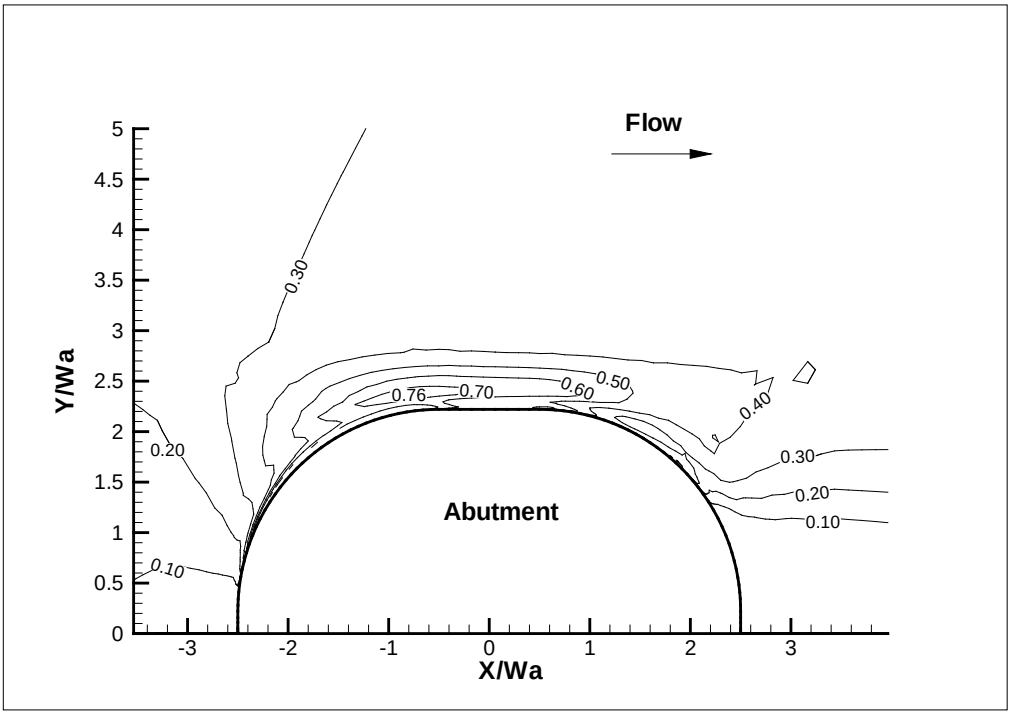

Figure 4-31 Bed friction coefficient ($\times 10^{-2}$) contour for L_a = 3.33ft (ST abutment).

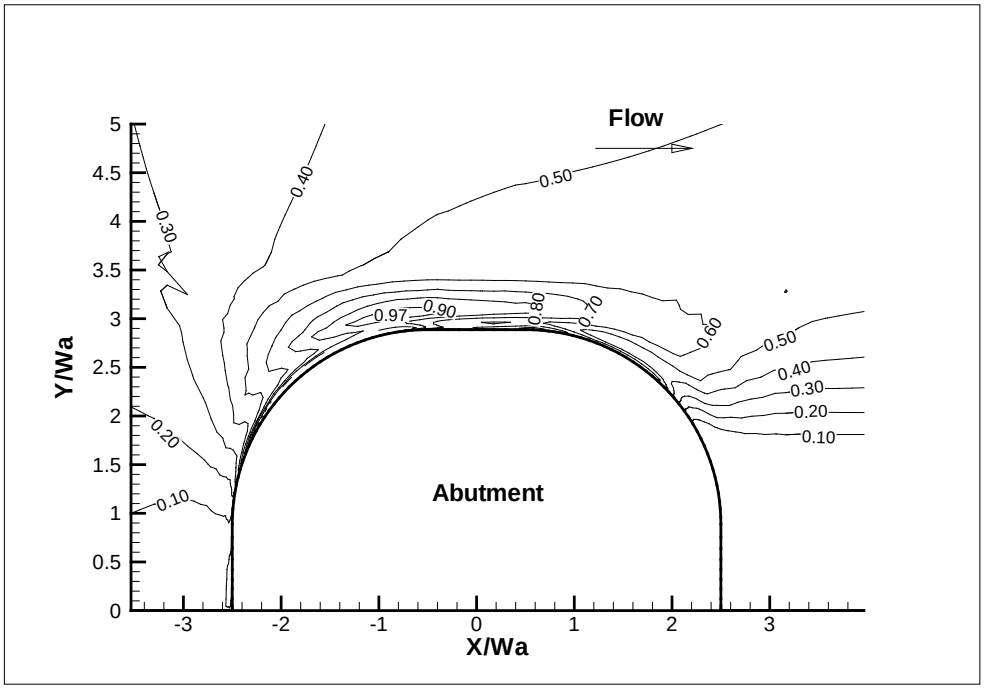

Figure 4-32 Bed friction coefficient ($\times 10^{-2}$) contour for L_a = 4.33ft (ST abutment).

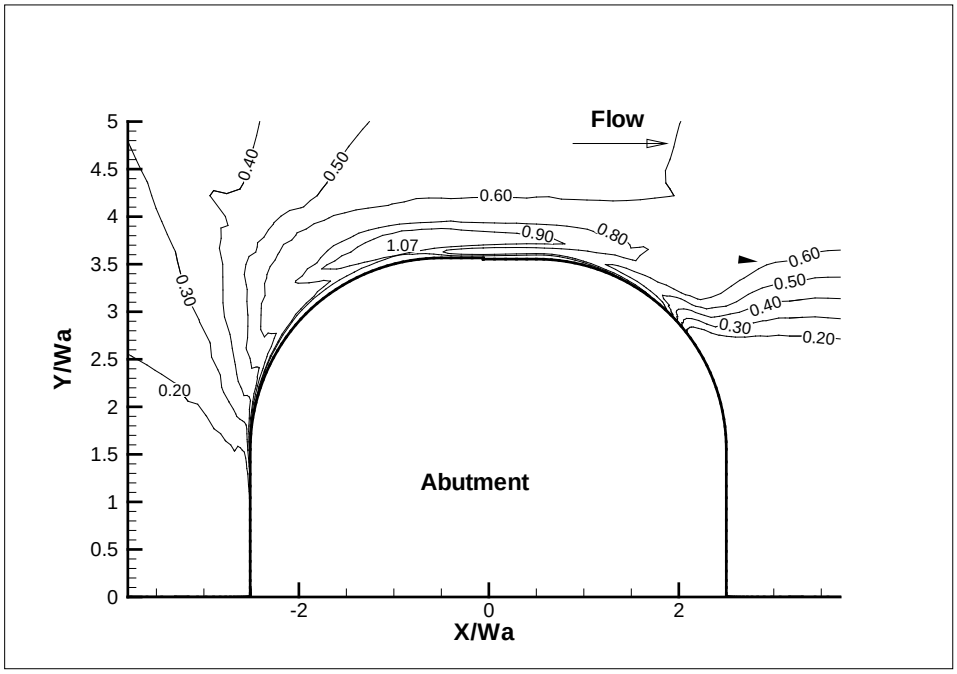

Figure 4-33 Bed friction coefficient ($\times 10^{-2}$) contour for L_a = 5.33ft (ST abutment).

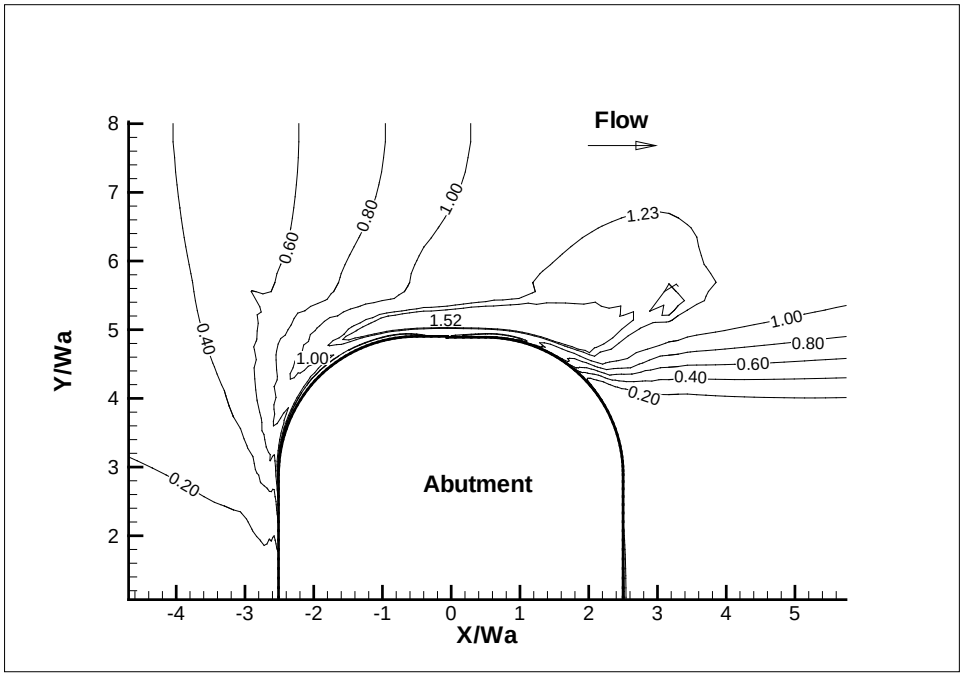

Figure 4-34 Bed friction coefficient ($\times 10^{-2}$) contour for L_a = 7.33ft (ST abutment).

4.3.6 Influence of the skew angle

The objective of this section is to obtain the relationship between the maximum bed shear stress $\tau_{\max}$ and the skew angleΘ of abutment (defined in figure 4-1). Five cases are simulated with the same projected abutment length L_a of 3.33 ft normal to the flow direction. The abutment is of vertical wall shape and the skew angle varies from 60 to 120 degree. Approach velocity is 1.09 ft/s and water depth is 1.2ft. Half width of the channel is 12ft. The results are shown in figures 4-35, 4-36, 4-37, 4-38, 4-39. One way to present the result is to plot $\tau_{\max}/\tau_{\max(90)}$ as the function of skew angleΘ. The parameter $\tau_{\max(90)}$ is the value of $\tau_{\max}$ for the case with 90 degree skew angle. The skew angle correction factor, K_{sk}, is the ratio of $\tau_{\max}/\tau_{\max(90)}$. The data points in figure 4-35

correspond to the results of the five simulations. The case with 90 degree skew angle has the highest maximum bed shear stress. The maximum bed shear stress decreases when the abutment is skewed towards either the upstream or downstream directions. For the same inclination from the normal direction, the maximum bed shear stress is higher when the abutment skews toward upstream. Considering the bridge is usually designed to be normal to the flow direction, the correction factor for skewed angle is proposed to be one in order to provide a conservative prediction of the maximum bed shear stress. Especially, the influence of skew angle on the maximum bed shear stress is negligible for spill-through abutment. This can be observed in the later NCHRP 24-15(2) studies. Case 1, Case 10, Case 23 and Case 24 have difference skew angle. But the maximum bed friction coefficients are almost same. Hence, it is reasonable to assume $K_{sk}=1$.

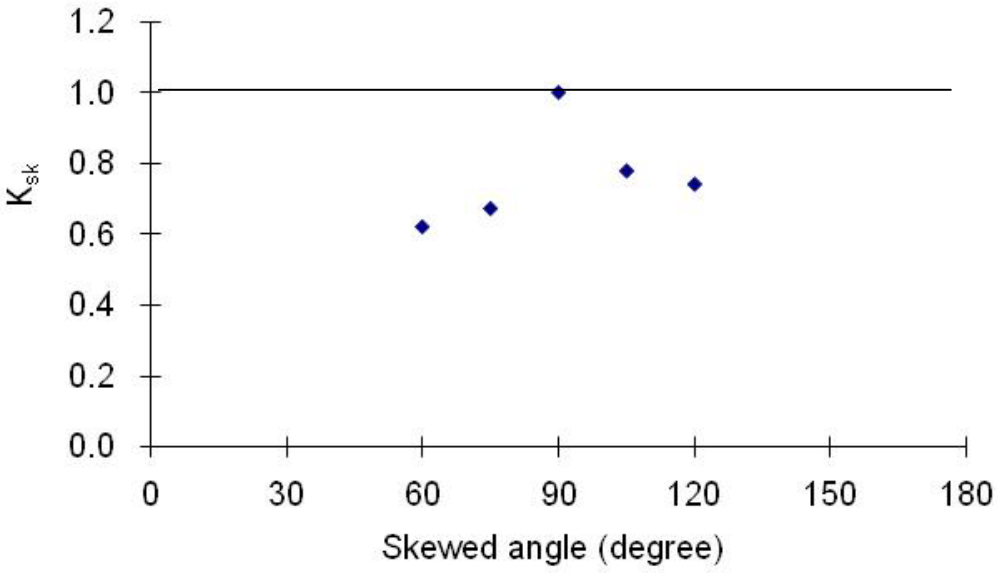

Figure 4-35 Correction factor for the skew angle of vertical wall abutment.

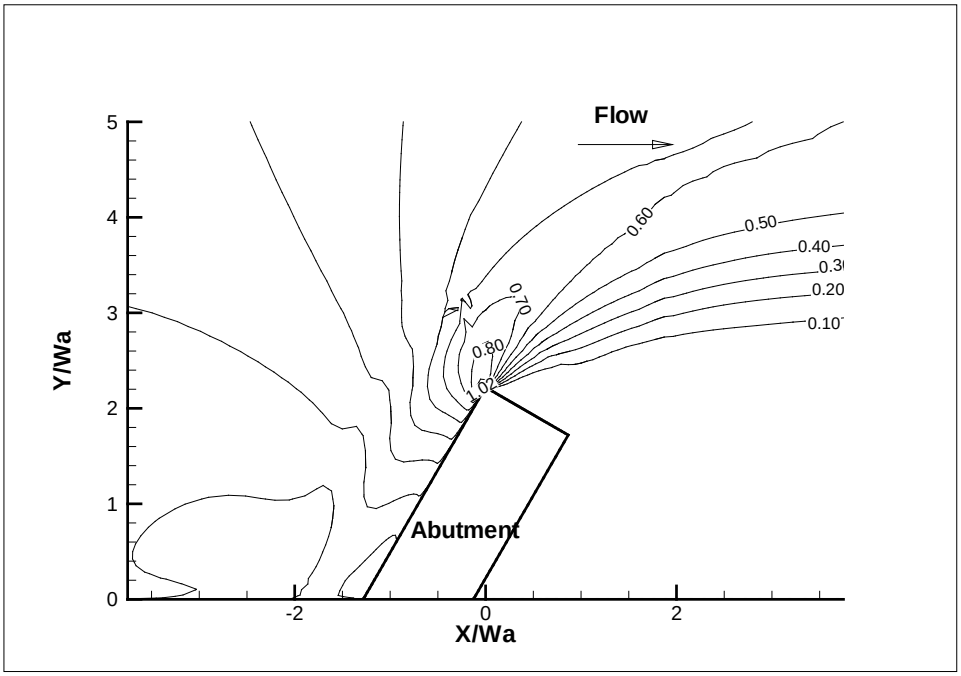

Figure 4-36 Bed friction coefficient ($\times 10^{-2}$) contour for 60 degree.

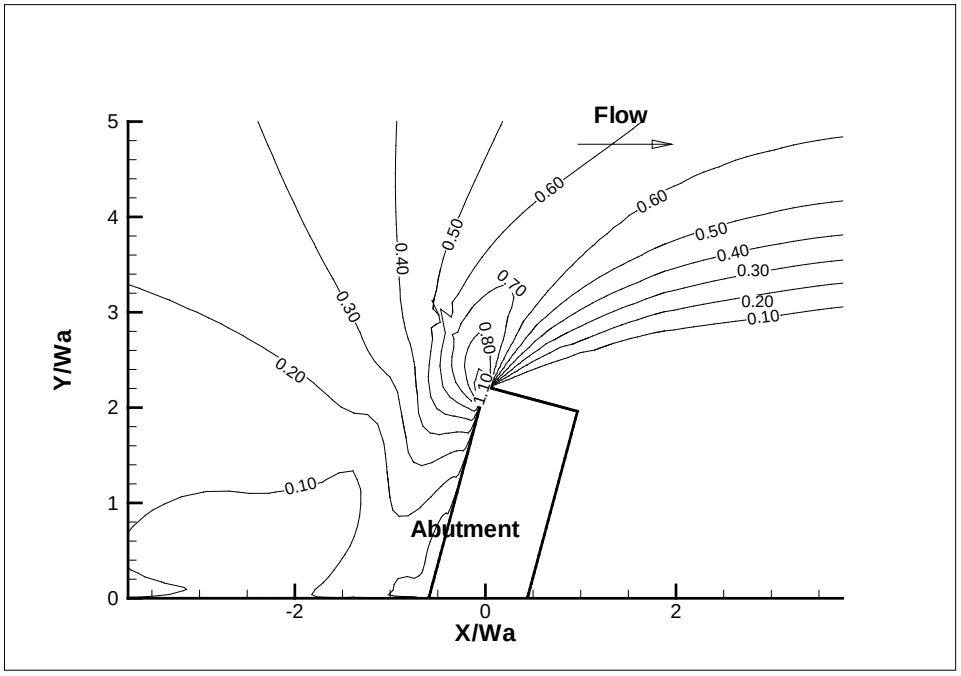

Figure 4-37 Bed friction coefficient ($\times 10^{-2}$) contour for 75 degree.

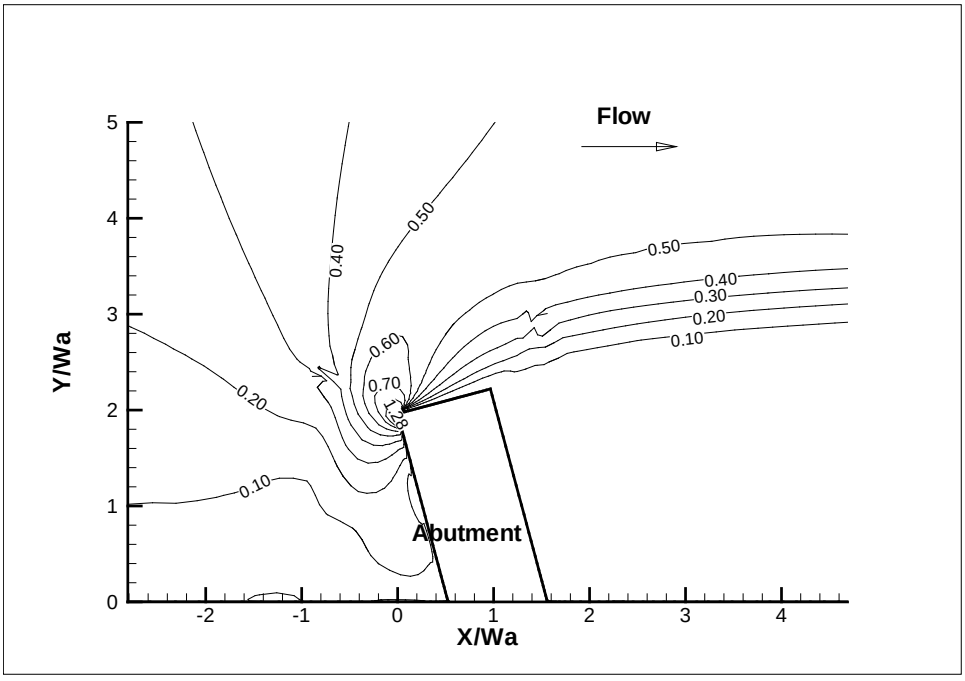

Figure 4-38 Bed friction coefficient ($\times 10^{-2}$) contour for 105 degree.

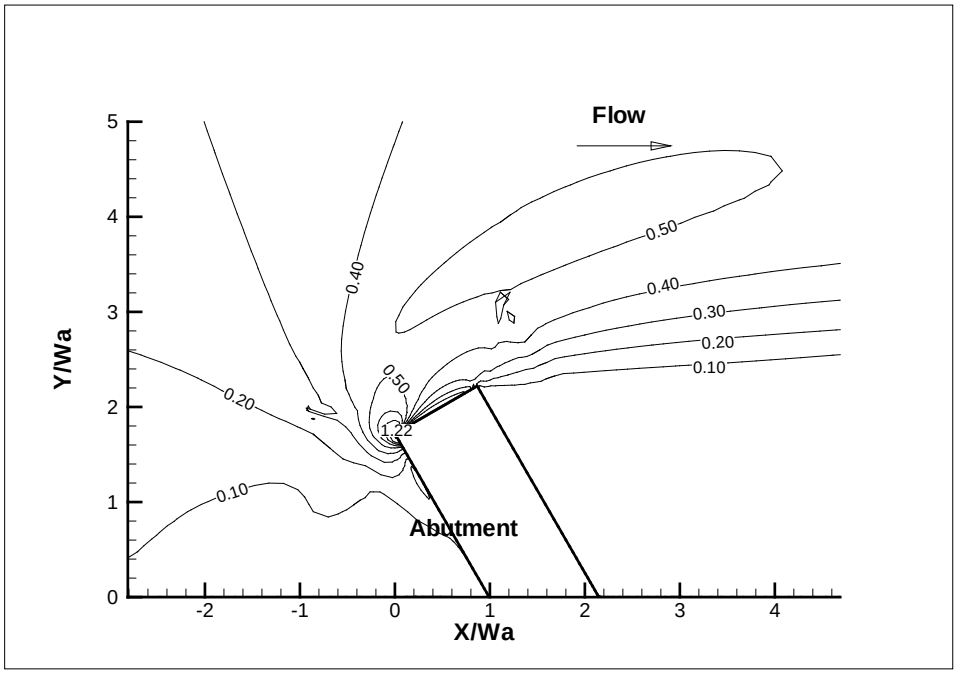

Figure 4-39 Bed friction coefficient ($\times 10^{-2}$) contour for 120 degree.

4.4 Maximum Bed Shear Stress Equation in Rectangular Channel

The basic formula of the equation is giving $\tau_{\max}$ for the half square pier in deep water condition (defined in figure 4-2). After the correction factors for channel contraction ratio, abutment aspect ratio, skew angle, water depth and abutment shape are determined, the maximum bed shear stress equation around abutment in rectangular channel can be generated as follows:

$$\frac{\tau_{\max}}{\rho V^2} = C_{f\_vw} \cdot K_{Cr} \cdot K_{sh} \cdot K_{Fr} \cdot K_s \cdot K_{sk}$$

where $\tau_{\max}$ = the maximum bed shear stress at the interface between the water and the river bottom near the abutment toe.

ρ = mass density of water

V = upstream mean depth velocity

y = upstream water depth

W_a = top width of the abutment

L_a = projected abutment length normal to the flow direction

C_r = contraction ratio; defined as $C_r = Q_{total} / (Q_{total} - Q_{blocked})$

Re = Reynolds number, defined as $\mathrm{Re} = VW_a / \nu$

ν = kinematic viscosity

C_{f_VW} = maximum bed friction coefficient near the toe of vertical wall abutment under deep water conditions

K_{Cr} = correction factor for channel contraction ratio

K_{sh} = correction factor for the aspect ratio of the approach embankment

K_{Fr} = correction factor for water depth

K_s = correction factor for abutment shape

K_{sk} = correction factor for skew angle

$$C_{f\_vw} = 2.1\mathrm{Re}^{-0.45}$$

$$K_{Cr} = 3.65C_r - 2.91$$

$$K_{sh} = 0.85 * (\frac{L_a}{W_a})^{-0.24}$$

$$K_{Fr} = \begin{cases} 2.07Fr + 0.8, & \mathrm{Fr} > 0.1 \\ 1.0, & \mathrm{Fr} \leq 0.1 \end{cases}$$

$$K_s = \begin{cases} 1, & \text{vertical-wall abutment} \\ 0.65, & \text{wing-wall abutment} \\ 0.58, & \text{spill-through abutment} \end{cases}$$

$$K_{sk} = 1.0$$

4.5 Influence of the Compound Channel Configuration

Natural rivers commonly have compound channels that consist of a main channel and flood plain. The channel can be taken as rectangular when the flow exists only in main channel. Then the preceding equation can be applied if the abutment is in main channel. When flooding, the flood plain is usually submerged; it is necessary to consider the influence of compound channel configuration on the maximum bed shear stress around abutment no matter if the abutment is in main channel or on flood plain. Main

channel usually conveys more flow and the unit discharge is generally higher in main channel than in flood plain. Especially, the flow pattern around the main channel slope could be quite complex because of the lateral momentum exchange between the main channel and flood plain. This may have a significant influence on the bed shear stress around the abutment when the abutment is close to the edge of the main channel.

Contraction ratio is still a good way to describe the blockage effect of the abutment and the approach embankment in compound channel. As defined in the methodology section, the contraction ratio is equal to $\frac{Q_{total}}{Q_{total} - Q_{blocked}}$ at upstream section. Only discharge is included in the definition, which means it can be applied in any type of river channel. However, the contraction ratio can only be used to reflect the averaged blockage effect. The location of the abutment on the compound channel could not be considered in this way. As mentioned above, the flow field could be very complex when the abutment toe is very close to the main channel slope. Hence, it may be necessary to include another correction for the abutment location in compound channel. Obviously, this is not necessary in the rectangular channel. And this correction is believed to be negligible when the abutment toe is far away from the main channel slope.

According to the flume tests in NCHRP 24-15(2), the clay surface is very smooth before scouring. And the difference of water depth is not large for main channel and flood plain. The velocity measurement shows that transverse depth averaged velocity is very uniform in the compound channel at upstream section. Hence, the uniform upstream velocity field is applied at the inlet in the numerical studies of compound

channel cases. And, the hydraulic smooth boundary is applied through the entire river bottom. This makes it reasonable to replace the discharge based contraction ratio by the area ratio of $\frac{A_{total}}{A_{total} - A_{blocked}}$ in the data analysis. And this can make it possible to apply the maximum bed shear stress equation for rectangular channel in the compound channel conditions with suitable correction.

The objective of this section is to study the relation between the abutment location on compound channel and the maximum bed shear stress. One flume test case in NCHRP 24-15(2) is selected to perform the numerical simulation and the spill-through abutment in the flume test is replaced by vertical wall abutment to avoid the influence of abutment shape. The channel is assumed to be symmetric and only half is simulated. The 6ft long vertical wall abutment is sitting in the 12 ft wide flume with main channel water depth y_m of 1.63ft and flood plain water depth y_f of 0.96ft. Approach velocity is 1.41ft/s. Eight cases with different flood plain width L_f are simulated with CHEN3D program. The width of flood plain L_f varies from 2 ft to 10ft. Table 4-5 lists the parameters and the simulation results of the eight compound channel cases. The contours of friction coefficient are given in figure 4-41 to figure 4-48. The location of the maximum bed shear stress usually appears at the upstream corner of the abutment no matter if the abutment is in flood plain or in main channel. If the abutment is on flood plain, the main channel slope in front of the abutment will suffer higher bed shear stress. But the bed shear stress on main channel slope will be very low if the abutment protrudes into main channel.

y_f (ft)	0.96	0.96	0.96	0.96	0.96	0.96	0.96	0.96
L_a (ft)	6.00	6.00	6.00	6.00	6.00	6.00	6.00	6.00
L_f (ft)	10.00	9.00	8.00	7.00	6.00	4.00	3.00	2.00
$(L_f-L_a)/y_f$	4.17	3.13	2.08	1.04	0.00	-2.08	-3.13	-4.17
C_{f_max}	0.0215	0.0211	0.0189	0.0179	0.0199	0.0209	0.0222	0.0235
C_r	1.8378	1.7634	1.7011	1.6482	1.6028	1.7030	1.7715	1.8400
K_{Cr}	3.81	3.54	3.31	3.12	2.95	3.32	3.57	3.82
C_{f_max}/K_{Cr}	0.0056	0.0060	0.0057	0.0058	0.0067	0.0063	0.0062	0.0062
K_L	1.00	1.06	1.01	1.02	1.20	1.02	1.01	1.00

Table 4-5 Correction factors of compound channel effect.

As shown in table 4-5, the contraction ratios C_r of these eight cases are not same. The smallest contraction ratio appears when the toe of the abutment lies at the edge of the main channel slope. As mentioned above, the abutment length, water depth and the flume width are all kept constant. Then the contraction ratio will always increase no matter the flood plain width increases or decreases. Hence, C_r reaches the lower limit when $L_a = L_f$. And the upper limit of the contraction ratio is achieved when the flood plain width goes to the limit, either zero or the width of the flume. Meanwhile, the compound channel becomes rectangular one. But the water depth will be different under these two limiting conditions. Based on the study of contraction ratio in rectangular channel, the maximum bed friction coefficient $C_{f\_\max}$ is linear proportional with the contraction ratio C_r. Then the case with the smallest contraction ratio (when $L_f = L_a$) should have the lowest $C_{f\_\max}$. To investigate the influence of the abutment location, the influence of the contraction ratio must be excluded by correcting $C_{f\_\max}$ with the

correction factor K_{Cr} derived from rectangular channel study. When the abutment toe is far away from the main channel slope, the influence of lateral momentum exchange between main channel and flood plain should vanish. Actually, this can be observed clearly after the correction of $C_{f\_\max} / K_{Cr}$. It should be noted that the influence of water depth is not constant for these eight cases. It can fall into two categories, abutment on flood plain and abutment on main channel. The one with abutment toe right at the edge of main channel slope should be put in the category of flood plain because the main channel slope is 1to1 and the water depth at the toe is same to water depth on flood plain. The results of $C_{f\_\max} / K_{Cr}$ indicate that the big difference among $C_{f\_\max}$ for these eight cases results mainly from the difference of contraction ratio. To eliminate the contribution from water depth and other parameters, it is desirable to normalize the values of $C_{f\_\max} / K_{Cr}$ with the one far away from the main channel slope $C_{f\_\max\_reference} / K_{Cr\_reference}$. The case of $L_f = 10\,ft$ is chosen to normalize the cases with abutment on flood plain. And the case of $L_f = 2\,ft$ is chosen to normalize the cases with abutment on main channel. Value of $(C_{f\_\max} / K_{Cr}) / (C_{f\_\max\_reference} / K_{Cr\_reference})$ is called abutment location correction factor K_L. $\frac{L_f - L_a}{y_f}$ is preferred to represent the abutment location because it show the relative distance of abutment toe to the main channel slope. Figure 4-40 shows the relationship between K_L and $\frac{L_f - L_a}{y_f}$. The bed

shear stress is about 20% higher when the abutment toe is right at the edge of the main channel slope. And this influence will exist only in a small range.

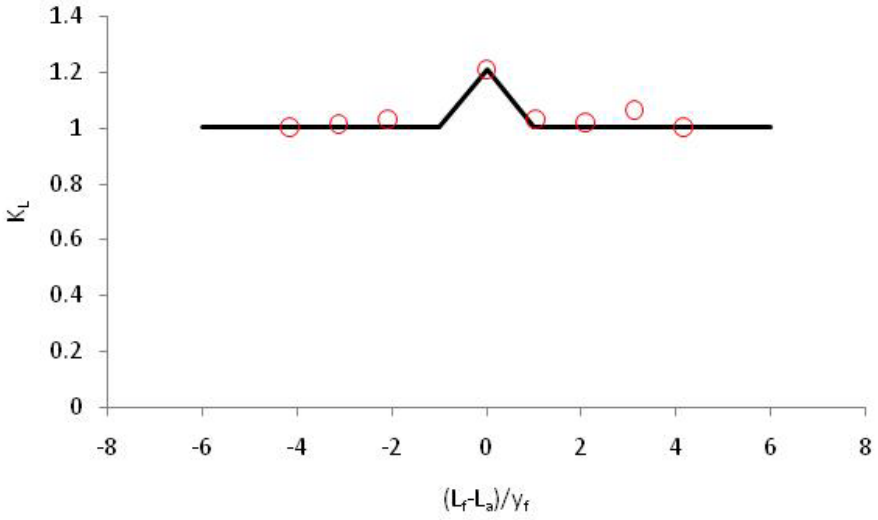

Figure 4-40 Correction factor of abutment location in compound channel.

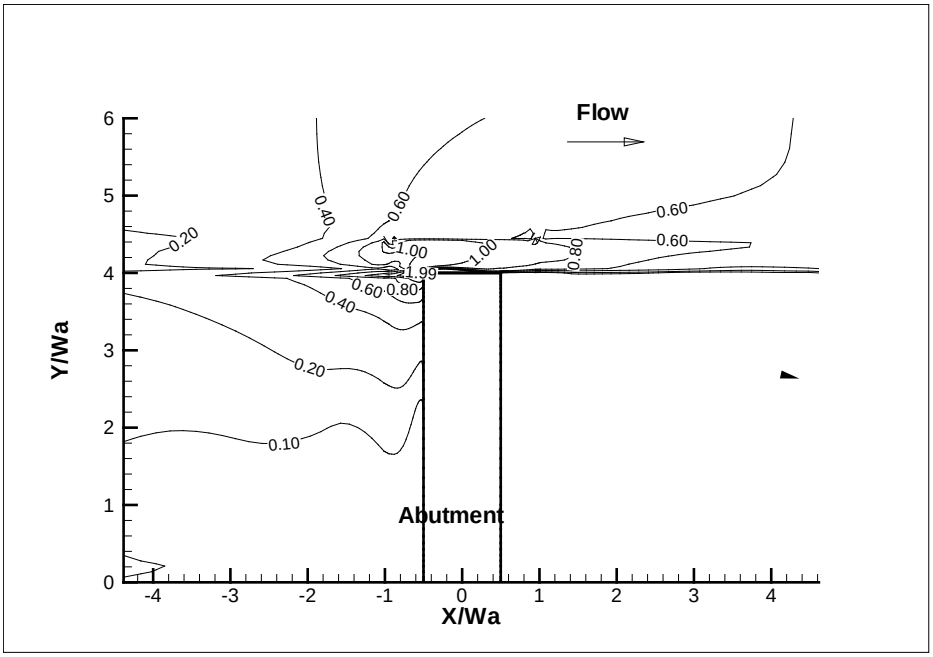

Figure 4-41 Bed friction coefficient ($\times 10^{-2}$) contour for L_m = 6ft.

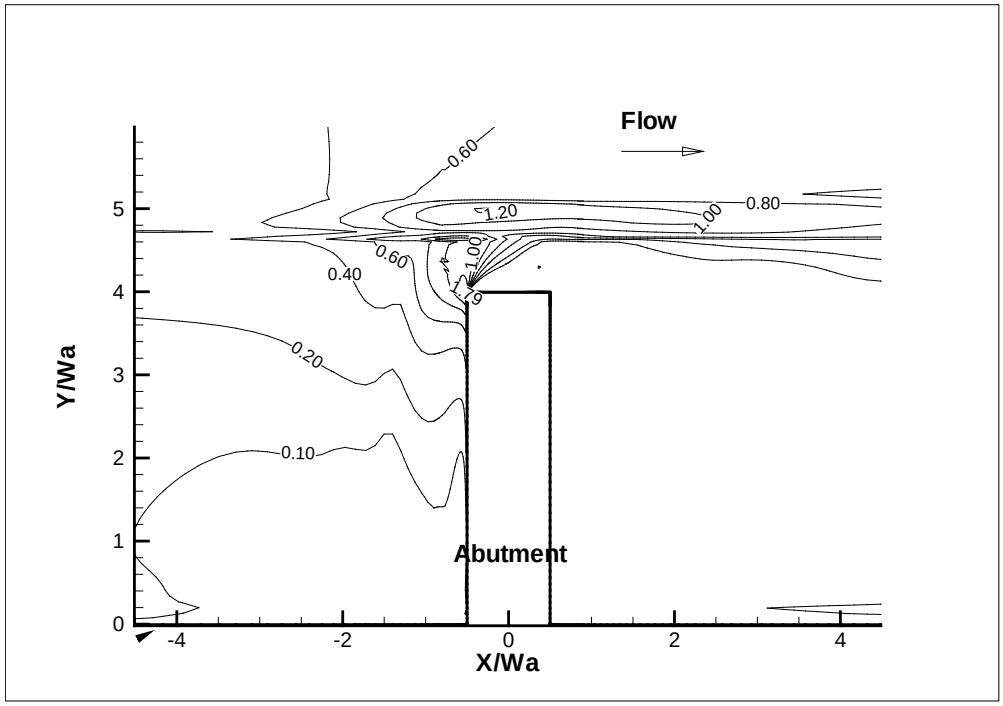

Figure 4-42 Bed friction coefficient ($\times 10^{-2}$) contour for L_m = 5ft.

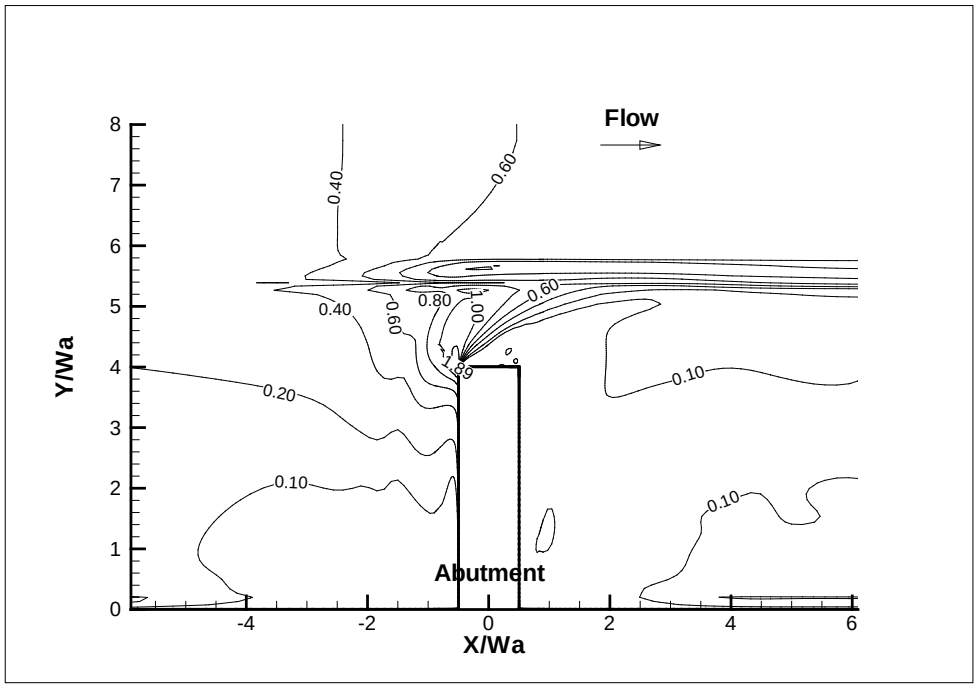

Figure 4-43 Bed friction coefficient ($\times 10^{-2}$) contour for L_m = 4ft.

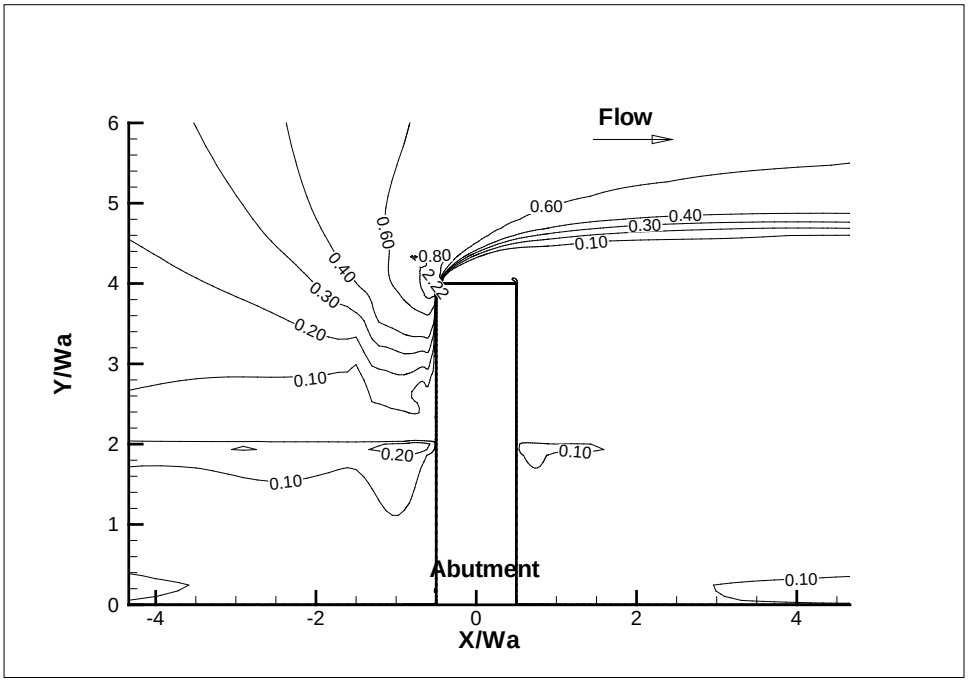

Figure 4-44 Bed friction coefficient ($\times 10^{-2}$) contour for L_m = 9ft.

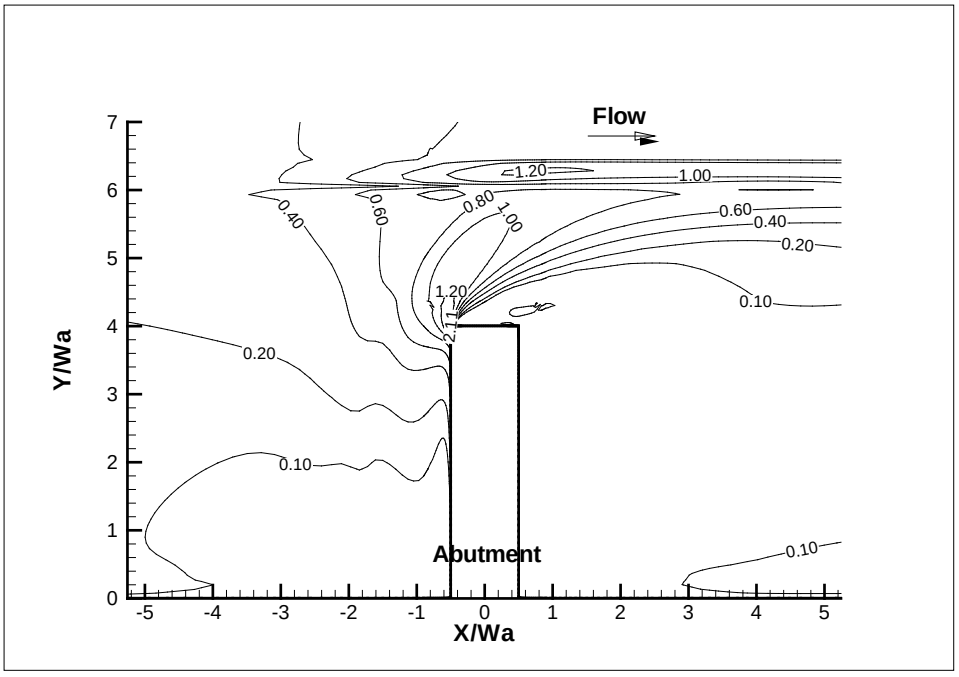

Figure 4-45 Bed friction coefficient ($\times 10^{-2}$) contour for L_m = 3ft.

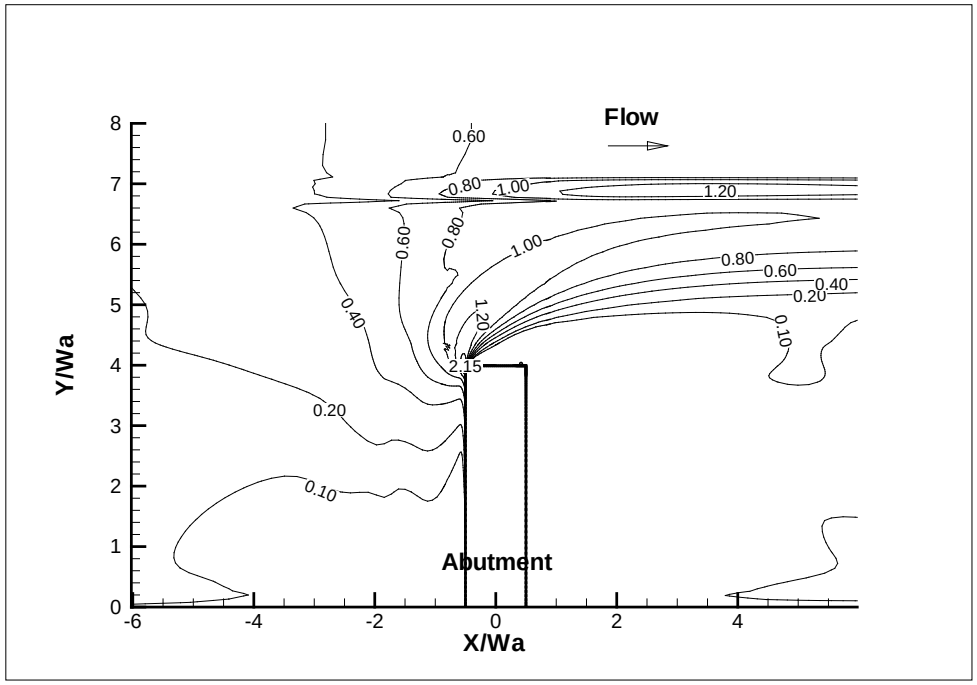

Figure 4-46 Bed friction coefficient ($\times 10^{-2}$) contour for L_m = 2ft.

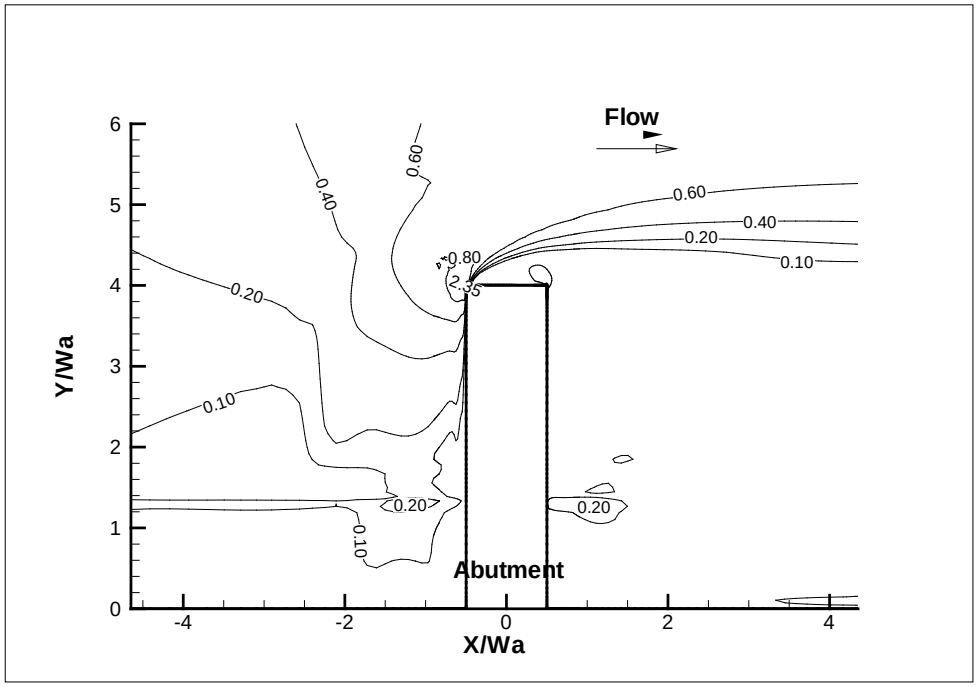

Figure 4-47 Bed friction coefficient ($\times 10^{-2}$) contour for L_m = 10ft.

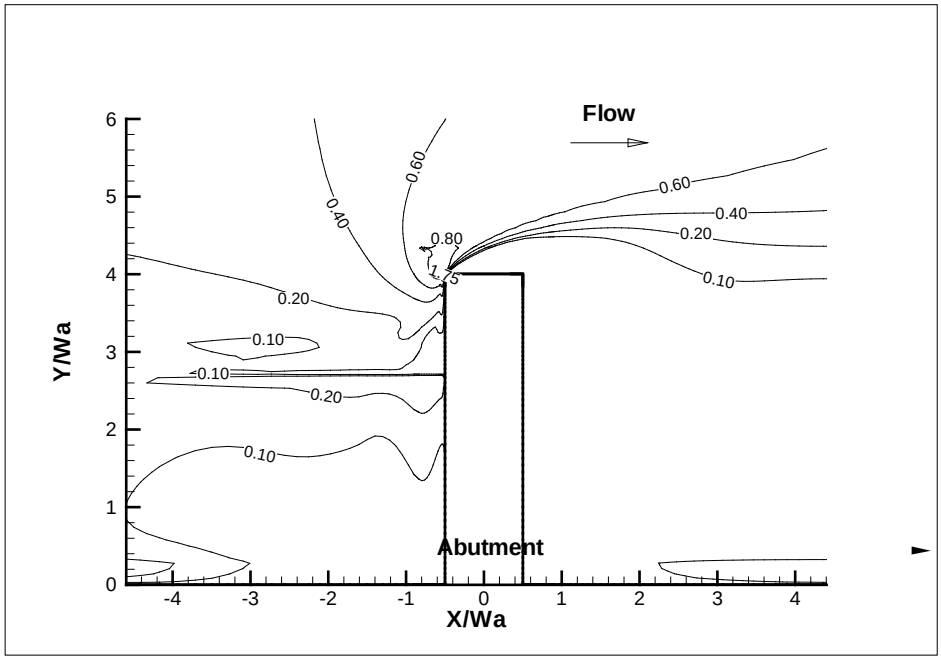

Figure 4-48 Bed friction coefficient ($\times 10^{-2}$) contour for L_m = 8ft.

4.6 Maximum Bed Shear Stress Equation in Compound Channel

With the correction of the abutment location in the compound channel, the maximum bed shear stress can be computed with in the following equation:

$$\frac{\tau_{\max}}{\rho V^2} = C_{f\_vw} \cdot K_{Cr} \cdot K_{sh} \cdot K_{Fr} \cdot K_s \cdot K_{sk} \cdot K_L$$

Where C_{f_vw}, K_{Cr},, K_{sh},, K_{Fr}, K_s, K_{sk} are same to the definition in the rectangular channel.

K_L = correction factor for abutment location in compound channel.

$$K_L = \begin{cases} 1, \ (\mathrm{L_f} - L_a)/y_f \le -1 \\ 1.2(\mathrm{L_f} - L_a)/y_f + 1.2, \ -1 < (\mathrm{L_f} - L_a)/y_f \le 0 \\ -1.2(\mathrm{L_f} - L_a)/y_f + 1.2, \ 0 < (\mathrm{L_f} - L_a)/y_f \le 1 \\ 1, \ 1 \le (\mathrm{L_f} - L_a)/y_f \end{cases}$$

It should be noted that the proposed equations in this chapter are based on the channel contraction ratio defined by the channel cross section area ratio. The reason is that the water is relatively deep in these simulations and the bed surface roughness is same for flood plain and main channel. The upstream velocity is found to be uniformly distributed from the numerical simulations. And this is also true in the flume tests. Hence the channel conveyance ratio is same to the area ratio. In the engineering practice, the area ratio may not represent the conveyance ratio very well. So the contraction ratio should be determined based on the actual conveyance ratio to get better prediction.

4.7 Verification of the Maximum Bed Shear Stress Equation

The proposed equation consists of several correction factors. The assumption is that these dimensionless parameters are independent and they can be superposed simply. The verification needs to be conducted to check the performance of this method. And the data regression of each parameter may not reflect the trend perfectly and have discrepancy. The simple product of these parameters could accumulate these errors. This is going to be studied in this section.

One way to check the performance of the equation is to predict the database used in the equation development. All the cases have been tabulated in table 4-6. Those six dimensionless parameters have been marked. In the parametric studies, only one parameter will be changed one time in theory. And the predicted maximum bed friction coefficients are also listed in the table. The overall performance of the equation is shown in figure 4-49. The good agreement can be observed for most of the cases. It proves that the method has been well conducted during the data regressions.

Re	C_r	L_a/W_a	y/W_a	Abutment Shape	Skew Angle (^{o})	C_{f_vw}	K_{Cr}	K_{sh}	K_{Fr}	K_s	K_{sk}	C_{f_max} CHEN3D	C_{f_max} Prediction
1.00E+04	1.07	0.50	2	VW	90	0.0327	0.99	1.00	1.00	1	1	0.0333	0.0325
2.00E+04	1.07	0.50	2	VW	90	0.0239	0.99	1.00	1.00	1	1	0.0235	0.0237
5.00E+04	1.07	0.50	2	VW	90	0.0158	0.99	1.00	1.00	1	1	0.0148	0.0157
1.00E+05	1.07	0.50	2	VW	90	0.0115	0.99	1.00	1.00	1	1	0.0103	0.0115
5.00E+05	1.07	0.50	2	VW	90	0.0056	0.99	1.00	1.00	1	1	0.0064	0.0055
1.00E+06	1.07	0.50	2	VW	90	0.0041	0.99	1.00	1.00	1	1	0.0048	0.0040
5.00E+06	1.07	0.50	2	VW	90	0.0020	0.99	1.00	1.00	1	1	0.0034	0.0020
1.00E+07	1.07	0.50	2	VW	90	0.0014	0.99	1.00	1.00	1	1	0.0025	0.0014
1.00E+05	1.25	0.50	2	VW	90	0.0115	1.66	1.00	1.00	1	1	0.0189	0.0192
1.00E+05	1.67	0.50	2	VW	90	0.0115	3.19	1.00	1.00	1	1	0.0369	0.0370
1.00E+05	2.50	0.50	2	VW	90	0.0115	6.23	1.00	1.00	1	1	0.0718	0.0721
1.00E+05	1.11	0.80	2	VW	90	0.0115	1.15	0.90	1.00	1	1	0.0119	0.0119
1.00E+05	1.25	1.60	2	VW	90	0.0115	1.66	0.76	1.00	1	1	0.0146	0.0145
1.00E+05	1.38	2.22	2	VW	90	0.0115	2.13	0.70	1.00	1	1	0.0169	0.0173
1.00E+05	1.56	2.89	2	VW	90	0.0115	2.79	0.66	1.00	1	1	0.0221	0.0212
1.00E+05	1.80	3.55	2	VW	90	0.0115	3.67	0.63	1.00	1	1	0.0283	0.0266
1.00E+05	2.57	4.89	2	VW	90	0.0115	6.48	0.58	1.00	1	1	0.0412	0.0435
1.00E+05	1.07	0.50	1	VW	90	0.0115	0.99	1.00	1.01	1	1	0.0111	0.0116
1.00E+05	1.07	0.50	0.75	VW	90	0.0115	0.99	1.00	1.10	1	1	0.0126	0.0126
1.00E+05	1.07	0.50	0.375	VW	90	0.0115	0.99	1.00	1.23	1	1	0.0147	0.0141
1.00E+05	1.07	0.50	0.1875	VW	90	0.0115	0.99	1.00	1.41	1	1	0.0159	0.0161
1.67E+05	1.38	2.22	0.8	WW	90	0.0091	2.15	0.70	1.16	0.65	1	0.0107	0.0104
1.67E+05	1.56	2.89	0.8	WW	90	0.0091	2.81	0.66	1.16	0.65	1	0.0138	0.0128
1.67E+05	1.80	3.55	0.8	WW	90	0.0091	3.67	0.63	1.16	0.65	1	0.0161	0.0159
1.67E+05	2.57	4.89	0.8	WW	90	0.0091	6.48	0.58	1.16	0.65	1	0.0260	0.0260
1.67E+05	1.22	2.22	0.8	ST (2:1)	90	0.0091	1.53	0.70	1.16	0.58	1	0.0076	0.0066
1.67E+05	1.35	2.89	0.8	ST (2:1)	90	0.0091	2.04	0.66	1.16	0.58	1	0.0097	0.0083
1.67E+05	1.52	3.55	0.8	ST (2:1)	90	0.0091	2.66	0.63	1.16	0.58	1	0.0107	0.0103
1.67E+05	2.04	4.89	0.8	ST (2:1)	90	0.0091	4.56	0.58	1.16	0.58	1	0.0152	0.0164
1.67E+05	1.38	2.22	0.8	VW	60	0.0091	2.15	0.70	1.16	1	1	0.0102	0.0161
1.67E+05	1.38	2.22	0.8	VW	75	0.0091	2.15	0.70	1.16	1	1	0.0111	0.0161
1.67E+05	1.38	2.22	0.8	VW	90	0.0091	2.15	0.70	1.16	1	1	0.0165	0.0161
1.67E+05	1.38	2.22	0.8	VW	105	0.0091	2.15	0.70	1.16	1	1	0.0128	0.0161
1.67E+05	1.38	2.22	0.8	VW	120	0.0091	2.15	0.70	1.16	1	1	0.0122	0.0161

Table 4-6 Cases used to derive the maximum bed shear stress equation around abutment.

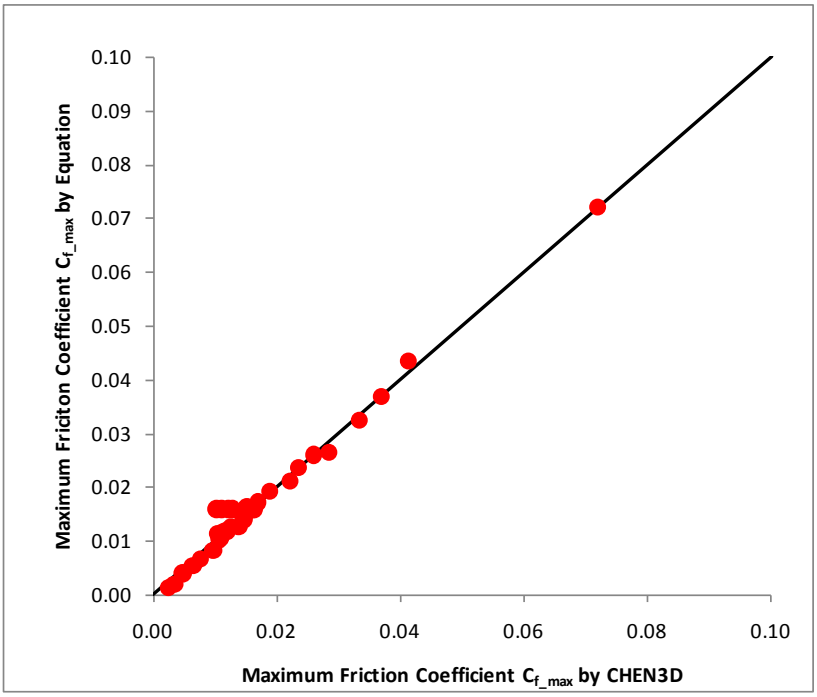

Figure 4-49 Comparison of simulated and predicted cases in rectangular channel study.

Forty one CHEN3D simulations have been proposed in the NCHRP 24-15(2), as shown in table 4-7. It should be noted that these cases are basically with compound channel. It is a good chance to check the consistency of the CHEN3D and the performance of the proposed equation with a new data base. The prediction of these 41 cases and the correction factors are tabulated in table 4-8. The comparison of the agreement is presented in figure 4-50.

Case #	Abutment Shape	Channel Type	L (m)	y_m (m)	y_f (m)	L_f (m)	L_a (m)	V_{avg} (m/s)	W_a (m)	Skew Angle (°)	C_{f_max} CHEN3D	CHEN3D (Pa)
Case1	ST (2:1)	Comp.	3.658	0.497	0.293	2.438	1.829	0.430	0.457	90	0.0087	1.6
Case2	ST (2:1)	Comp.	3.658	0.387	0.183	2.438	1.829	0.357	0.457	90	0.0076	0.97
Case3	ST (2:1)	Comp.	3.658	0.607	0.402	2.438	1.829	0.491	0.457	90	0.0098	2.37
Case4	ST (2:1)	Comp.	3.658	0.497	0.293	2.438	1.829	0.335	0.457	90	0.0094	1.06
Case5	ST (2:1)	Comp.	3.658	0.497	0.293	2.438	1.829	0.521	0.457	90	0.0072	1.96
Case6	ST (2:1)	Comp.	3.658	0.497	0.293	2.438	1.219	0.366	0.457	90	0.0057	0.76
Case7	ST (2:1)	Comp.	3.658	0.497	0.293	2.438	2.438	0.485	0.457	90	0.0149	3.5
Case8	ST (3:1)	Comp.	3.658	0.497	0.293	2.438	1.829	0.430	0.457	90	0.0084	1.56
Case9	WW	Comp.	3.658	0.497	0.293	2.438	1.829	0.430	0.457	90	0.0117	2.16
Case10	ST (2:1)	Comp.	3.658	0.497	0.293	2.438	1.829	0.430	0.457	60	0.0086	1.59
Case11	ST (2:1)	Comp.	3.658	0.497	0.293	2.438	1.829	0.430	0.457	120	0.0081	1.49
Case12	WW	Comp.	3.658	0.497	0.293	2.438	1.829	0.335	0.457	90	0.0120	1.35
Case13	WW	Rect.	3.658	0.366	0.366	2.438	1.015	0.332	0.457	90	0.0108	1.19
Case14	WW	Rect.	3.658	0.366	0.366	2.438	1.625	0.332	0.457	90	0.0161	1.78
Case15	WW	Rect.	3.658	0.366	0.366	2.438	2.234	0.332	0.457	90	0.0260	2.87
Case16	WW	Rect.	3.658	0.366	0.366	2.438	2.743	0.332	0.457	90	0.0138	1.52
Case17	WW	Rect.	3.658	0.366	0.366	2.438	1.320	0.332	0.457	90	0.0138	1.52
Case18	ST (2:1)	Comp.	3.658	0.497	0.293	2.438	1.829	0.244	0.457	90	0.0111	0.66
Case19	ST (2:1)	Comp.	3.658	0.497	0.293	2.438	1.829	0.616	0.457	90	0.0062	2.35
Case20	ST (2:1)	Comp.	3.658	0.497	0.293	2.438	1.829	0.710	0.457	90	0.0059	3
Case21	ST (2:1)	Comp.	3.658	0.442	0.238	2.438	1.829	0.393	0.457	90	0.0081	1.25
Case22	ST (2:1)	Comp.	3.658	0.552	0.347	2.438	1.829	0.460	0.457	90	0.0086	1.82
Case23	ST (2:1)	Comp.	3.658	0.497	0.293	2.438	1.829	0.430	0.457	75	0.0087	1.61
Case24	ST (2:1)	Comp.	3.658	0.497	0.293	2.438	1.829	0.430	0.457	105	0.0086	1.59
Case25	ST (2:1)	Comp.	3.658	0.448	0.244	2.438	1.524	0.399	0.457	90	0.0078	1.24
Case26	ST (2:1)	Comp.	3.658	0.546	0.341	2.438	2.134	0.457	0.457	90	0.0108	2.26
Case27	ST (2:1)	Comp.	3.658	0.497	0.293	0.914	1.829	0.479	0.457	90	0.0084	1.92
Case28	ST (2:1)	Comp.	3.658	0.497	0.293	2.743	1.829	0.418	0.457	90	0.0096	1.67
Case29	ST (2:1)	Comp.	3.658	0.497	0.293	3.048	1.829	0.408	0.457	90	0.0101	1.69
Case30	ST (2:1)	Comp.	3.658	0.497	0.293	1.219	1.829	0.469	0.457	90	0.0080	1.76
Case31	ST (2:1)	Comp.	3.658	0.497	0.293	0.610	1.829	0.488	0.457	90	0.0081	1.93
Case32	ST (2:1)	Comp.	7.315	0.994	0.585	4.877	3.658	0.607	0.914	90	0.0055	2.03
Case33	ST (2:1)	Comp.	14.630	1.987	1.170	9.754	7.315	0.858	1.829	90	0.0037	2.75
Case34	ST (2:1)	Comp.	21.946	2.981	1.756	14.630	10.973	1.051	2.743	90	0.0023	2.56
Case35	ST (2:1)	Comp.	29.261	3.975	2.341	19.507	14.630	1.213	3.658	90	0.0019	2.84
Case36	ST (2:1)	Comp.	36.576	4.968	2.926	24.384	18.288	1.357	4.572	90	0.0017	3.13
Case37	WW	Comp.	7.315	0.994	0.585	4.877	3.658	0.607	0.914	90	0.0070	2.56
Case38	WW	Comp.	14.630	1.987	1.170	9.754	7.315	0.858	1.829	90	0.0036	2.64
Case39	WW	Comp.	21.946	2.981	1.756	14.630	10.973	1.051	2.743	90	0.0031	3.47
Case40	WW	Comp.	29.261	3.975	2.341	19.507	14.630	1.213	3.658	90	0.0026	3.89
Case41	WW	Comp.	36.576	4.968	2.926	24.384	18.288	1.357	4.572	90	0.0025	4.62

Table 4-7 Numerical simulations proposed in NCHRP 24-15(2).

Case #	C_r	Re	C_{f_vw}	K_{Cr}	K_{sh}	K_{Fr}	K_{sk}	K_s	K_m	C_{f_max} Prediction	Prediction (Pa)
Case1	1.530	1.96E+05	0.0085	2.68	0.61	1.33	1.00	0.58	1.00	0.0107	1.97
Case2	1.505	1.63E+05	0.0093	2.59	0.61	1.35	1.00	0.58	1.00	0.0115	1.46
Case3	1.510	2.24E+05	0.0080	2.61	0.61	1.31	1.00	0.58	1.00	0.0097	2.33
Case4	1.530	1.53E+05	0.0095	2.68	0.61	1.21	1.00	0.58	1.00	0.0109	1.23
Case5	1.530	2.38E+05	0.0078	2.68	0.61	1.44	1.00	0.58	1.00	0.0106	2.88
Case6	1.269	1.67E+05	0.0091	1.73	0.67	1.25	1.00	0.58	1.00	0.0077	1.03
Case7	1.934	2.22E+05	0.0081	4.16	0.57	1.39	1.00	0.58	1.20	0.0185	4.34
Case8	1.456	1.96E+05	0.0085	2.41	0.61	1.33	1.00	0.58	1.00	0.0096	1.78
Case9	1.701	1.96E+05	0.0085	3.31	0.61	1.33	1.00	0.58	1.00	0.0132	2.43
Case10	1.530	1.96E+05	0.0085	2.68	0.61	1.33	1.00	0.58	1.00	0.0107	1.97
Case11	1.530	1.96E+05	0.0085	2.68	0.61	1.33	1.00	0.58	1.00	0.0107	1.97
Case12	1.530	1.53E+05	0.0095	2.68	0.61	1.21	1.00	0.65	1.00	0.0122	1.37
Case13	1.384	1.52E+05	0.0096	2.15	0.70	1.16	1.00	0.65	1.00	0.0109	1.20
Case14	1.799	1.52E+05	0.0096	3.67	0.63	1.16	1.00	0.65	1.00	0.0166	1.83
Case15	2.570	1.52E+05	0.0096	6.48	0.58	1.16	1.00	0.65	1.00	0.0272	3.00
Case16	4.000	1.52E+05	0.0096	11.71	0.55	1.16	1.00	0.65	1.00	0.0468	5.16
Case17	1.565	1.52E+05	0.0096	2.81	0.66	1.16	1.00	0.65	1.00	0.0134	1.48
Case18	1.530	1.11E+05	0.0110	2.68	0.61	1.10	1.00	0.58	1.00	0.0114	0.68
Case19	1.530	2.81E+05	0.0072	2.68	0.61	1.55	1.00	0.58	1.00	0.0106	4.03
Case20	1.530	3.25E+05	0.0068	2.68	0.61	1.67	1.00	0.58	1.00	0.0107	5.40
Case21	1.526	1.80E+05	0.0089	2.67	0.61	1.33	1.00	0.58	1.00	0.0111	1.72
Case22	1.523	2.10E+05	0.0082	2.66	0.61	1.32	1.00	0.58	1.00	0.0102	2.16
Case23	1.530	1.96E+05	0.0085	2.68	0.61	1.33	1.00	0.58	1.00	0.0107	1.97
Case24	1.530	1.96E+05	0.0085	2.68	0.61	1.33	1.00	0.58	1.00	0.0107	1.97
Case25	1.386	1.83E+05	0.0088	2.16	0.64	1.33	1.00	0.58	1.00	0.0094	1.49
Case26	1.707	2.09E+05	0.0083	3.33	0.59	1.32	1.00	0.58	1.00	0.0124	2.58
Case27	1.619	2.19E+05	0.0081	3.01	0.61	1.25	1.00	0.58	1.00	0.0108	2.47
Case28	1.571	1.91E+05	0.0086	2.83	0.61	1.31	1.00	0.58	1.00	0.0113	1.97
Case29	1.621	1.87E+05	0.0087	3.01	0.61	1.30	1.00	0.58	1.00	0.0120	2.01
Case30	1.556	2.15E+05	0.0082	2.78	0.61	1.24	1.00	0.58	1.00	0.0100	2.19
Case31	1.682	2.23E+05	0.0080	3.24	0.61	1.26	1.00	0.58	1.00	0.0116	2.75
Case32	1.530	5.55E+05	0.0053	2.68	0.61	1.32	1.00	0.58	1.00	0.0067	2.46
Case33	1.530	1.57E+06	0.0033	2.68	0.61	1.32	1.00	0.58	1.00	0.0042	3.07
Case34	1.530	2.88E+06	0.0025	2.68	0.61	1.32	1.00	0.58	1.00	0.0032	3.50
Case35	1.530	4.44E+06	0.0021	2.68	0.61	1.32	1.00	0.58	1.00	0.0026	3.84
Case36	1.530	6.20E+06	0.0018	2.68	0.61	1.32	1.00	0.58	1.00	0.0022	4.13
Case37	1.701	5.55E+05	0.0053	3.31	0.61	1.32	1.00	0.65	1.00	0.0092	3.40
Case38	1.701	1.57E+06	0.0033	3.31	0.61	1.32	1.00	0.65	1.00	0.0058	4.25
Case39	1.701	2.88E+06	0.0025	3.31	0.61	1.32	1.00	0.65	1.00	0.0044	4.84
Case40	1.701	4.44E+06	0.0021	3.31	0.61	1.32	1.00	0.65	1.00	0.0036	5.31
Case41	1.701	6.20E+06	0.0018	3.31	0.61	1.32	1.00	0.65	1.00	0.0031	5.71

Table 4-8 Prediction of the numerical cases proposed in NCHRP 24-15(2).

The comparison between table 4-7 and table 4-8 shows good match between the simulations results and the predicted values with the proposed equation. It also proves that the multiplication of K factors is a reasonable approach in current study.

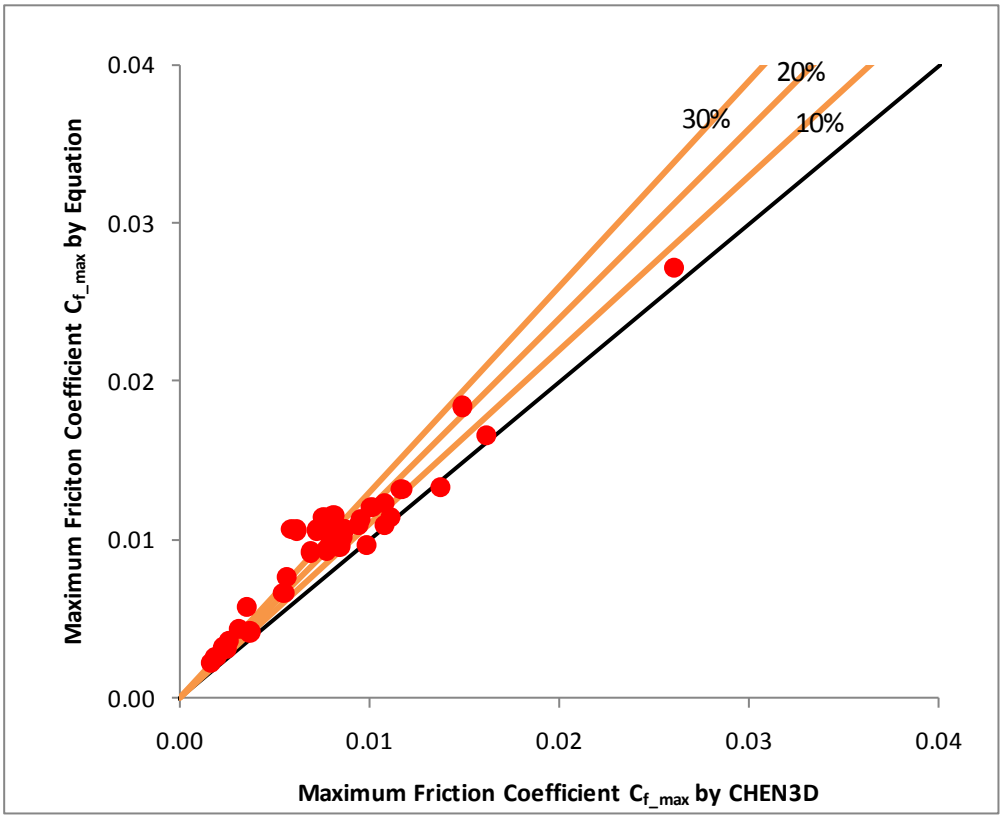

Figure 4-50 Comparison of the simulated and predicted cases in NCHRP 24-15(2).

As shown in figure 4-50, the prediction by equation can match the CHEN3D simulation reasonably. For some cases, the predicted values can be about 20% to 30% higher than the simulated values. One possible reason for this discrepancy is that the influence of the compound channel configuration on the flow redistribution is not evaluated very well with the channel geometric contraction ratio.

4.8 Real Maximum Bed Shear Stress around Abutment in SRICOS Method

Eighteen flume test cases (Oh, 2008) have been conducted in NCHRP 24-15(2) as shown in table 4-9. In the original design, these cases are identical to the corresponding cases in numerical study. During the testing, the flow conditions were changed in several

cases for convenience. The detail parameters of these 17 cases are provided in table 4-9 together with the predicted maximum bed shear stresses. The values of τ_{max} are calculated according to the actual parameters and the proposed equation. And the proposed maximum bed shear stresses are independent of the bed materials and based on hydraulic smooth boundary condition (roughness is not included in the prediction).

case #	V_{avg}(m/s)	y_f(m)	y_m(m)	L (m)	L_f (m)	L_a (m)	Q (m^3/s)	C_R	W_a (m)	C_{f_vw}	K_R	K_{sh}	K_{Fr}	K_s	K_{sk}	K_m	$\tau_{\_max}$(Pa) Prediciton
case1	0.442	0.293	0.496	3.658	2.438	1.829	0.573	1.53	0.457	0.0084	2.69	0.61	1.34	0.58	1	1	2.09
case1II	0.432	0.293	0.497	3.658	2.438	1.829	0.562	1.53	0.457	0.0085	2.69	0.61	1.33	0.58	1	1	2.00
case2	0.357	0.183	0.386	3.658	2.438	1.829	0.32	1.50	0.457	0.0092	2.59	0.61	1.35	0.58	1	1	1.46
case3	0.481	0.4	0.603	3.658	2.438	1.829	0.813	1.50	0.457	0.0081	2.58	0.61	1.30	0.58	1	1	2.22
case4	0.342	0.291	0.494	3.658	2.438	1.829	0.442	1.52	0.457	0.0094	2.66	0.61	1.22	0.58	1	1	1.27
case5	0.51	0.293	0.496	3.658	2.438	1.829	0.662	1.52	0.457	0.0079	2.65	0.61	1.42	0.58	1	1	2.72
case6	0.432	0.293	0.496	3.658	2.438	1.219	0.561	1.25	0.457	0.0085	1.65	0.67	1.33	0.58	1	1	1.35
case7	0.437	0.291	0.494	3.658	2.438	2.438	0.564	1.86	0.457	0.0084	3.87	0.57	1.34	0.58	1	1.2	3.30
case8	0.442	0.29	0.493	3.658	2.438	1.829	0.57	1.43	0.457	0.0084	2.31	0.61	1.34	0.58	1	1	1.80
case9	0.436	0.294	0.497	3.658	2.438	1.829	0.568	1.64	0.457	0.0084	3.08	0.61	1.33	0.65	1	1	2.61
case10																	
case11																	
case12	0.333	0.293	0.497	3.658	2.438	1.829	0.433	1.68	0.457	0.0095	3.23	0.61	1.21	0.65	1	1	1.64
case12B	0.583	0.294	0.497	3.658	2.438	1.829	0.759	1.69	0.457	0.0074	3.29	0.61	1.51	0.65	1	1	4.95
case13	0.322	0.365	0.365	3.658	3.658	1.015	0.43	1.38	0.457	0.0097	2.15	0.70	1.15	0.65	1	1	1.13
case14	0.32	0.371	0.371	3.658	3.658	1.625	0.433	1.80	0.457	0.0097	3.66	0.63	1.15	0.65	1	1	1.70
case15	0.302	0.377	0.377	3.658	3.658	2.234	0.416	2.57	0.457	0.0100	6.49	0.58	1.13	0.65	1	1	2.51
case16	0.208	0.373	0.373	3.658	3.658	2.743	0.285	4.00	0.457	0.0118	11.71	0.55	1.03	0.65	1	1	2.20
case17	0.364	0.364	0.364	3.658	3.658	1.32	0.484	1.56	0.457	0.0092	2.81	0.66	1.20	0.65	1	1	1.75

Table 4-9 Flume test cases in NCHRP 24-15(2).

Hyperbolic model is found to be able to describe the development of the maximum scour depth over time in the bridge scour problems (Briaud et al., 1999). Based on measurements in the flume tests, the initial erosion rate and the maximum scour depth can be estimated through data regression of the maximum scour depth history with hyperbola function. Table 4-10 lists all the initial erosion rates $\dot{Z}_{ini}$ and the ultimate scour depths Z_{max} .

Case #	$\dot{Z}_{ini}$ (mm/hr)	$Z_{\max}$ (mm)	$\tau_{\max\_\max}$ (Pa)	$\tau_{\max\_\min}$ (Pa)	$\tau_{\max}$ (Pa) EFA	$\tau_{\max}$ (Pa) Prediction	$\tau_{\max\_EFA} / \tau_{\max\_prediction}$
Case1	5.37	439	22	8	13.59	2.09	6.50
Case1 II	6.16	490	22	8	14.79	2.00	7.40
Case2	0.74	282	9	1.5	6.54	1.46	4.48
Case3	1.05	589	10	2	7.01	2.22	3.16
Case4	1.14	300	10	2	7.15	1.27	5.63
Case5	1.66	808	10	2	7.94	2.72	2.92
Case6	1.25	351	10	2	7.32	1.35	5.42
Case7	4.55	1190	20	5	12.34	3.30	3.74
Case8	2.20	413	11	3	8.76	1.80	4.87
Case9	1.80	667	10	2	8.15	2.61	3.12
Case10							
Case11							
Case12	0.24	155	4	0.7	5.78	1.64	3.52
Case12B	1.47	1429	10	2	7.65	4.95	1.55
Case13	0.54	66	7	1.1	6.24	1.13	5.52
Case14	2.37	304	11	3	9.02	1.70	5.31
Case15	1.73	334	10	2	8.05	2.51	3.21
Case16	3.21	448	20	3	10.3	2.20	4.68
Case17	1.96	262	11	3	8.40	1.75	4.80

Table 4-10 Maximum bed shear stresses based on EFA results.

Porcelain clay has been chosen in the flume tests. Eleven samples of the clay have been tested during the entire flume test period from 2005 to 2008 to monitor the change of erosion property. Some of the samples are quite different from the fresh clay after long time of storage. The EFA results are shown in figure 4-51 and found to scatter in a wide range. This shows the difficulty in the erosion problem. Even for a well controlled lab testing, the erosion property of the same type of soil from the same company could have such a big difference. The regression curve is given in figure 4-51. Based on the linear regression, the critical shear stress of the porcelain clay is 5.43 Pa, which is the shear stress when erosion rate is zero. However, the initiation of the scour is defined as 0.1mm/hr in experimental evaluation of soil erosion property.

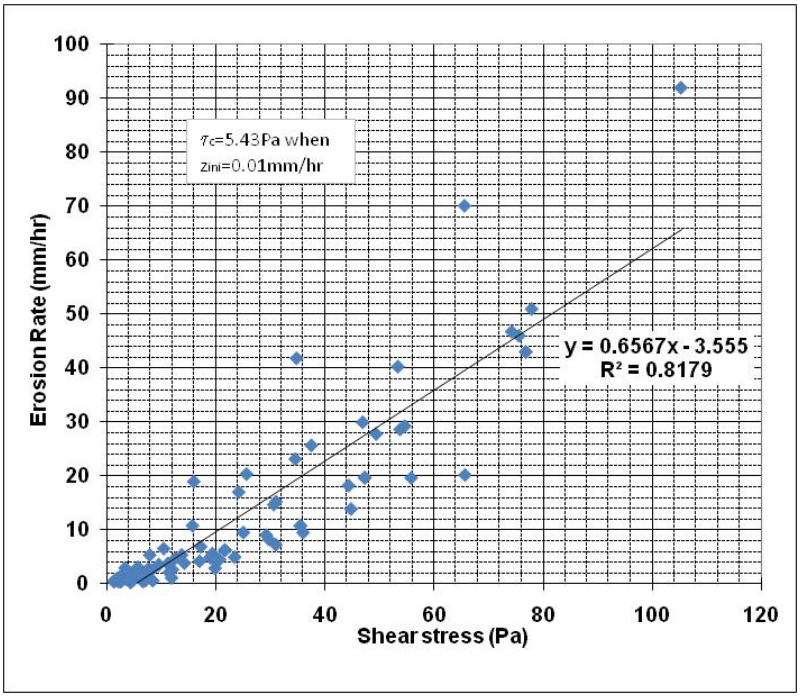

Figure 4-51 EFA testing results of the porcelain clay used in the flume tests (Oh, 2008).

In SRICOS method, maximum bed shear stress is used to read the initial erosion rate from the erosion function of the bed soils. Based on the estimated initial erosion rate from table 4-10, the corresponding bed shear stress can be read from figure 4-51. And the readings are listed in table 4-10. The highest initial erosion rate appears in Case 1 and the lowest erosion rate appears in Case 12. The deepest scour depth is in Case 7 and the lowest scour depth is in Case 12B. Obviously, higher initial erosion rate does not mean deeper ultimate scour depth, vice versa. For a certain initial erosion rate, the corresponding bed shear stress varies in a wide range. The maximum and minimum values are listed in table 4-10. The representative value is given based on the regression curve. Compared with the predicted maximum bed shear stress, the EFA readings are

much higher. The average of the ratios of $\tau_{max\_EFA} / \tau_{max\_prediction}$ is about 4.46 and the standard deviation is 1.47. The huge difference of the maximum bed shear stresses between the actual flume test and the prediction is believed to come from two sources. The first one is that the initial erosion rate prediction is based on the regression of the maximum scour depth history. Generally speaking, the bed shear stress is not the only contributor of the scour development. Many researchers have found the contribution from the turbulence property of the local flow. And the turbulence could even have the same contribution to the scour as the bed shear stress. The second one is the bed form roughness. In the flume test, the initial bed channel is very smooth. This is identical to the hydraulic smooth boundary condition in the numerical study. However, the surface of the bed is getting rougher and rougher with the scour development. This is not same to the particle roughness in sand bed. It is more similar to the sand dunes but not as regular as sand bed forms. All these possible influence makes the prediction of the initial erosion rate difficult. To represent the real scour development in SRICOS method, the influence of turbulence and the bed form roughness have to be carried by the maximum bed shear stress. For engineering practice, the simplest way is to fudge the maximum bed shear stress equation with $\tau_{max\_EFA} / \tau_{max\_prediction}$ to get the real initial erosion rate reading from the EFA result. And the fudged maximum bed shear stress is called τ_{max_real}. The fudge number, $\tau_{max\_EFA} / \tau_{max\_prediction}$, is proposed with the summation of average value and the standard deviation, which will be 5.93. Figure 4-52 shows the

comparison of $\tau_{\max\_EFA}$ and $\tau_{\max\_real}$. It shows that the fudged maximum bed shear stress can make the prediction reasonably conservative.

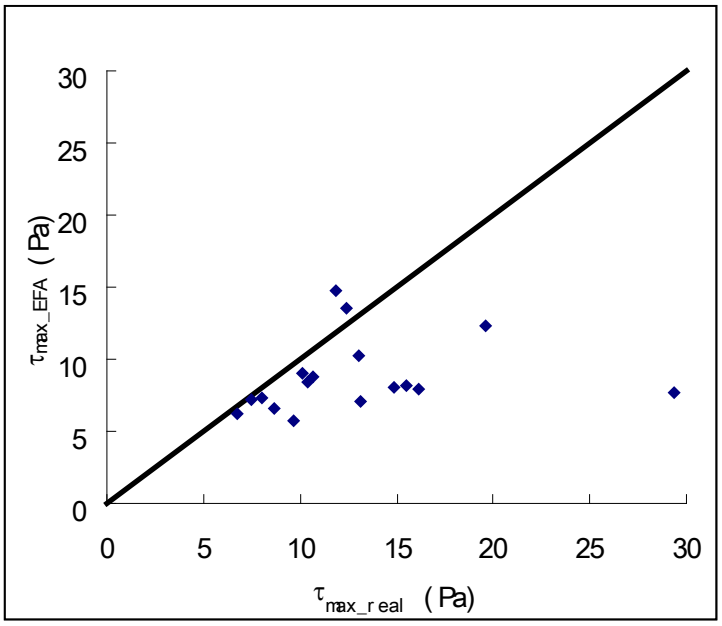

Figure 4-52 Comparison of the τ_{max_EFA} and τ_{max_real}.

CHAPTER V

MAXIMUM BED SHEAR STRESS AROUND ABUTMENT IN OVERTOPPING FLOW

The bed shear stress around abutment in overtopping flow is studied in this section. Overtopping is usually defined as the situations when the flow of water is over a dam or embankment. In current research, overtopping means only the situation when the bridge deck becomes inundated during the flood; and what concerned is the changing of bed shear stress around abutment when overtopping occurs. Typical understanding of the influence of overtopping is that flow is slightly pressurized and higher bed shear stress is created to aggravate scour conditions. To look into the overtopping problems, different channel configurations are studied, including overtopping in constant channel, overtopping in compound channel, overtopping in nonsymetric channel, overtopping in channel bend. At last the flow at the confluence of the river channel is also studied.

5.1 Verification of the Overtopping Flow Simulation

Kerenyi (personal communication, December, 2007) investigated bed shear stress distribution under inundated bridge deck with shear stress sensor. The experiment was conducted in FHWA lab in washington. Bridge model is shown in figure 5-1 and the notations are explained in figure 5-2. Bed surface was roughened by sands with d_{50} equal to 1mm. Approach velocity is 1.44 ft/s; water depth h_u is 0.83ft; Froude number is 0.28. The bridge deck could be adjusted vertically during the testing. The experiments focused on the influence of the bridge deck elevation on the bed shear stress distribution. Kerenyi

provided four experiment results with h_b equal to 13cm, 16cm, 19cm, and 22cm. To save CPU time, two dimensional simulations with CHEN3D program have been performed for the cases of h_b=13cm and h_b=16cm. The free surface is simulated with rigid lid, which is believed to be reasonable for these two cases.

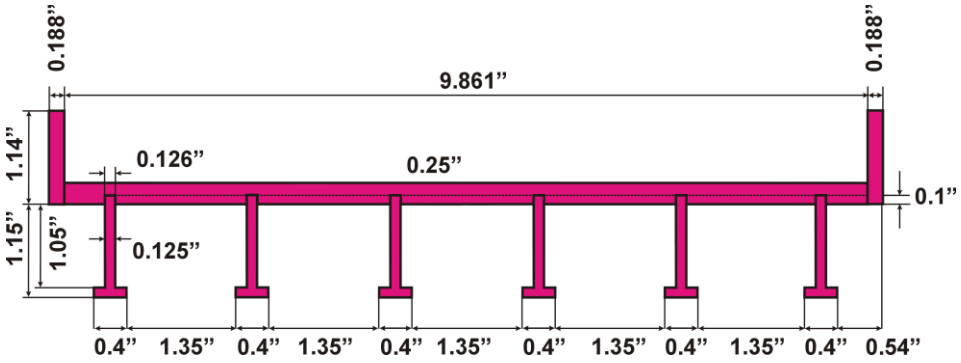

Figure 5-1 Bridge model for shear stress experiments (after Kerenyi, 2007).

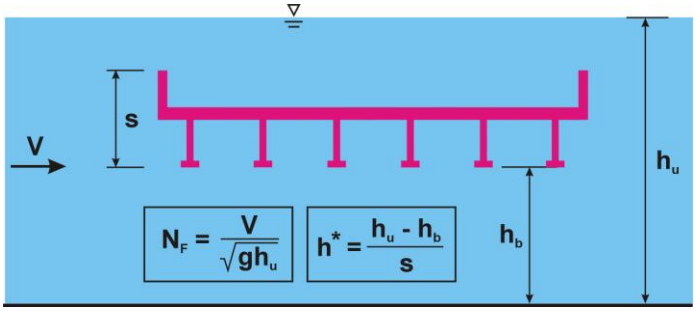

Figure 5-2 Explanation of notations (after Kerenyi, 2007).

Roughness model of Patel & Yoon (1995) has been implemented in CHEN3D to simulate the effect of surface roughness. No slip boundary condition is still applied on the river bottom when applying roughness model. To check the performance of the roughness model, three different roughness conditions are considered, including d_{50} = 0mm, d_{50} = 1mm, and d_{50} = 2mm. Figures 5-3 and 5-4 show the comparison of the

simulated results with the measurements. All the simulation results can provide the correct trend. The shear stress will increase significantly under the bridge deck and decrease at downstream sides. X position of 0cm is the upstream edge of the deck. And the width of the deck is 26cm. The τ_{max} occurs under the deck at the upstream half. Obviously, the smooth boudary condition seriously underestimates the maximum bed shear stress under the bridge deck. When the k_s in the roughness model is taken as d_{50} = 1mm, the bed shear stress is still underestimated even if there is a big improvement. It turns out that the prediciton will be in good agreement with measurement when taking d_{50} = 2mm. These two simulations of overtopping cases show the significant influence of bed roughness on the bed shear stress. And this influence is closely related to the deck location. Also, the current roughness model needs further refinement because the roughness has to be exaggerated to yield the real roughness effects.

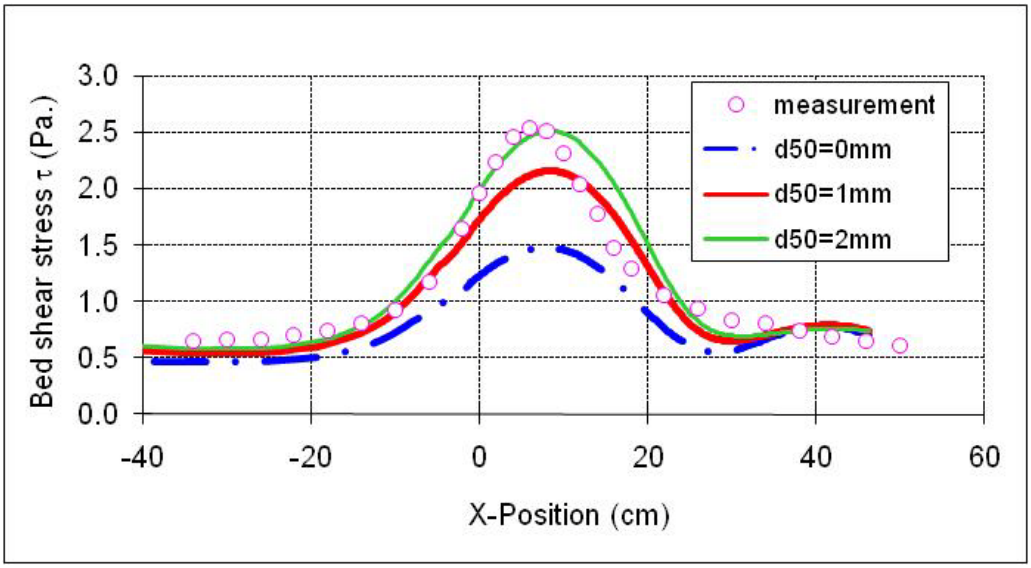

Figure 5-3 Bed shear stress distribution of h_b = 13cm.

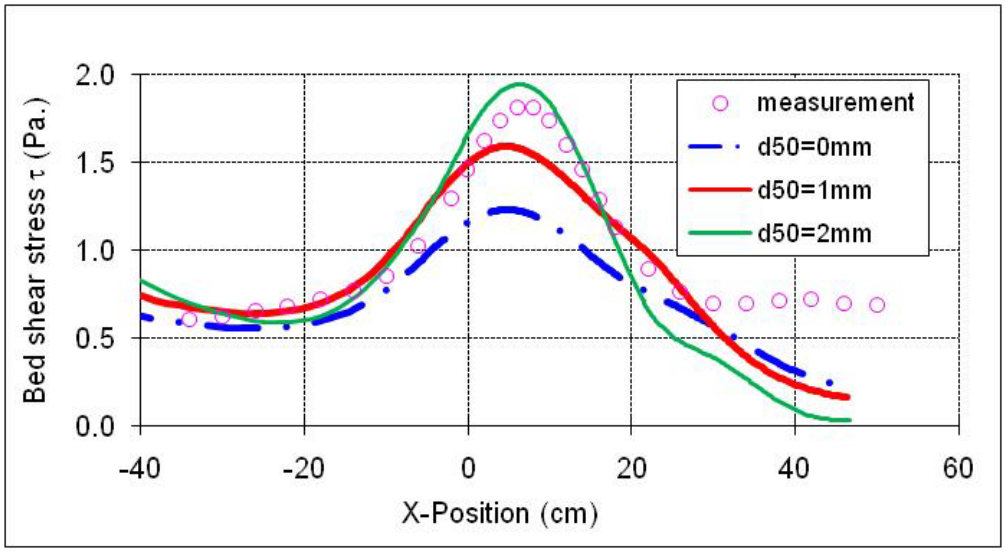

Figure 5-4 Bed shear stress distribution of h_b = 16cm.

5.2 Overtopping in Rectangular Channel

If the water surface is lower than low chord of bridge deck, it is the open channel flow conditions having been studied in chapter IV. Hence, it is desirable to start from the case with the water surface elevation flush with low chord of bridge deck. The overtopping study is to further increase the water depth to investigate the changing of bed shear stress at the different level of overtopping.

The bridge is in rectangular channel with 3.33ft long vertical wall abutment and the deck of 0.4 ft thick by 1.5ft wide. The clearance of the deck is 1.2ft. The approach velocity is 1.09ft/s. The channel is 24ft wide. Four cases are performed with different water depth. Case (a) is designed with 1.2ft deep water depth and the water surface is not in contact with low chord. This is the limiting case of overtopping flow. Case (b) has the same water depth as the Case (a) except that the water surface is in contact with the low chord. Actually, the only difference between these two cases is the water surface

boundary condition under the deck. Case (c) has water depth of 1.6 ft and water surface flush with deck surface. In this case, the flow is not overtopping the deck. Case (d) has water depth of 2.0ft. The water surface is 0.4 ft higher than the deck surface. All the parameters in these four cases have been given in figure 5-5. The diagrams are the transvert cross sections at the middle of abutment. The channel is in symmetry and only half is shown.

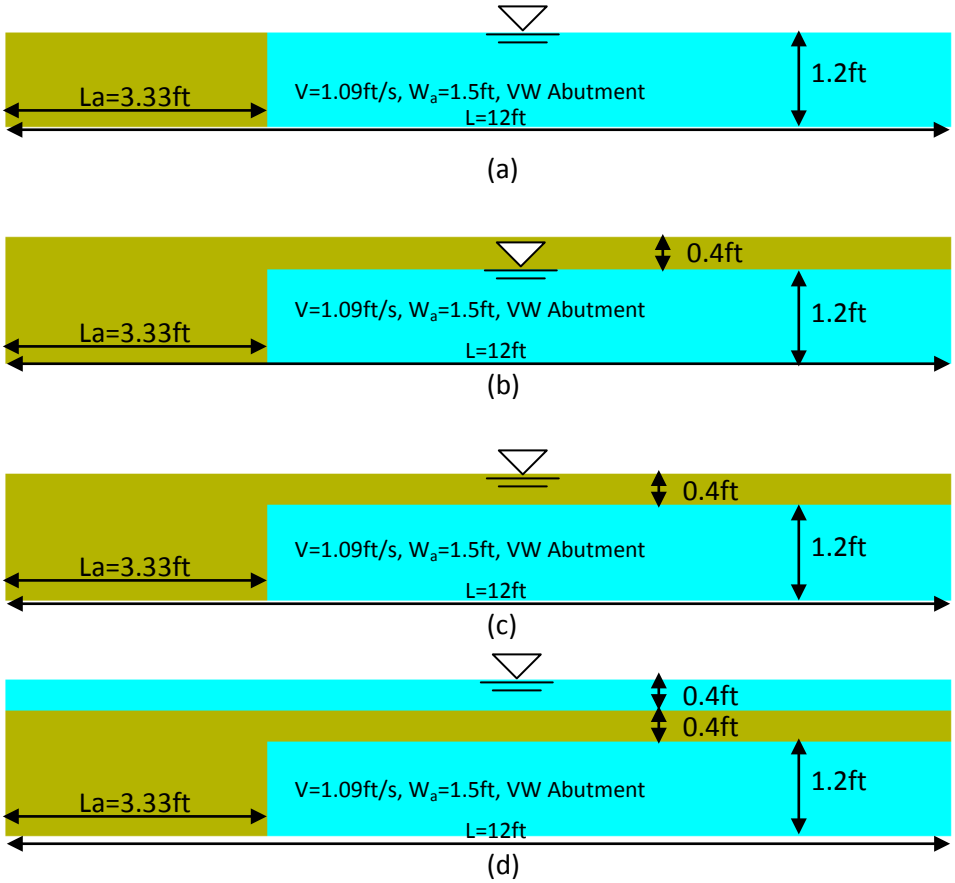

Figure 5-5 Cross sections at the middle of the abutment for rectangular channels.

To explain the grid system used in the overtopping simulations, the grid of Case (d) is shown in figure 5-6. The entire computation domain is divided into 10 blocks. Actually, this grid can be simplified for the simulation of the other three cases. Case (a) consists of block1 to block4. These four blocks are fully connected. The grid of Case (a) with block7 emedded in block2 and block3, can be used for the simulation of Case (b). The purpose of block7 is to provide the no-slip boundary condition on the deck bottom surface. Case (c) is made up of the grid of caes (b), block 5, and block9. Chimera technique is applied for the data communication between blocks.

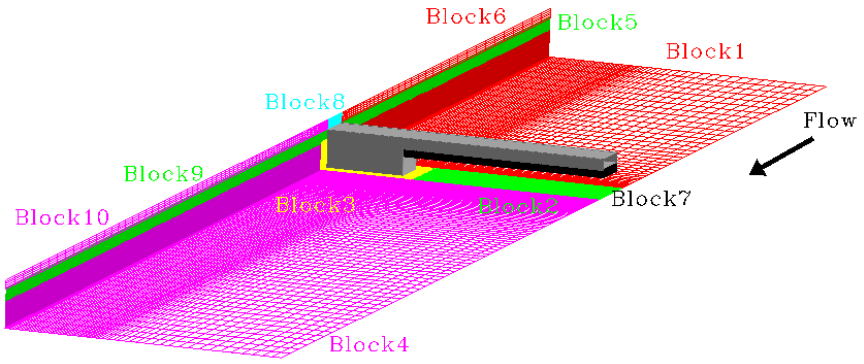

Figure 5-6 Numerical grid for overtopping case.

Case #	V	y	L_a	W_a	Shape	C_r	C_{f_max}	C_{f_center}	C_{f_max}/C_{f_center}
	ft/s	ft	ft	ft	----	----	----	----	----
(a)	1.09	1.20	3.33	1.5	VW	1.38	0.0165	0.0060	2.74
(b)	1.09	1.20	3.33	1.5	VW	1.38	0.0158	0.0060	2.64
(c)	1.09	1.60	3.33	1.5	VW	1.85	0.0316	0.0180	1.75
(d)	1.09	2.00	3.33	1.5	VW	1.58	0.0210	0.0100	2.10

Table 5-1 Simulation results of overtopping in rectangular channel cases.

As listed in table 5-1, for Case (a) and Case (b), the contraction ratio is same (C_r = 1.38). The channel is blocked only by the abutment. Bridge deck will not affect the

channel blockage since no flow is blocked by the deck. Flow will transit from open channel flow to overtopping flow once the water surface exceeds the low chord. When the water surface is in betweeen the low chord and deck surface, the flow is preferred to be called pressurized flow since there is no flow really overtopping the deck. The contraction ratio will keep increasing until the water surface up to deck surface. Case (c) is the specific condition of the pressurized flow since it reaches the largest contraction ratio for a given bridge. The contraction ratio will decrease once the flow really overtopps the deck surface. And the flow under the deck is still pressurized. Case (d) is one of this conditions with the contraction ratio of 1.58, smaller than Case (c).

Table 5-1 presents the maximum friction coefficients $C_{f\_\max}$ and the friction coefficients along the channel center and in the middle of the abutment C_{f_center}. The bed friction coefficient contours are presented in figure 5-7 to figure 5-10.

The friction coefficient contours for Case (a) and Case (b) are almost identical. The values of C_{f_max} are about 0.016. It shows that the change of water surface boundary condition has little influence on the bottom bed shear stress. At the middle of the abutment, C_{f_center} is about 0.006 for both cases. The ratio of the C_{f_max} to C_{f_center} is 2.74.

It is expected that the bed shear stress of Case (c) is the highest among all these cases because of its highest contraction ratio. As shown in table 5-1, C_{f_max} is 0.03 for Case (c), almost twice of the values for Case (a) and Case (b); C_{f_center} is 0.018 for Case (c), three times of the results for Case (a) and Case (b). The ratio of the C_{f_max} to C_{f_center} is 1.75 for Case (c). It is worthwile to note that the increasing of bed shear stress is much faster at the center of the channel than around abutment. The bridge deck is all the way

through the river cross section. This is not like abutment acting only on the bank sides of the channel. Hence, for the same blockage ratio, the influence of the bridge deck on the channel center will be greater than that of the abutment. This implies that the pressurized flow tends to be more unifrom than open channel flow in rectangular channel.

The contraction ratio of Case (d) is the second largest in these four cases. Accordingly, C_{f_max} and C_{f_center} of Case (d) is the second highest among them. Part of the flow blocked by the bridge deck will go over bridge deck and makes the flow rate under bridge deck than that of Case (c). This again proves that the worst condition is with the water surface up to the deck surface.

Based on the these simulations, it is found that the higher the contraction ratio, the higher the friction coefficient.

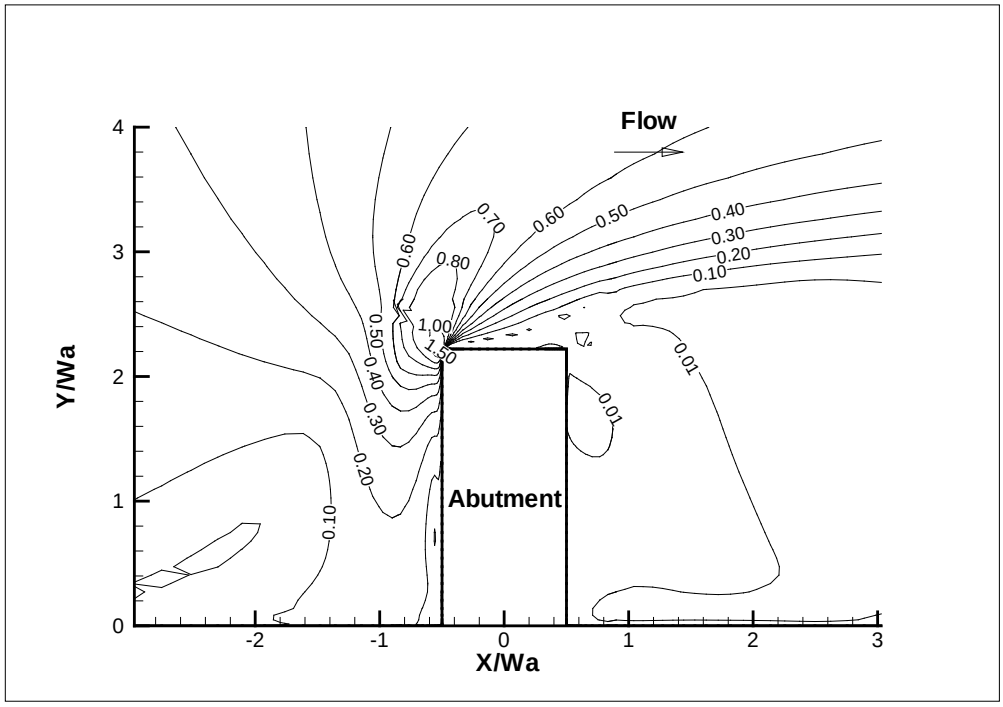

Figure 5-7 Bed friction coefficient ($\times 10^{-2}$) contours for Case (a).

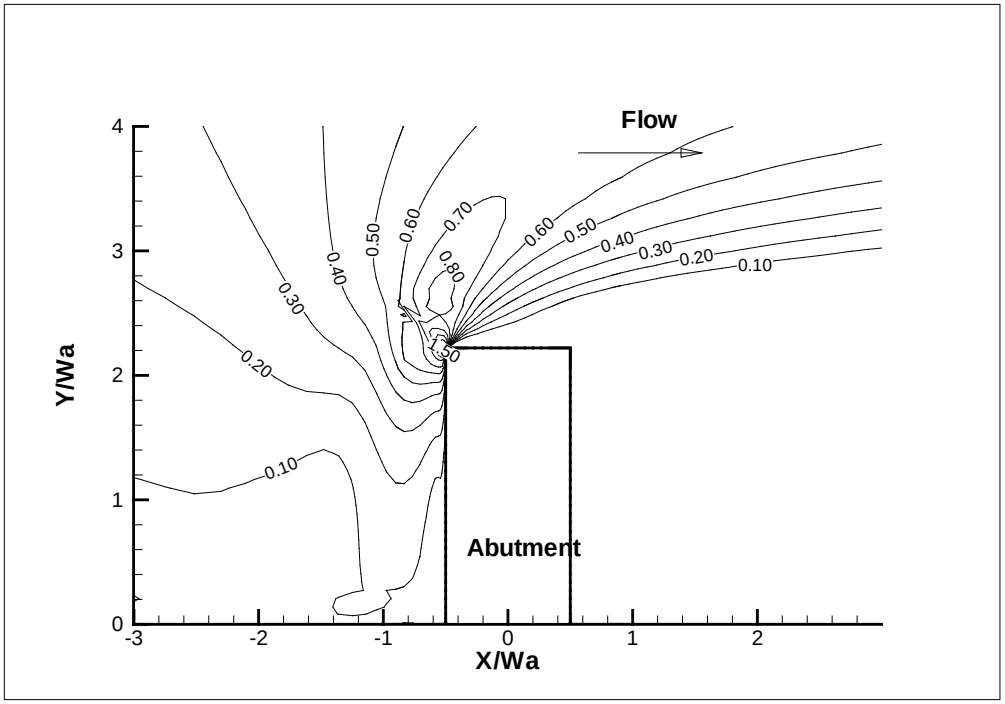

Figure 5-8 Bed friction coefficient ($\times 10^{-2}$) contours for Case (b).

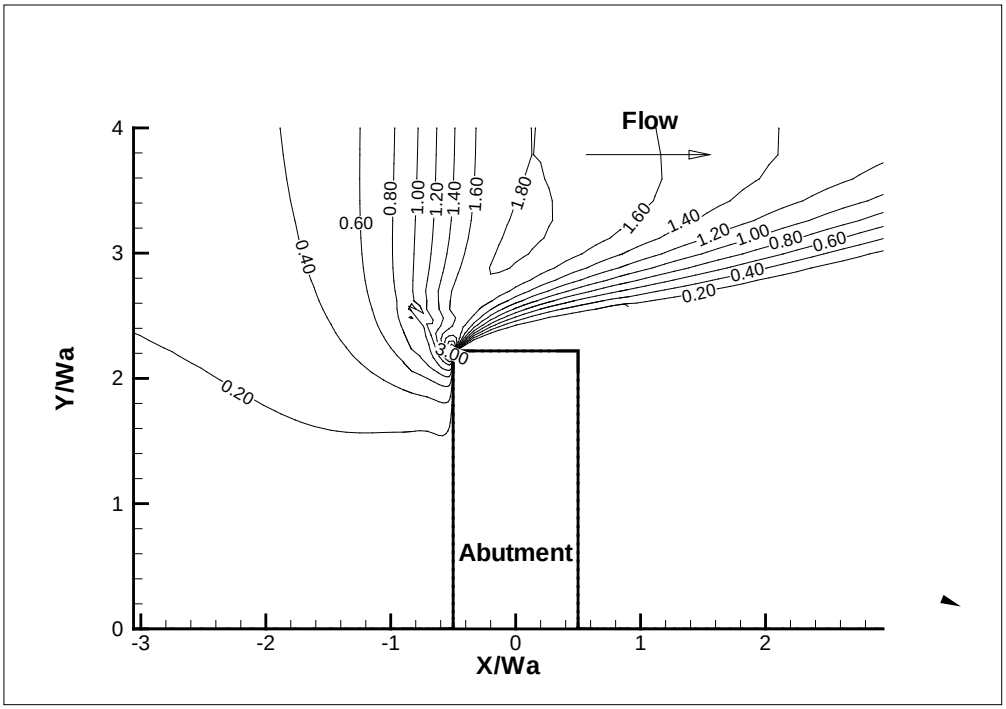

Figure 5-9 Bed friction coefficient ($\times 10^{-2}$) contours for Case (c).

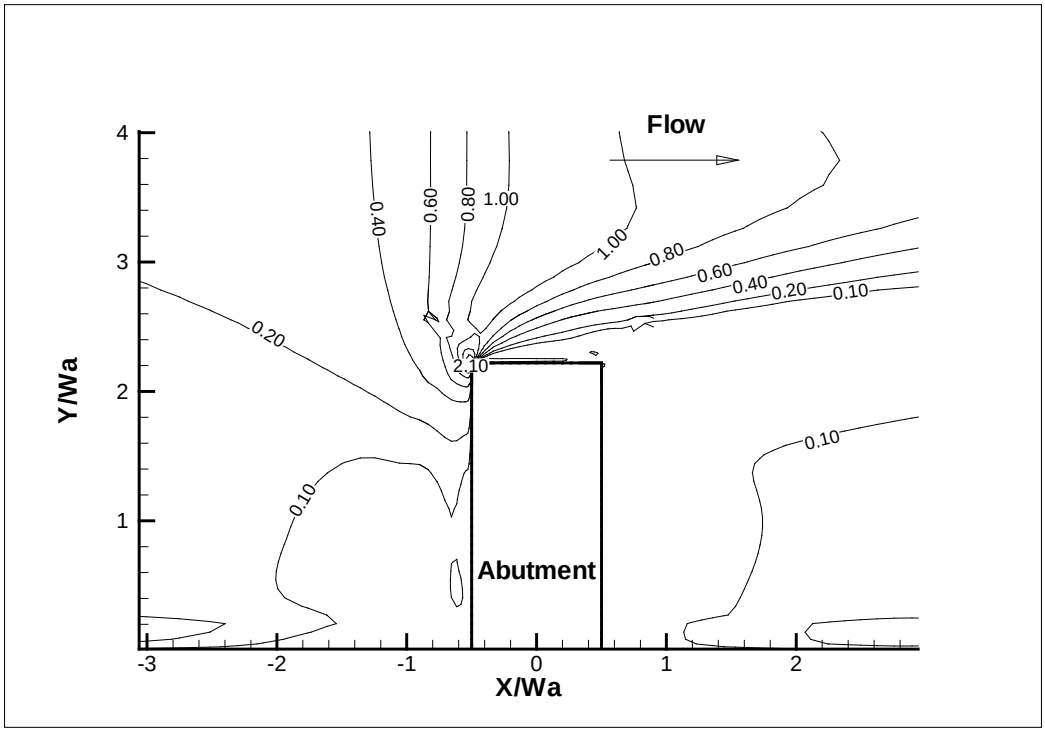

Figure 5-10 Bed friction coefficient ($\times 10^{-2}$) contours for Case (d).

Case #	Re	Cr	C_{f_vw}	K_{Cr}	K_{sh}	K_{Fr}	K_s	K_{sk}	C_{f_max}
	----	----	----	----	----	----	----	----	----
(a)	1.52E+05	1.38	0.0098	2.15	0.70	1.16	1.00	1.00	0.0172
(b)	1.52E+05	1.38	0.0098	2.15	0.70	1.16	1.00	1.00	0.0172
(c)	1.52E+05	1.85	0.0098	3.84	0.70	1.11	1.00	1.00	0.0294
(d)	1.52E+05	1.58	0.0098	2.86	0.70	1.08	1.00	1.00	0.0212

Table 5-2 Prediction of C_{f_max} in rectangluar channel cases with overtoppping.

To predict the maximum bed shear stress around abutment under overtopping conditions, the equation proposed in Chapter IV is applied. The basic ideal is to assume that the overtopping condition is equivalent to open channel flow condition with same contraction ratio. The detailed calculation is presented in table 5-2. The predicted maximum friction coefficients are close to the simulated results. The comparison is

given in figure 5-11. It shows that the overtopping situations may be predicted by the existent method within 10% difference in rectangular channel.

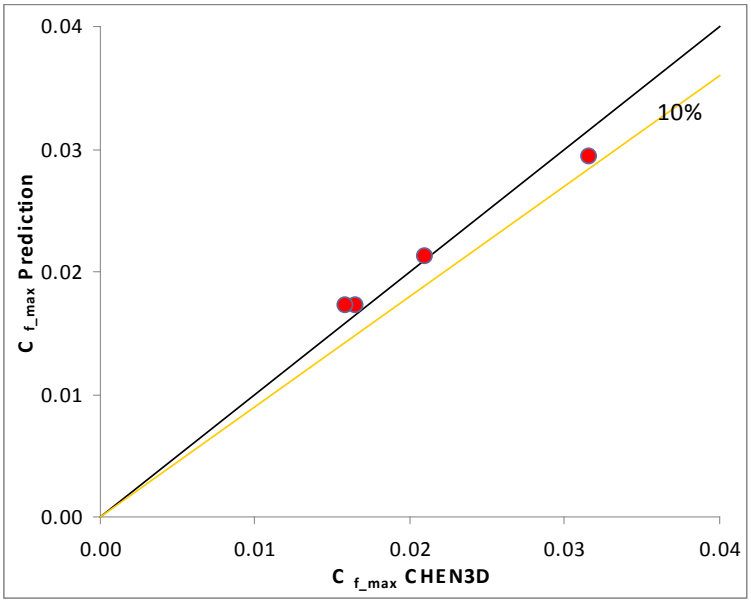

Figure 5-11 Comparison of the predicted and simulated C_{f_max} in overtopping cases.

5.3 Overtopping in Compound Channel

5.3.1 Overtopping in symmetric compound channel

Two overtopping cases, T1WW (wing-wall abutment) and T1ST (spill-through abutment), have been conducted to investigate the bed shear stress on the river bed in compound channel. Similar grid systems as shown in figure 5-6 have been used except the replacement of rectangular channel with compound channel. Figure 5-12 shows the detail parameters. For convenience, these two cases are designed based on the flume test Case 01 and Case 09. The bridge deck is of 0.4 ft thickness and 1.5 ft width. Wate surface is 0.4ft higher than the deck surface.

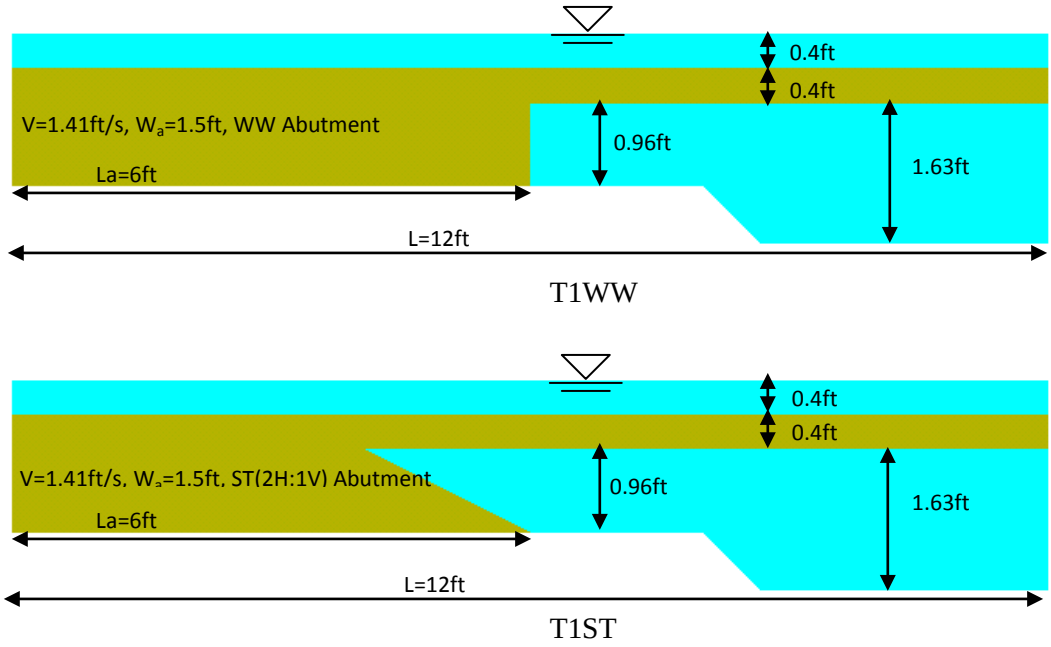

Figure 5-12 Cross sections at the middle of the abutment for compound channels.

Figures 5-13 to 5-16 present the bed shear stress contours for T1WW, Case 09, T1ST, and Case 01. The bed shear stresses around abutment increase significantly from open channel flow to the designed overtopping flow. For wing-wall abutment, C_{f_max} increases from Case 09 of 0.0117 to T1WW of 0.018; for spill-through abutment, C_{f_max} increases from Case 01 of 0.0097 to T1ST of 0.016. At channel center, however, the change of the bed shear stress on the main channel is not as remarkable as on the rectangular channel. C_{f_center} increases from about 0.004 to 0.005 for Case 09 and Case 01 to around 0.006 for T1WW and T1ST.

Regarding the bed shear stresses on the main channel slope, higher values can still be found in overtopping flow same as the observation on open channel flow. This indicates that the erosion of main channel slope will still be faster under overtopping flow conditions.

Overtopping affects the distribution of bed shear stress around the toe of the abutment. For open channel flow cases, the bed shear stress increases gradually when getting closer to the abutment from upstream side. After reaching the maximum bed shear stress right at the toe of abutment, the bed shear stress depresses quickly toward dowstream. For overtopping cases, the trend is totally opposite. And for the same loaction at upstream side, the bed shear stress is smaller than that in open channel case. It is believed that the existence of the bridge deck has little influence on upstream. And the bed shear stress will decrease with the increase of water depth. When getting very close to the bridge deck, the contraction effect of deck results in the quick increase of the bed shear stress. At downstream side, the highly contracted flow can remain the intensity in a large range and make the bed shear stresses decrease gradually.

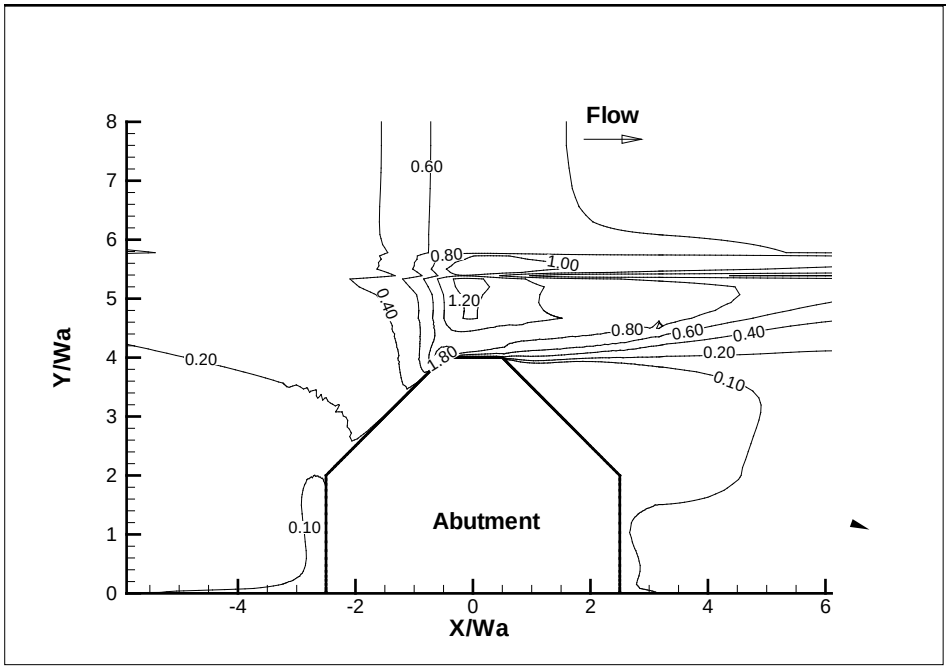

Figure 5-13 Bed friction coefficient ($\times 10^{-2}$), T1WW.

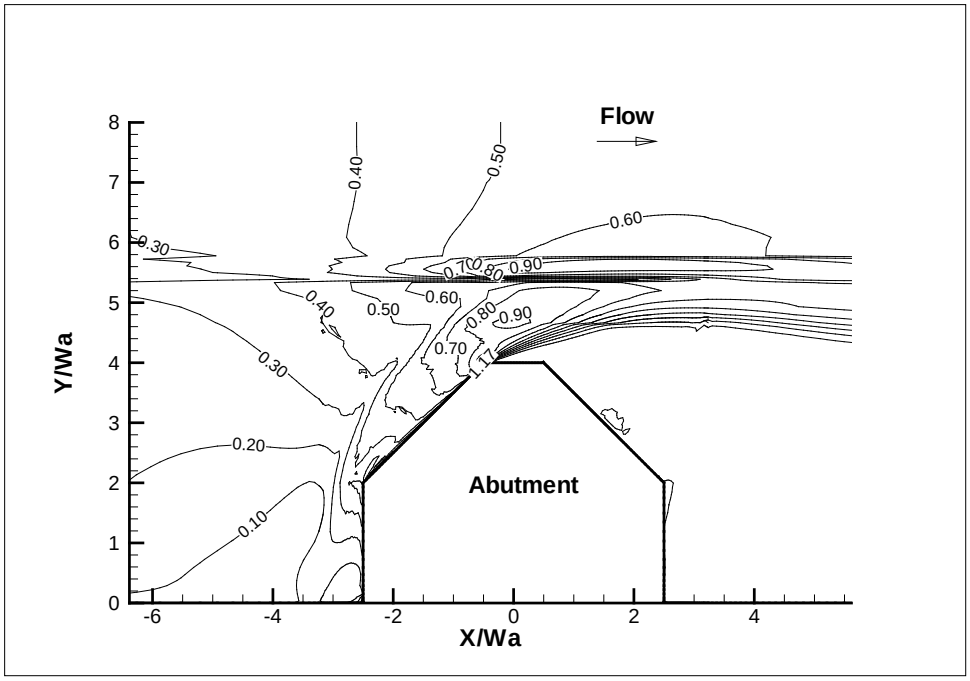

Figure 5-14 Bed friction coefficient ($\times 10^{-2}$), Case 09.

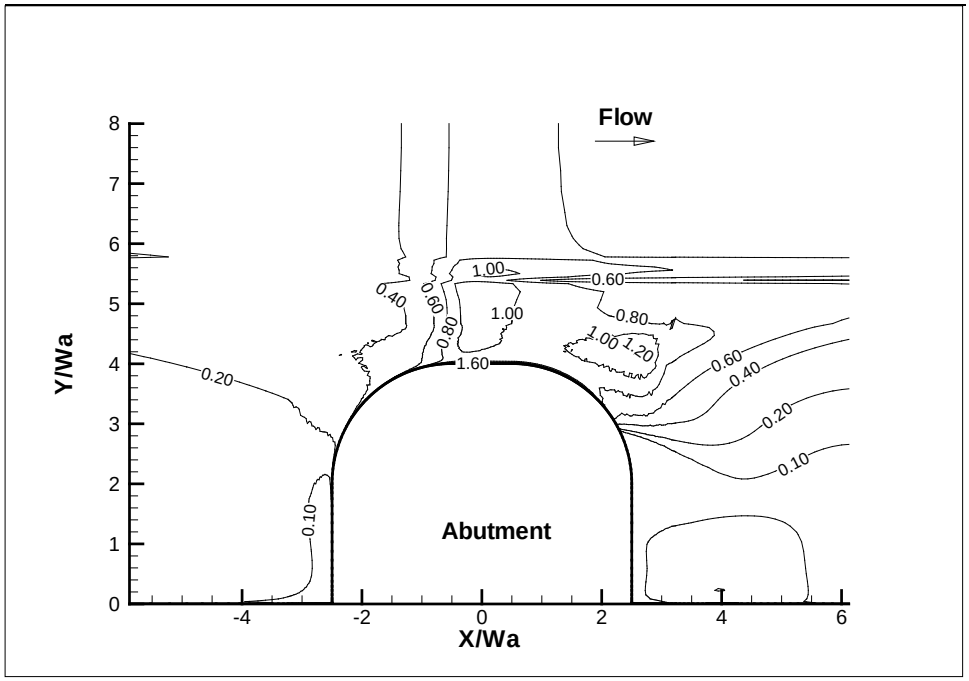

Figure 5-15 Bed friction coefficient ($\times 10^{-2}$), T1ST.

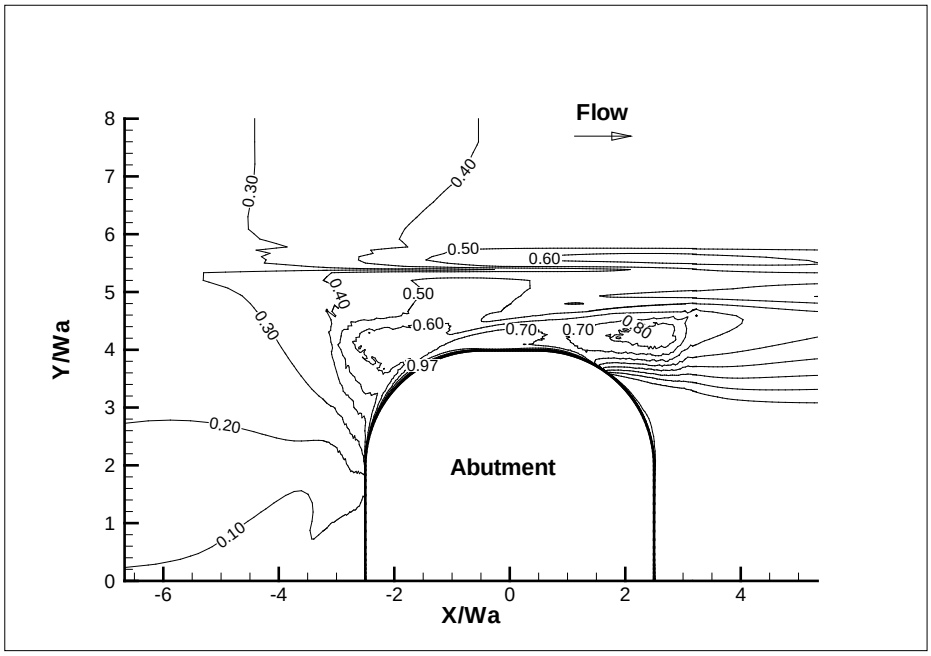

Figure 5-16 Bed friction coefficient ($\times 10^{-2}$) Case 01.

Case #	V	y	L_a	W_a	Shape	C_r	C_{f_max}	C_{f_center}	C_{f_max}/C_{f_center}
	ft/s	ft	ft	ft	----	----	----	----	----
T1WW	1.41	1.76	6	1.5	WW	1.81	0.0194	0.0060	3.24
Case09	1.41	0.96	6	1.5	WW	1.70	0.0117	0.0050	2.34
T1ST	1.41	1.76	6	1.5	ST	1.69	0.0163	0.0060	2.71
Case01	1.41	0.96	6	1.5	ST	1.53	0.0097	0.0040	2.43

Table 5-3 Simulation results of overtopping in symmetric compound channel cases.

Case #	Re	Cr	C_{f_vw}	K_{Cr}	K_{sh}	K_{Fr}	K_s	K_{sk}	C_{f_max}
	----	----	----	----	----	----	----	----	----
T1WW	1.96E+05	1.81	0.0087	3.71	0.61	1.19	0.65	1.00	0.0152
Case09	1.96E+05	1.70	0.0087	3.31	0.61	1.33	0.65	1.00	0.0151
T1ST	1.96E+05	1.69	0.0087	3.27	0.61	1.19	0.58	1.00	0.0120
Case01	1.96E+05	1.53	0.0087	2.68	0.61	1.33	0.58	1.00	0.0109

Table 5-4 Prediction of C_{f_max} in compound channel cases with overtoppping.

Simulation results are shown in table 5-3. The prediction with the equation in chapter IV for compound channel has been listed in table 5-4. The predicted values in overtopping are lower than the simulated results with about 30% difference as shown in figure 5-17. It is opposite to the prediction of open channel flow.

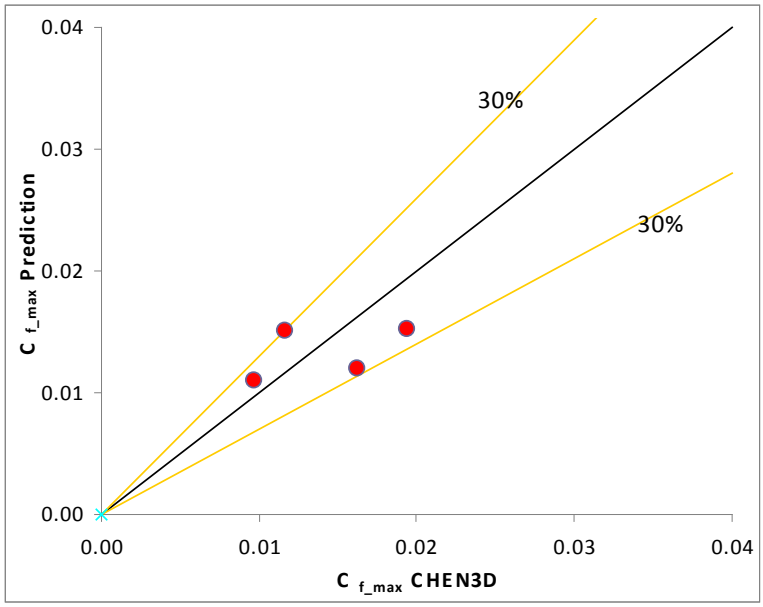

Figure 5-17 Comparison of the predicted and simulated C_{f_max} in overtopping cases.

5.3.2 Overtopping in non-symmetric compound channel

All the overtopping simulations completed so far are assumed to be in symmetric channel. In the real rivers, channels are very likely to be non-symmetric. So it is helpful to investigate the bed shear stress distribution in non-symmetric channel. For convenience, half of the channel is kept same to the one in symmetric compound channel study. And the other half is designed to have shallower water depth on flood plain. The top width of abutment is same for both sides since the bridge deck will not change through the river. Both of spill-through and wing-wall abutment are studies, called Case

T2ST and Case T2WW respectively. The parameters are given on figure 5-18, showing the cross sections in the middle of the abutment. And figure 5-18 is looking upstreamward. The grid system is similar to the one for rectangular channel shown in figure 5-6 except that the full channel is simulated. Rigid lid is still applied on the water surface. No slip boundary condition is applied on the solid surface.

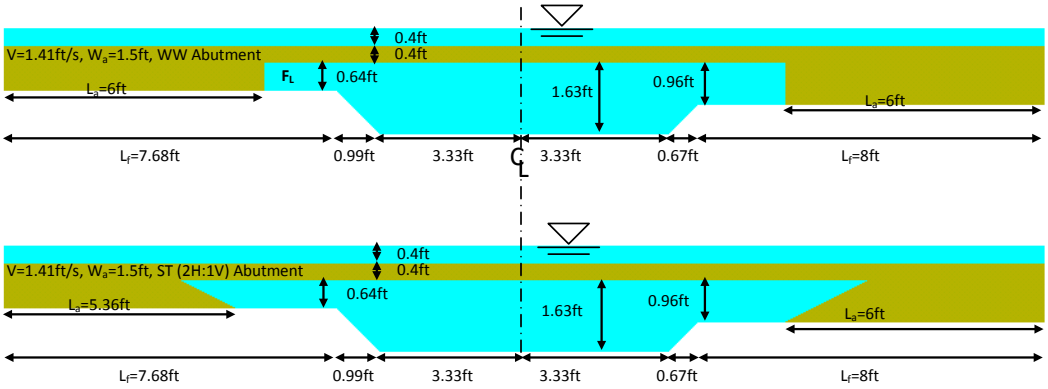

Figure 5-18 Cross sections for non-symmetric compound channels.

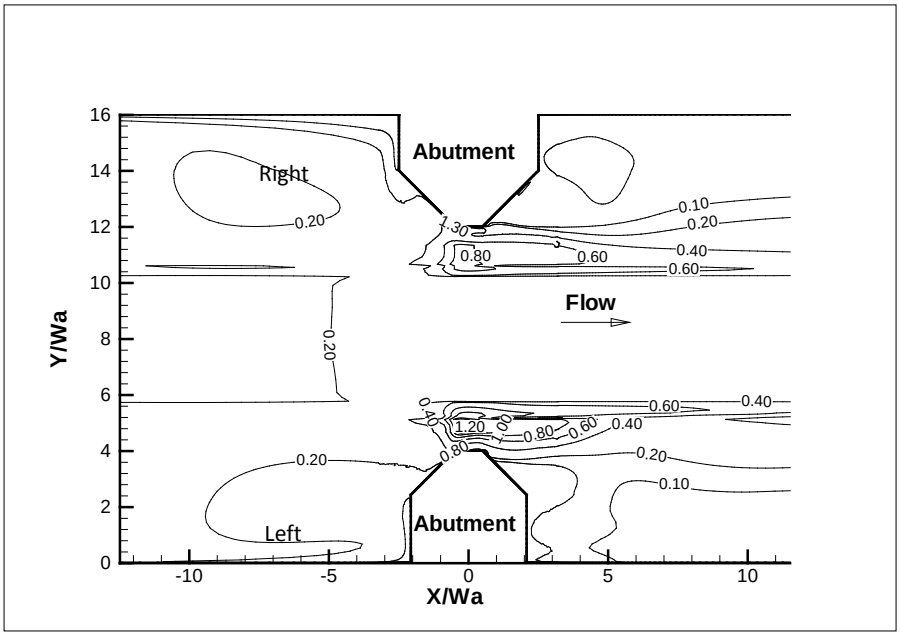

Figure 5-19 Bed friction coefficient ($\times 10^{-2}$) contours, T2WW.

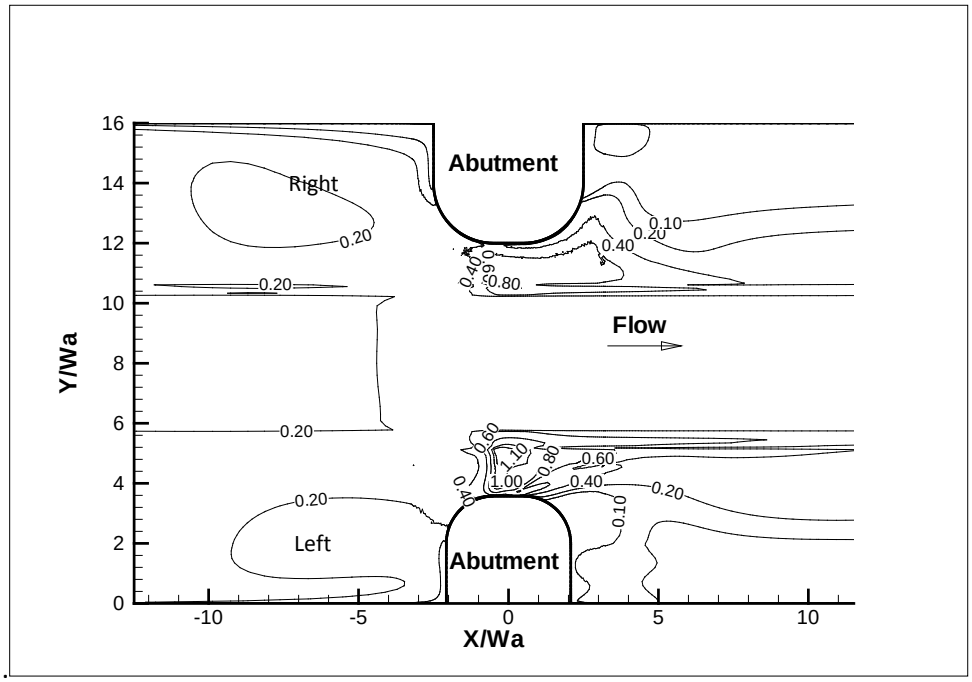

Figure 5-20 Bed friction coefficient ($\times 10^{-2}$) contours, T2ST.

Figure 5-19 and figure 5-20 show the bed friction coefficient contours of Case T2WW and Case T2ST. Assuming the channel is divided into to two parts along the center of the channel, there is not influence between each other. Then, the left side has shallower water depth on flood plain and higher contraction ratio. The bed friction coefficient on left flood plain should have higher values than on right flood plain. This is consistent with the observations from both of figure5-19 and figure 5-20. The right sides of the channels are identical to the symmetric compoud channels of Case T1WW and Case T1ST, respectively. But the C_f values are lower than those on the corresponding symmetric cases. As shown in figure 5-19, C_f in front of the right abutment face on flood plain is about 0.008, while in symmetric channel the value is 0.012 for Case T1WW. The friction coefficient at the main channel center for Case T2WW is 0.0032, which is about

half of the value at the same location in Case T1WW. Similar trend can also be observed between Case T2ST and Case T1ST. These comparisons show that the the prediction of bed shear stress based on half of the channel under symmetric channel assumption could cause large discrepency for non symmetric channel.

Case #		V	y	L_a	W_a	Shape	C_r	C_{f_max}	C_{f_center}	C_{f_max}/ C_{f_center}
		ft/s	ft	ft	ft	----	----	----	----	----
T2WW	right	1.41	1.76	6	1.5	WW	1.81	0.0131	0.0032	4.09
	left	1.41	1.44	6	1.5	WW	2.00	0.0128	0.0032	3.99
T2ST	right	1.41	1.76	6	1.5	ST	1.69	0.0077	0.0032	2.42
	left	1.41	1.44	6	1.5	ST	1.94	0.0116	0.0032	3.62

Table 5-5 Simulation results of overtopping in non-symmetric compound channel cases.

Case #		Re	Cr	C_{f_vw}	K_{Cr}	K_{sh}	K_{Fr}	K_s	K_{sk}	C_{f_max}
		----	----	----	----	----	----	----	----	----
T2WW	right	1.96E+05	1.81	0.0087	3.71	0.61	1.19	0.65	1.00	0.0152
	left	1.96E+05	2.00	0.0087	4.42	0.61	1.23	0.65	1.00	0.0187
T2ST	right	1.96E+05	1.69	0.0087	3.27	0.61	1.19	0.58	1.00	0.0120
	left	1.96E+05	1.94	0.0087	4.18	0.61	1.23	0.58	1.00	0.0158

Table 5-6 Prediction of C_{f_max} in non-symmetric compound channel cases (overtoppping).

Table 5-5 presents the simulated the maximum bed shear stress around abutment and the bed shear stress at the channel center in the middle of the abutment. The former is about 2.5 to 4 times of the the latter. Wing-wall abument tends to generate slightly higher bed shear stress.

The maximum bed shear stress equation has also been tried for the non-symmetric channel based on the asumption that the left and right part of the channel are independent. The detail calculation are given in table 5-6. Figure 5-21 presents the direct comparison of the predictions with the measurements. The prediciton can be 50%

higher than the simulated results. This is contrary to the findings in the previous study of ovetopping in rectangular channel and in symmetric compound channel.

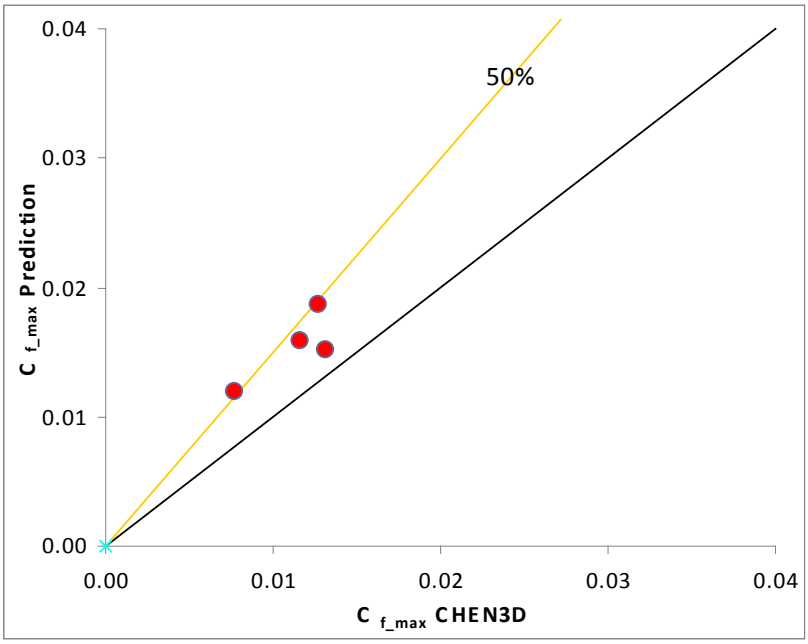

Figure 5-21 Comparison of the predicted and simulated C_{f_max} in overtopping cases.

5.4 Open Channel Flow on Channel Bend

Channel bend can redistribute the flow along the cross section and further change the bed shear stress distribution. In the abutment scour analysis, it is interesting to look into the influence of channel bend on the bed shear stress around abutment. The geometry of the channel bend is usually characterized by the ratio of R/W. R is the radius of the bend and W is the width of the channel. Two types of bend are studies in current research with the R/W equal to 1:1 and 2:1. The bend is fixed with the angle of 90 degree from the inlet to the outlet. The location of the abutment on the channel bend will also be studied. Two representive locations, middle of the bend and downstream end

of the bend, are considered. To study the influence of abutment shape, both spill-through and wing-wall abutment are included in the analysis. Overall, eight cases are designed for the study of open channel flow on channel bend, as listed in figure 5-22. The grid system is similar to Figure 5-6 and fully connected grids are utilized. The parameters , such as approach velocity, water depth, abutment length, compound channel configuration are exactly same to Case 09 and Case 01 so that the effect of channel bend can be investigated easily. Figure 5-23 shows the cross section at the middle of abutment for wing-wall abutment in this study. Case T1WW with overtopping in straight channel is also shown.

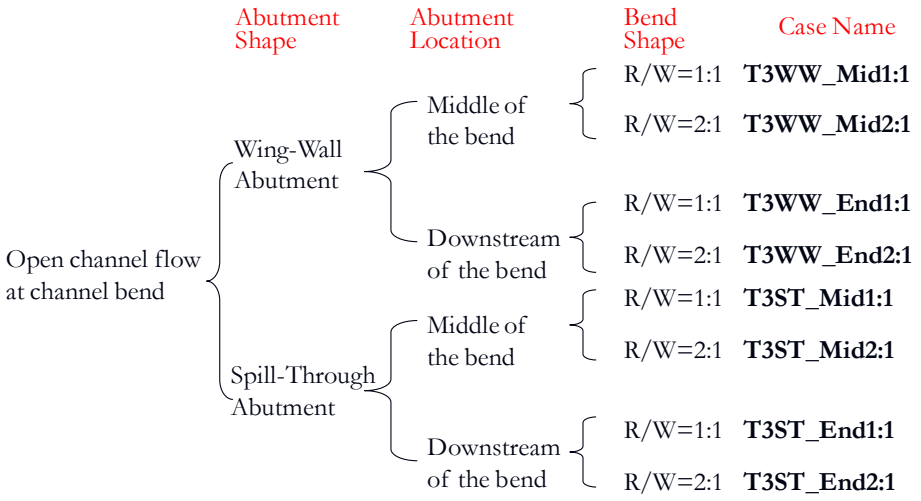

Figure 5-22 Numerical cases for channel bend study in open channel flow.

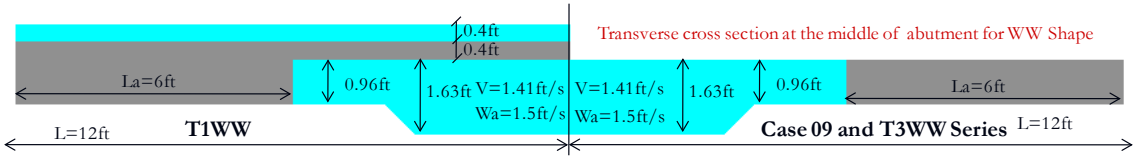

Figure 5-23 Cross section of the wing-wall abutment cases in channel bend study.

Figure 5-24 to figure 5-31 show the simulation results of all the eight cases. The results will be analyzed from the influence of R/W, abutment location and abutshape.

5.4.1 Influence of R/W

The influence of bend geometry can be observed among the cases varying only R/W. As shown in figure 5-22, four groups with different abutment shape and location can satisfy this requirement. Among them, the cases with wing-wall abutment at the middle of the bend, will be discussed in detail, namly Case T3WW_Mid 2:1 and Case T3WW_Mid 1:1.

Maximum bed friction coefficient C_{f_max} is 0.013 for Case T3WW_Mid 1:1 and 0.011 for Case T3WW_Mid 2:1. Both of them have C_{f_max} at the downstream inner main channel slope. In traight channel, C_{f_max} ususally occurs at upstream corner of the wing-wall abutment, such as Case 09 of C_{f_max} equal to 0.017. On the other hand, the bed shear stress contours are highly non-symmetric when R/W equal to 1:1. The inner flood plain has much higher bed shear stress than outer part at right downstream of the abutment. At far downstream, the outer main channel slope suffers much higher shear stress than inner part. When R/W equal to 2:1, the difference is not significant between inner and outer flood plains and the entire bed shear stress level is a lot lower than the case of R/W equal to 1:1. At far downstream, the outer main channel slope still suffers higher bed shear stress. All these indicates that the channel with lower R/W tends to cause higher bed shear stress and make the shear stress contours more non-symmetric. But C_{f_max} may not change too much. These can also be found on the other threee groups except that the phenomena may not be as remarkable as the current study.

The influence of the bend geometry can also be observed from the flow field either on the plan view of water suface or on the cross section plots. For the straight channel, the ratio of R/W is equal to infinity. The flow distribution in the transverse direction will be symmetric as long as the channel and abutment is in symmetry. However, the symmetric flow will be disturbed when passing the channel bend. At the beginning of the bend, the inner part of the channel will have higher velocity. Then the higher velocity region will move to the outer side along with the bend. This can be observed from approach section of Case T3WW_Mid 1:1. The unit flow rate at the inner half of the channel is higher than the outer half. However, for Case T3WW_Mid 2:1, the flow distribution is still in symmetry even if approaching the abutment. This indicates the sharp bend can cause higher asymmetric flow, which is consistant with the finding in bed shear stress distribution.

Velocity plan view of Case T3WW_Mid 1:1 shows highly non-symmetric pattern at the downstream. The highest velocity appears at the inner side of the main channel and close to the main channel slope. The higher velocity region is very strong and extending from main channel to the outside flood plain. This indicates that the change of flow could not follow change of the channel geometry if the R/W is small.

For Case T3WW_Mid 2:1, the flow at the downstream is close to symmetric.The highest velocity appears in the middle of the main channel with the contours skewed slightly to the inner abutment. And the higher velocity region bascically remains in the main channel at the downstream side. All these show that the influence of bend with R/W equal to 2:1 is not as significant as the bend of R/W equal to 1:1.

5.4.2 Influence of abutment location

When the bridge is located at the middle of the bend, the bend turns 45 degree from the inlet to the location of abutment. The main flow direction may not change as large as 45 degree because of the delay of the bend effect. The bed shear stress distribution around the inner and outer abutment will be different since the flow field is not going to be as symmetric as in straight channel. The magnitude of the bed shear stress could be affected by lots of other factors, such as R/W ratio , and abutment shape. But the bed shear stresses around the inner abutment always tend to be higher than the values around the outer abutment. This can be observed from all the four simulations with the abutment in the middle of the channel bend. In straight channel, the maximum bed shear stress usually appears at the upstream corner of the abutment, especially for the abutments with sharp corner, such as vertical wall and wing-wall abutments. For the abutment in the middle of the channel bend, however, the maximum bed shear stress appears at downstream inner main channel slope. This is closly related to the flow field of bend channel. When approaching the middle of the channel bend, the inner side of the main channel already has higher velocity than outer side. The high velocity region will continue to move gradually from inner to outer part along the bend. The existing of the inner abutment further forces the flow going toward outer bank. However, the local accelaration at the upstream corner of the inner abutment is not as intensive as in the straight channel. Obviously, the deflected higher velcoity region does not reach the outer over bank when passing the middle of the bend since the local flow is not highly accelerated yet. So, the outer abutment will have little influence on the deflected flow.

This implies that the abutments located in the middle of the bend tends to strenghten the deflection of the flow toward outer bank. Hence, downstream outer bank will be attacked by the flow more seriously.

When the bridge is located at downstream end of the bend, the bend direciton changes 90 degree from inlet to the location of the abutment. In the approaching cross section in front of the abutment, the velocity on the main channel is increasing from inner side to outer side. And the highest velocity appears at the outer side main channel slope and part of the flood plain. The trend is totally opposite to the observation when the abutment is in the middle of the bend. This indicates that the outer over bank will experience higher erosion even if there is no contraction from the abutment. Actually, this is the reason for the channel meander. And this trend is strengthened further at the middle of the abutment. As shown in figure 5-26, the velocity on the inner main channel slope is even lower than the veloicty on the main channel center. The existence of the outer abutment will further acclerate the flow on the outer side of the main channel and generate higher bed shear stress. However, the result of the acceleration also tends to force the deflected flow back to the channel center. As shown in the figures, the magnitude of the bed shear stress at downstream on both sides of the main channel tends to be similar as well as the high shear stress area. At the downstram, outer overbank will not be attacked directly by the channel bended flow. The flow at the downstream of the abutments may recover the uniform condition very quick. Hence, the existing of the abutment at the end of the bend tends to weaken the non uniform flow caused by the channel bend and protect the outer bank from erosion.

5.4.3 Influence of abutment shape

In chapter IV, the correction factor for abutment shape has been proposed to correct the result based on vertical wall abutment. The constant number of 0.65 is recommended for wing-wall abutment; and the constant number of 0.59 is recommended for spill-through abutment. To study the influence of abutment shape on channel bend, two sets of simulations are compared directly. Ratio of R/W and abutment location are same for each pair. It should be noted that the contraction ratio is not same for each pair because of the abutment shape. The results are tabulated in table 5-7. All these results are the maximum values at the toe of the abutment. Overall, the spill-through abutment tends to cause lower bed shear stress. This is consistant with the previous study. So the shape effect is still observable in the channel bend. There is no simulation with vertical wall abutment. The comparison can only be conducted based on results of spill-through and wing-wall abutment. It should be noted that the bed shear stress ratio between these two shapes is lower than 0.59/0.65 for all four pairs. The contracton ratio difference between spill-through abutment and wing-wall abutment can decrease the ratio. Considering this reason, the shape effect may be similar for the abutment on channel bend to the proposed one.

Case #	$C_{f\_max\_WW}$	Case #	$C_{f\_max\_ST}$	$C_{f\_max\_ST}/C_{f\_max\_WW}$
T3WW_Mid 1:1	0.0130	T3ST_Mid 1:1	0.0098	0.75
T3WW_Mid 2:1	0.0109	T3ST_Mid 2:1	0.0087	0.80
T3WW_End 1:1	0.0108	T3ST_End 1:1	0.0095	0.88
T3WW_End 2:1	0.0092	T3ST_End 2:1	0.0070	0.76

Table 5-7 Influence of abutment shape on channel bend.

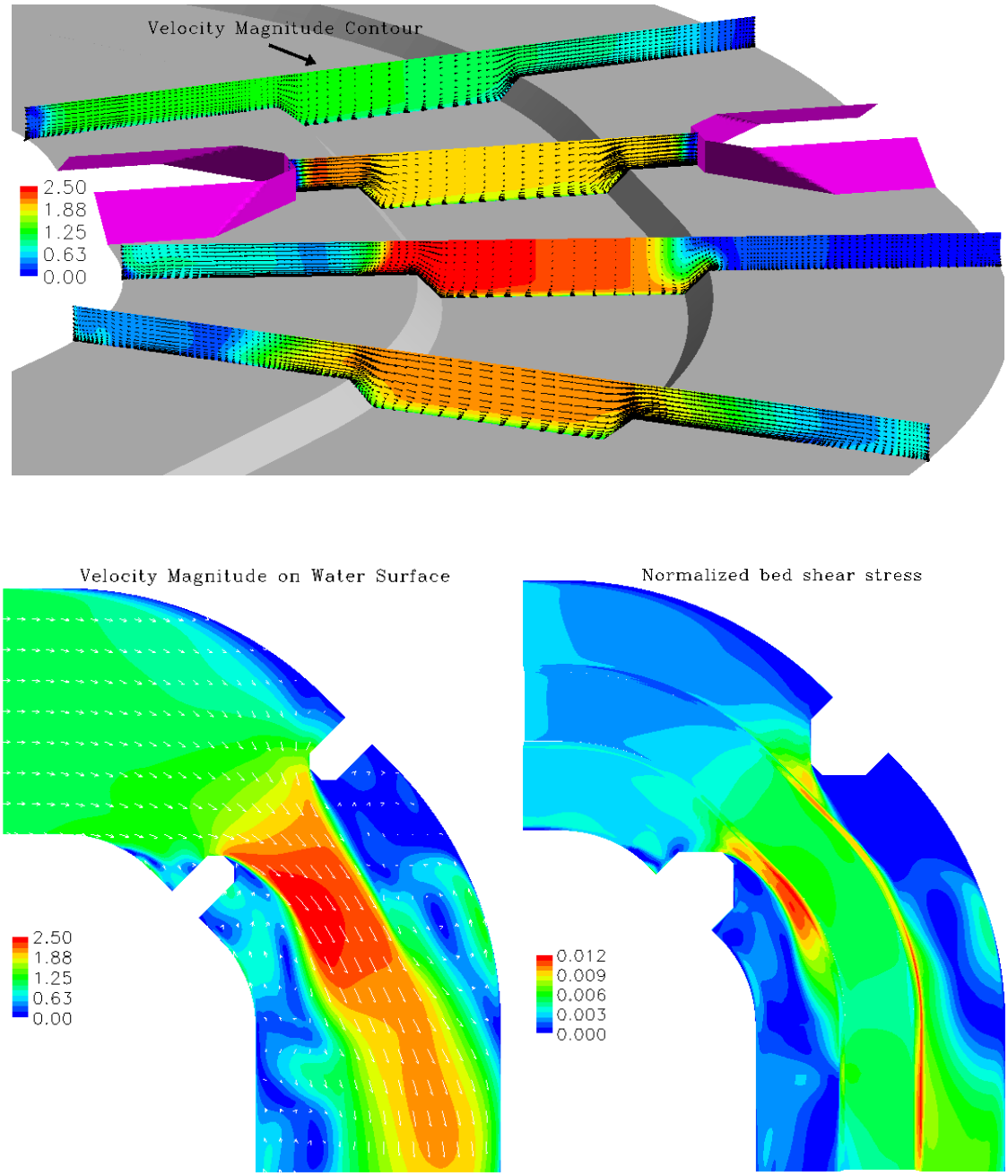

Figure 5-24 Simulation results of Case T3WW_Mid 1:1.

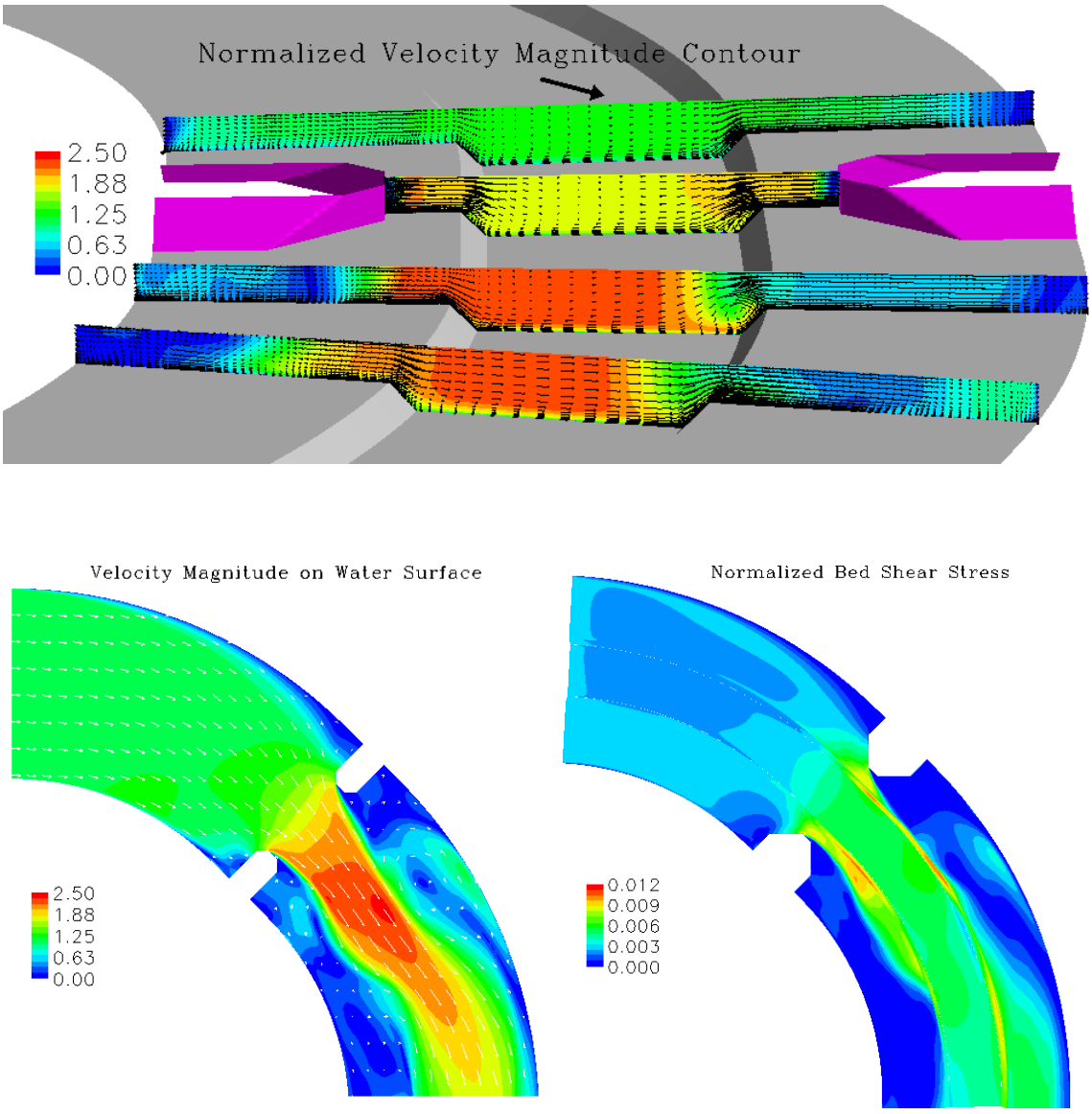

Figure 5-25 Simulation results of Case T3WW_Mid 2:1.

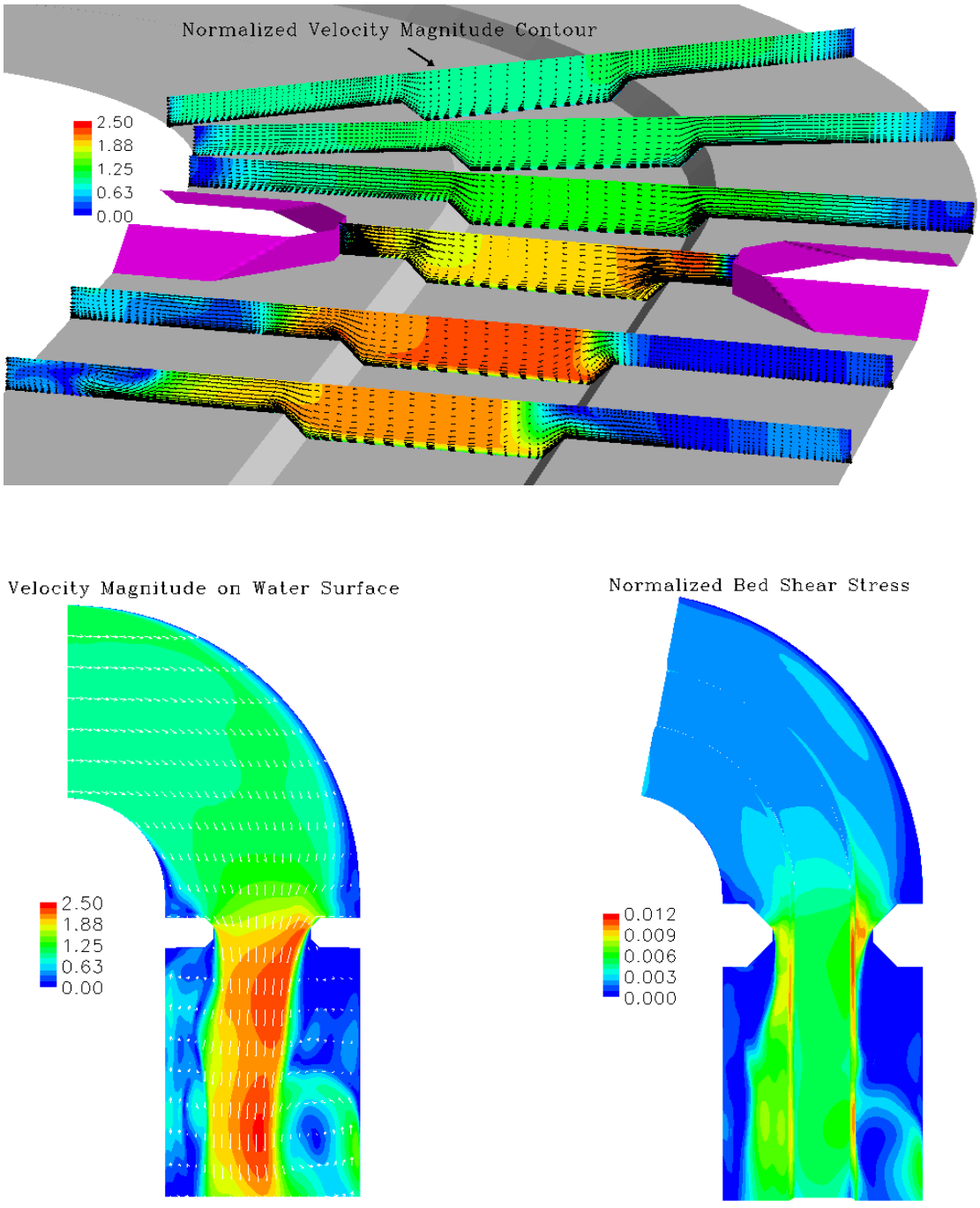

Figure 5-26 Simulation results of Case T3WW_End 1:1.

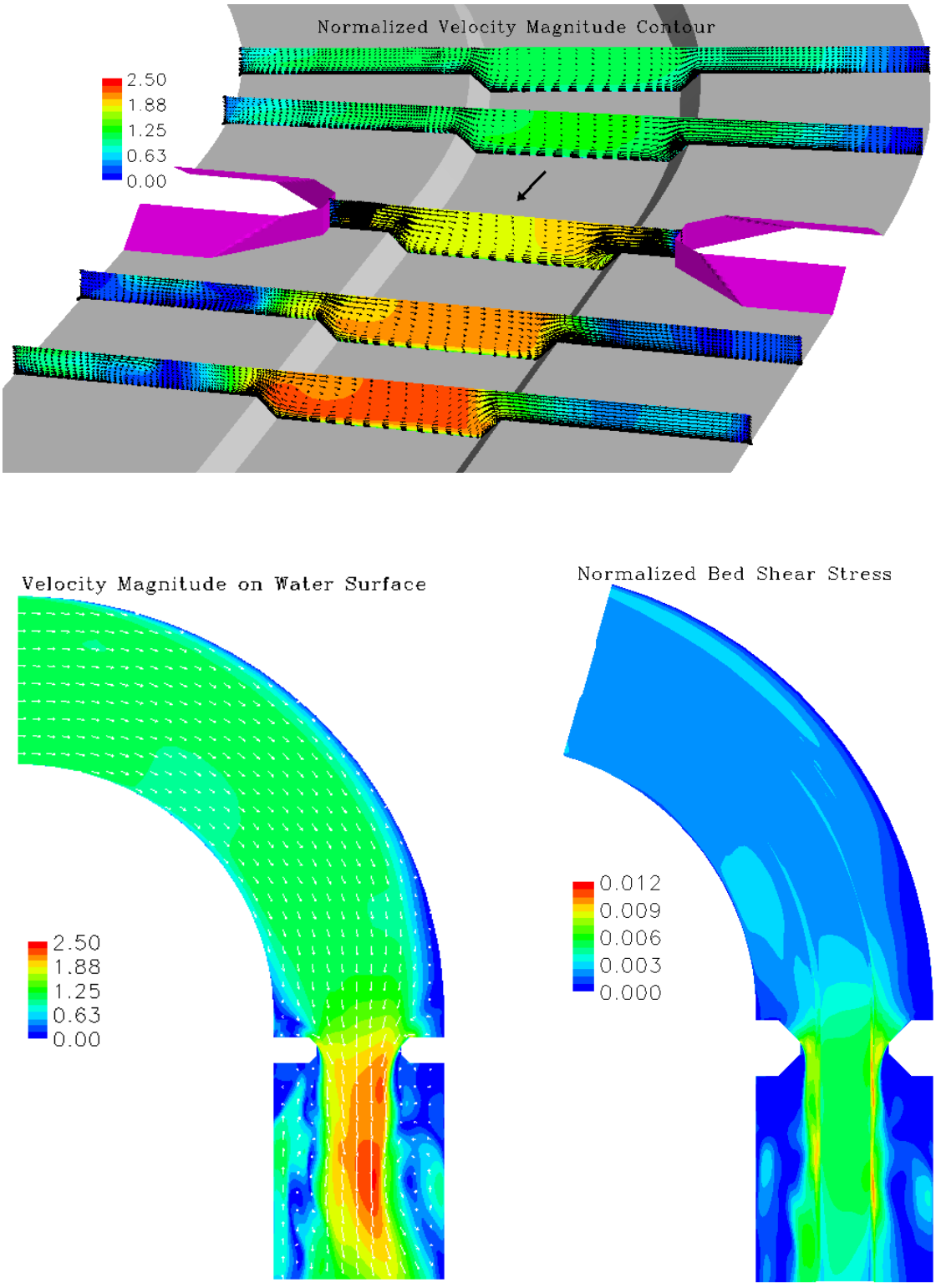

Figure 5-27 Simulation results of Case T3WW_End 2:1.

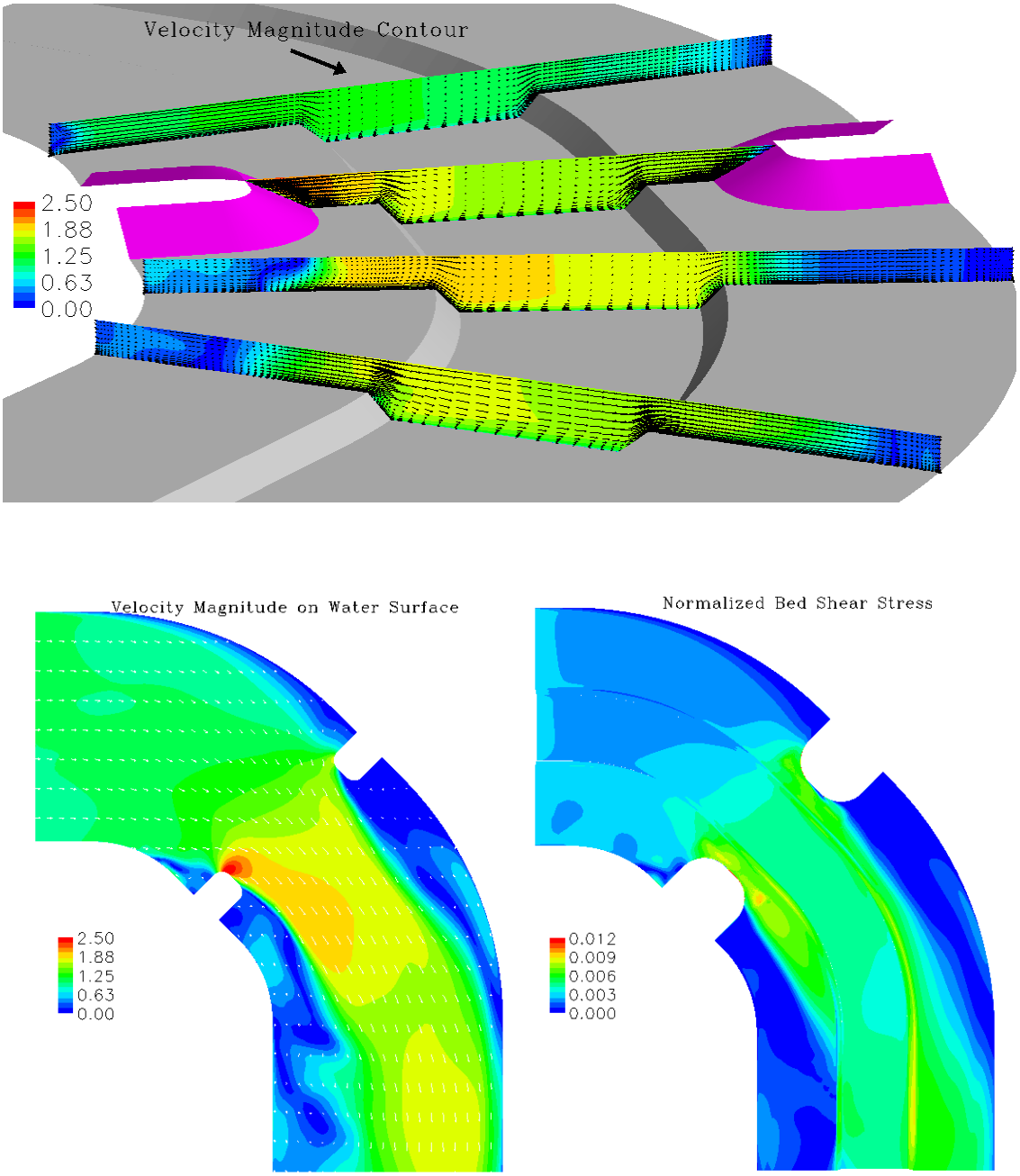

Figure 5-28 Simulation results of Case T3ST_Mid 1:1.

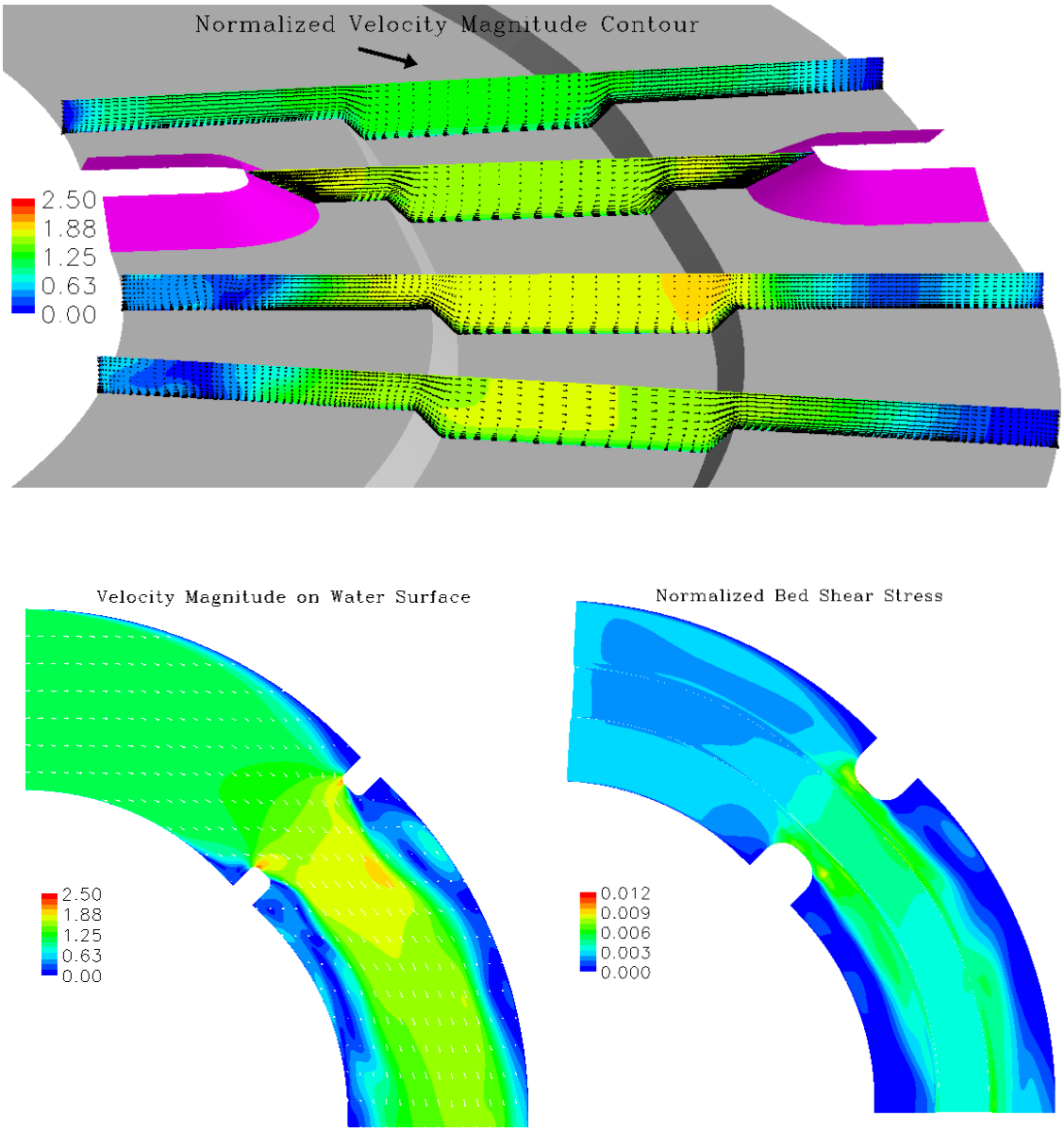

Figure 5-29 Simulation results of Case T3ST_Mid 2:1.

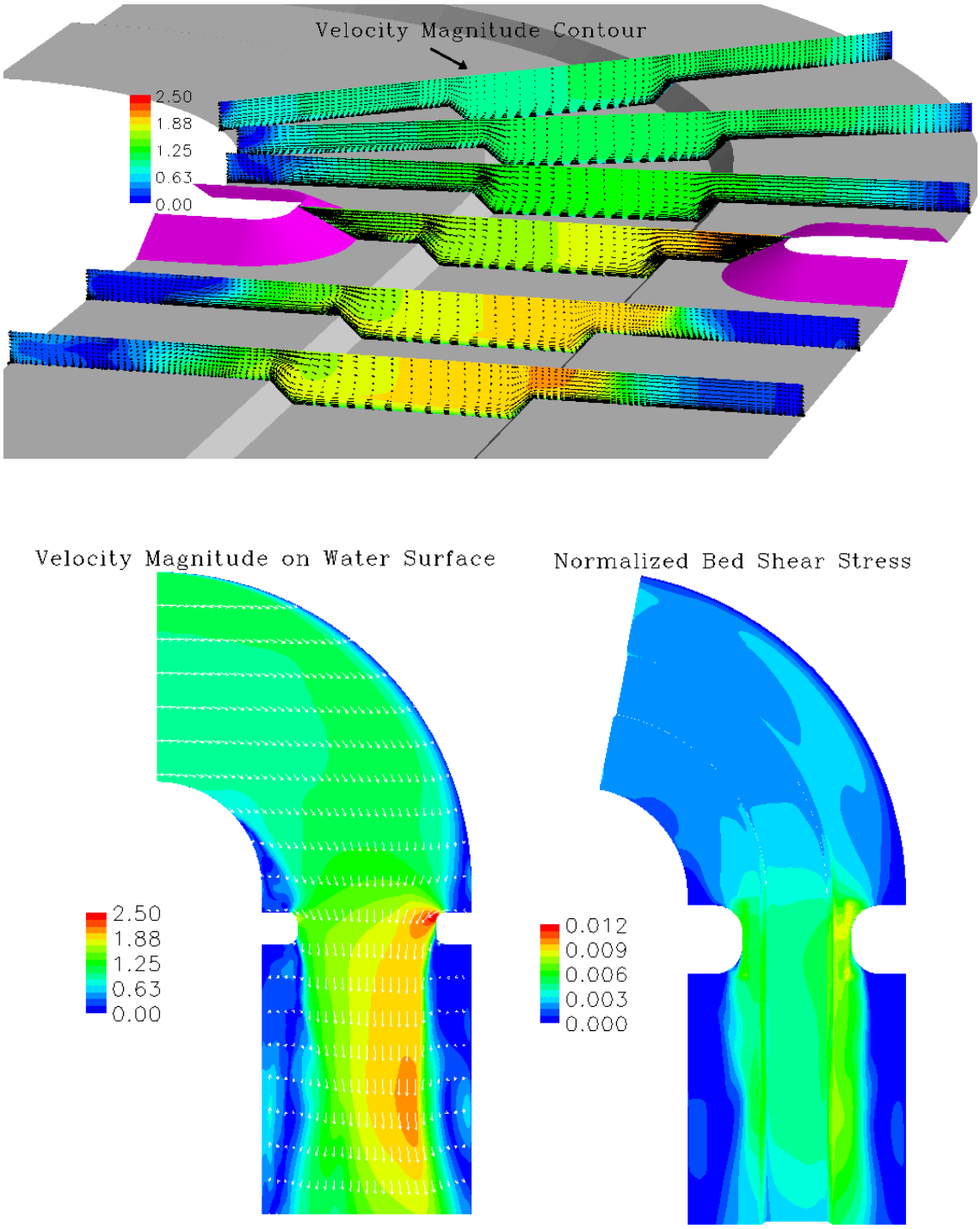

Figure 5-30 Simulation results of Case T3ST_End 1:1.

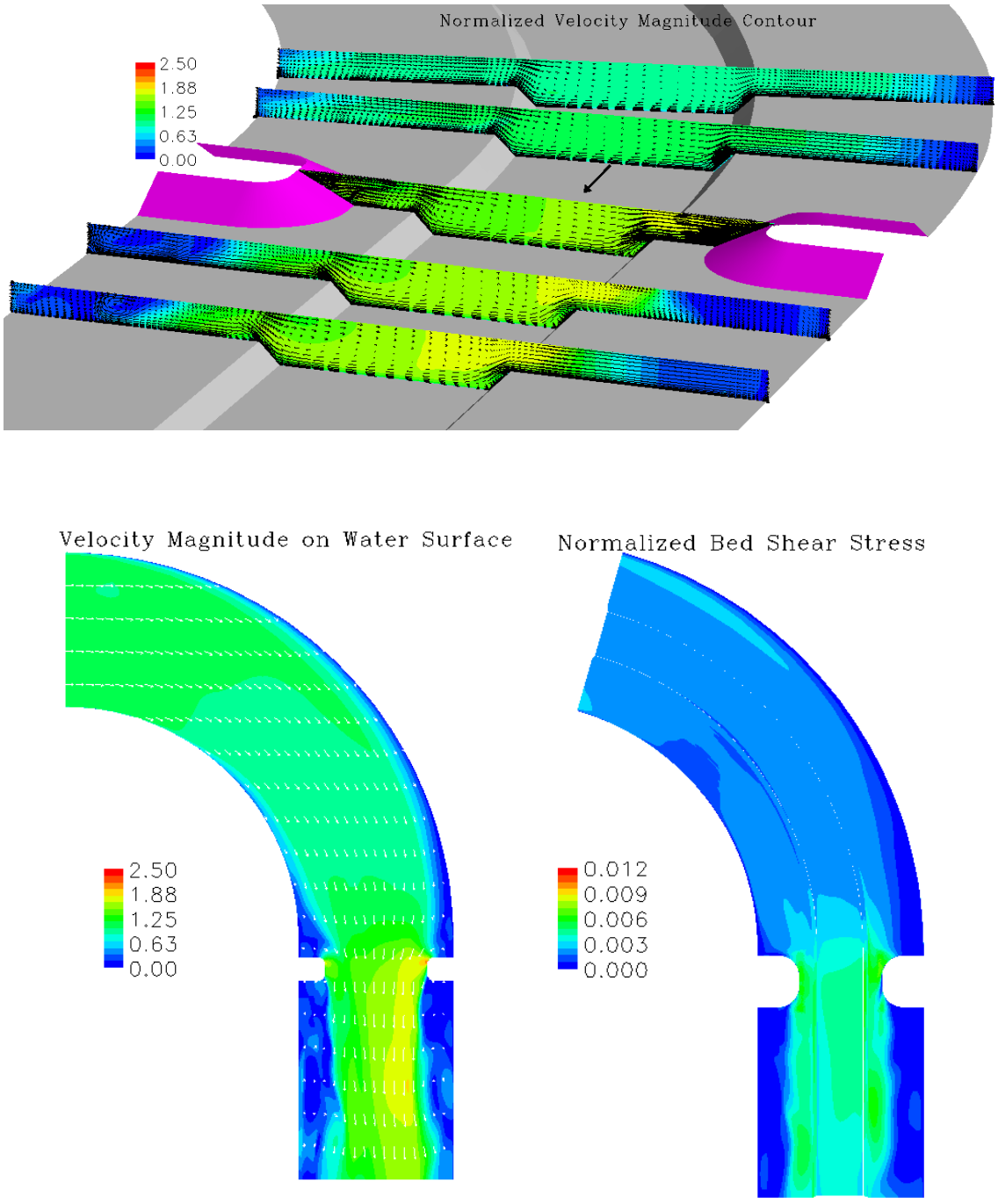

Figure 5-31 Simulation results of Case T3ST_End 2:1.

5.5 Overtopping Flow on Channel Bend

Overtopping conditions have been discussed in straight channel with or without floodplain. The bridge deck is found to be able to make the flow more uniformly ditributed under the bridge deck. So the bed shear stress in channel center will increase much faster than around abutment when overtopping. To study the influence of bridge deck at the channel bend, the cases in section 5.4 have been modified to simulate overtopping conditions. Same bridge to previous overtopping studies, including the deck of 0.4ft thickness by 1.5ft width is used again. Figure 5-32 lists all the eight cases for the overtopping study. Figure 5-33 shows the cross section at the middle of the abutment.

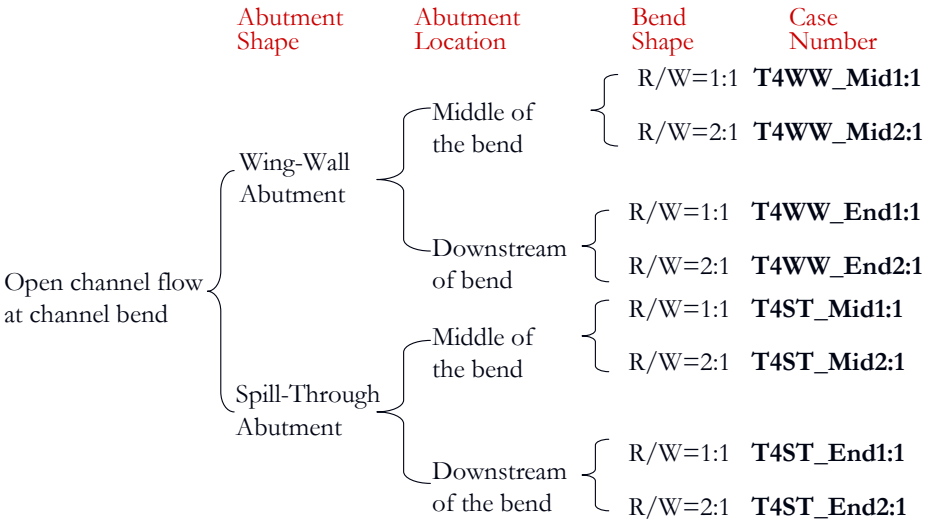

Figure 5-32 Numerical cases for channel bend study in overtopping flow.

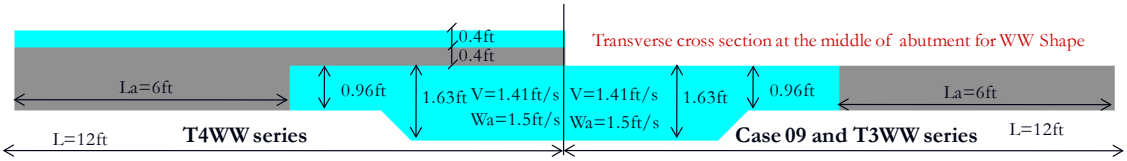

Figure 5-33 Cross section of the wing-wall abutment cases in channel bend study.

5.5.1 Comparison of open channel flow to overtopping flow on channel bend

Comparing two sets of simulations on channel bends for open channel flow and overtopping flow, the bed shear stress is found to have significant increase under overtopping conditions. The overtopping cases has a higher channel contraction ratio than the corresponding open channel cases. The increment of the contraction ratio is about 6.5% and 10.5% for wing-wall and spill-through abutment respectively. Table 5-8 shows the comparison of the maximum bed shear stresses. The increment is from 32% to 90%.

open channel flow	$C_{f\ max\ open}$	Overtopping flow	$C_{f\ max\ over}$	$C_{f\ max\ over}/ C_{f\ max\ open}$
T3WW_Mid 1:1	0.0130	T4WW_Mid 1:1	0.0187	1.44
T3WW_Mid 2:1	0.0109	T4WW_Mid 2:1	0.0167	1.53
T3WW_End 1:1	0.0108	T4WW_End 1:1	0.0178	1.65
T3WW_End 2:1	0.0092	T4WW_End 2:1	0.0175	1.90
T3ST_Mid 1:1	0.0098	T4ST_Mid 1:1	0.0129	1.32
T3ST_Mid 2:1	0.0087	T4ST_Mid 2:1	0.0134	1.54
T3ST_End 1:1	0.0095	T4ST_End 1:1	0.0132	1.39
T3ST_End 2:1	0.0070	T4ST_End 2:1	0.0130	1.86

Table 5-8 Results under overtopping and open channel conditions.

At the upstream of the bridge, the overtopping cases have lower bed shear stresses than the corresponding open channel flow cases in section 5.4. This is consistant to the influence of the water depth. Generally, the bed shear stress will decrease with the increase of the water depth. While at downstream side of the bridge, the influnce of the bridge deck can last for a long distance. This has been observed in strainght channel study.

5.5.2 Influence of R/W

The comparison will still be conducted between the two cases with wing-wall abutment at the middle of channel bend. Comparing with the open channel flow cases, these two overtopping cases have a significant increase on the maximum bed shear stress. For R/W equal to 1:1, with the increase of water depth, C_{f_max} increases from 0.010 to 0.019. At the same time, the location of C_{f_max} changes from downstream main channel slope back to upstream corner of the abutment. For R/W equal to 2:1, with the increase of water depth, C_{f_max} increases from 0.011 to 0.017. The location of maximum bed shear stress also changes back from downstream main channel slope to the upstream corner of the abutment. The interesting finding is that the bed shear stress on the both overbank areas under the bridge deck has a remarkable increase. And the bed shear stress in this area is uniformly high. This is quite different from the open channel flow conditions. At the middle of the abutment, the difference between inner and outer abutment are not big even for R/W equal to 1:1. For the case with R/W equal to 2:1, the shear stress distribution is almost in symmetry. The high bed shear stress at down stream inner overbank in Case T3WW_Mid 1:1 is not observable in overtopping conditions. Overall, the effect of bridge deck tends to decrease the effect of channel bend and make the flow more uniform. However, the influence of the channel bend can still be found at the far downstream outer main channel slope. Both Case T3WW_Mid 1:1 and Case T4WW_Mid 1:1 have this feature. It is believed that the channel bend after the abutment is responsible for the highly asymmetric result.

For overtopping flow, the most concerned is the flow under bridge deck since it is highly related with the bed shear stress distribution. So the plan view of 0.5ft above the flood plain surface is presented in the figures. For Case T4WW_Mid 1:1, the flow has became asymmetric when approaching the abutment. The inner half channel has higher velocity magnitude. However, at the middle of the abutment, the velocity contours are almost symmetric. Even at the downstream side of the abutment, the velocity contour can still keep in symmetry for some distance. The asymmetric velocity contour begins from the end of the channel bend. This is consistent to the observation in the bed shear stress distribution. For Case T4WW_Mid 2:1, the flow basically remains symmetric when approaching the abutment. And this symmetric flow extends to the end of the channel bend. At the far downstream side, the asymmetric trend begins to show up. But it is not as serious as T4WW_Mid 1:1.

The cross section plots are also presented in figure 5-34 and figure 5-35. Same to the straight channel, higher velocity appears on the bridge surface. And under the bridge deck, the velocity is stratified and remains constant in the horizontal direction. The higher velocity appears in the bottom half channel. At downstream of the bridge deck, the surface velocity drops very quick. The higher velocity region extends far from the bridge toward downstream.

5.5.3 Influence of abutment location

For open channel flow, the higher bed shear stress is found to be around inner abutment when the bridge is located at the middle of the channel bend. And the inner abutment tends to force the flow further toward outer bank. The influence of the outer

abutment is not obvious. However, the trend is opposite when the bridge is located at the end of the channel bend. Higher bed shear stress is observed around the outer abutment. And the outer abutmet tends to force the skewed flow back to the main channel and decrease the impact of the flow on the outer overbank. The effect of inner abutment is not obvious.

For over topping cases, the space under the deck is closed by the abutments and the bridge deck. The flow passing through this closed sapce will be pressurized and redistributed. At upstream side, there is no-slip boudnary only on the river bottom. The velocity is higher at the free surface. Under the bridge deck, there is no-slip boundary for both the top and bottom. So the flow will be squeezed to the center. The adjustment of the flow will take place at both vertical and horizontal direction. This adjustment will make the flow more uniformly distributed. This can be refected by the bed shear stress contours. For all the eight simulation results shown in Figures 5-34 to 5-38, the difference on the both sides of overbank under the bridge deck is not as large as open channel flow cases. The influence of abutment location on the bed shear stress distribution under bridge deck can not be observed under overtopping conditions.

At far downstream, the influence of the bridge deck is not strong. And the bend effect retakes the domination of the flow. For the cases with abutment in the middle of the channel bend, the asymmetric bed shear stress contours appear again. This is very close to the distribution observed in open channel flow cases. It is believed that the second half the channel bend after bridge causes the asymmetry of the flow. However, this asymmetry is not found for the results with abutment at the end of the channel bend.

This further proves that the bridge deck tends to make bed stress uniformly distributed and the channel bend tends to cause asymmetry.

5.5.4 Influence of abutment shape

The channel contraction ratio for current designed overtopping geometry is higher than the open channel conditions in section 5.4. According to the study in chapter IV, the bed shear stress is linear propotional to the channel contraction ratio. And the correction factor for wing-wall abutment is not sensitive with the change of contraction ratio. However, the correction factor for spill-through abutment will decrease with the increase of the contraction ratio. The constant correction factor is proposed in chapter IV for convenience. Hence, the maximum bed shear stress difference between wing-wall abutment and spill-through abutment cases will be enlarged with the increase of the contraction ratio. Table 5-9 lists the comparison of the maximum bed shear stress for wing-wall and spill-through abutment under overtopping conditions. Obviouly, the difference is larger than in open channel flow conditions.

Case #	$C_{f\ max\ WW}$	Case #	$C_{f\ max\ ST}$	$C_{f\ max\ ST}/ C_{f\ max\ WW}$
T4WW_Mid 1:1	0.0187	T4ST_Mid 1:1	0.0129	0.69
T4WW_Mid 2:1	0.0167	T4ST_Mid 2:1	0.0134	0.80
T4WW_End 1:1	0.0178	T4ST_End 1:1	0.0132	0.74
T4WW_End 2:1	0.0175	T4ST_End 2:1	0.0130	0.74

Table 5-9 Results of Wing-Wall abutment and Spill-Through Abutment.

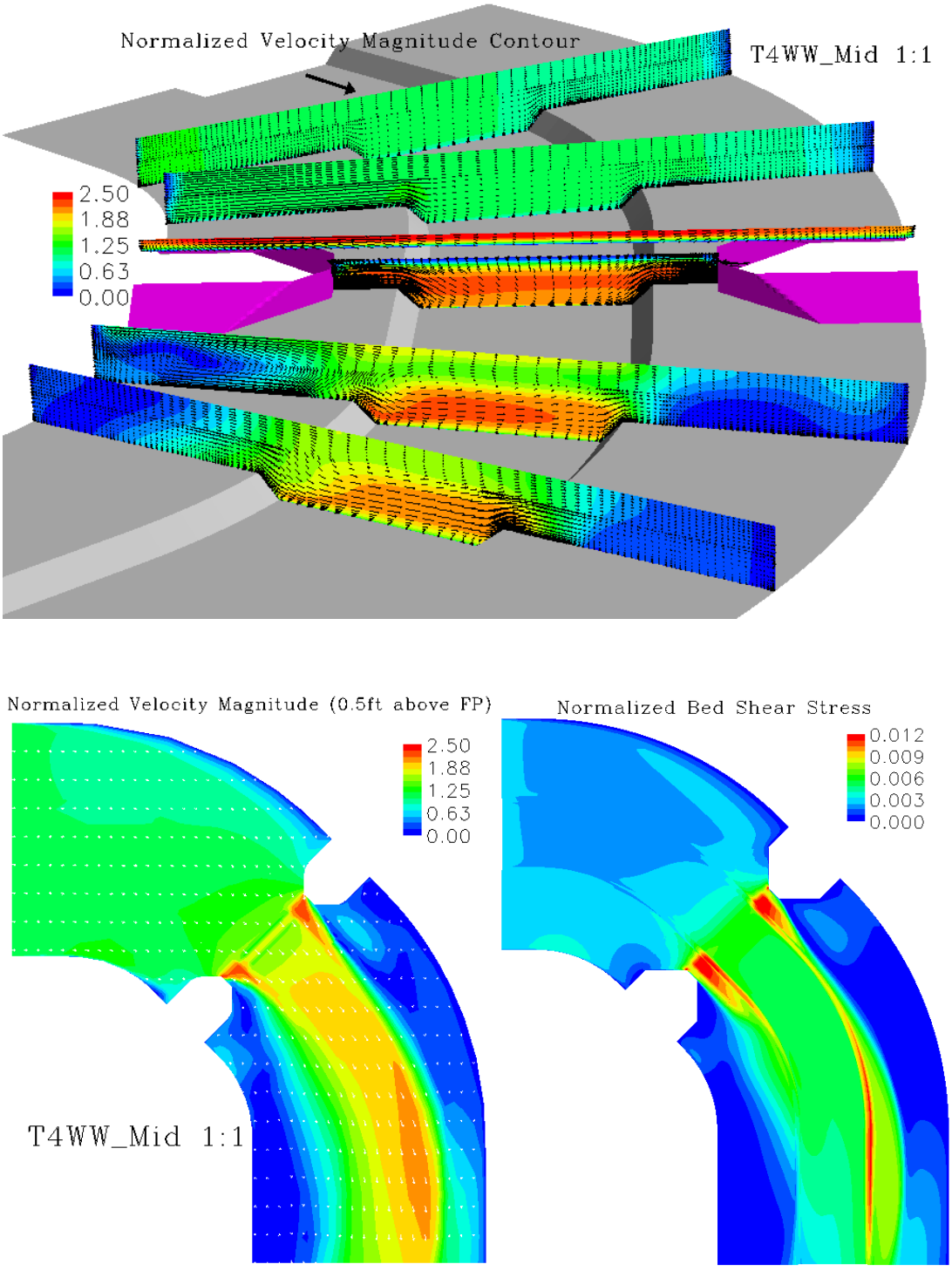

Figure 5-34 Simulation results of Case T4WW_Mid 1:1.

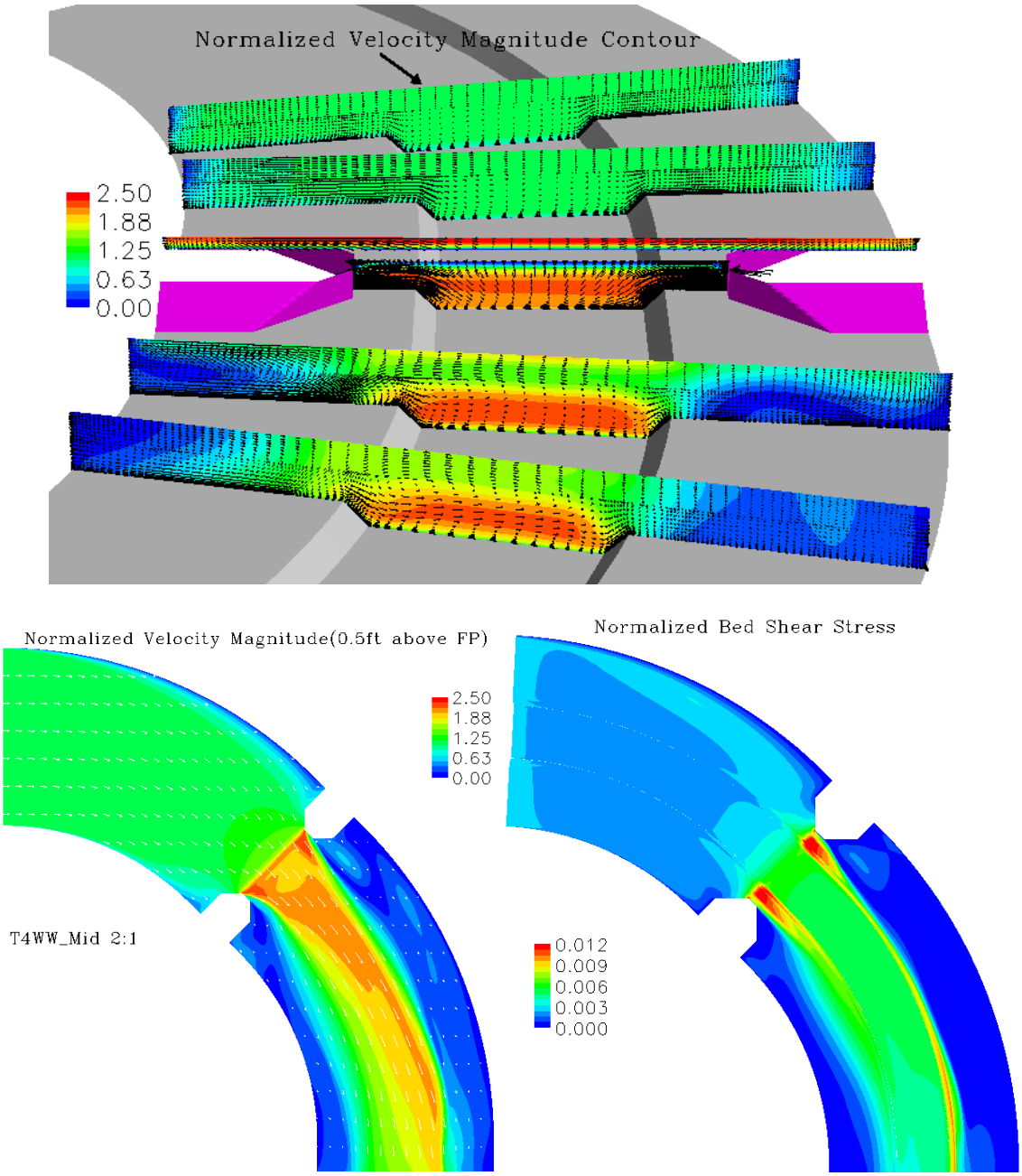

Figure 5-35 Simulation results of Case T4WW_Mid 2:1.

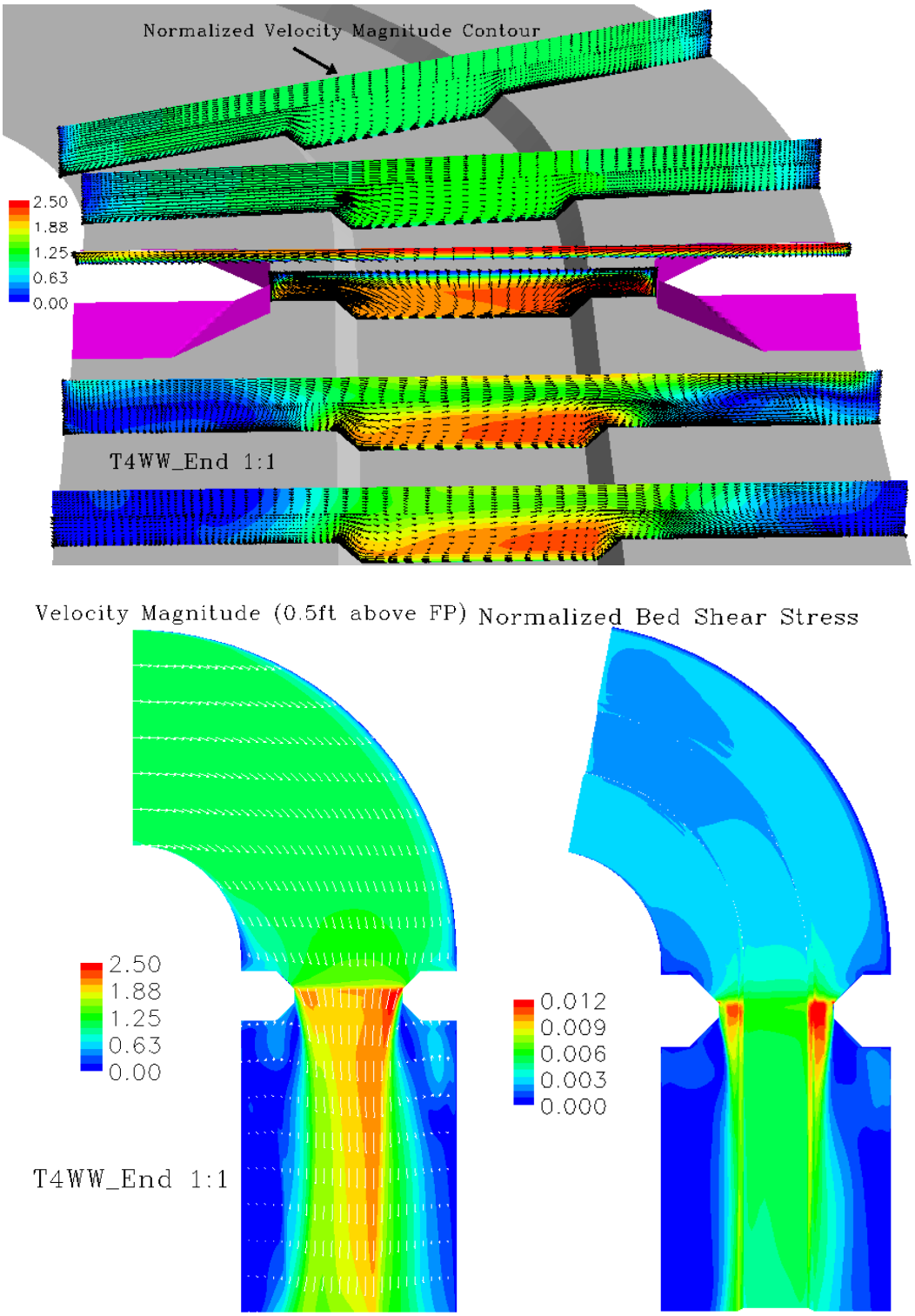

Figure 5-36 Simulation results of Case T4WW_End 1:1.

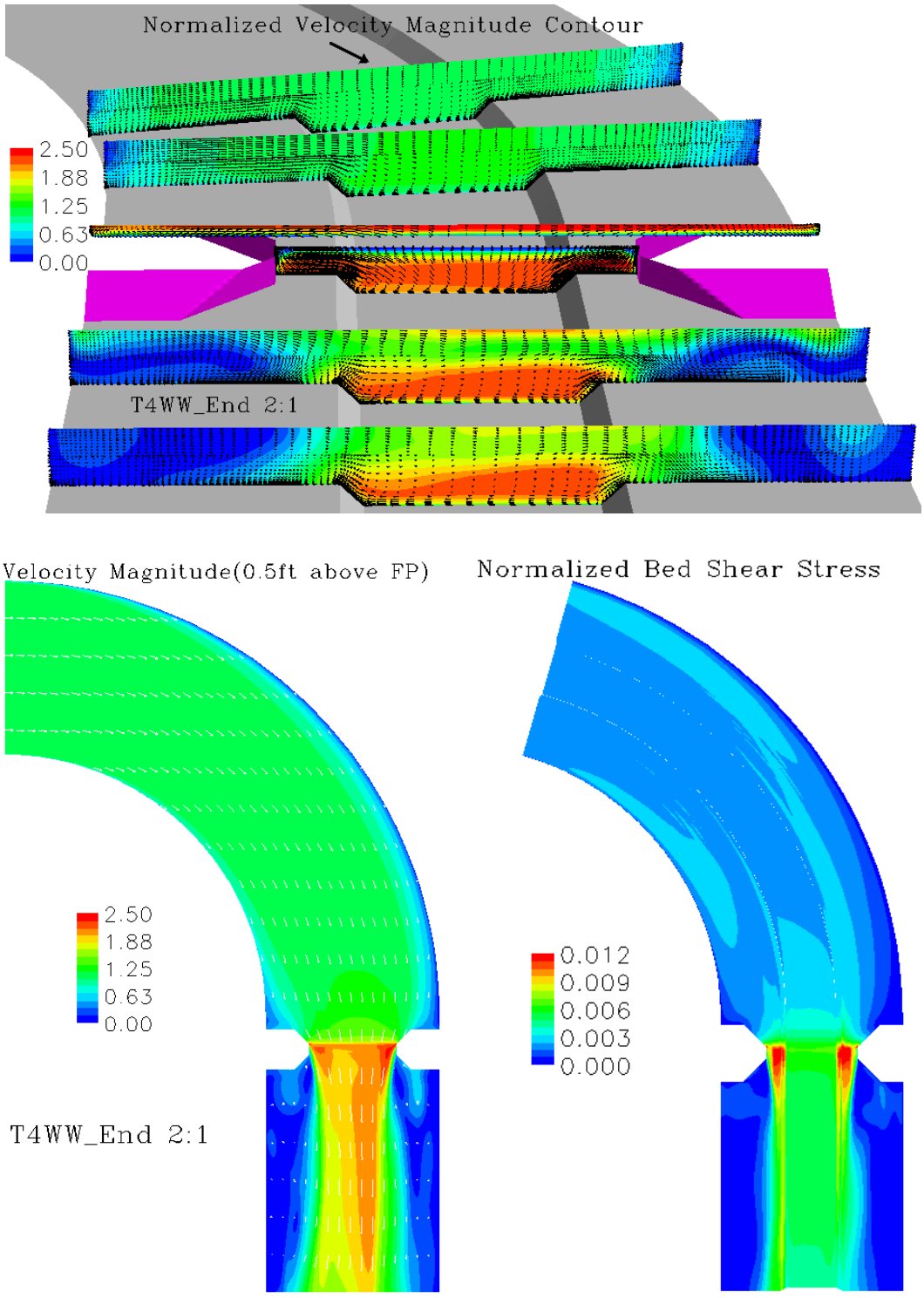

Figure 5-37 Simulation results of Case T4WW_End 2:1.

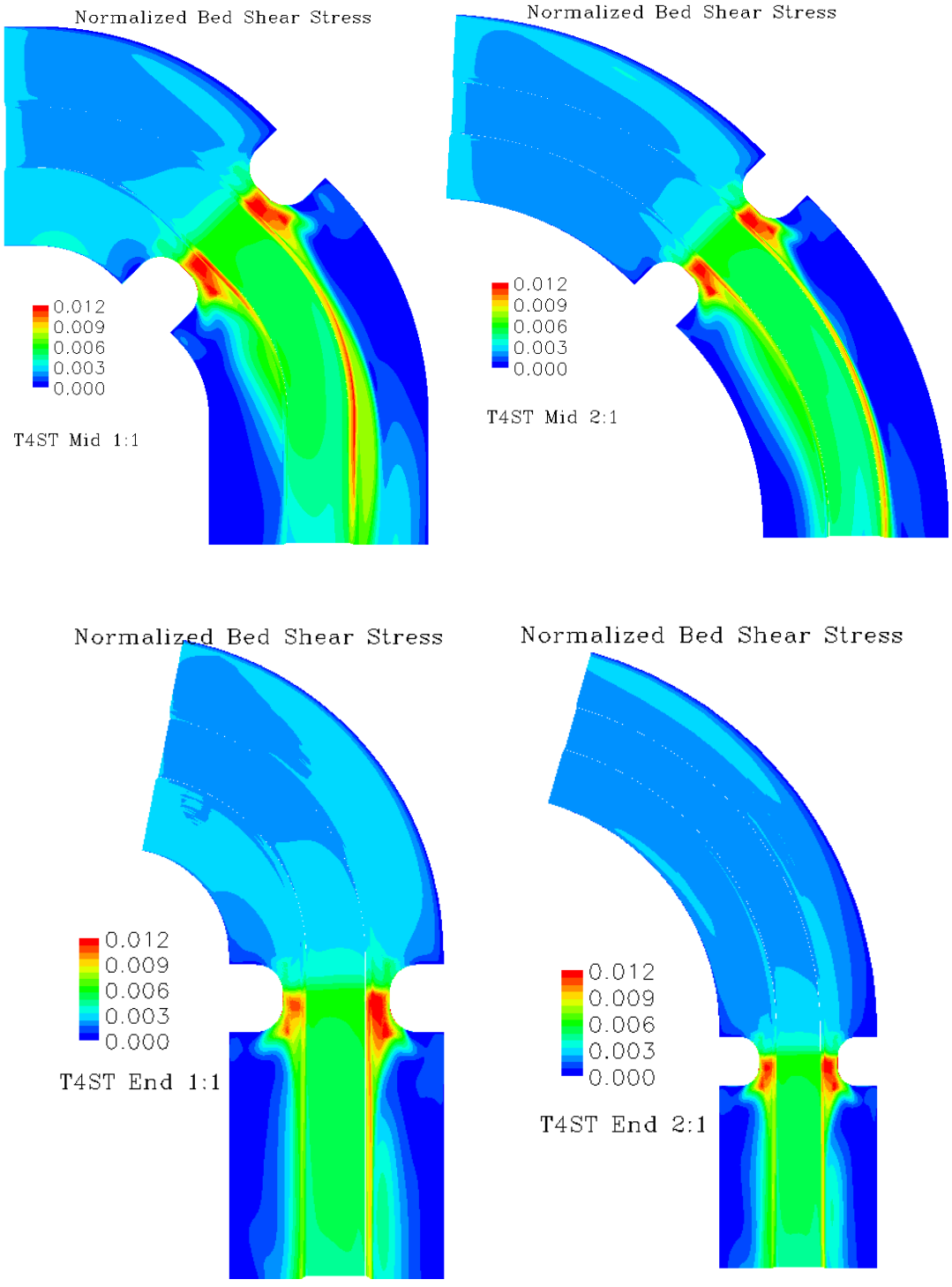

Figure 5-38 Normalized bed shear stress contours of the spill-through abutment cases.

5.6 Confluence of Tributary Upstream of a Bridge

Many situations can cause the asymmetric flow in channel. The confluence of tributary upstream is one of those. It is simulated by modifing the flume test Case 14 to include a tributary at upstream. The Case 14 is a symmetric channel. To simplify the study, overtopping is not considered. In techniqe, CHEN3D program is capable to handle the overtopping and confluence at the same time. In Case 14, the channel is rectangular of 24ft wide; abutment is 4.33 ft long of wing-wall shape; water depth is 1.2ft; approach velocity is 1.09 ft/s. To study the non-symmetric flow, the full channel is simulated instead of half channel as before. A tributary is added to the straight channel 24ft ahead of the abutment. The width of the tributary is 12ft. Water depth and velocity are all same to Case 14. The tributary channel is at an angle of 30 degree from the straight channel. Constant velocity is applied at the inlets of straight channel and the tributary channel. The free surface is assumed to be rigid lid.

Figure 5-39 shows the velocity magnitude contours on the free surface. It is expected to see the asymmetric contours. The shape of the contours depicts clearly the confluence of the flow from two inlets. The flow rate from the tributary is only half of the contribution from the straight channel. Obviously, the high flow rate component will dominate the direction of the confluence. The asymmetric flow starts from the confluence location and the high unit flow rate region gradually moves toward the channel center. When passing around the abutment, the highest unit flow rate is still on the tributary side. And the shape of the contours are quite different for two sides. The contours are in smooth transition around the lower abutment. This indicate that the lower

abutment has smaller influence on the flow. On the other side, there is sharp transition from the upstream corner of the abutment to the channel center. This shows that the upper abutemnt impacts the skewed the flow significantly. The higherst velocity appears at the downstream of the abutment, and the direction is relatively steady. The entire flow field at downstream is not in symmetry. The half straight chanel with tributatry has the higher flow rate. It is believed that the influence of upstream confluence will decrease with the increase of the distance between tributary to abutment.

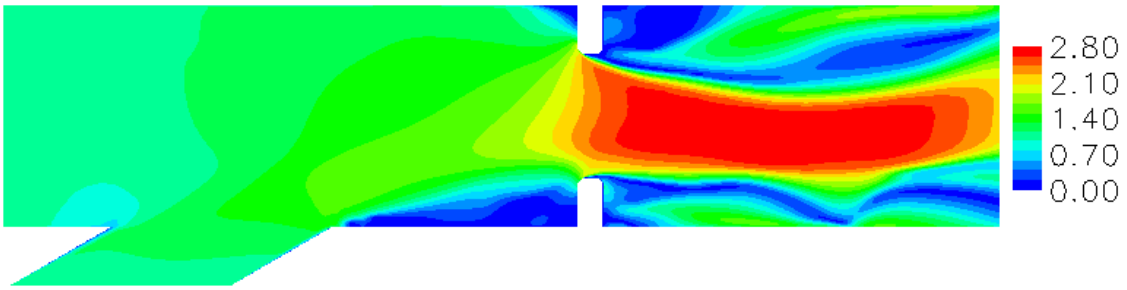

Figure 5-39 Velocity magnitude contours on the water surface.

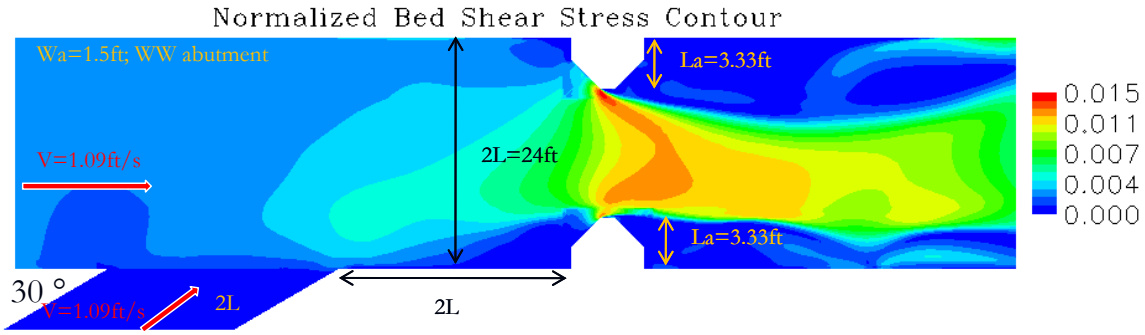

Figure 5-40 Normalized bed shear stress contours.

Figure 5-40 shows the bed shear stress contours. The pattern at upstream is very similar to the velocity magnitude contours on water surface. The bed shear stress is also

asymmetric. At upstream side, the high bed shear stress region start from the confluence location and skewed to the opposite abutment. The maximum bed shear stress appears at the abutment opposite to the tributary channel. At the downstream side, the bed shear stress contour skews back to the side of the tributary channel.

CHAPTER VI

ABUTMENT SCOUR IN COHESIVE SOILS

The main purpose of this section is to study scour model in cohesive soils and simulate the flume test cases in NCHRP 24-15(2). The numerical method described in chapter III has been applied to perform the simulations. There are two steps in scour prediction; first step is to establish the initial flow field without scour development; the second step is to simulate the scour process based on the scour model embedded in CHEN3D code. The second purpose of this section is to study the influence of overtopping flow on scour process in cohesive soils. Correction factors for overtopping flow have been proposed based on the numerical studies.

6.1 Soil Properties

Porcelain clay was used in the flume tests of NCHRP 24-15(2). Geotechnical tests were performed according to ASTM standards. The results of two testing have been tabulated in table 6-1. Erosion properties of the porcelain clay were tested through EFA (Erosion Function Apparatus). Eleven EFA testing were performed using tap water. These samples were from different testing conditions. The first testing was conducted with the fresh sample which should represent most of the clay used in the flume tests. The regression curve in figure 6-1 is based on the first EFA testing, which is used as the erosion function of the soils in all the numerical simulations of scour prediction. There were several samples taken from the clay stored for a long time or the leftover after the

flume tests. And they may have lower erosion rate because of losing water or some other reasons. This is shown in figure 6-1 with the data points scattering in a wide range.

Property	Test1	Test2
Liquid Limit (%)	30.9	29.8
Plastic Limit (%)	16.9	17.24
Plasticity Index (%)	14.0	12.56
D_{50} (mm)	0.004	0.003
Shear Strength (kPa)	13.5	15.3

Table 6-1 Soil properties of the clay used in NCHRP 24-15(2) (After Oh, 2008).

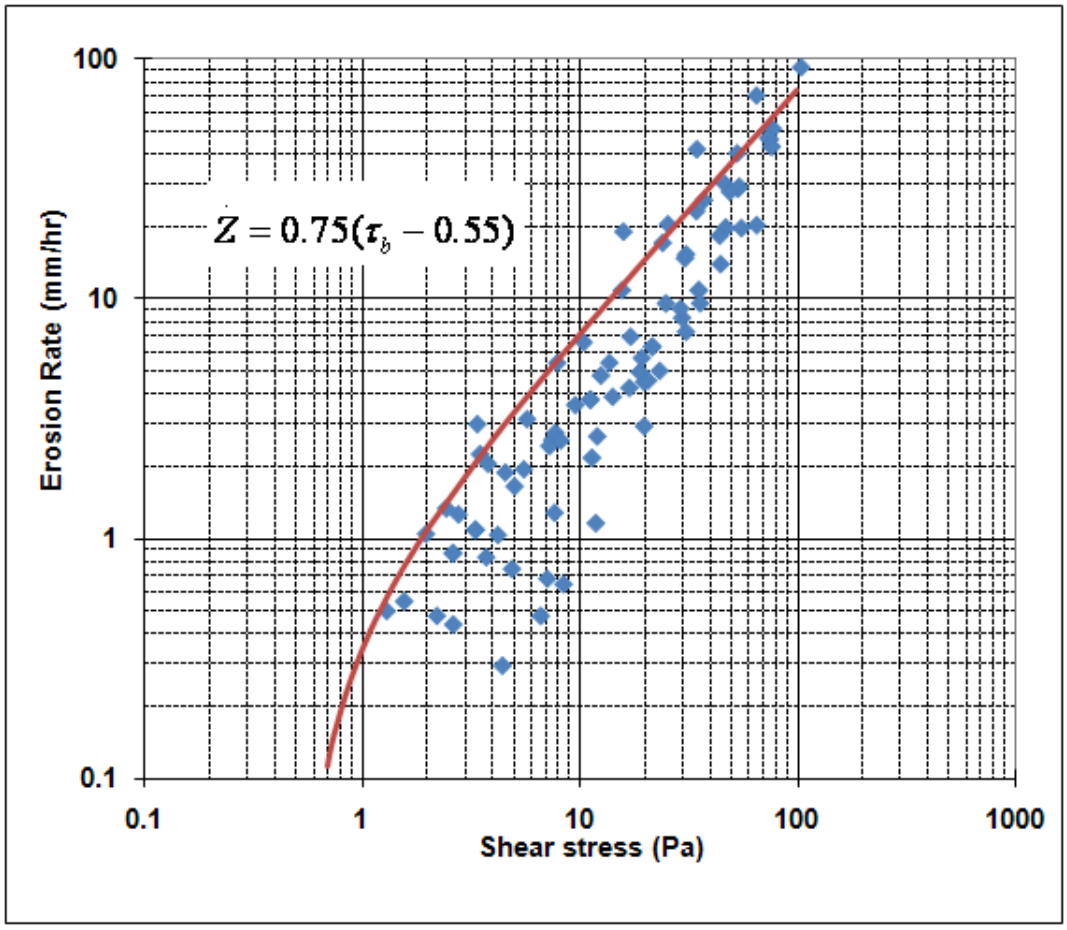

Figure 6-1 Relation between shear stresses and erosion rates (After Oh, 2008).

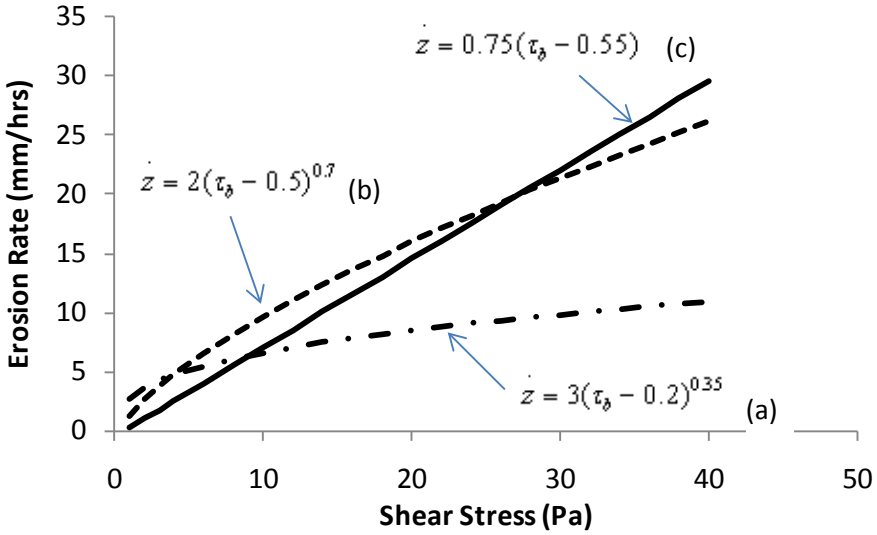

Figure 6-2 Comparison of erosion functions of porcelain clay.

Porcelain clay has been kept using in the studies of bridge scour in Texas A&M University (Briaud et al., 1999, 2001, 2003). Figure 6-2 shows the comparison of the EFA results for the porcelain clay used in simple pier scour (a), complex pier scour and contraction scour (b), and the abutment scour (c). The figure shows that the erosion function may be quite different even for the same kind of well controlled commercial clay. The clay used in current study has the lowest erodibility when the bed shear stress is less than 10 Pa; while the erosion rate will increase a lot faster than the other two clays when the bed shear stress is higher than 25Pa, which is hard to reach in the flume tests.

6.2 Scour Models in Cohesive Soils

The shear stress model mentioned in chapter II has been applied by Nurtjahyo (2003) to study pier scour and contraction scour. Soil erosion rate is assumed to be the function of shear stress applied on riverbed surface and the critical shear stress of the soils. According to Nurtjahyo's study, this shear stress model can provide reasonable

prediction for the deepest scour depth. However, the scour pattern is not in good agreement with the measurement. For example, in pier scour study, the maximum bed shear stress appears only in front of pier facing the flow where the flow is mostly accelerated. While in the wake region behind the pier, the bed shear stress is very low. Hence, the deepest scour hole can only be generated in front of the pier based on shear stress model. Actually, deep scour occurs at both upstream and downstream sides of the pier, where the magnitudes of the scour depths are similar in most cases. This indicates that bed shear stress is not the only contributor to the development of scour hole around hydraulic structure. A promising assumption has been proposed in Nurtjahyo's dissertation, which says that the turbulence could affect the scour development and its contribution might be as same as bed shear stress. Nurtjahyo further proposed a scour model including the shear stress and turbulent kinetic energy and performed the numerical studies with the new scour model. The maximum value of turbulent kinetic energy in the vertical direction above the bed at about 10% of water depth was used in the simulations. According to his study, the new model could generate deep scour hole at both upstream and downstream sides of pier, which is consistent to the finding in experiments. The scour model proposed by Nurtjahyo (2003) is as follows:

$$\dot{z} = \dot{z}(\tau_b, \tau_c, k) = c(\tau_b - \tau_c) + b \cdot k \tag{6.1}$$

Where, $\dot{z}$ is the erosion rate (mm/hour); τ_b is the bed shear stress (Pa); τ_c is the critical shear stress of the soils (Pa); c is the slope of erosion rate versus shear stress curve ($m^3/(N \cdot hr)$; k is turbulent kinetic energy $(m/s)^2$ and b is the constant (s/m).

In Nurtjahyo's study, the hydraulic smooth boundary condition has been applied throughout all the simulations. The influence of the surface roughness has been discussed in chapter V. In the verification case of overtopping, there is no scour during the testing and the roughness of the river bottom is constant. The bed shear stress in the roughened channel is amplified significantly compared to the result in the hydraulic smooth channel. As for clay, the soil particles are extremely fine, and the flat surface without scouring can definitely be taken as smooth. However, this is only suitable for the initial conditions of flume test. When scour developing, the surface of the channel bottom is no longer flat. This non smooth surface observed in cohesive soil channel is somehow similar to the bed form configuration on sand beds. And this is not believed to be able to predict with the roughness model used in chapter V since it is hard to determine the equivalent roughness of the bed form. To compensate the bed form effect, the correct factor β is used to augment the directly calculated bed shear stress from CHEN3D (with hydraulic smooth surface boundary conditions). Then, the shear stress model will be modified to be:

$$\dot{z} = \dot{z}(\tau_b, \tau_c, k) = c(\beta\tau_{num} - \tau_c) + b \cdot k \tag{6.2}$$

To determine the unknown parameters of β and b, the trial and error method has been used. As mentioned above, the shear stress is believed to be the dominant parameters in scour processing. Hence, the erosion function from EFA testing was trialed first with original shear stress model of $c = 0.75 mm/hour$, $\tau_c = 0.55$ Pa, $\beta = 1.0$, and $b = 0.0$ (called Model I). According to the trials, the predicted scour depth is

generally underestimated seriously. This is consistent with the fact of ignoring the contributions of bed form roughness and the turbulence. Then the calculated bed shear stress τ_{num} was scaled up by β. After several trials, β is found to be no more than 1.5. Otherwise, the scour depth on main channel will be too large. So Model II is defined with $c = 0.75 mm/hour$, $\tau_c = 0.55$ Pa, $\beta = 1.5$, and $b = 0.0$. With the correction factor of β, the deepest holes around abutment are still shallower than the measured results for most cases. This indicates turbulence properties should also be included to improve the scour pattern. For the normalized erosion function used in CHEN3D, term b = 0.01 is found to be able to yield the best prediction of the maximum scour depth around abutment. Model III is defined with $c = 0.75 mm/hour$, $\tau_c = 0.55$ Pa, $\beta = 1.5$, and $b = 0.01$. The application of these models will be given in the following section.

6.3 Scour Prediction of the Flume Tests in NCHRP 24-15(2)

The purpose of simulating flume tests is to study scour models and determine the unknown parameters. Five of seventeen flume tests (Oh, 2008) were selected to conduct the numerical simulations. To cover most parameters studied in the flume test matrix, two rectangular cases and three compound channel cases were chosen. The dimensional parameters of these five cases are tabulated in table 6-2.

Flume tests	L (ft)	L_m (ft)	L_f (ft)	L_a (ft)	y_f (ft)	V (ft/s)	Abutment Shape	θ (°)
Case 1	12	4	8	6	0.96	1.41	ST	90
Case 4	12	4	8	6	0.96	1.10	ST	90
Case 9	12	4	8	6	0.96	1.41	WW	90
Case 13	12	0	12	3.33	1.2	1.10	WW	90
Case 14	12	0	12	5.33	1.2	1.10	WW	90

Table 6-2 Dimensional parameters for the cases selected for scour prediction.

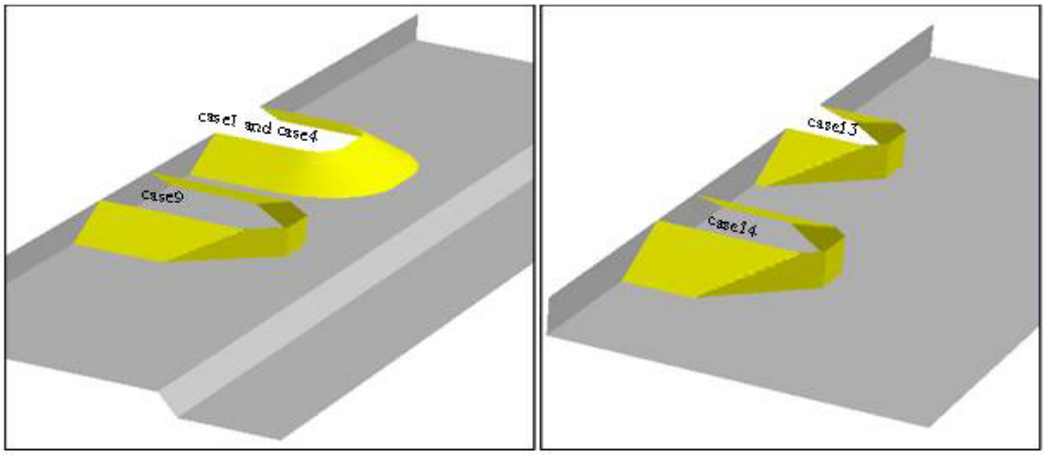

Figure 6-3 Geometries of the flume test cases for scour prediction with CHEN3D.

Case 13 and Case 14 are in rectangular channel as shown in figure 6-3, having the same water depth, approach velocity, and wing-wall abutment. The abutment in Case 14 is two feet longer than that in Case 13. The influence of channel contraction ratio on scour development can be investigated based on these two cases. The other three are compound channel cases, having the same abutment setback of L_a/L_f = 0.75. The influence of approach velocity on scour process can be studied by Case 1 and Case 4 because they have the same parameters except velocity as shown in table 6-2. Case 9 has wing-wall abutment. It is performed to study the influence of the abutment shape on the scour. All the other parameters like the channel geometry, water depth, abutment length, and approach velocity are all kept same to Case 1.

Two steps procedure is used in the scour development. First step is to calculate the fully developed flow field without scour development, and then the second step is to simulate scour processing based on the first step flow field. Same dimensionless time increment 0.2 has been used in both of the two steps. In the second step, one time step is

defined as 2.5 minutes. And accordingly the slope in the erosion rate equation is adjusted. The assumption is that the scouring process in a short time, like 2.5 minutes, is very small and its influence to the flow field can be negligible.

6.3.1 Scour prediction on compound channel

Figure 6-4 Scour patterns for the cases on compound channel (After Oh, 2008).

1) Observations from the flume tests

Figure 6-4 shows the scour patterns of the three compound channel cases. The observations from the flume tests are summarized in the following:

1. Deep scour hole can be observed at the abutment toe for all three cases. In Case 9 and Case 1, the scour hole in front of the abutment face extends from the toe all the way to the main channel. And the flood plains together with the main channel slope in front of the abutment face are totally removed. In Case 4, however, the scour hole

around that abutment toe is limited on the flood plain and the main channel slope including part of the flood plain is still remained after two weeks' scouring.

2. At the downstream side, the original main channel slope was completely washed away for Case 1 and Case 9 after the testing. And the bottom was eroded to the same level as the main channel or even lower for Case 1. The main channel slope regresses toward the over bank to the location in line with the abutment toe. As for Case 4, the erosion of the original main channel slope was not very serious. The scour hole started from the upstream corner of the abutment and extended toward downstream main channel slope, which shows the skewed flow stream lines forced by the abutment. However, this trend is not observed in Case 1 and Case 9 when the approach velocity is higher.

3. The surface of the channel bottom after scouring is not as smooth as the initial conditions. In the region without obvious erosion, like the upstream part far from the abutment and the flood plain behind the abutment at downstream, the surface is still flat. As for the region with serious erosion, the bed surface is highly uneven.

4. Main channel has much smaller scour depth than main channel slope and flood plain. The scour hole on the main channel slope can be as deep as the hole at the abutment toe.

2) Simulation result and analysis of Case 9

Figure 6-5 shows the plan view of the measured and simulated scour patterns of Case 9 after 240 hours. The comparison of three scour models will be conducted one by one in the following:

Compare to the measurement, Model I generated smaller eroded area, which indicates the calculated bed shear stress is less than the real bed shear stress applied by the flow. As mentioned before, this difference might result from the effect of bed form roughness. Turbulence should not relate with this issue since it contributes only the specific area and will not affect the main channel much. The deepest scour hole with model I is on the main channel slope with the depth of 0.4ft, which is about half of the measured deepest scour depth. However, the deepest scour hole observed in the flume test is at the downstream corner of the abutment, which could not be observed from this simulation.

Model II shows similar eroded area to the measurement. In most area, the simulated scour depth is in good agreement with the measurement, especially for the contraction scour in main channel. This proves that the bed form roughness should be considered in scour model. However, the deepest scour depth, mostly concerned in bridge design, could not be matched by scaling up the calculated bed shear stress uniformly.

For model III, the plan view shows that the scour pattern can be improved compared with model 1 and model 2. The deep scour holes can be found in front of abutment face and on main channel slope. And the magnitude of the maximum abutment scour depth is very close to the measurement. However, the kinetic energy model contributes to not only the scour around abutment but also the scour in the main channel. It makes the scour prediction on the main channel higher than the measurement. Hence, the turbulence term in the model still needs to be further studied.

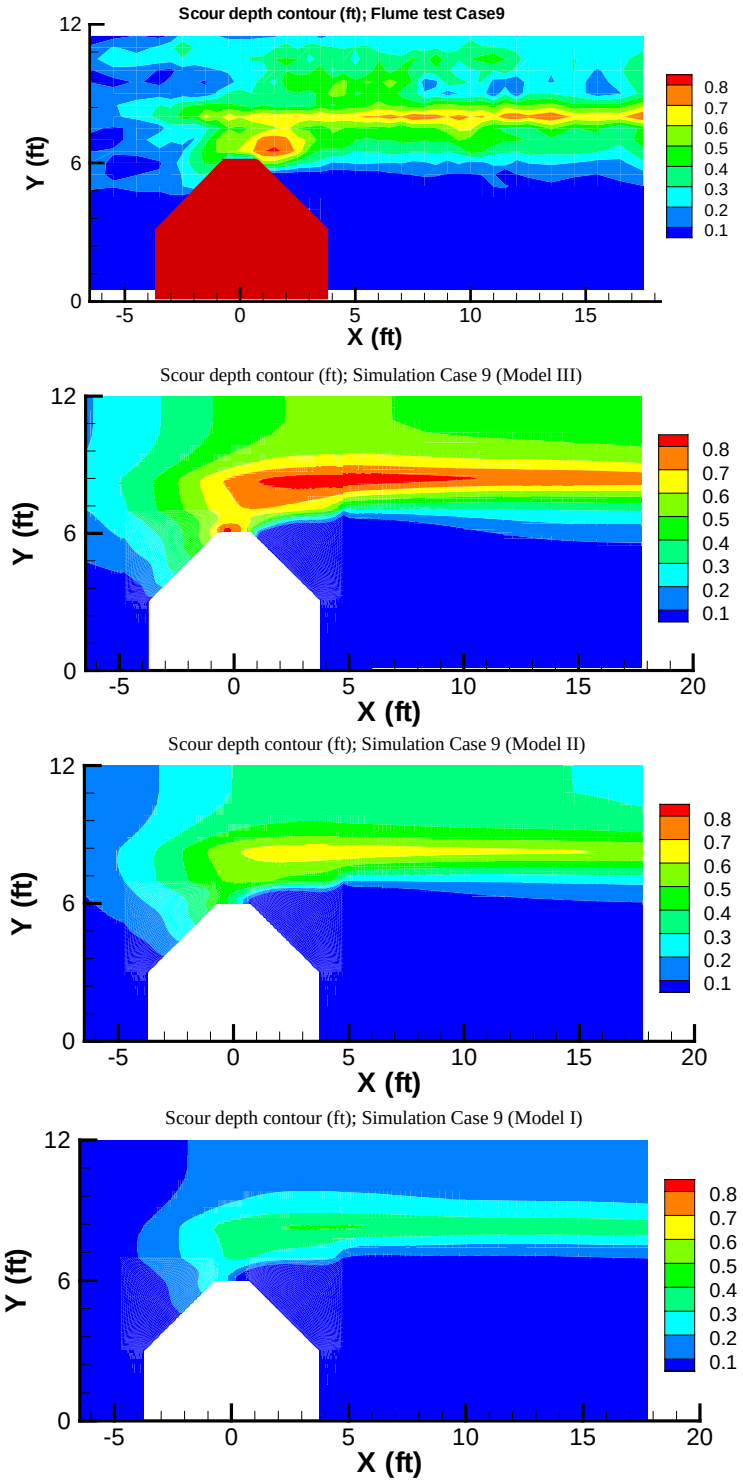

Figure 6-5 Scour depths after 10 days for different scour models (Case 9).

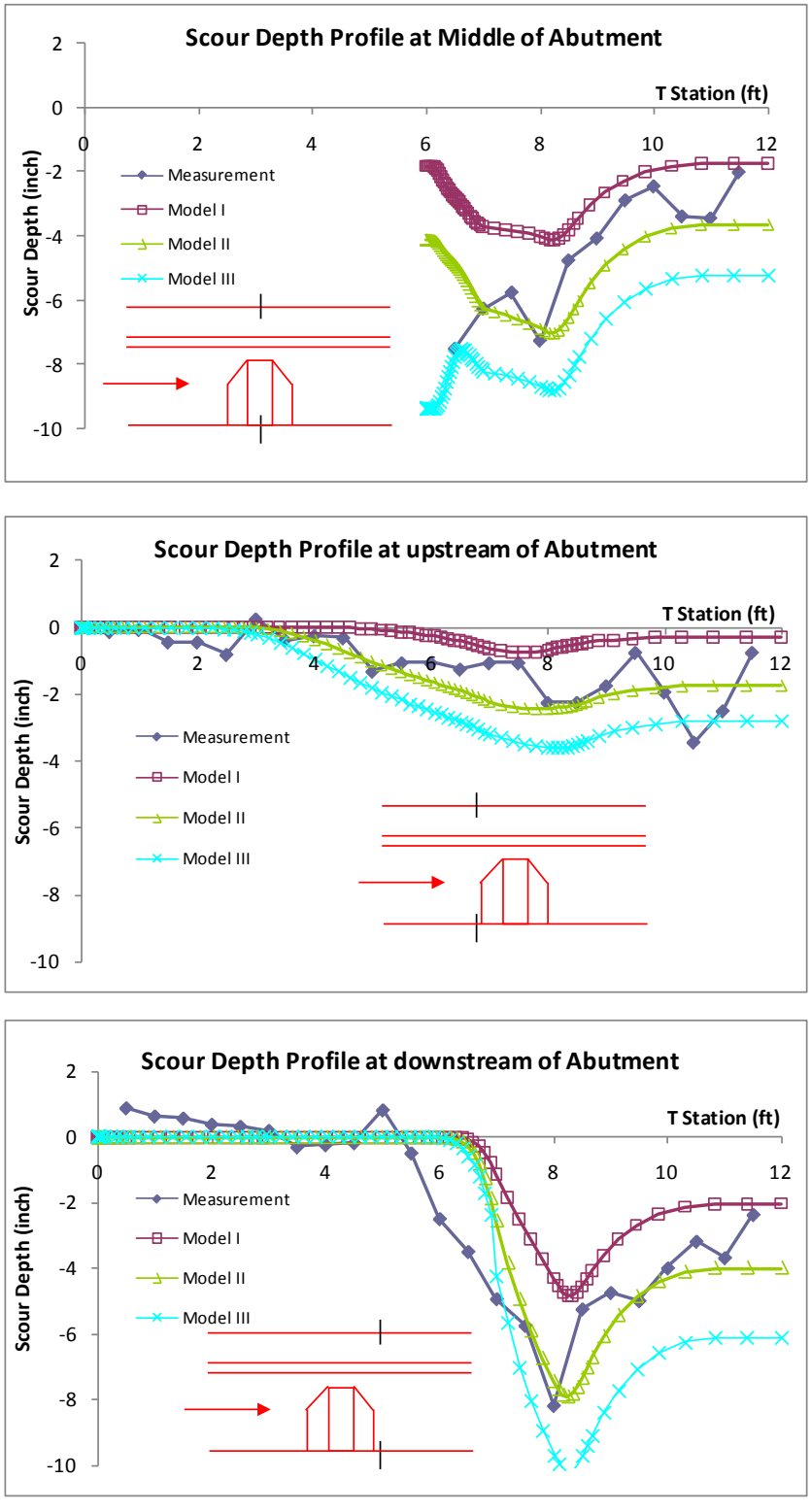

Figure 6-6 Scour profiles for Case 9 after 10 days at different cross sections.

Figure 6-6 shows the comparison of the predicted scour depth profile to the measurement at different cross sections. These three cross sections were selected around the abutment at upstream side, in the middle, and at downstream side of the abutment. The deepest scour may occur at other locations. However, the scour pattern around abutment is most concerned in the engineering practice.

At upstream side of the abutment, the flow starts to accelerate at the opening part of the channel and slow down at the region blocked by the abutment. The measured scour depth in the opening part from T station 6ft to 12 ft is about 2inches. Actually, the erosion begins from 4.5 ft where the flow begins to be squeezed into the unblocked area. Model I underestimates the scour depth along the entire cross section. Prediction of model II is very close to the measurement. And Model III predicts higher scour depth in most area. But both model II and model III can reflect the trend correctly at upstream.

In the middle of the abutment, the measured scour depth is about 8 inches at the abutment toe and about 3 inches on the main channel. It should be noted that the scour is deep on location of main channel slope from T station 8ft to 8.67 ft, which is consistent with the bed shear stress trend. Model I still underestimates the scour depth. Model II yields good prediction in most part except at abutment toe. For model III, the predicted scour depth increases entirely across the channel. The advantage is that the kinetic energy term can generate the deep scour hole at the abutment toe.

At downstream side of the abutment, the measured scour depth behind the abutment from 0ft to 6ft is negligible. The deepest hole appears on the main channel slope of 8 inches. The contracted scour depth on the main channel is about 4 inches. All

three models can predict trend correctly. And the best agreement is given by scour model II.

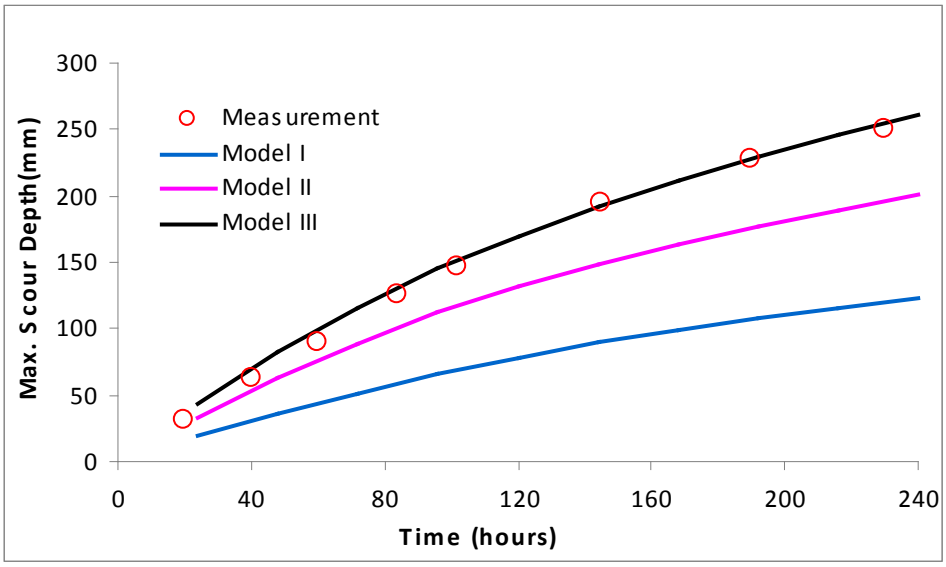

Figure 6-7 Maximum scour depths history for Case 9.

Usually, the most concerned is the deepest scour depth, which is needed in the bridge design and analysis. All the abutment scour equations listed in HEC-18 intend to predict only the value of Z_{max} and have nothing to do with the scour pattern. Hence it is necessary to study Z_{max} as well as studying the scour pattern. Figure 6-7 presents the comparison of the simulated Z_{max} over time based on different scour models. The Z_{max} in figure 6-7 is the deepest scour depth at each time instant; the location of Z_{max} is not constant over time. For Case 9, the deepest hole is always in front of the abutment face according to the flume test, although the scour on the main channel slope is also very deep. As expected, the model with the correction of bed form roughness and kinetic energy could match the measurement very well in the point of Z_{max}.

3) Simulation result and analysis of Case 1

Figure 6-8 shows the scour profiles at same three cross sections. The trends of the simulation results are basically similar to the measurements. Model I underestimates the scour depth at all three cross sections. Model II could generate closer prediction to the measurements at upstream and in the middle of the abutment. This time, the deep scour depth at the abutment toe can be observed from the simulation. However, the scour hole on the main channel slope could not be captured clearly. At downstream side, model II yields similar trend to the measurement. But the magnitude is a lot lower. Model III, in this case, increases the scour depth in the entire opening part and has little improvement on the scour pattern. This can only provides better prediction on the flood plain at the downstream cross section. But, the prediction on the main channel is much larger than the measurement. Overall, the simulated scour depths for Case 1 are smaller than the predicted in Case 9. This is consistent with the widely accepted conclusion that wing-wall abutment can generate deeper scour depth than spill-through abutment. CHEN3D simulation could reflect this trend very well.

It should be noted that the profile at the downstream part for Case 1 is very strange. The scour hole on the main channel slope is as deep as 13 inches. While the deepest hole at abutment toe is only about 5 inches. The deep hole may come from the non uniform of the soil properties and the testing setup. The porcelain clay used in the flume test may not be in the same batch. So the erosion properties may not be consistent like discussed in the soil properties section. And during the experiment setup, the compaction may also cause problem. There is the possibility that the downstream main

channel slope is not compacted as well as other regions. The conditions will be quite different if there is space left in between the clay blocks.

Figure 6-9 shows the measured plan view of the scour pattern and the prediction with scour model III. According to the measurement, there is a larger area on the downstream main channel slope with very deep scour depth. This is identical to the profile in the transverse profile. This is not the typical trend in abutment scour. At the abutment toe, the scour hole can still be found to be deep. It is not very obvious compared to the hole on main channel slope. And these two holes are almost connected. According to the numerical simulation with model III, there are two deep scour holes. One is around the abutment toe on flood plain; the other one is on the main channel slope. There is always a deep scour hole on the main channel slope no matter what kind of abutment exists. This is identical to the shear stress prediction. Along the center of the main channel, the predicted scour depths at upstream and in the middle of the channel are larger than the measured values. But they are closer at far downstream area.

Figure 6-10 shows the comparison of the maximum scour depth history of the measurement and the results of the three models. The reading is from the deep hole on the main channel slope close to the abutment. As discussed above, this is not the general trend. Hence, all these three models can not underestimate the maximum scour depth seriously, as shown in figure 6-10.

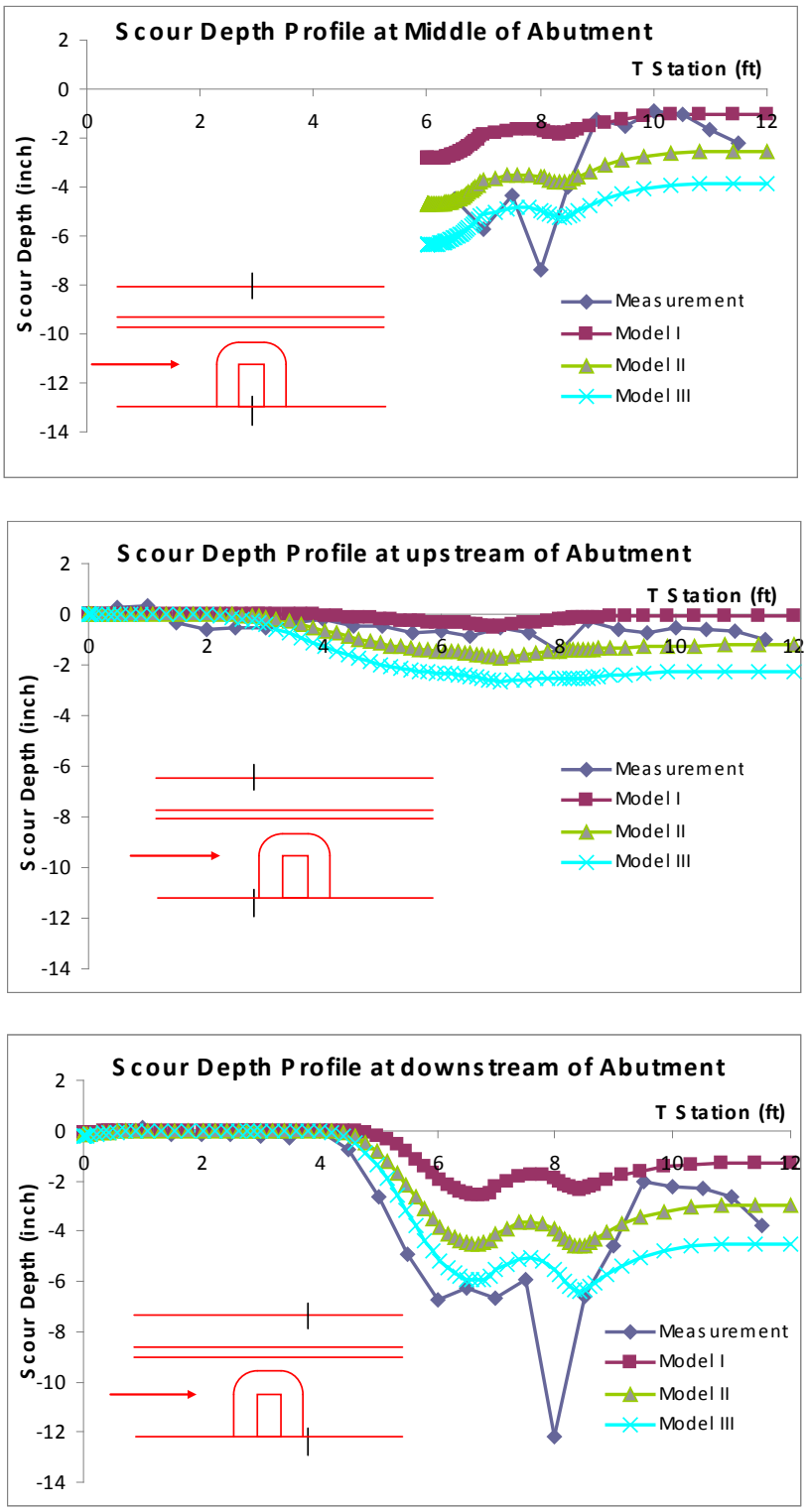

Figure 6-8 Scour profiles for Case 1 after 10 days at different cross sections.

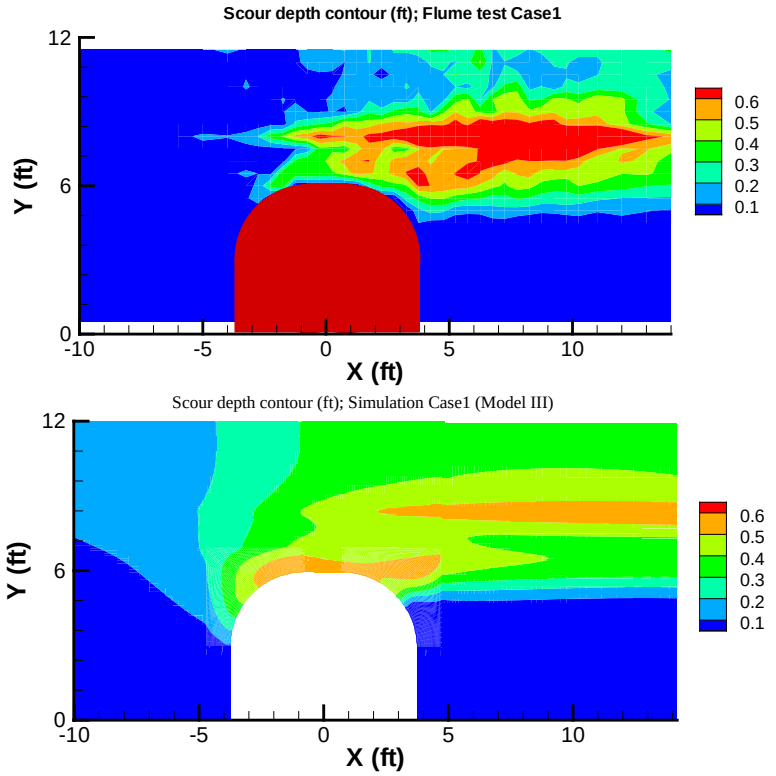

Figure 6-9 Scour depths for case 1 after 10 days for different scour models.

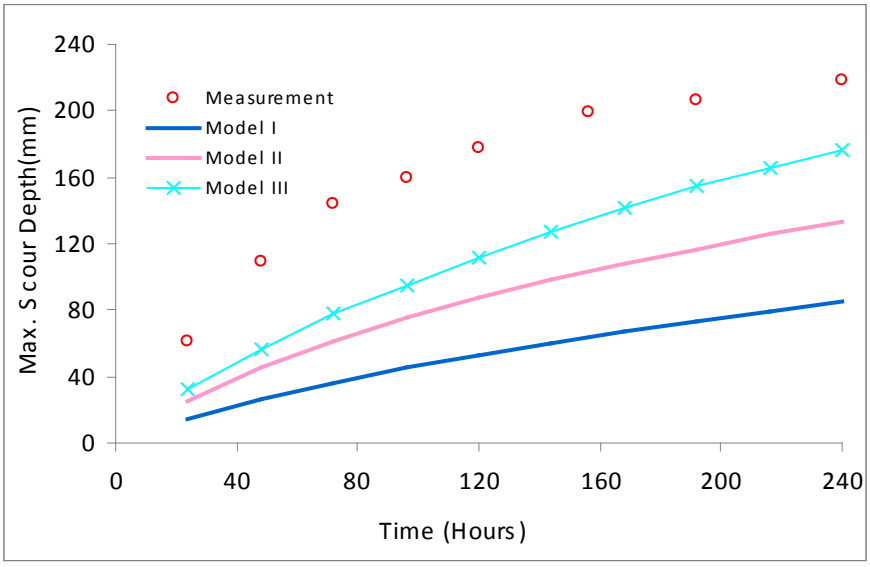

Figure 6-10 Maximum scour depths history for Case 1.

4) Simulation result and analysis of Case 4

Figure 6-11 shows the scour profiles of Case 4. Case 4 has lower approach velocity than Case 1 and Case 9. According to figure 6-11, scour depths for both the numerical simulations and the measurements are smaller than the corresponding conditions in Case 1. This is consistent with the influence of the velocity. At the upstream side, all three scour models underestimates scour depth. This is opposite to the finding in Case 9 and Case 1. In the middle of the abutment, all these three scour models can predict the deep scour hole at abutment toe. But the predicted scour depths on main channel are quite different from each other. Actually, the measured scour depths on main channel for upstream and middle of the abutment are very close. It indicates the abutment on flood plain has little influence on main channel. At downstream, both scour model I and II can predict close result to the flume test. Scour model II can be closer on the main channel. Scour III can match the deepest scour hole very well. But the prediction on the main channel is too large.

Figure 6-12 shows the comparison of the plan views of the measured and simulated scour pattern. The scour model predicted two scour holes at the abutment toe and on the downstream main channel slope. In the flume tests, there are deep scour holes observed at the same locations. However, the eroded area from the prediction is much larger than the measurement.

Figure 6-13 presents the comparison of the maximum scour depth history. The Z_{max} can be predicted very well with scour model III.

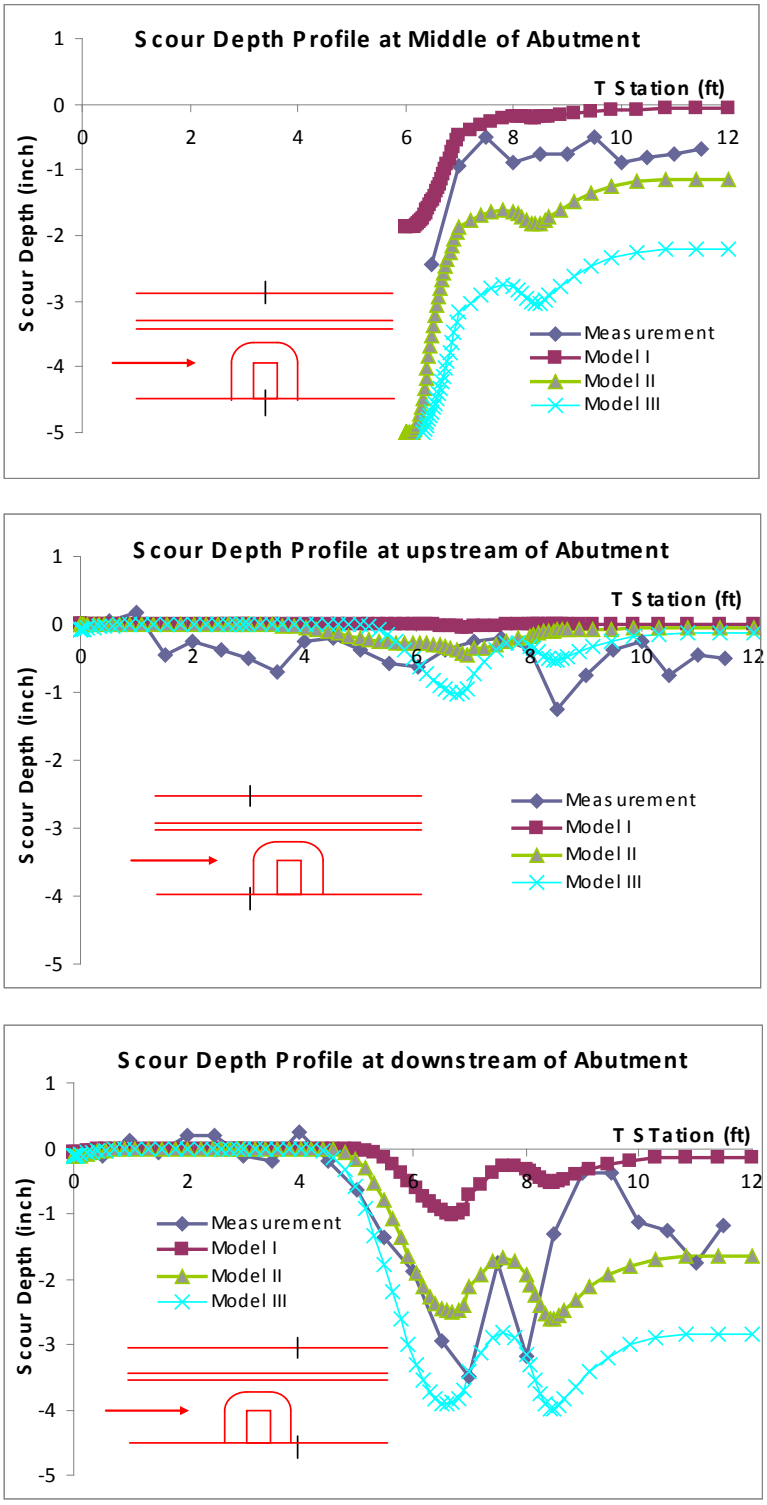

Figure 6-11 Scour profiles for Case 4 after 9 days at different cross sections.

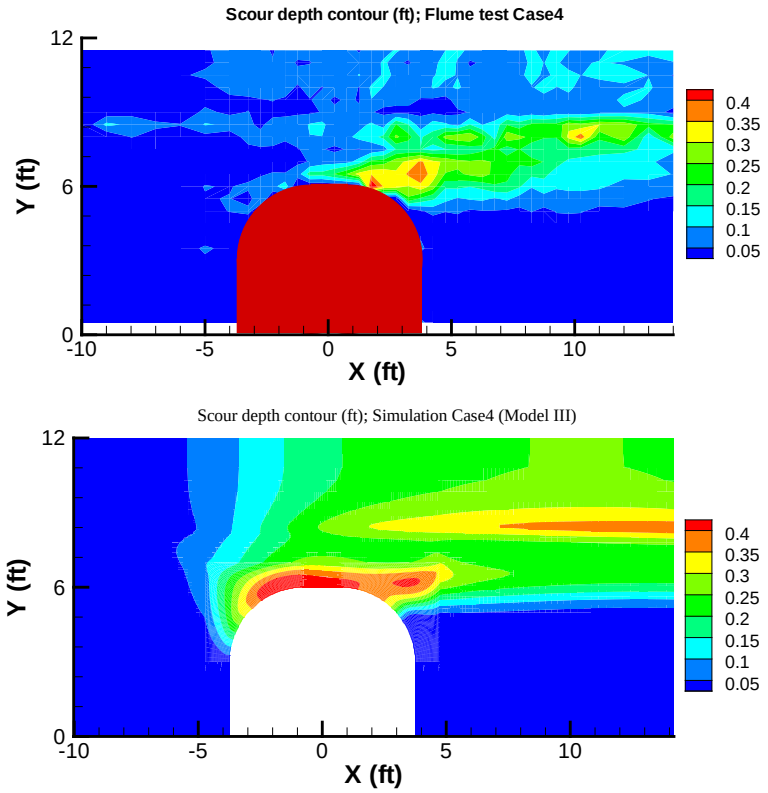

Figure 6-12 Scour depths for Case 4 after 9 days for different scour models.

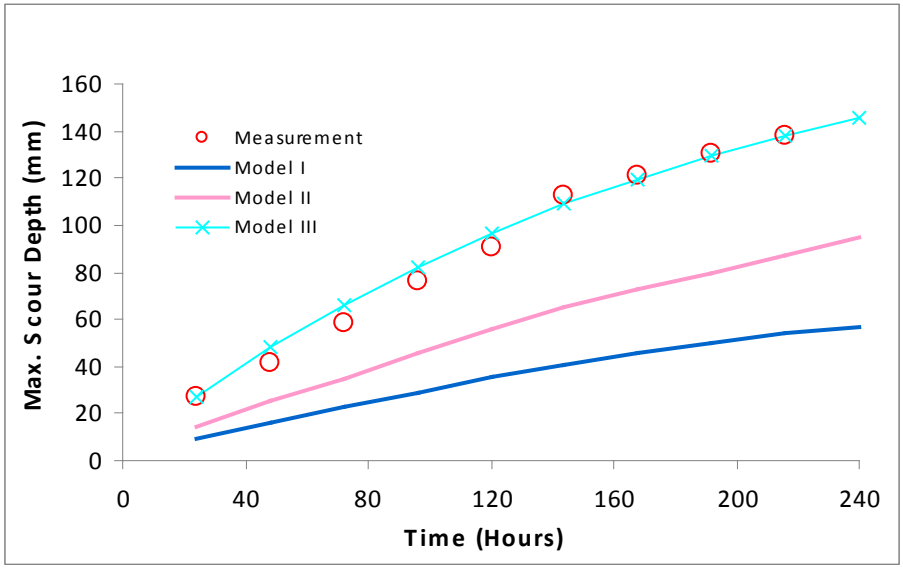

Figure 6-13 Maximum scour depths history for Case 4.

5) Conclusion of the scour simulations on compound channel

Deep scour depth on main channel slope results mainly from the local high bed shear stress, which can be captured by the shear stress term in scour model;

Deep scour hole at the toe of the abutment results from both the local high bed shear stress and the turbulence properties. The bed shear stress can only yield the scour hole at the upstream corner of the abutment. Actually, in most cases, the deep hole exists at the downstream corner. This is not fully solved so far even if including the turbulent kinetic energy into the scour model.

6.3.2 Scour prediction on rectangular channel

Figure 6-14 Scour patterns for the cases on rectangular channel (After Oh, 2008).

1) Observations from the flume tests

Figure 6-14 shows the scour patterns of the two rectangular channel cases. The observations from the flume tests are summarized in the following:

1. For Case 14, deep scour hole can be observed at the abutment toe. The scour hole extends from the upstream corner of abutment toward downstream for a long

distance. The scour depth along the channel center is smaller than the scour hole around the abutment. The bed surface after scouring is uneven as shown in the picture.

2. For Case 13, the scour hole is shallower at the toe of the abutment than at downstream. However, this is not believed to be normal and repeatable. Many reasons can cause this problem, like bad compaction and non uniform clay. Contrary to the other cases, the bed surface of Case 13 is still very smooth after the testing.

2) Simulation result and analysis of Case 14

Figure 6-15 shows the scour depth profiles. At upstream side, the scour depth is very uniform, about 0.7 inches in the open area. In the middle of the abutment, the scour depth at the channel center is about 2 inches. The scour hole is as deep as 7.5 inches around the toe of abutment. At downstream, the scour depth at channel center is about 2.5 inches. And the deep hole extends downstream in line with abutment toe. The blockage effect of abutment on the contraction scour is clearly observed according to the scour depth variation along the channel center. The deepest contraction scour depth occurs at the downstream instead of the middle of the abutment. This shows the delay of the flow contraction against the channel contraction. The contracted scour depth is predicted well by scour model I in the profiles. However, around the abutment toe and at the wake region, the model has to be modified so that the prediction can match the measurement. Scour model II and III can get closer scour depth to the measurement around the abutment. But they overestimate the contraction seriously. The corrections of roughness and turbulent properties are required in theory. However, further research need to be conducted to study how the scour model should be constructed to represent

the erosion rate in all area, not just the location of most concerned by the engineering application.

Figure 6-16 shows the comparison of the measured scour depth contour and the predicted contour with scour model III. The deepest scour hole around abutment has been captured by this model. In the flume test, the deepest hole is at downstream corner of the abutment. But the predicted one is at the upstream corner of the abutment, where is the location of the maximum bed shear stress. This indicates that the shear stress term is still dominant in the computation. Although the turbulence kinetic energy has been included in the computation, the improvement on the scour pattern is not as significant as Nurtjahyo's pier study. The eroded area from scour model III is found to be larger than the actual measurement. And the contraction scour at the channel center is much higher than the flume test as shown in the profiles.

Figure 6-17 presents the comparison of the measured maximum abutment scour depth history to simulated results with three scour models. The most concerned maximum scour depth can be predicted very well with scour model III. The other two models predicted much smaller scour hole. It proves again that current scour model is not perfect and can only be used to estimate the maximum value after carefully tuned.

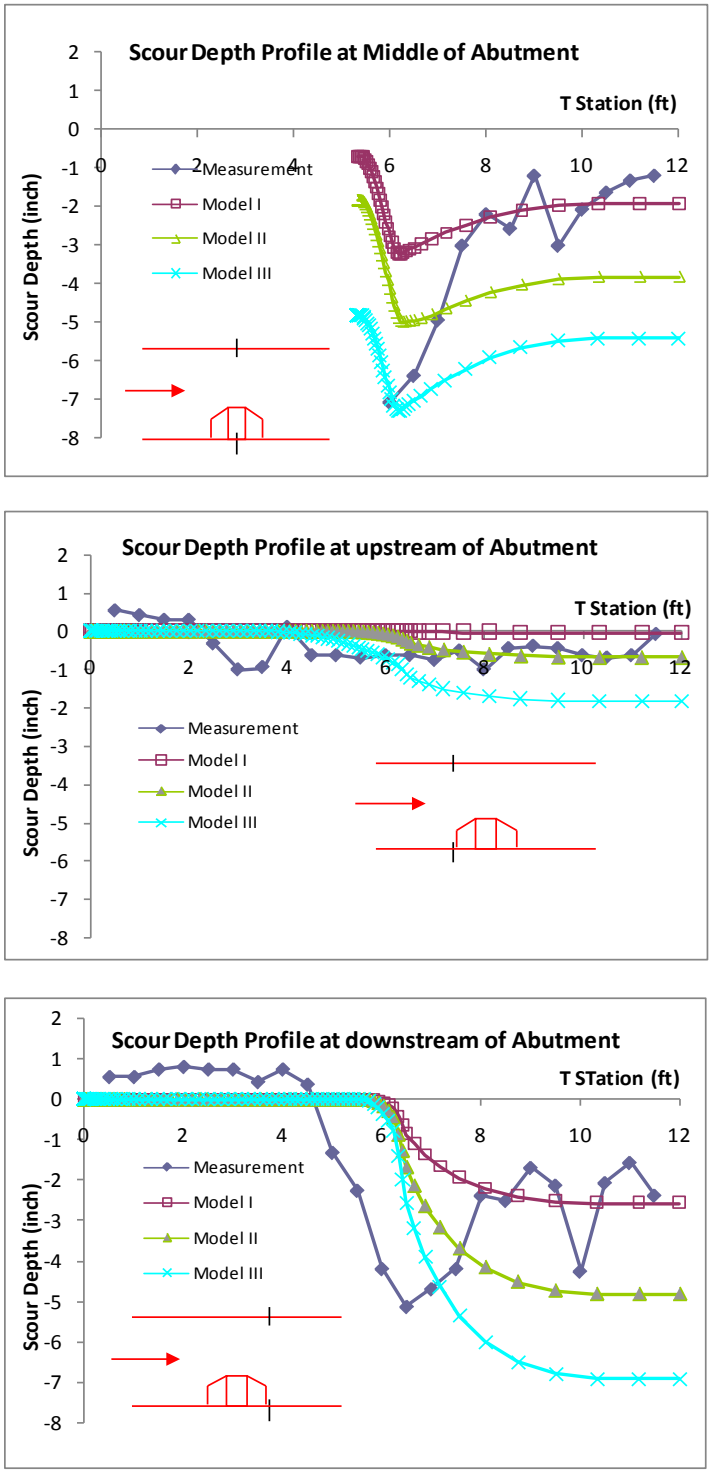

Figure 6-15 Scour profiles for Case 14 after 10 days at different cross sections.

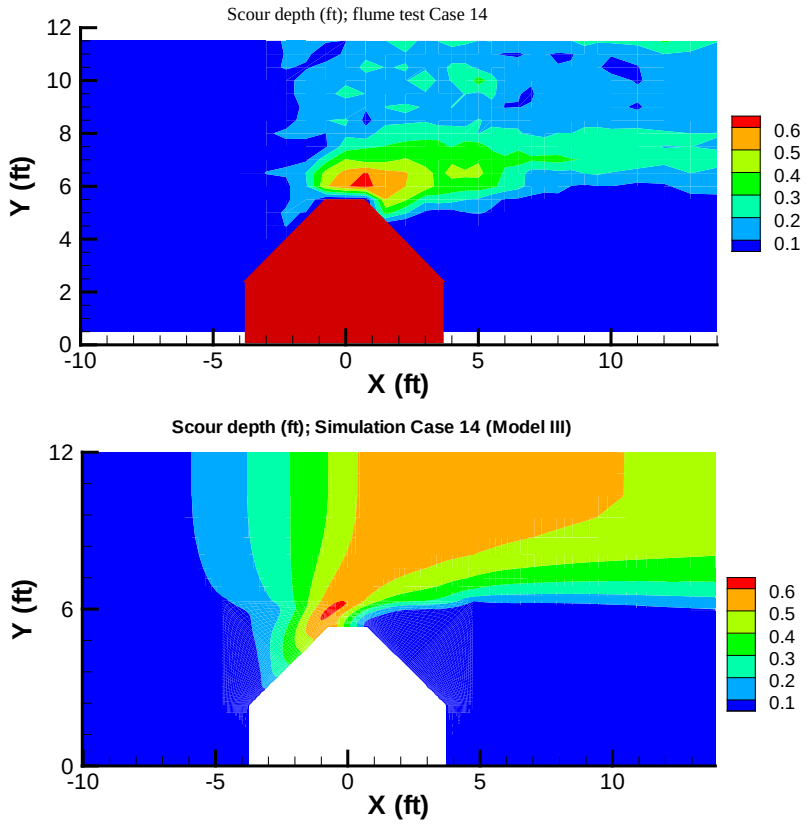

Figure 6-16 Scour depths for Case 14 after 10 days for different scour models.

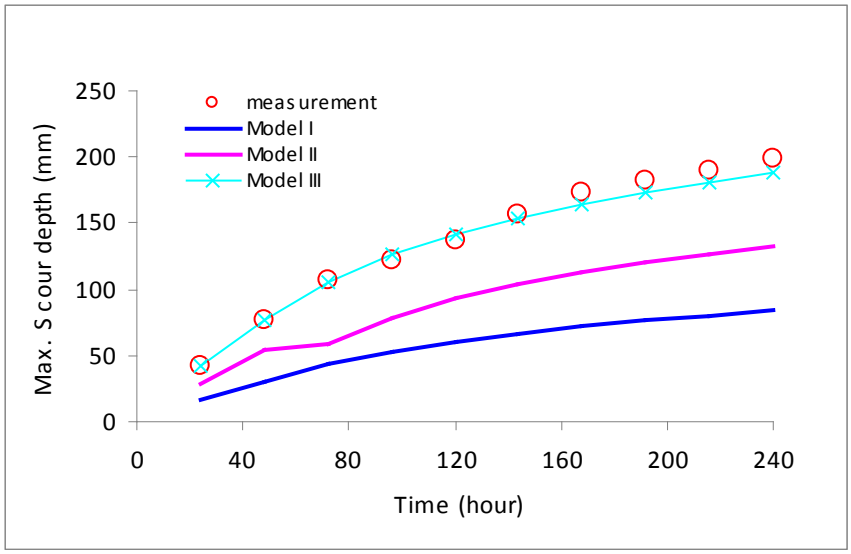

Figure 6-17 Maximum scour depths history for Case 14.

3) Simulation result and analysis of Case 13

Case 13 is a low contracted case and with the designed approach velocity of 1.1ft/s. According to EFA testing, the critical velocity of the porcelain clay is about 2ft/s, defined as the velocity generating 0.1mm/hour erosion rate. So, the accelerated flow around abutment in Case 13 may still lower than the critical velocity. After 10 days, the deepest scour depth is about 40mm at the abutment toe, which turns out to be close to the erosion under the critical velocity.

As shown in Figure 6-18, the scour profiles of scour model I are close to the measurement. Model II overestimates the scour depth too much. This is expected since the river bed surface for Case 13 is still smooth after the testing (shown in Fig 6-14). Hence, the correction of the bed form roughness should not be applied in the simulation. Model III is not tried for this case. The simple superposition of kinetic energy term to the shear stress term will further increase the scour depth in the entire region. This case indicates that the influence of turbulence is negligible when the erosion rate is not large. The shear stress term and the turbulent term may not function independently. This may explain why scour model III tends to overestimate contraction scour.

Figure 6-19 shows the comparison of scour depth contours. This case proves the consistent of EFA testing and the shear stress model in the ideal testing conditions (little influence of roughness and turbulence). Once the contraction is higher, the flow tends to be more turbulent and the bed surface tends to be more irregular. Then Model I will not be able to predict the scour process very well.

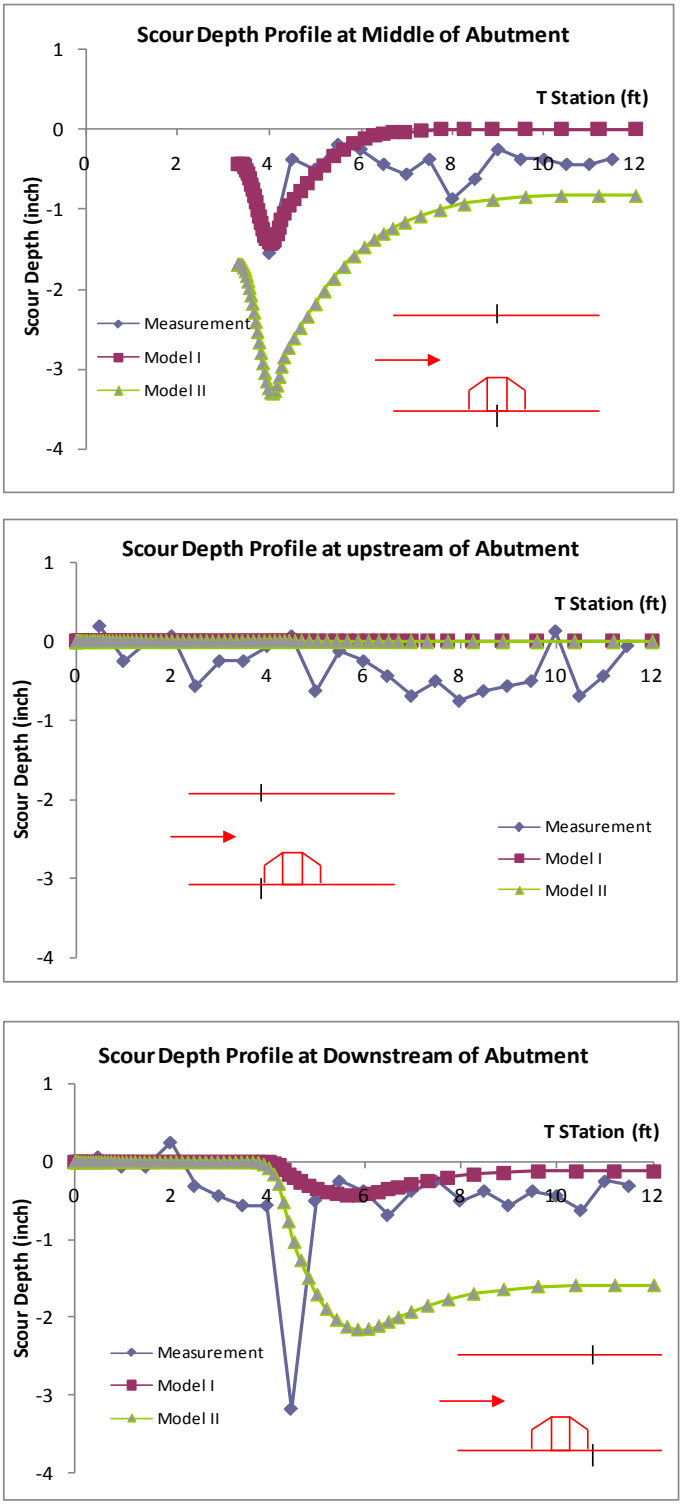

Figure 6-18 Scour profiles for Case 13 after 10 days at different cross sections.

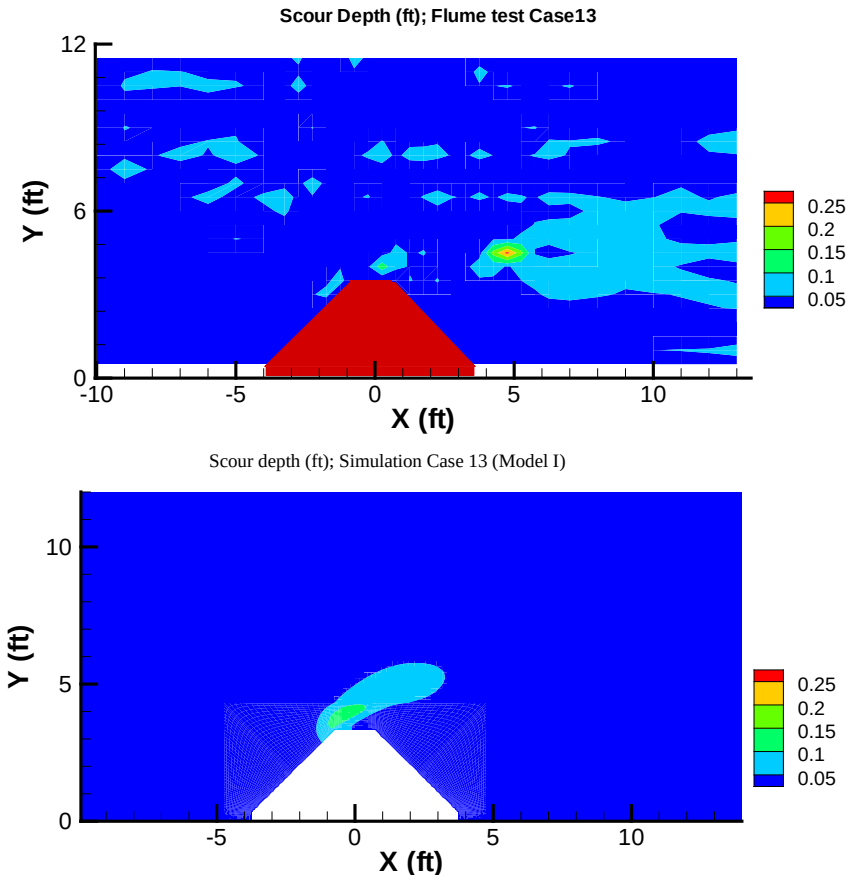

Figure 6-19 Scour depths pattern for Case 13 after 10 days.

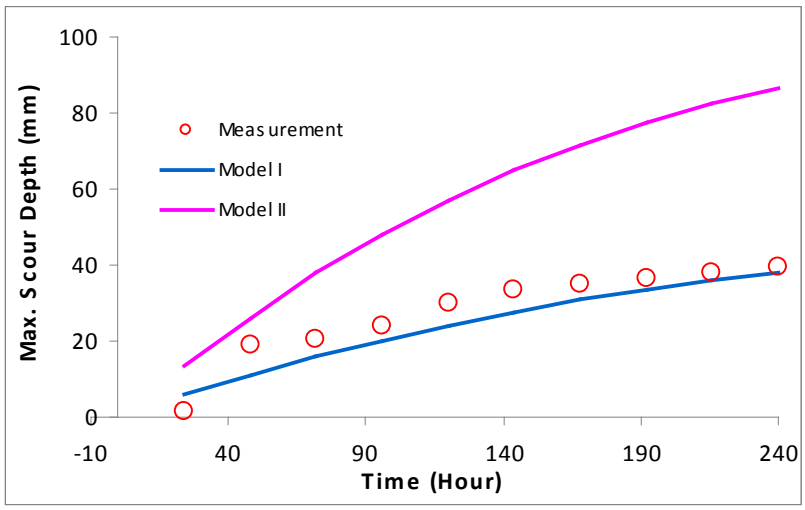

Figure 6-20 Maximum scour depths history for Case 13.

Figure 6-20 shows the variation of the maximum scour depth at the toe of the abutment over time. The shear stress model without correction can predict the measurement very well.

4) Conclusion of the scour simulations on rectangular channel

1. The corrections of roughness and turbulence are required when the contraction effect of abutment on the rectangular channel is large enough. And scour model III is still applicable in rectangular channel.

2. Scour model I is applicable to predict the maximum abutment scour depth only when the bed surface is very smooth and the turbulence is not strong.

6.4 Scour Prediction with Overtopping

Abutment scour under overtopping flow conditions is studied numerically. The purpose is to get the basic knowledge about the scour development when the flow is pressurized under the bridge deck. In the numerical study, the bridge is designed with 0.4ft thick deck and 1.2ft clearance. Vertical wall abutment is chosen in the overtopping flow study. The approach velocity is 1.09 ft/s; the abutment is 3.33ft long; the half width of the channel is 12ft. For the same designed bridge and above mentioned parameters, seven cases have been conducted with the upstream water depth varying from 1.2 ft to 2.8 ft. Figure 6-21 shows the cross sections and the velocity magnitude contours of four representative cases. Case (a) has open channel flow and water surface is almost touching low chord; Case (b) is the case with water surface just touching low chord. Case (c) has water surface in flush with deck surface; Case (d) has water surface

elevation 0.4 ft over the bridge deck surface. The other three cases are of the upstream water depth of 1.4 ft, 2.4 ft, and 2.8 ft.

Rigid lid is applied on the water surface. The scour model I has been applied in the scour development with the same erosion function from EFA testing as used in the simulations of flume tests cases in NCHRP 24-15(2).

$$\dot{z} = c(\tau_{num} - \tau_c) \tag{6.3}$$

Where, $\dot{z}$ is the erosion rate (mm/hour); τ_{num} is the directly calculated bed shear stress (Pa); $\tau_c = 0.55Pa$, the critical shear stress of the soils (Pa); c = 0.75mm/(Pa*hour) is the slope of erosion rate versus shear stress curve ($m^3/(N \cdot hr)$).

Same two steps procedures have been used. First step is to calculate the fully developed flow field; the second step is to develop scour based on the first step flow field. Same dimensionless time increment 0.2 has been used in both of the two steps. As pointed out by (Nurtjahyo, 2003), it is not practical to resolve the vortex shedding in the simulation of the scour process. To save the computation time, the flow field is assumed to be constant during short erosion time period. In the second step, one time step is defined as 2.5 minutes. And accordingly the slope in the erosion rate equation is adjusted.

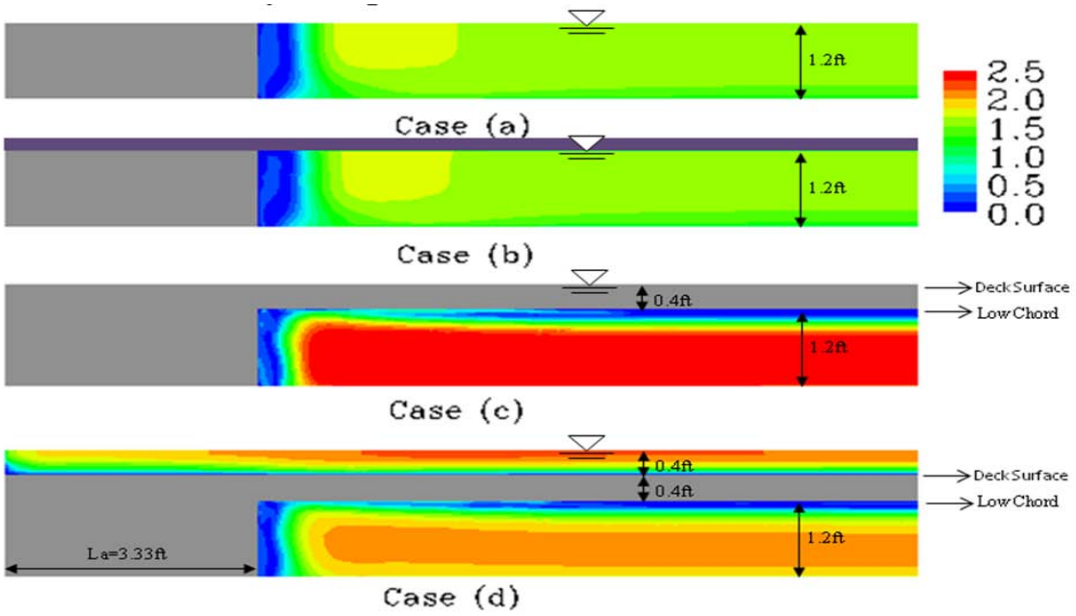

Figure 6-21 Cross sections and the velocity magnitude contours.

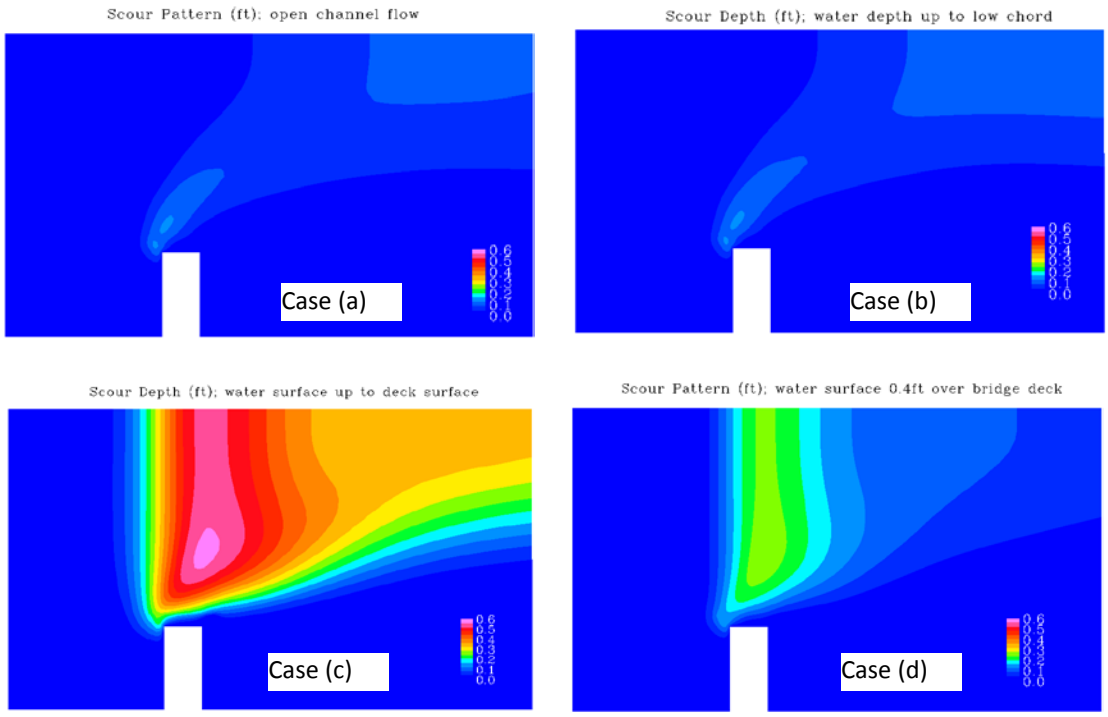

Figure 6-22 Scour depth contours for overtopping cases.

Figure 6-22 shows the scour depth contours of the four representative cases. These are the simulation results after 10 days. The only difference between Case (a) and Case (b) is the water surface boundary conditions. Case (a) has the symmetric boundary condition applied in the entire water surface; while Case (b) has no slip boundary condition applied at the area touching low chord instead of rigid lid. It turns out that the change of boundary condition on low chord area has little influence on the scour development. This is consistent with the finding in the bed shear stress study in chapter V. The scour depths of Case (a) and (b) are very shallow and the deepest scour holes are located right at the upstream corner of the abutment. Meanwhile, the contraction scour can be observed at downstream channel center. Under the bridge deck on the channel center, there is no sign of scour hole. Case (c) is the case of highest blockage when flow is pressurized. All the flow above the low chord is forced to go through under the bridge deck. According to the scour contours, the river bed under the bridge deck is eroded seriously. The influence of the bridge deck is on the entire cross section, not just around abutment. And the scour depth does not vary too much along the transverse direction under the bridge. The deepest hole in Case (c) is not as adjacent to the abutment as in Case (a) and Case (b). Case (d) is the case with bridge deck totally immersed in the flow. And part of the flow blocked by the bridge deck will go over the deck, which can release the pressure under the bridge. Figure 6-21 shows that scour depth in Case (d) is shallower than Case (c) and still deeper than Case (a), (b). This is expected according to the bed shear stress and the scour model I. Similar to Case (c), the deepest scour hole in Case (d) is not very close to the abutment. And the contraction scour under the bridge

deck is also well developed. However, the affected area at downstream is quite smaller compared with Case (c). When overtopping, the influence of the bridge deck is also on the entire cross section.

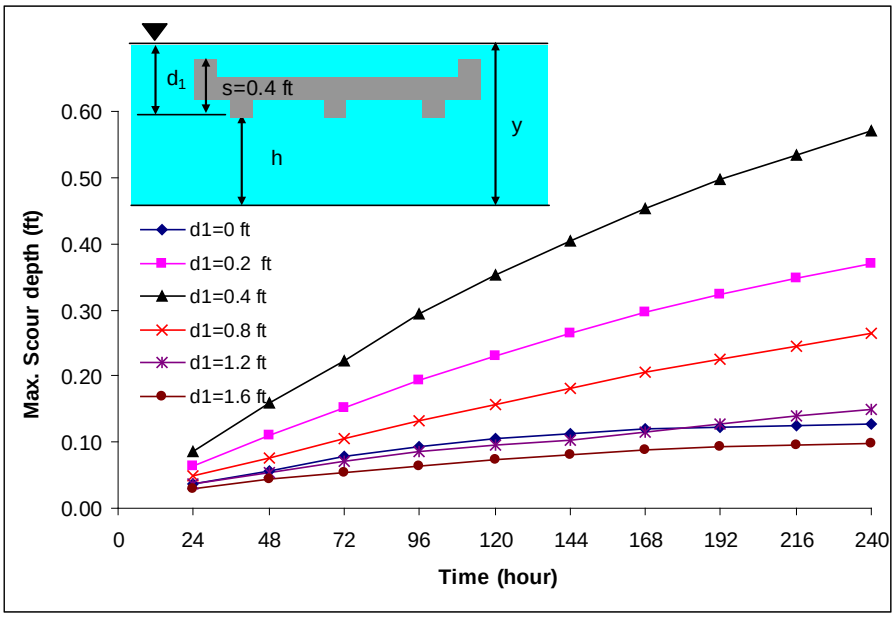

Figure 6-23 Scour histories of the simulations with overtopping flow.

Figure 6-23 presents the scour histories of the six cases with different water depth. These six cases can be divided into two groups, pressurized flow and overtopping flow. If the water surface is between low chord and deck surface, the flow is called pressurized flow. Actually, the flow with water surface just touching low chord (like Case (b)) is hardly pressurized. If the water surface is higher than the bridge deck surface, the flow is called overtopping flow. It should be noted that the flow under the bridge deck is still pressurized when overtopping occurs. For the three pressurized cases, water surface elevation varies from low chord to the high chord. The channel contraction ratio

increases with the increase of water depth. And the scour depth will also increase. This can be observed in figure 6-23. For the three overtopping cases, the channel contraction ratio decreases with the increase of water depth. This explains why the scour depth decreases with the increase of the water depth when overtopping. Hence, the deepest scour depth can be reached when water surface is in flush with deck surface. This is the limiting condition that a flow can generates for a certain bridge. However, the influence of the water depth on scour development is not large for overtopping conditions when the water deep enough. This is supported by the difference of the curves of 0.8 ft overtopping and 1.2 ft of overtopping.

The correction factor of overtopping flow for maximum abutment scour depth equation will be proposed based on these numerical studies. The influence is evaluated based on the condition of open channel flow with water surface elevation flush with the low chord of bridge. Scour is the interaction between flow and soils. All those parameters affecting shear stress in chapter IV and soil erosion property will impact the scour development in overtopping situations. The primary actions of flow on soils are the fluctuating stresses applied on the soil particles. Shear stress component is believed to be dominant. The maximum bed shear stress is commonly used to represent the erosion capacity of the flow. The critical shear stress of the soil is used to represent the erosion resistance of the soil. Hence, the correction is proposed based on the difference between the maximum bed shear stress and the critical shear stress of soils. However, the location of the initial maximum bed shear stress may not be same to the final deepest

scour hole. So the initial maximum bed shear stress has to be corrected. The form of the equation is proposed as:

$$K_p = \frac{Z_{\max}}{Z_{\max\_low\ chord}} = \frac{\gamma\tau_{\max\_overtopping} - \tau_c}{\gamma\tau_{\max\_low\,\text{chord}} - \tau_c} \tag{6.4}$$

What concerned is the final deepest scour hole that can be generated by certain flow. The scour history presented in figure 6-23 is only for 10 days. For most cases, $Z_{\max}$ at 10 days is much lower than the final $Z_{\max}$. To get the final $Z_{\max}$, hyperbolic model is utilized to do the prediction. The form of the hyperbolic model is as same as in SRICOS method and defined as:

$$Z(t) = \frac{t}{\frac{1}{\dot{Z}_{ini}} + \frac{t}{Z_{\max}}} \tag{6.5}$$

Where $Z(t)$ is the maximum scour depth at time instant t; $\dot{Z}_{ini}$ is the initial erosion rate; $Z_{\max}$ is the final maximum scour depth.

d_1 (ft)	0	0.2	0.4	0.8	1.2	1.6
Z_{max} (mm)	55.25	263.16	500.00	178.57	72.46	42.92
Z_{max} (mm) @240hr	39.00	113.00	174.00	80.00	45.72	29.87
τ_{max} (Pa)	1.82	2.61	3.49	2.32	1.89	1.74
Z_{max}/Z_{max_Low}	1.00	4.76	9.05	3.23	1.31	0.78
$(r\tau_{max}-\tau_c)/(r\tau_{max\_low}-\tau_c)$	1.00	4.75	8.88	3.36	1.33	0.61
Note	r = 0.342; τ_c=0.55Pa					

Table 6-3 Simulation results of overtopping cases.

The predicted final maximum scour depths for these six cases are tabulated in table 6-3. According to the results, the small increase of bed shear stress could cause a

huge increase in scour depth. For example, $\tau_{\max}$ in Case (c) is 3.49 Pa, which is about two times of the maximum bed shear stress in Case (a). And the final $Z_{\max}$ turns out to be as high as nine times of the deepest hole in Case (a). Based on these six simulations, the constant number of $\gamma = 0.342$ is found to suitable for getting the correction factor K_p. The critical shear stress of 0.55 Pa is used in the analysis.

The $\tau_{\max\_overtopping}$ can be evaluated with the proposed equation in chapter IV. Another way is to correct $\tau_{\max\_lowchord}$. The correction factor is proposed based on the simulation results. One way is to plot the ratio of $\tau_{\max\_overtopping} / \tau_{\max\_lowchord}$ as the function of d_1 / h, shown in figure 6-24. K_o is the correction factor of overtopping flow, equal to $\tau_{\max\_overtopping} / \tau_{\max\_lowchord}$. K_o reaches the maximum when the water depth is flush with deck surface. Correction factor of 1 is recommended when the d_1/h is greater than 1.

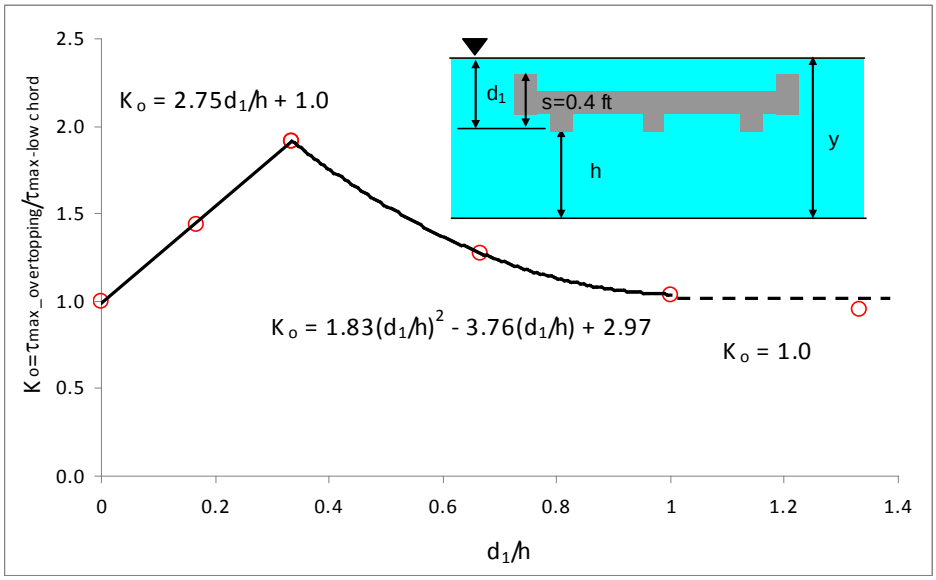

Figure 6-24 Shear stress correction factor for overtopping flow.

CHAPTER VII

CONCLUSIONS AND RECOMMENDATIONS

7.1 Conclusions

The CHEN3D program has been applied to study the bed shear stress around abutment in river channel. Based on the systematic parametric studies, the equation has been proposed to estimate the maximum bed shear stress at the initial conditions of the scouring. The chimera technique incorporated in the program makes it possible to simulate the complex channel geometries, such as the channel overtopping, confluence of the channel. Scour models for clear water scour have been studied. The influence of bed form roughness and the flow turbulence has been considered in the scour prediction of the flume tests. The scour under overtopping condition has also been studied numerically. The followings are the main conclusions obtained in this research:

1. Reynolds number is dominant for the maximum bed shear stress around abutment. The relationship is not identical to the pier equation because of the retarding effect of the lateral bank wall and the abutment shape.
2. The shallow water effect is observed in the maximum bed shear stress study when the relative water depth is small. Froude number is chosen to present the result.
3. The maximum bed shear stress around abutment is found to be linear proportional with the channel contraction ratio. The channel contraction ratio

should be calculated based on the flow conveyance ratio. The area ratio can be used only when the upstream flow is uniformly distributed.

4. The maximum bed shear stress decreases with the increase of the aspect ratio of the approach embankment. When the aspect ratio is large, the influence tends to be constant.
5. Among the studied abutment shapes, vertical wall abutment can cause the highest bed shear stress and the spill-through abutment can cause the lowest one. The shape factor of wing-wall abutment is slightly higher than that for spill-through abutment.
6. For the abutments with same projected length normal to the flow, the skew angle of 90 degree can cause the highest bed shear stress. The influence of the skew angle will decrease when the abutment inclines to either upstream or downstream.
7. In compound channel, the maximum bed shear stress will increase when the abutment is very close to the main channel slope.
8. The maximum bed shear stress equation is limited to the hydraulic smooth boundary. In the actual scouring process, both of the turbulence and the bed roughness contribute the initial erosion rate. The apparent maximum bed shear stress has been recommended to compensate the underestimation of the proposed equation.
9. When channel is overtopping, the maximum bed shear stress around abutment is found to be the highest when the water surface is in flush with the deck surface.

If the water depth continues to increase, the bed shear stress will begin to decrease.

10. Assuming the blockage effect of the deck is same to the abutment, the proposed maximum bed shear stress equation is found to be able to predict the maximum bed shear stress in rectangular channel under overtopping condition with 10% of difference.
11. Bridge deck tends to make flow more uniform when overtopping occurs. For rectangular channel, the bed shear stresses increase much faster at channel center than around abutment. In compound channel, the change of the bed shear stress at the channel center is not as significant as the rectangular channel because of the water depth difference between the main channel and the flood plain.
12. For the abutment exists in channel bend suffering open channel flow, the bed shear stress around the abutment is affected by the channel geometry significantly when the R/W is small. High curvature can cause the highly non-symmetric bed shear stress distribution. If the abutment is located in the middle of the bend, the inner flood plain will have higher bed shear stress. If the abutment is located at the end of the bend, the outer flood plain will have higher bed shear stress. The influence of the abutment shape is similar to the straight channel condition.
13. When overtopping in channel bend, the deck tends to diminish the non-symmetric feature of flow caused by the bend. The bed shear stress distribution observed under the deck is basically in symmetry. The abutment location on the

bend has little influence to the bed shear stress under the deck. But it will affect the downstream bed shear stress pattern. If the abutment is in the middle of the bend, the downstream bed shear stress can recover the non-symmetric pattern. The influence of the abutment shape still exists under overtopping condition.

14. The tributary upstream can cause the non-symmetric flow and bed shear stress pattern when the confluence is close to the bridge. The abutment opposite the tributary may have higher bed shear stress than the other side.
15. Bed shear stress, roughness and flow turbulence all contribute to the scour development. The contribution of roughness and turbulence may be as same as the bed shear stress around the abutment. But the turbulence effect is negligible in the scour development away from the hydraulic structures.
16. The correction factor of the scour under overtopping conditions is found to depend on both the maximum bed shear stress and critical shear stress of the soils. The variation of the scour depth with water depth is similar to the trend for shear stress since the simple shear stress model is applied. But the increase of the scour depth is much faster than the increase of the bed shear stress when exceeding the critical shear stress of the bed soils.

7.2 Recommendations

The current research is mainly simulating small scale channels of the flume size with CHEN3D program (two layer turbulence model). The model scale, the turbulence model, and the boundary condition might all constrain the universal application of the major conclusions. The followings are recommended for the future investigations:

1. Large eddy simulation should be performed to check the influence of the turbulence model in the shear stress simulation and the scour prediction.
2. Roughness model should be further developed to reflect the bed roughness effect, especially the bed form roughness.
3. Based on the flume tests, the velocity fluctuation is found to be related with the scour development at the downstream side of abutment. The study of the scour model in clear water scour can be performed toward that direction.

REFERENCES

Abed, L. M. 1991 Local scour around bridge piers in pressure flow. Ph.D. Dissertation, C.E. Dept., Colorado State Univ., Fort Collins, CO.

ABSCOUR USERS MANUAL 2007 Maryland State Highway Administration, Baltimore, MD.

Arneson, L.A. 1997 The effects of pressure flow on local scour in bridge openings. Ph.D. Disseration, C.E. Dept., Colorado State Univ., Fort Collins, CO.

Arulanandan, K. 1975 Fundamental aspects of erosion in cohesive soils. *J. of Hydraulic Division, ASCE*, **101**, 635-639.

Arulanandan, K., Loganathan, P. & Krone, R.B. 1975 Pore and eroding fluid influences on surface erosion of soil. *J. of Geotechnical Engineering*, **101**, 51-66.

Awazu, S. 1967 On scour around spur dikes. In *Proc. of 12th Congr. of the Intl. Assn. for Hydraulic Research*, **3**, C12, Delft, The Netherlands.

Briaud, J.-L., Ting, F., Chen, H.C., Gudavalli, S.R., Kwak, K., Philogene B., Han S.-W, Perugu, S., Wei, G., Nurtjahyo, P., Cao Y.W. & Li, Y. 1999 SRICOS: prediction of scour rate in cohesive soils at bridge piers, *TTI Report No. 2937-1*, Department of Civil Engineering, Texas A&M University, College Station, Texas.

Briaud, J.-L., Ting, F., Chen, H.C., Cao, Y., Han, S.-W., Kwak, K. 2001 Erosion function apparatus for scour rate predictions. *J. of Geotechnical and Geoenvironmental Engineering, ASCE*, **127**, 105-113

Briaud J.-L., Chen H.-C., Li Y., Nurtjahyo P., Wang J. 2003 Complex pier scour and contraction scour in cohesive soils, *NCHRP Report 24-15*, Transportation Research Board, National Research Council, Washington, DC.

Cao, Y. 2001 The influence of certain factors on the erosion functions of cohesive soil. M.S. Thesis, Texas A&M University, College Station, TX.

Cebeci, T. & Bradshaw, P. 1977 *Momentum transfer in boundary layers*. Hemisphere Publishing Corporation, Washington, DC.

Chabert, J., & Chauvin, J.L. 1963 Formation de dunes et de rides dans les modeles fluviaux. *Bull. Cen. Rech. Ess. Chatou*, **4**, 345-376.

Chen, C.J & Chen, H.C. 1982 The finite analytic method. *IIHR Report No. 232-IV*, Iowa Institute of Hydraulic Research, University of Iowa, Iowa City.

Chen, C.J & Chen, H.C. 1984 Finite analytic numerical method for unsteady two-dimensional Navier-Stokes equation. *J. of Computational Physics*, **53**, 210-226.

Chen, H.C. & Patel, V.C. 1988 Near-wall turbulence models for complex flows including separation. *AIAA Journal*, **26**, 641-648.

Chen, H.C. & Patel, V.C. 1989 The flow around wing-body junctions. In Proc. 4th Symposium on Numerical and Physical Aspects of Aerodynamic Flows, 1-15, Long Beach, CA.

Chen, H.C., Patel, V.C., & Ju, S. 1990 Solutions of Reynolds-averaged Navier-Stokes equations for three-dimensional incompressible flows. *J. of Computational Physics*, **88**, 305-336.

Chen, H.C. & Korpus, R.A. 1993 A multi-block finite-analytic Reynolds-averaged Navier-Stokes method for 3D incompressible flow. *Individual Papers in Fluids Engineering, ASME*, **150**, 113-121.

Chen, H.C. 2002 Numerical simulation of scour around complex piers in cohesive soil. In Proc. of First International Conference on Scour of Foundation, 14-33, Texas A&M University, College Station.

Dufresne, M., Vazquez, J., Terfous, A., Ghenaim, A., Poulet, J.-B. 2007 Prediction of sedimentation in a storm-water tank pilot using computational fluid dynamics. *Ninth International Symposium on Fluid Control, Measurement and Visualization*, ID 27 Tallahassee, FL.

Dunn, I. S. 1959 Tractive resistance of cohesive channels. *J. of Soil Mechanics and Foundation Division, ASCE,* **85**, 1-24.

Durbin, P.A., Medic, G., Seo, J.M., Eaton, J.K. and Song, S. 2001 Rough wall modification of two-layer $k-\varepsilon$. *J. of Fluids Engineering*. **123**, 16-21.

Hjorth, P. 1975 Studies on nature of local scour. *Bulletin Series A. No. 46*, Department of Water Resources Engineering, Lund Institute of Technology/University of Lund, Sweden.

Ivarson, W.R. 1998 Scour and erosion in clay soils. *ASCE Compendium of Conference Scour Papers (1991 to 1998)*, 104-119.

Jiang, J., Ganju, N.K. & Menta, A.J. 2004 Estimation of contraction scour in riverbed using SERF. *J. of Waterway, Port, Coastal, and Ocean Engineering*, **130**, 215-218

Jones, J.S., Bertoldi, David, A. & Umbrell, E.R. 1993 Preliminary studies of pressure flow scour, In Proceedings of the ASCE Hydraulic Engineering Conference, San Francisco, CA.

Knight, D.W. & Demetriou, J.D. 1983 Flood plain and main channel flow interaction. *J. of Hydraulic Engineering,* **109**, 1073-1092.

Li, Y. 2002 Bridge pier scour and contraction scour in cohesive soils on the basis of flume test. Ph.D. Dissertation, Department of Civil Engineering, Texas A&M University, College Station.

Liu, H.K. 1957 Mechanics of sediment-ripple formation. *J. Hyd. Div. ASCE,* **183** (HY2), 1-23

Liu, T.J. 2002 Time-domain simulation of large-amplitude ship motions including capsizing. Ph.D. Dissertation, Department of Civil Engineering, Texas A&M University, College Station.

Melville, B. W. 1997 Pier and abutment scour: integrated approach. *J. of Hydraulic Engineering, ASCE,* **123**, 125-136.

Mirtskhoulava, 1988 *Basic physics and mechanics of channel erosion.* Gidometeoizdat, Leningrad.

Molinas, A., Kheireldin, K. & Wu, B. 1998 Shear stress around vertical wall abutments. *J. of Hydraulic Engineering,* **124**, 822-830

Munson, B.R., Young, D.F. & Okiishi, T.H. 1998 *Fundamentals of fluid mechanics,* Wiley, New York

Myers, W.R.C. & Brennan, E.K. 1990 Flow resistance in compound channels. *J. of Hydraulic Research*, **28 (**2), 141-155

Naot, D., Nezu, I. & Nakagawa, H. 1993 Hydrodynamic behavior of compound rectangular open channels. *J. of Hydraulic Engineering*, **119**, 390-408

Nurtjahyo, P. 2003 Chimera RNAS simulations of pier scour and contraction scour in cohesive soils. Ph.D. Dissertation, Texas A&M University, College Station.

Oh, S.J., 2008 Experimental study of bridge scour in cohesive soils. Ph.D. Dissertation, Department of Civil Engineering, Texas A&M University, College Station.

Parchure, T.M. & Mehta, A.J. 1985 Erosion of soft cohesive sediment eeposit. *J. of Hydraulic Division*, ASCE, **111**, 1309-1326

Patel, V.C. & Yoon, J.Y. 1995 Application of turbulence models to separated flow over rough surfaces. *J. of Fluid Engineering*, **117**, 234-241.

Rajaratnam, N. & Ahmadi, M. 1979 Interaction between main channel and flood-plain flows. *J. of Hydraulic Division*, **105 (**HY5), 573-588.

Rajaratnam, N. & Nwachukwu, B. 1983 Flow near groin-like structure. *J. of Hydraulic Engineering*, **109**, 463-480.

Richardson, E. V. & Davis, S. M. 2001 Evaluating scour at bridges, *FWHA-IP-90-017*, *HEC No.18*, US Department of Transportation, Washington, D. C.

Shaikh, A., Ruff, J. F., & Abt, S. R. 1988 Erosion rate of compacted Na-Montmorillonite soils. *J. of Geotechnical Engineering*, ASCE, **114**, 296–305.

Shirole, A.M., and Holt, R.C. (1991), "Planning for comprehensive bridge safety assurance program." *Transp. Res. Rec. 1290*, Transportation Research Board, Washington, D.C., 137-142.

Simons, D.B.& Richardson, E.V. 1963 Form of bed roughness in alluvial channels. Trans. ASCE, **128**, 284-323

Simons, D.B.& Richardson, E.V. 1966 Resistance to flow in alluvial channels. *Professional Paper 422-J*. Washington, D.C., U.S. Geological Survey,

Smerdon, D.B. & Beasley, M.L. 1959 Tractive force theory applied to stability of opens channels in cohesive soils. *Research Bulletin No. 715*, Agricultural Experiment Station, The University of Missouri, Columbia.

Suhs, N. E. & Tramel, R. W. 1991 *PEGSUS 4.0 Users Manual*. Arnold Engineering Development Center Report, *AEDC-TR-91-8,* Arnold Air Force Station, TN.

Tingsanchali, T. & Maheswaran, S. 1990 2-D Depth averaged flow computation near groyne. *J. of Hydraulic Engineering*, **116**, 71-86.

Umbrell, E.R., Kenneth, Y.G., Stein, S.M. & Jones, J.S. 1998 Clearwater contraction scour under bridges in pressure flow. *J. of Hydraulic Engineering, ASCE,* **124**, 236-240

van Rijn, L. C. 1984a Sediment transport: Part I: bed load transport *J. of Hydraulic Engineering*, **110**, 1431-1456.

van Rijn, L. C. 1984b Sediment transport: Part II: suspended load transport. *J. of Hydraulic Engineering*, **110**, 1613-1641.

van Rijn, L. C. 1984c Sediment transport: Part III: bed form and alluvial roughness. *J. of Hydraulic Engineering*, **110**, 1733-1754.

Wei, G., Chen, H.C., Ting, F, Briaud, J.-L, Gudavalli, S.R. & Perugu, S. 1997 Numerical simulation to study scour rate in cohesive soils. *Research Report prepared for the Texas Department of Transportation*, Department of Civil Engineering, Texas A&M University, College Station.

Winterwerp, J.C. 1989 *Cohesive sediments, flow included erosion of cohesive beds.* Rijkswaterstaat / Delft Hydraulics, Delft.

Wolfstein, M. 1969 The velocity and temperature distribution in one-dimensional flow with turbulence augmentation and pressure gradient. *Intl. J. of Heat and Mass Transfer*, **12**, 301-318.

Wormleaton, P.R. & Merrett, D.J. 1990 An improved method of calculation for steady uniform flow in prismatic main channel/flood plain sections. *J. of Hydraulic Research*, **28**, 157-174

Yalin, M.S. 1964. Geometrical properties of sand waves. *J. Hyd. Div. ASCE*, **90** (HY5), 105-119.

Zaghloul, N.A. 1974 Analytical and experimental investigation of flow around spur dikes. Ph.D. Dissertation, Department of Civil Engineering, University of Windsor, Ontario, Canada.

Zhang, H., Faghri, M. & White, F.M. 1996 A New low-Reynolds-number $k-\varepsilon$ model for turbulent flow over smooth and rough surfaces. *J. of Fluids Engineering*, **118**, 255-259.

VITA

Xingnian Chen was born in Liaoning, China. He earned his Bachelor of Engineering in Civil Engineering in July 1997 and sequentially the Master of Engineering in Geotechnical Engineering in June 2000 from Tongji University, China. From March 2000 to July 2003, he was a researcher with Shanghai Seakon Engineering Research and Consulting Center, China. In August 2003, he entered Texas A&M University, where he served as a research assistant with the Texas Transportation Institute. He completed his Ph.D. in Civil Engineering in December 2008. His research was on numerical study of abutment scour. His research interests are fluid-structure-soil interaction, and soil improvement.

Permanent Address

Xingnian Chen

c/o: Dr. Jean-Louis Briaud

Zachry Department of Civil Engineering

Texas A&M University

College Station, TX, 77840-3136